INVESTIGATION OF COASTAL DYNAMICS OF THE ANTARCTIC ICE SHEET USING SEQUENTIAL RADARSAT SAR IMAGES

A Thesis

by

SHENG-JUNG TANG

Submitted to the Office of Graduate Studies of
Texas A&M University
in partial fulfillment of the requirements for the degree of

MASTER OF SCIENCE

May 2007

Major Subject: Geography

INVESTIGATION OF COASTAL DYNAMICS OF THE ANTARCTIC ICE SHEET USING SEQUENTIAL RADARSAT SAR IMAGES

A Thesis

by

SHENG-JUNG TANG

Submitted to the Office of Graduate Studies of
Texas A&M University
in partial fulfillment of the requirements for the degree of

MASTER OF SCIENCE

Approved by:

Chair of Committee,	Hongxing Liu
Committee Members,	Andrew G. Klein
	John R. Giardino
Head of Department,	Douglas J. Sherman

May 2007

Major Subject: Geography

ABSTRACT

Investigation of Coastal Dynamics of the Antarctic Ice Sheet Using
Sequential Radarsat SAR Images. (May 2007)
Sheng-Jung Tang, B.Eng., National Taiwan University of Science and Technology
Chair of Advisory Committee: Dr. Hongxing Liu

Increasing human activities have brought about a global warming trend, and cause global sea level rise. Investigations of variations in coastal margins of Antarctica and in the glacial dynamics of the Antarctic Ice Sheet provide useful diagnostic information for understanding and predicting sea level changes. This research investigates the coastal dynamics of the Antarctic Ice Sheet in terms of changes in the coastal margin and ice flow velocities. The primary methods used in this research include image segmentation based coastline extraction and image matching based velocity derivation.

The image segmentation based coastline extraction method uses a modified adaptive thresholding algorithm to derive a high-resolution, complete coastline of Antarctica from 2000 orthorectified SAR images at the continental scale. This new coastline is compared with the 1997 coastline also derived from orthorectified Radarsat SAR images, and the 1963 coastline derived from Argon Declassified Intelligence Satellite Photographs for change detection analysis of the ice margins. The analysis results indicate, in the past four decades, the Antarctic ice sheet experienced net retreat and its areal extent has been reduced significantly. Especially, the ice shelves and glaciers on the Antarctic Peninsula reveal a sustained retreating trend. In addition, the advance, retreat, and net change rates have been measured and inventoried for 200 ice shelves and glaciers.

A multi-scale image matching algorithm is developed to track ice motion and to measure ice velocity for a number of sectors of the Antarctic coast based on 1997 and 2000 SAR image pairs. The results demonstrate that a multi-scale image matching algorithm is much more efficient and accurate compared with the conventional algorithm. The velocity measurements from the image matching method have been compared with those derived from InSAR techniques and those observed from conventional ground surveys during 1970-1971. The comparison reveals that the ice velocity in the front part of the Amery Ice Shelf has increased by about 50-200 m/a. The rates of ice calving and temporal variation of ice flow pattern have been also analyzed by integrating the ice margin change measurement with the ice flow velocity at the terminus of the outlet glacier.

DEDICATION

Dedicated to

My father, A-Ho Tang,

My mother, Yueh-Lan Lin, and

My sisters, Chin-Mei Tang and Shu-Mei Tang

ACKNOWLEDGMENTS

I would like to express my greatest gratitude to Dr. Hongxing Liu who not only guided me into the fascinating world of remote sensing and GIS, but also enriched my geospatial knowledge and research capability; his patient guidance and unceasing encouragement were added to the fuel tank to complete my academic journey.

Special thanks go to Dr. Andrew G. Klein and Dr. John R. Giardino for giving me their insightful advice and valuable comments on this research as my thesis committee members.

I feel grateful to Dr. Lei Wang who helped me to solve many technical and C programming problems and provided useful suggestions for improving research methods and algorithms. I also want to thank Bing-Sheng Wu, Bailiang Li, Zheng Cheng, Songgang Gu, Yige Gao, Kevin Merritt, and Joni Kincaid, for their big-hearted support and the wonderful time we spent together during the past two years. Especially, thanks to Joni Kincaid who helped me proof-read and edit my draft thesis.

Furthermore, Dr. Ken Jezek and Ms Katy Farness at Byrd Polar Research Center have provided the orthorectified Radarsat SAR images. This research could not have been completed timely without their assistance in preparing source image data.

Last, but not least, I would like to share my joy and happiness for Master thesis research with my heartfelt friends, Chih-Hung Wang, Min-Hua Tang, Shu-Ching Yang, and Tzu-Hsuan Chiu in Taiwan, for their support and help during my stay in the United States.

TABLE OF CONTENTS

LIST OF FIGURES

FIGURE Page

FIGURE Page

FIGURE Page

FIGURE Page

FIGURE Page

LIST OF TABLES

1 INTRODUCTION

1.1 Background

Over 98% of the Antarctic continent is covered by a great ice sheet. Despite its remote location, Antarctica plays an important role in the global climate system. The Antarctic continent covers approximately 14 million square kilometers, which is equivalent to the area of United States of America and Mexico. Glaciers, ice shelves and the ice sheet in Antarctica store over 70% of Earth's fresh water resource (Hooke, 2005; Paterson, 1994). The ice sheet is extremely sensitive to both atmospheric and oceanic temperature changes, and the ice sheet influences the ocean and atmosphere in a complicated manner (Bender et al., 2002; Petit et al., 1999; Schwerdtfeger, 1984).

Global warming significantly influences the mass balance of the Antarctica ice sheet and outlet glaciers (IPCC, 2001). Melting glaciers and ice sheets may contribute to an increase in sea level and threaten the existence of coastal cities around the world by the end of the twenty-first century (Arendt et al., 2002; Joughin, 2006; Oerlemans, 2005). Were the Antarctic ice sheet to melt completely, it would contribute more than 57 m of global sea level. Measuring the coastal dynamics of the Antarctic ice sheet and its outlet glaciers is important because our knowledge and understanding of Antarctica's mass input into the Southern Ocean is still limited. This leads to imprecise estimations in global sea level changes.

Knowledge of the variation in the ice margins along the Antarctic coast can aid the

---

This thesis follows the style of *Remote Sensing of Environment.*

interpretation of mass balance and its mass contribution to the global sea level changes (Bamber & Payne, 2004). Ice shelves, glacial tongues and ice terminus are the most dynamic features in the Antarctic coast. Comparing ice margin (coastline) changes over time is an effective approach to investigate coastal dynamics. Although some researchers have studied ice margin changes for some specific locations of the Antarctic coast, the advance, retreat and change rates at the continental scale are poorly known (Fox & Cooper, 1994; Remy & Minster, 1997; Remy & Legresy, 2004). This is due to the previous lack of continental scale data sources and formidable data processing effort required.

Antarctica is the coldest, windiest, and highest continent on Erath. Satellite remote sensing technology overcomes the obstacles of surface travel and provides the comprehensive observations needed for modern scientific investigations of ice dynamics of the Antarctic Ice Sheet. Optical sensors are affected by often cloudy weather and long polar nights in Antarctica. With the ability to fly unimpeded by the harsh climate and to peer through clouds and to observe day and night, space-borne radar instruments can provide continental scale coverage of the Antarctic Ice Sheet at very high spatial resolution. During September and October, 1997, the entire Antarctic continent was imaged at a 25 m resolution by Radarsat-1 Synthetic Aperture Radar (SAR) sensor as the first Antarctic Mapping Mission (AMM-1) (Jezek et al., 1998). From September to November 2000, the Antarctic Ice Sheet up to 82°S latitude was imaged three times by Radarsat-1 SAR sensor during the second Antarctic Mapping Mission 2 (AMM-2) (Jezek et al., 2003). The availability of the 1997 and 2000 satellite radar image data make it possible to examine the ice dynamics of the Antarctic coast at the continental scale.

Traditionally, ice margins or coastlines were delineated manually by tracing image overlays on a light table or by on-screen digitizing. In the past decades, a great deal of research efforts has been devoted to the automation of coastline delineation technique (Allen & Long, 2006; Collings et al., 2006; Dash et al., 2001; Herzfeld, 1999; Liu & Jezek, 2004a). The automatic numerical method is essential for deriving accurate coastlines for different years at the continental scale by processing massive high-resolution satellite data.

The ice flow magnitude and pattern is the another important aspect in studying coastal ice dynamics. The ice flow information is related to the stability of the ice sheet, and the ice flow velocity is required for determining the amount of ice that is carried from the accumulation zone to the ablation zone (Paterson, 1994). Many methods have been employed previously to measure ice velocity, including the repeated measurements of ground marks (stakes) using conventional survey instruments or GPS units, the feature tracking method based on time series of remote sensing images, and the interferometric SAR technique. In the recent decade, a large number of applications have demonstrated that the InSAR technique is most effective in generating highly precise two dimensional velocity measures at a high spatial resolution. However, the InSAR technique is limited by the availability and cost of interferometric data and may fail by temporal decorrelation. The feature tracking method is a low-cost alternative and only requires images acquired at different times. The image matching algorithm has been used by various researchers to automate the feature tracking method (Scambos et al., 1992). Although inferior to the InSAR technique in the velocity measurement precision, the image matching based feature tracking method is much less influenced by temporal decorrelation. Both optical and radar images can be utilized in the feature tracking method to derive dense velocity measurements. Therefore, the feature tracking method and the InSAR method are complementary.

This research will exploit the orthorectified Radarsat SAR images acquired in 1997 and 2002 to conduct the continental scale of analysis on the ice dynamics of the Antarctic coast. The technical deficiencies associated with the image segmentation based coastline extraction method and the image matching based ice velocity derivation method will be addressed, and the coastal margin changes and ice flow pattern will be analyzed.

1.2 Research Scope and Objectives

The general goal of this research is to investigate the ice dynamics in the Antarctic coast with the high-resolution sequential satellite images. Specific objectives include:

- Improving the automated coastline extraction method and extracting a complete, high resolution (25 m) coastline of the Antarctic continent by processing the 2000 Radarsat SAR images;
- Determining the advance, retreat, and net change rates of the Antarctic ice margins at the continental scale by comparing the newly extracted 2000 coastline with the 1997 and 1963 coastlines, and making a change rate inventory for major ice shelves and outlet glaciers.

- Developing a multi-scale, hierarchical image matching method to improve the computational efficiency and matching quality for ice velocity measurements.
- Deriving two-dimensional ice velocity measurements for selected ice shelves and outlet glaciers in the Antarctic coast by applying the multi-scale image matching method to the 1997 and 2000 SAR image pairs.
- Analyzing the spatial-temporal pattern and behaviors of the Antarctic margin changes and coastal ice flow by comparing and integrating coastlines and ice velocities of different times.

1.3 Methodology

The primary data sources used in this research are the SAR images acquired in 1997 and 2000. In 1997, the entire Antarctic continent was imaged over 30 days by the Canadian Satellite Radarsat-1 using a C-band (5.6 cm wavelength) radar sensor. During the mission, Radrasat-1 was maneuvered in orbit to rotate the normally right-looking SAR to a left-looking mode to image the interior of the Antarctica for the first time. In 2000, the Antarctic continent was imaged up to 86°S latitude by the Radarsat-1 SAR sensor. The coastal regions were imaged mainly using the standard beam 2 with a nominal incidence angle of 24° to 31°, and the acquired SAR images have a 25 m spatial resolution. The geocoding, terrain correction and rigorous orthorectification of both 1997 and 2000 SAR images have been completed at the Byrd Polar Research Center. The data analysis of this research is based on the orthorectified SAR images at 25 m spatial resolution. The SAR images are in Polar Stereographic projection with the reference to WGS84 ellipsoid. The absolute geolocation accuracy of the SAR images is about 50-100 m. The precisely orthorectified SAR images warrants the fidelity of geographical position of the extracted coastline and the accuracy of the derived ice flow velocity.

Two major methods have been employed to process the sequential SAR images at the continental scale: image segmentation based coastline extraction and image matching based velocity derivation. These two methods combine a chain of digital image processing algorithms that greatly automate the coastline extraction and velocity derivation. The tedious and labor-intensive on-screen delineation and visual feature tracking are avoided. The processing chain and data flow involved in this research is illustrated in Figure 1.1.

The image segmentation based coastline extraction method has been proposed and implemented by Liu and Jezek (2004a), and a high resolution coastline has been extracted based on the 1997 SAR images (Liu & Jezek, 2004b). The key algorithm element is to segment SAR images into water (ocean) objects and land (ice sheet) objects based on a locally adaptive thresholding. Before the image segmentation, the SAR images are preprocessed with Lee filter and anisotropic diffusion operator to suppress the radar speckle noise and enhance coastline features. After segmentation, the region grouping and labeling algorithm is applied to perform two passes of removal of small noisy image objects, and morphological operations and a robust recursive edge-tracing algorithm are applied to refine and extract the vector coastlines. In this research,

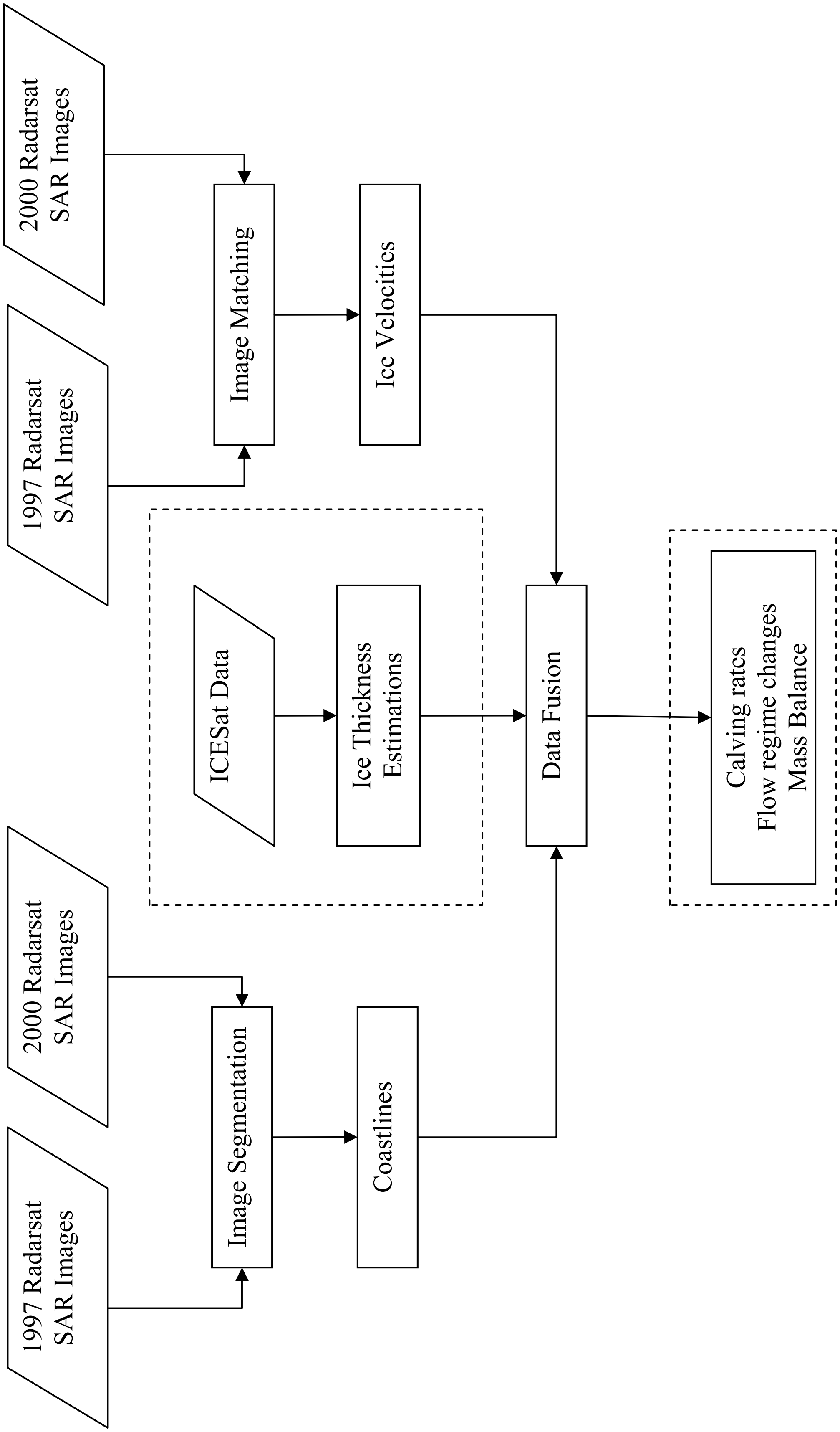

Figure 1.1 Image processing methods and data flow chart

the image segmentation based coastline extraction method developed by Liu and Jezek (2004a) is further modified to improve the computational efficiency by using the 1997 coastline as the initial approximate to the 2000 coastline position. By specifying a small buffering zone of the 1997 coastline, the data processing volume is greatly reduced and the reliability and accuracy of the extracted coastline for the year 2000 have been ensured and improved. In addition, the source C codes of the image segmentation based coastline extraction method are embedded into a graphical interface developed by using VB .NET and ArcObjects, and an extension module for automated coastline extraction has been built in ArcGIS. The newly derived coastline from the 2000 SAR images are overlaid and compared in ArcGIS environment with the 1997 coastline derived from the Radarsat SAR images and the 1963 coastline derived from the Argon DISP (Declassified Intelligence Satellite Photographs) images. The ice margin advance, retreat, and net change rates are determined for the Antarctic ice sheet during the past four decades.

Previous studies have demonstrated that the effectiveness of applying feature tracking methods to sequential satellite images to measure ice velocity. The early studies (Doake & Vaughan, 1991; Lucchitta & Ferguson, 1986) used a visual technique to manually track recognizable ice features (conjugate points) on two images acquired at different times. Small, sharp, distinctive surface features are identified on one image, and the corresponding locations (conjugate points) of the same features are then visually identified on the other (subsequent) image. Their positional differences, namely, spatial displacements, are manually or mechanically measured, and the flow velocities are calculated by incorporating the information about the time interval separating two sequential images. The traditional visual method is tedious and time-consuming, and measurement precision is also limited and subject to human operators. The introduction of image matching algorithms has largely automated the feature-tracking process (Bindschadler et al., 1996; Scambos et al., 1992). The commonly used image matching algorithm in the feature tracking applications is the areal based cross-correlation, in which each image chip (small rectangular image area) selected from the reference image (early image) is searched and correlated with a matching chip in a larger search area within the second image (late subsequent image). The correlation coefficient between the reference chip and the search chip is calculated at every center-pixel location in the search area for which the reference chip will fit entirely within the search area. Then, a mathematic function can be fitted in the peak region of correlation surface of the search area, and the match location of conjugate feature can be determined by identifying the maximum extreme of the mathematic surface at sub-pixel accuracy (0.1 pixel). The use of the image cross-correlation algorithm not only greatly improves the efficiency of feature tracking, but also relaxes the requirement of the presence of small distinctive features in the sequential image pair. The diffuse, extended features can be also utilized in the image cross-correlation algorithm to create precise velocity measurements. However, the conventional cross-correlation algorithm may be computationally very intensive to create a dense set of velocity measurements, especially in the high velocity-gradient areas or for sequential images with a relatively large temporal span. The velocity variation in the scene can create the variable position shifts of features. Features in the slow moving area may travel only a few pixels, while the features in the fast moving areas can travel tens or even a hundred of pixels. To accommodate and ensure successful matching for all features in the scene, a large search area has to be specified so that the correct match (conjugate) point is most likely within this search area. This will cause a dramatic increase in the computation intensity and processing time, and also generate unreliable and spurious matches since the greater the search area, the more likely one is to find a spurious match point.

To combat the above problems of conventional cross-correlation algorithm, a multi-scale, hierarchical image matching algorithm is developed and implemented in this research as an ArcGIS extension module. The idea of multi-scale, hierarchical image matching is to use rough and approximate match points obtained at a coarse resolution as a guide for searching for more precise matches at a higher resolution. First, an image pyramid, a sequence of copies of original images with a decreasing resolution and sample density, is first created. The cross-correlation matching is conducted on the coarsest resolution with a largely reduced image. The matching result is then employed as initial seed points to search for more accurate matches in a new iteration of matching operation based on the next level of higher resolution image. A robust statistical indicator is incorporated in each iteration of the hierarchical matching process to filter the match outliers and gross errors and enhance the reliability of the matching results. This iterative matching process continues until the final matching operation is performed on the full-resolution image. At each matching iteration, the locational accuracy of match points, and hence the accuracy of displacement measurements successively increase. Since most iterations are performed on images of reduced size with a small search range, the multi-scale, hierarchical image matching algorithm significantly speeds up the computation, and also reduces the occurrences of bad and spurious match points from false correlation maxima.

The velocity fields will be extracted for selected ice shelves and outlet glaciers by using the multi-scale, hierarchical image matching algorithm. The derived velocity fields will be compared with the historical velocity measurements and recent InSAR measurements, and the dynamic behavior of ice shelves and outlet glaciers will be examined. The ice advance and retreat rates derived from comparing sequential coastlines will be integrated with the ice flow velocity derived by multi-scale image matching to ice calving rates and gauge ice mass loss to the ocean.

1.4 Organization of the Thesis

This thesis consists of six sections. The present section introduces the research background and objectives and outlines the research methodology.

Section 2 reviews conventional methods for detecting ice margins (coastlines) and measuring ice motion. The advantages and disadvantages of these methods are discussed and evaluated. In addition, quantitative methods for determining ice calving rates and mass balance will be discussed.

Section 3 presents the method and findings about ice margin change detection for the Antarctica. The section starts with a discussion of an automated method to deal with satellite images. The data processing will be described step by step. Then, the automated method will be applied to extract the Antarctic coastlines from the 2000 Radarsat images. The extracted coastline will be and evaluated and validated for the accuracy. In the final section, the 2000 coastline will be compared with the 1997 coastline and 1963 coastline to determine the ice margin advance and retreat rates, and the comparison results will be reported.

Section 4 details the development of multi-scale image matching algorithm and its application results. At the start of the section, the basic idea and principle of image matching are introduced. Then, the steps and algorithm component of multi-scale image matching is presented, and its performance is evaluated. Next, the velocity fields extracted by the multi-scale image matching of the 1997 and 2000 SAR images will be analyzed by comparing with historical velocity observations and recent InSAR measurements. The observed changes in ice flow velocity magnitude and pattern will be reported.

The final section summarizes the research findings and contributions and discusses future research directions.

2 LITERATURE REVIEW ON METHODS FOR ICE DYNAMICS RESEARCH

This section reviews the literature related to the methods for ice dynamics studies. An overview of previous coastline extraction methods is presented, and then the image segmentation based automated coastline extraction is discussed in detail. Next, conventional methods for ice velocity measurements are reviewed. The final section introduce the basic concepts and principles of image matching based feature tracking method for measuring feature displacements and velocity.

2.1 Coastline Delineation Approaches

Traditionally, coastline delineation is conducted through visual interpretation and manual tracing of aerial photos or satellite imagery (Dellepiane et al., 2004). However, this technique can be very time consuming. Therefore, it is advantageous, especially for large spatial areas, to develop a more convenient and automated method. Coastlines as object boundaries can be detected by two possible image analysis methods: edge detection and image segmentation.

Object boundaries or edges are the most important image features that help people to sense objects and are compulsory in the application of image analysis or machine vision. Boundary detection identifies the boundaries between objects; in other words, the objects are extracted indirectly by their boundaries. First, this method makes use of the edge detector to identify points that may belong to a part of an edge. These points, extracted by the edge detector, possess properties that show regional discontinuities in certain features (e.g. grey value, contrast, texture or color). Specifically, the DN values for these pixels are dramatically different from those in their neighborhood. Second, after these points are extracted, they can be traced one by one, and then merged to form lines or object boundaries.

An edge detector is a boundary detection kernel. The zero-crossing operator is a popular edge detector. The zero-crossing approach is based on the calculation of first and second derivatives of the images. If the grey values of the image is uniform, the meaning of its first derivative, in mathematically, is zero; if the grey level has linear changes from blackness to whiteness, namely, the grey level shows a slope model, its first derivative will show a rectangular wave and the magnitude of this rectangular wave is proportional to its slope in grey level. Obviously, its second derivative will show a positive pulse located in the blackness portion, and a negative pulse located in the whiteness portion. When we connect pinnacles of both pulses together, the point where a line crosses the zero axis is called the zero-crossing. In this way, the edge location is precisely extracted.

The edge detection method is based on the strong variation and discontinuity of the digital number (DN) values near object boundaries. This method is operationally simpler than the segmentation method, but the disadvantage is that it can result in larger errors than are deemed acceptable for meaningful results. In addition, the application of the edge detection method to SAR images may be problematic due to the noise and speckles in SAR images (Touzi et al., 1988). Radar speckles can be reduced to improve the accuracy of boundary delineations from SAR images. For example, a median or Lee filter can be applied to SAR images before the use of edge detector (Lee & Jurkevich, 1990; Mason & Davenport, 1996). Although speckles in images can be largely reduced by these filters and edges in images can be increasingly detected with a better accuracy, some edges are still discontinuous. Numerically linking the broken edges from edge detectors is computationally very difficult. Therefore a post-processing step is needed to remove the false edges and then connect the separated true edges together. In contrast, the image segmentation method can automatically generate a continuous land boundary-coastline, although a complex procedure is involved.

There are several image segmentation techniques in use today. Image segmentation is used to separate a digital image into several significant sections that represent useful objects according to their homogeneity or differences. For example, the segmentation of water and land objects results in the land boundary-coastline. There are two main categories of image segmentation methods: region-based and histogram-based.

Region-based methods assume that pixels situated in a certain region or neighborhood have similar properties; therefore, analyzing the properties of neighborhoods of pixels can aid in identifying features for a region. The region-based method is relatively robust to image noise. The region growing algorithm is one type of region-based segmentation method. This algorithm starts with a set of seed pixels and the region of interest is expanded in all directions from these seed pixels until the image property significantly changes. In other words, a seed pixel in the interior of the object is assigned, and then the region grows around this pixel until the whole object is filled. The algorithm for the growing procedure measures the neighboring pixels around the seed pixel, then checks whether these pixels have the same property (e.g. grey value, color or texture) or not. Pixels that have been verified to be members of the object will be reiterated using the same algorithm until all of the particular pixels are examined.

The histogram-based method is the most straightforward approach used in the image segmentation process. In optical images, objects are recorded or acquired according to the light reflected from their surfaces by passive sensor systems. SAR images record the radar signals backscattered from the terrain surface. The histogram of image intensity can be analyzed to choose an appropriate threshold value to separate some meaningful objects from the background. Namely, the histogram-based method is used to define a certain range of digital number values (DN values) that represent objects in the images. The selection of a threshold is important, and an excellent scheme is to calculate thresholds (Pal & Pal, 1993). A dynamical thresholding algorithm was first conceived based on statistical principles in order to detect boundaries of the left ventricle of a human heart in radiographic images (Chow & Kaneko, 1972). A more comprehensive and automated method was derived by employing a local threshold determined by the algorithm to aid in sea ice classification (Haverkamp et al., 1995). A locally adaptive thresholding method has been developed to extract ice sheet margins and coastlines from SAR, SPOT and Landsat images (Liu & Jezek, 2004a; Sohn & Jezek, 1999). This research further improves the automated locally adaptive thresholding method developed by Liu and Jezek's (2004a) and applies it to the 2000 SAR image for automated coastline extraction.

2.2 Image Segmentation Based Coastline Extraction Method

The automated coastline extraction in this research is based on the locally adaptive thresholding algorithm, which belongs to image segmentation method. The basic idea of locally adaptive thresholding algorithm is to subdivide the entire image into small overlapping regions. It is not realistic to expect the entire image to have an ideal bimodal histogram. As a matter of fact, sometimes, the peak or valley in a bimodal histogram is not obvious, and the multimodal histogram dominates the intricate background or environment. Hence, it is hard to be assured of the positions of local maxima and minimum DN value. One strategy to deal with this situation is to subset an image into several small image regions. The local histograms of these regions contains land and water (namely coastline) should have a much higher chance to exhibit bimodal shape. If the local histogram does not present the bimodal type, the thresholding value can be calculated by interpolating the thresholding value of adjacent image regions (Bezdek et al., 1993; Cufi et al., 2002; Pal & Pal, 1993; Tarachandani & Boltz, 2006).

For each small image region, the histogram is analyzed and an optimal local threshold value is analytically determined for each image region to convert a grey level image into a binary image, consisting of the objects and the background. For example, an input image region I (x, y) can be transformed to an output binary image as follows:

$$\begin{aligned} I(x,y) &= 1, \quad if\ I(x,y) \geq T \\ &= 0, \quad if\ I(x,y) < T \end{aligned}$$

Where T is a thresholding value determined from the image histogram

Figure 2.1 illustrates the input image and Figure 2.2 indicates some image segmentation results using the histogram-based concept. If objects are clearly distinguishable from surrounding environments, the thresholding value is simple to define and the histogram-based method is appropriate to deal with image segmentation. Segmented images are shown in Figure 2.3, Figure 2.4, and Figure 2.5. Figure 2.5 illustrates the segmentation result using a thresholding value is too high, and in contrast, Figure 2.4 illustrates the segmentation result using a thresholding value is too low.

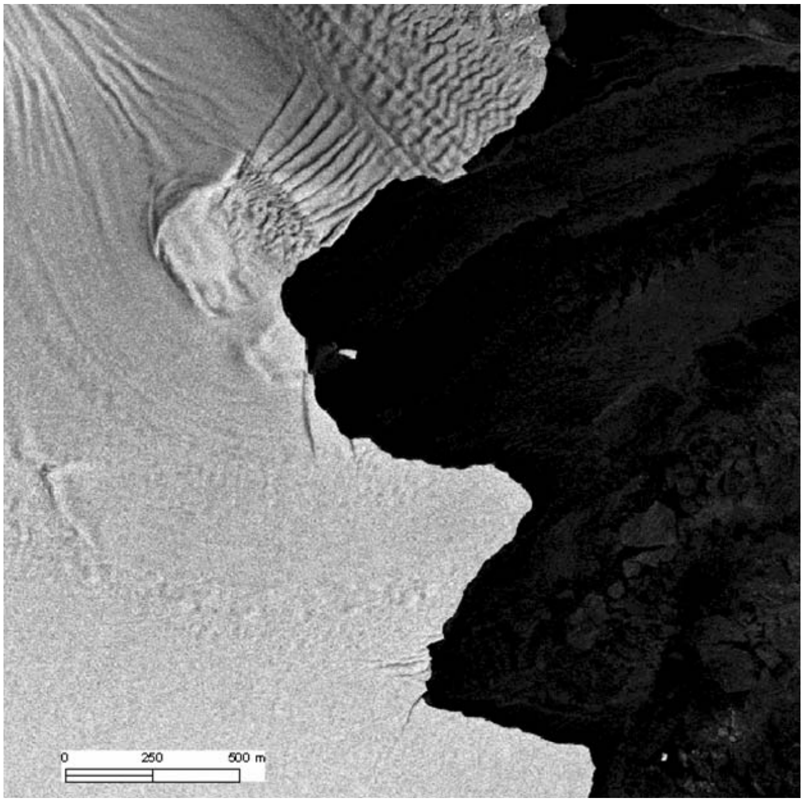

Figure 2.1 The original image

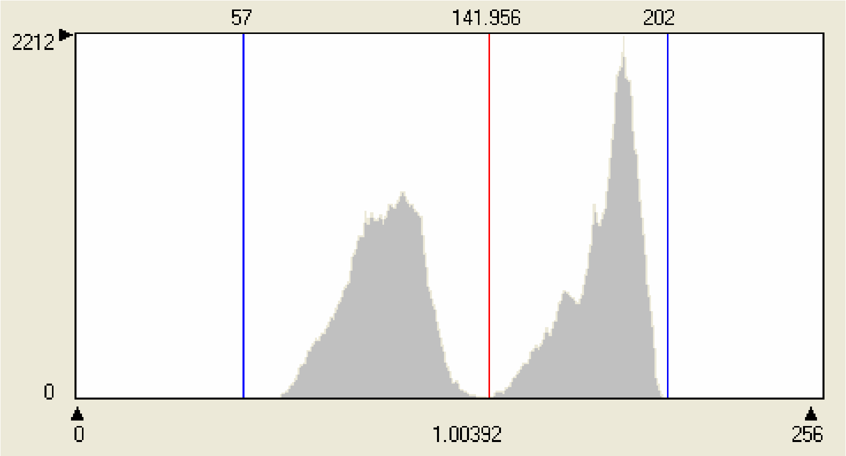

Figure 2.2 Histogram of the original image

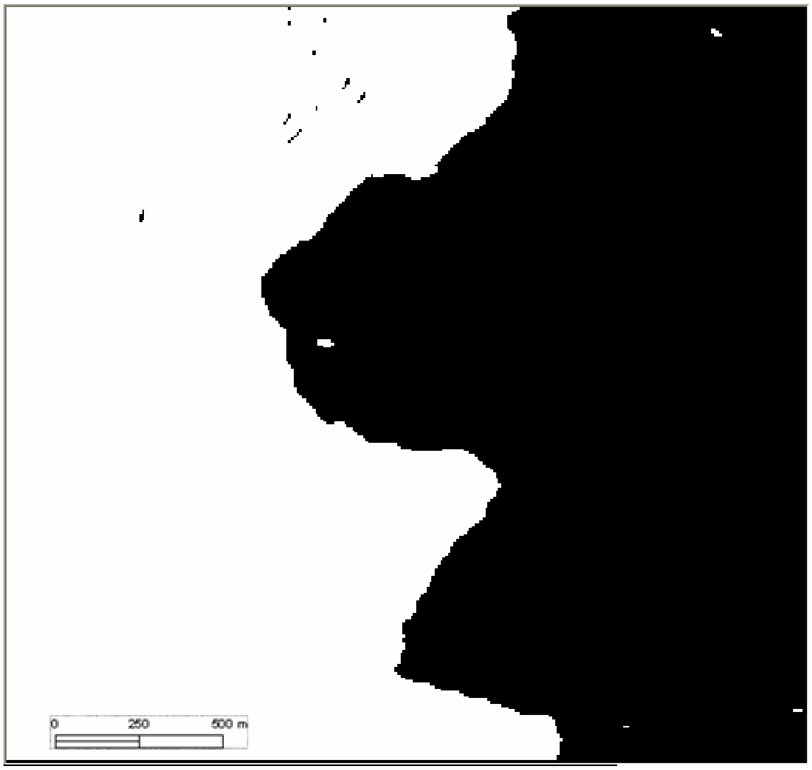

Figure 2.3 Segmentation with threshold=141

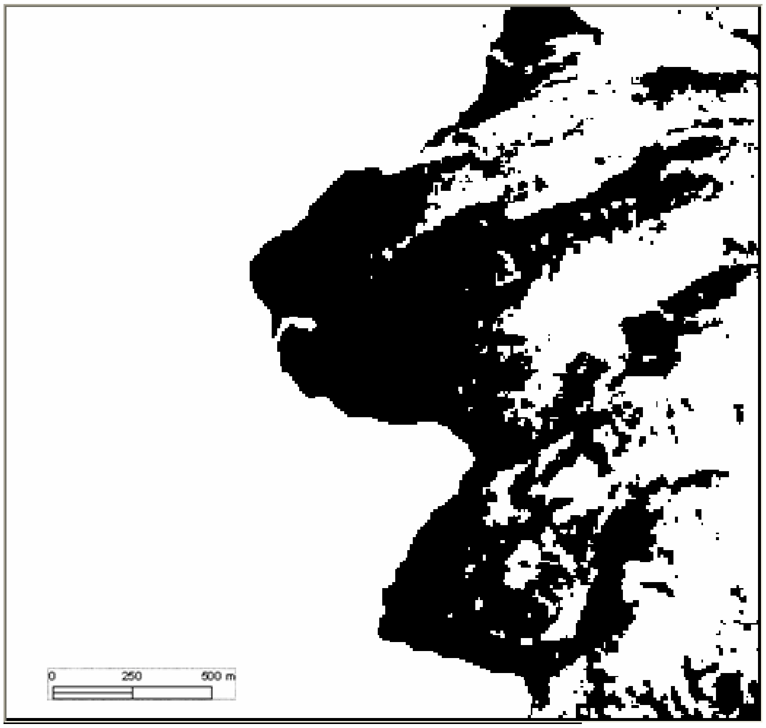

Figure 2.4 Segmentation with threshold =106

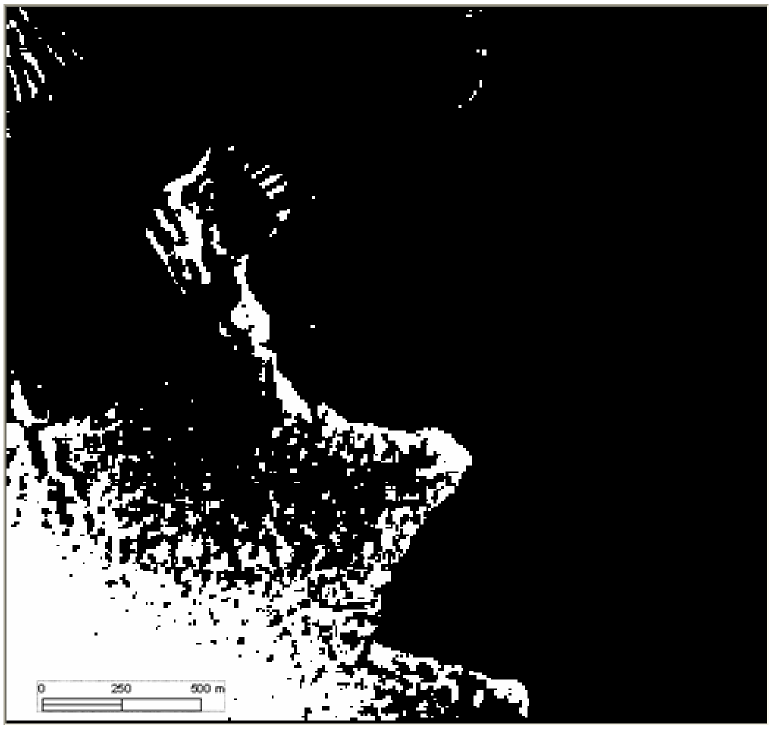

Figure 2.5 Segmentation with threshold = 187

These figures illustrate that determining the appropriate thresholding value or optimal thresholding value is the most crucial factor in acquiring good results using the histogram-based method. An ideal bimodal histogram is the best model to define the optimal thresholding value. An algorithm to determine the optimal threshold value detects the local minimum DN value between the highest local maxima and the second highest local maxima DN value. Low-pass filters are helpful in the process of determining the position of the local minimum DN value because there is usually some noise in the valley of the image histogram, which may cause the calculation of the local minimum DN value to fail. Consequently, image smoothing is necessary for filtering noise. Figure 2.3 illustrates the segmentation result with an optimal thresholding value.

2.3 Ice Flow Velocity Measurement Matching

Many studies, such as mass balance or other glaciological studies, require ice velocity information. The approaches include *in situ* repeated measurements of marks and stakes using conventional survey or GPS instruments, feature tracking from sequential aerial photos or satellite images, and SAR Interferometry (InSAR) technique.

2.3.1 Differential GPS

Differential GPS (DGPS) survey can be used to track the displacements of installed marks and stakes on the ice surface by precisely measuring their positions over a time interval (Hagen et al., 1999). By associating the positional displacements and the time span for two repeated position measurements, ice velocities can be calculated (El-Rabbany, 2002; Manson et al., 2000). DGPS technique uses two stationary GPS receivers, a base receiver and a remote receiver, to correct for atmospheric error to ensure high positional measurement accuracy. The base receiver is established at a specific point with precisely known geographical coordinates. The remote receivers are installed in stakes drilled into the ice used for ice motion measurements. After post DGPS processing, highly precise geographical coordinates can be derived for the installed stakes and marks. Although high accurate, the DGPS technique is costly and limited by hostile environmental conditions, meaning only sparse and small spatial coverage of velocity measurements can typically be obtained.

2.3.2 InSAR

Over the past decade, remote sensing technology has significantly enhanced our ability to measure and observe ice motion over large areas with high spatial resolution. InSAR techniques and feature tracking on sequential images have been widely used to derive accurate and dense ice velocity measurements (Young & Hyland, 2002). InSAR uses two SAR images acquired from the same satellite orbit but with slightly different positions. The acquired images are processed to generate complex SAR images, which contain backscatter amplitudes and phase information. The phase difference between two images can be used to generate an interferogram, which can be unwrapped to determine the ice motion (displacement) at centimeter level. The data processing procedure for InSAR technique is illustrated in Figure 2.6.

It has been demonstrated by many applications that InSAR technique is very effective and precise for producing dense ice velocity measurements. However, there are some limitations the InSAR approach. First, the InSAR technique is sensitive to temporal decorrelation. Environmental changes, caused by snow falls, strong winds, melting, and other processes, may greatly reduce the coherence and lead to decorrelation of interferometric SAR image pair. This causes the phase unwrapping operation to fail and make ice velocity measurements impossible. In addition, the availability of interferometric data is very limited. The interferometric SAR data are the complex radar image data acquired from repeated orbits with a small space baseline. Such data are only available for limited areas after 1990s (Gens & Van Genderen, 1996; van der Kooij et al., 1996).

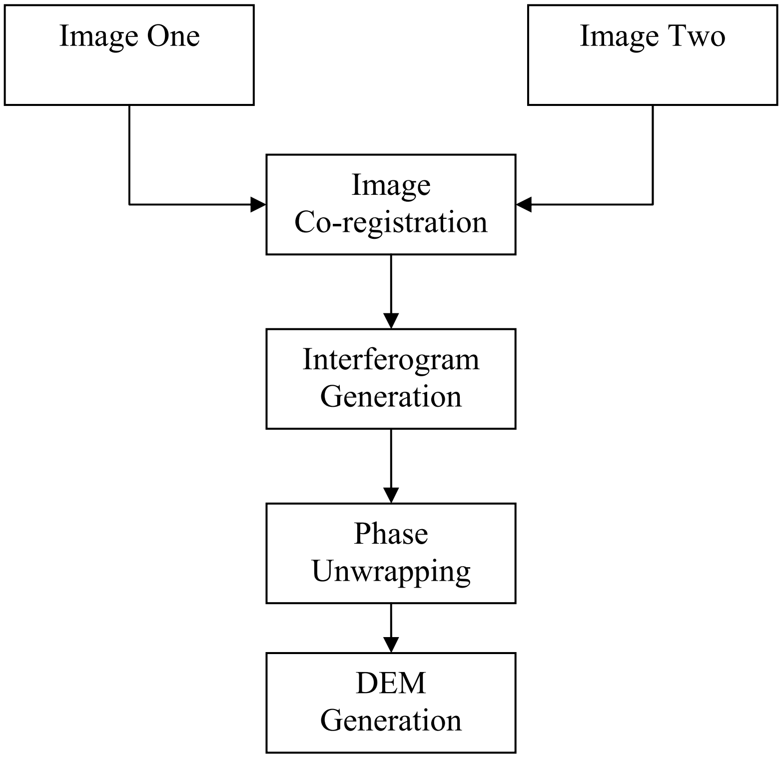

Figure 2.6 The procedure to generate InSAR image

2.3.3 Feature tracking

Feature tracking methods are based on the basic idea that the persistent surface features common to successive images can be recognized, and their displacements can be measured. Orthorectified and co-registered sequential images are essential for the featuring tracking approach. In two sequential images, for instance acquired in different years, the same features can be identified as conjugate points in the two images. Small distinctive surface features such as ice crevasses or rifts on the glaciers can serve as tracking targets. The displacements of conjugate points can be translated into velocity measurements given the known time span between two image acquisitions. Both optical and radar images can be utilized in feature tracking method. Sequential satellite images from optical sensors, such as SPOT, Landsat ,and ASTER have been widely used for feature tracking and ice velocity monitoring (Evans, 2000; Kääb et al., 2003; Lucchitta & Ferguson, 1986; Scambos et al., 1992). Optical images are limited by clouds, which can be overcome by SAR images. In recent decade, SAR images have been also employed for extracting ice velocity using the featuring tracking method (Fahnestock et al., 1993; Lucchitta et al., 1995)

Conventionally, the feature tracking was conducted manually. First, the recognizable, small features common to two sequential images need to be identified and selected visually by a human operator, and then the coordinates and displacements of these features have to be extracted and measured manually or mechanically. Such a manual method was used in an early application by Lucchitta and Ferguson (1986). In this study, the sequential Landsat images were co-registered, the geographic coordinates and positional displacements of surface features were manually extracted, and hence ice surface motion velocities were calculated for Byrd glacier. However, the manual feature tracking method is tedious and time consuming. An automated feature tracking method was developed by Bindschadler and Scambos (1991) and Scambos et al. (1992). This automated method is based on image matching approach, which has long been used in photogrammetry and computer vision to process stereo image pairs for 3D surface reconstruction. The basic task for image matching operation is to identify conjugate points in the two images, namely, tie points corresponding to the same features in two images. Image matching was first proposed in the late 1950s (Hobrough, 1959). Subsequently, a variety of algorithms were developed for diverse applications. Generally, these different algorithms can be grouped into two categories: area-based matching and feature-based matching (Gruen, 1985; Moctezuma et al., 1995; Schenk, 1999). The most widely employed algorithm in the image matching is the area-based cross-correlation. With this algorithm, a small image chip around a selected center pixel in the reference image will be compared with an image chip in the second image (search image) to identify the conjugate (corresponding) point of that center pixel within a certain search range. The maximum correlation coefficient in the search area is used to define the location of the conjugate (match) point. The feature-based matching method uses image edges for matching operation, which is not well tested for tracking features of sequential images for velocity measurements.

Although its accuracy is not as high as that derived from InSAR technique, the automated feature tracking method has several advantages over InSAR techniques. First, the automated feature tracking method applies to both optical and radar sequential images. Such data have been available for most of areas since 1970s. Second, the feature tracking method is much more robust to temporal decorrelation, and sequential images acquired several years apart still can be employed in the image matching to create dense and quite accurate velocity measurements.

2.4 Image Matching Methods for Measuring Ice Velocity

2.4.1 Area-based matching

The area-based cross-correlation method measures correlation coefficient (similarity measure) of grey values between small chips of two images (i.e. the reference image and search image). Comparing the grey value of one specific pixel between two images is insufficient, because one pixel only contains limited intensity information and there could be several candidate points with the same information as found in the search image. Consequently, comparing two chips (arrays of pixels) solves this dilemma. Figure 2.7 illustrates the concept of area-based matching method. Point A, in the reference image, and point A′, in the search image, are conjugate points. The objective is to identify point A′ using the grey value and coordinate of point A.

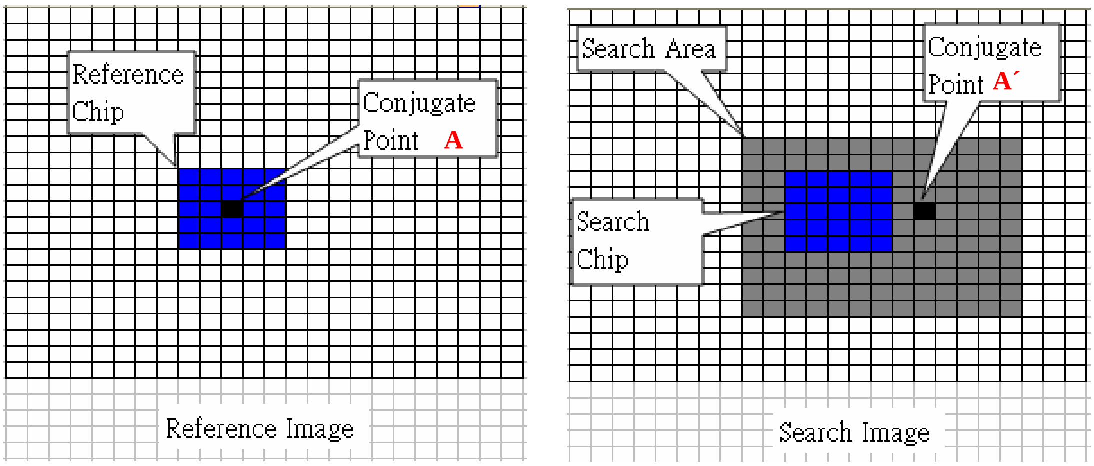

Figure 2.7 The concept of area-based method

The area-based method is as follows:

Step 1: Select a conjugate point and place it in the center of the reference chip (template window or reference window) in the reference image.

Step 2: Establish the extent of the search area in the search image according to the coordinates of the conjugate point in the reference image to give an initial approximate.

Step 3: Select a suitable size for both reference chip (template window) and search chip (window).

Step 4: Compute the cross correlation value ρ of the reference and search chips based on the similarity of grey levels.

$$\rho = \frac{\sum_{i=1}^{n}\sum_{j=1}^{m}(R(x_i, y_j) - \overline{R})(S(x_i + \Delta c, y_j + \Delta r) - \overline{S})}{\sqrt{\sum_{i=1}^{n}\sum_{j=1}^{m}(R(x_i, y_j) - \overline{R})^2 \cdot \sum_{i=1}^{n}\sum_{j=1}^{m}\ (S(x_i + \Delta c, y_j + \Delta r) - \overline{S})^2}} \tag{2.1}$$

Where: $R(x_i, y_j)$ = The reference chip (window)

$S(x_i, y_j)$ = The search chip (window)

$\overline{R}$ = The mean grey level value in the reference chip (window)

$\overline{S}$ = The mean grey level value in the search chip (window)

Step 5: Analyze the cross correlation coefficient ρ, which has a valid range $-1 \le \rho \le +1$.

If $\rho = +1$, then the reference window and the search window are identical.

If $\rho = 0$, then there is no correlation between the reference window and the search window.

If $\rho = -1$, then there is exact inverse correlation between the reference window and the search window.

Step 6: Move the search chip by one pixel, and then calculate another correlation coefficient between the reference chip and the new search chip. Continue the above process until the correlation coefficients are calculated for all locations within the search area.

Step 7: Fit a mathematical function to the correlation coefficients in the search area and then identify the maximum correlation peak (i.e. differential) on the mathematic surface at the sub-pixel level as the location of the conjugate point.

Step 8: Identify additional conjugate points in the reference image and repeat above steps 1-7 to find their conjugate points, respectively.

Generally, there are four strategies in step 7 to determine the correlation peak as the correct matched conjugate point. The easiest way is to compare correlation coefficients in the search area and find the pixel with the largest correlation coefficient as the matched conjugate point. This nearest neighbor search can determine the best match at pixel level. The other way is to fit a mathematical function such as a bivariate paraboloid, Gaussian, or reciprocal function on the correlation coefficients in the search area. Figure 2.8 is a simplified, one dimension illustration of the paraboloid function. Clearly, the location (coordinates) of the peak correlation can be modeled and determined at sub-pixel level.

The green stars in Figure 2.8 indicate the value of each correlation coefficient at each pixel in the search area. When we compare the correlation between reference chip and search chip, a single value correlation value will be generated (i.e. one green star). Then we continually compare reference chip and search chip that centers on the next pixel within the search area. In this way, a series of correlation coefficients are generated, and a parabolic curve can be fitted to these values. The position of peak (maxima value) on the curve can be determined very precisely at sub-pixel level.

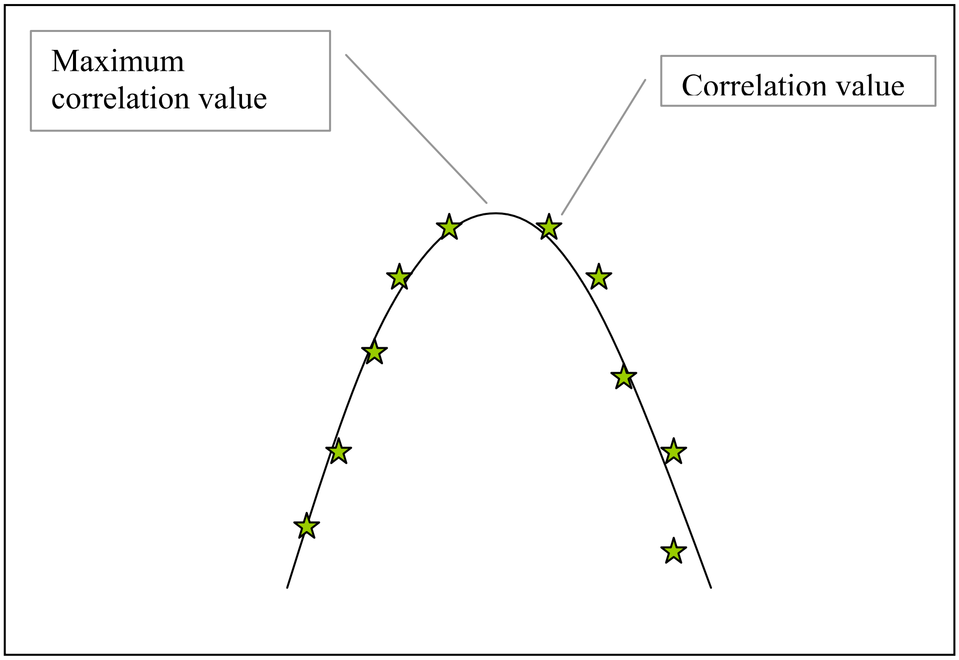

Figure 2.8 Parabolic curve dotted with correlation values

2.4.2 Feature-based matching

In contrast to area-based cross-correlation matching algorithm, the feature-based image matching method uses image edges for matching operation. Edges can be extracted by edge detectors. The extracted edges, as objects, have a variety of characteristics and properties (e.g., length, curvature, orientation, edge strength, and geographic coordinate), enabling each discrete edge to be described as a unique object, and thus, for conjugate features to be matched. Some algorithms like the $\psi - s$ approach have been developed to measure similarities of these properties between the reference image and the search image. The $\psi - s$ approach describes edges in the $\psi - s$ plane using a transform function to isolate rotational, shift, curvature, and orientation effects (McConnell et al., 1991; Schenk et al., 1991). ψ, the vertical axis, represents the accumulative changes in the object's orientation, and s, the horizontal axis, represents the object's length. Table 2.1 shows the relationship between the spatial domain and the $\psi - s$ domain.

Table 2.1 The mapping of the spatial domain and the $\psi - s$ domain

Spatial domain	$\psi - s$ **domain**
Straight lines	Horizontal straight lines with different amplitudes
Circles	Straight lines with different slopes
Rotations	Vertical shifts

The main advantage of the $\psi - s$ method is that it reduces complex edges to simple straight lines according to the mapping between the spatial and the $\psi - s$ domain. The procedure to implement the $\psi - s$ method is as follows:

Step 1: Transform edges in the reference image into the $\psi - s$ domain.

Step 2: Transform edges in the search image into the $\psi - s$ domain.

Step 3: Segment the straight lines in the $\psi - s$ domain into several lines for both the reference and the search image.

Step 4: Compare the vertices of each segment in the search image with those in the reference image, and then analyze their characteristics to find the matched edges. In addition, the angle and orientation of vertices can be compared between the reference and search image.

If we make the inverse transformation from the $\psi - s$ domain to the original spatial domain, we will find that the straight lines in the $\psi - s$ domain represent curvy edges in the spatial domain because straight lines with different slopes in the $\psi - s$ domain indicate different curves in the spatial domain with the amount of ψ orientation. In step 4, we compare the similarity of vertices; that is comparing the similarity of shape in the spatial domain because vertices, in the $\psi - s$ domain, represent different curvatures than in the original curvy edges. This method was used in ice floes tracking research based on two sequential Seasat SAR images (McConnell et al., 1991). The results have proven that this method has a good performance in tracking rotated ice floes. However, deformations reduced its abilities to match ice floes.

In this research, the area-based cross-correlation algorithm will be further developed with multi-scale and hierarchical matching scheme to improve the computation efficiency and matching reliability. The details will be presented in Section 4.

3 ICE MARGIN CHANGES

This section first introduces the algorithm elements of the locally adaptive thresholding method for automated coastline extraction, and then discusses the algorithm modification and improvements implemented in this research. Next, an ArcGIS extension module-Coastline Extraction Module is presented, which was developed by using ArcObjects and VB .NET programming. It is followed by the presentation of the 2000 coastline of the Antarctic continent and its comparison with the 1997 coastline and 1963 coastline. Finally, the advance and retreat rates for ice shelves and coastal outlet glaciers are analyzed and inventoried.

3.1 Locally Adaptive Thresholding Algorithm for Coastline Extraction

The Antarctic continent consists of the ice sheet grounded on the bedrock, small portion of rock exposure areas (about 5%), and surrounding floating ice shelves. The Antarctic coastline is defined as the boundary between the ocean and the continental ice sheet, including coastal rock outcrops and ice shelves. The Antarctic coastline (ice margin) is very sensitive to atmospheric and oceanic environmental changes. Temporal changes in the Antarctic coastline may provide the diagnostic information for global environmental changes.

A locally adaptive thresholding technique has been developed Liu and Jezek (2004a). By using this automated technique, Liu and Jezek (2004b) has extracted a complete, high-resolution coastline from the 1997 Radarsat SAR images. In this research, the locally adaptive thresholding technique is further modified and improved to derive another set of complete, high resolution coastline for Antarctica from the 2000 Radarsat SAR images.

3.1.1 Overview of algorithm elements

The locally adaptive thresholding technique is based on a chain of digital image processing algorithms. The key component is the histogram-based segmentation. The technique includes three processing stages: a pre-processing stage, a segmentation stage, and a post-processing stage. The purpose of pre-processing stage is to reduce noise and speckle in the SAR images using smoothing filters. In addition, this stage can enhance the edges of ice margins and reduce the weak edges inside the ice sheet and ocean using an anisotropic diffusion method. Image segmentation stage aims to separate an image into regions that correspond to meaningful objects in the scene such as ice sheets and ocean. A locally adaptive thresholding method improves the accuracy of the segmentation. The Levenberg-Marquardt and Canny edge detector are used to increase the computation speed for this stage. The post-processing stage removes misclassified objects in the images and traces the coastline between ocean and ice margins. The extracted coastlines are then converted into GIS format data as needed for change detection.

The following chart (Figure 3.1) illustrates the algorithm elements and data flow in the locally adaptive thresholding technique. The basic ideas and key algorithm components will be explained in the following sections.

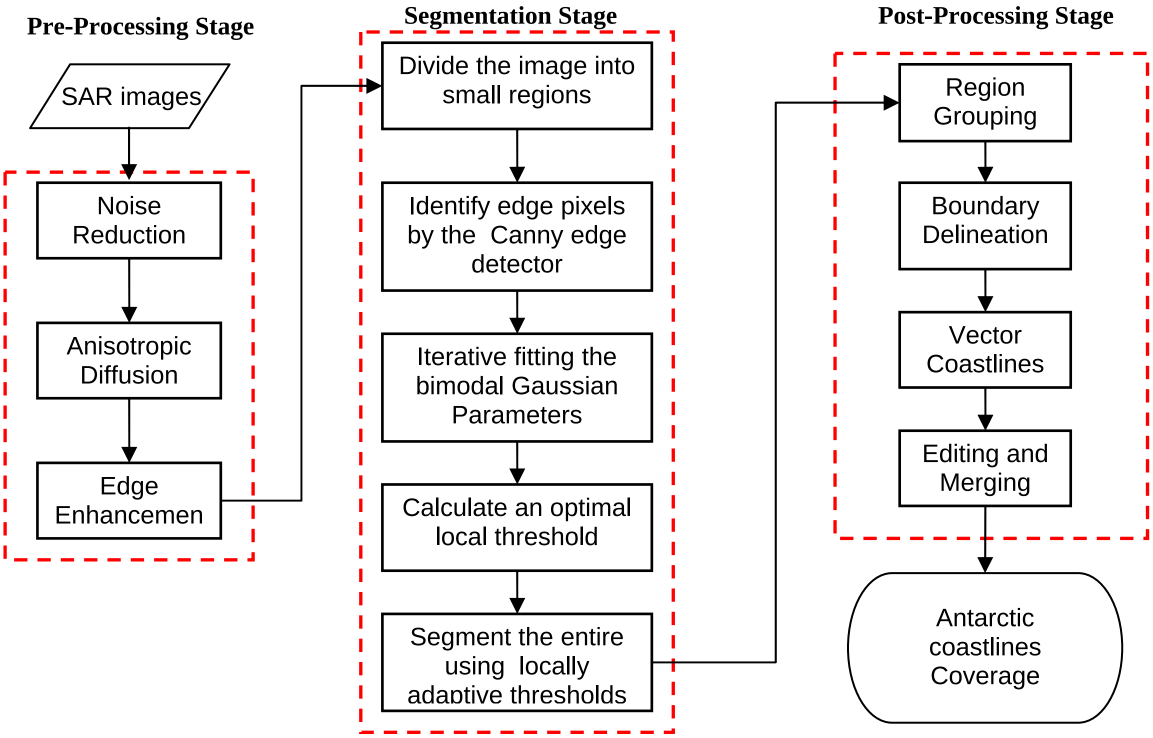

Figure 3.1 The automated extraction algorithm

3.1.2 Segmentation based on bimodal histogram

The purpose of image segmentation is to separate a SAR image into its constituent homogenous image regions, which define the boundaries between icy land and ocean. A reliable threshold value can be determined to classify ice and land pixels from water pixels by analyzing the histogram of image pixel values.

For a small image region, the shape of the histogram can be uni-modal or bi-modal. If the small image region covers either icy land or ocean water, the histogram will be uni-modal, indicating that the image region is homogenous and coastline edges are not included. If the image region covers both icy land and ocean water, the histogram will be bi-modal as shown in Figure 3.2. The bi-modal histogram indicates that the coastline is present in the image region.

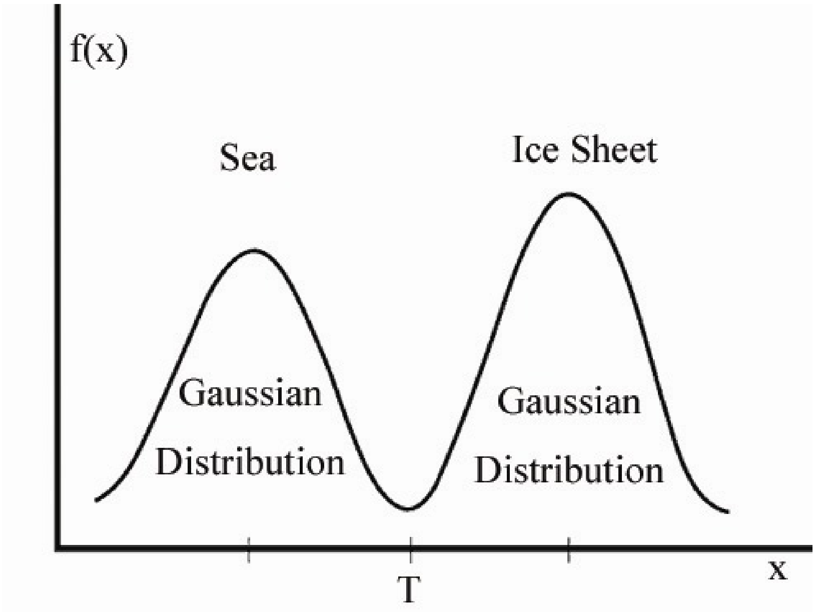

Figure 3.2 Using two Gaussian distribution modal to simulate bimodal

Experiments show that as long as an image region contains both icy land and ocean water, namely, containing coastline, the pixel values within the image region will be grouped into two dominant modes. One mode represents the ocean water pixels, and the other represents icy land pixels. These two modes have relatively distinct mean values. To classify the land pixels from water pixels, an optimal threshold value is required.

3.1.3 Determining the optimal threshold

The optimal threshold value corresponds to the valley point in the bi-modal histogram. The valley point can be determined analytically by modeling the bimodal histogram. The assumption is that the bimodal histogram is a mixture of two Gaussian (Normal) distribution functions (Figure 3.2). The mean and standard deviation parameters can be determined by an iterative computation scheme. This iterative computation needs initial approximate values for the mean and standard deviation parameters of two Gaussian distribution functions.

The initial parameter values influence the converging speed and success of the iterative parameter fitting. The edge pixels derived from Canny edge detector are used to obtain good initial values for mean and standard deviation parameters. The Canny edge detector (Canny, 1986) is the optimal edge detector. It detects locally maximum gradient magnitudes in the gradient direction.

The bimodal histogram is represented by the sum of two Gaussian distribution functions as follows:

$$s(x) = \frac{1}{\sqrt{2\pi}\sigma_1} \exp\left[-\frac{(x-\mu_1)^2}{2\sigma_1^2} \right]$$

$$i(x) = \frac{1}{\sqrt{2\pi}\sigma_2} \exp\left[-\frac{(x-\mu_2)^2}{2\sigma_2^2} \right]$$

Where $s(x)$ is the Gaussian distribution function of sea water.

$i(x)$ is the Gaussian distribution function of icy land.

Therefore the probability density function is:

$$F(x) = ps(x) + (1 - p)i(x)$$

As mentioned before, the objective is to use two Gaussian distribution functions to simulate the bimodal histogram $h(x)$. If the sum-of-squares error (SSE) between the probability distribution functions and the observed bimodal histogram is minimized, the derived function F(x) can be used as optimal representation of the observed histogram to determine the threshold (valley) point.

$$SSE = \sum_{x=0}^{255} \left[F(x) - h(x) \right]^2$$

To minimize the SSE, the Levenberg-Marquardt algorithm is used iteratively to compute the optimal mean and standard deviation parameters (Gill & Murray, 1978; Levenberg, 1944; Marquardt, 1963). The best-fitting parameters μ_1, σ_1, μ_1, σ_2, and p from the Levenberg-Marquardt algorithm can be used to analytically determine the optimal threshold value (Chow & Kaneko, 1972).

3.1.4 Locally adaptive threshold values

If a single threshold value is used for the entire image to determine the land/water boundaries, some local coastline edges will remain undetected due to the heterogeneity of the image intensity contrast, causing the discontinuity of coastline edges in low contrast areas in the image. To get the most reliable coastline, the threshold value must be spatially adaptive according to the image statistical property of local image regions.

The entire image is subdivided into a set of small overlapping regions. The image region should be small enough to ensure that only one or two types of pixels exist in the small region. It also should be big enough to ensure reliable statistical analysis of the histogram of the region. For each image region, the use of the above computation procedure can produce an optimal threshold for that region. Different image regions have different threshold values. In other words, the threshold value is locally varying. By spatially interpolating these local threshold values, an threshold value can be estimated for each individual pixel. The inverse distance weight (IDW) interpolation method is utilized for this purpose:

$$NT = \frac{\sum_{i=1}^{n}\left(\frac{RT_i}{D_i}\right)}{\sum_{i=1}^{n}\left(\frac{1}{D_i}\right)}$$

Where NT= new threshold value for a pixel

RTi= the *i*th reliable threshold values determined for image regions

Di= distance from the pixel to the *i*th surrounding threshold values

3.1.5 Coastline tracing and vectorization

By applying the locally varying threshold values, the original satellite image can be segmented into land and water pixels, namely, a binary image as shown in Figure 3.3 Continued . After image segmentation, some small objects remain in the binary image, which are not related to coastlines. These small objects are scattered in ocean water or in the ice covered land. They can be removed by two passes of post processing. In the first pass, small white objects in ocean water are changed to black ones and combined with surrounding ocean water. In the second pass, the small black objects in ice covered land are changed to white ones (ice/land) and merged with the surrounding land (Figure 3.4).

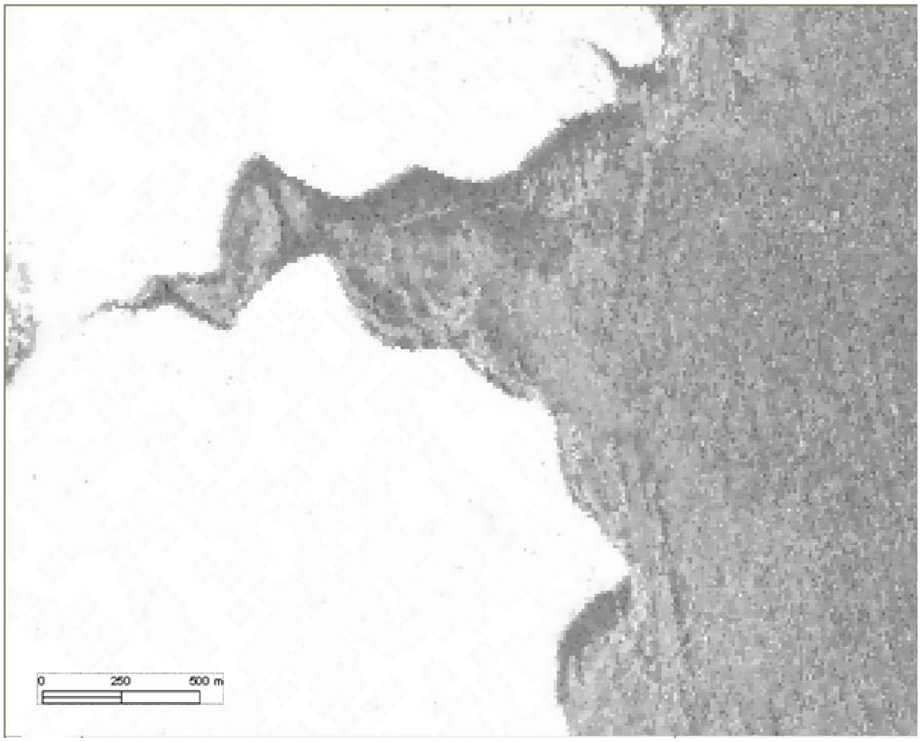

(a)

Figure 3.3 (a) The original image. (b) The binary image after segmentation.

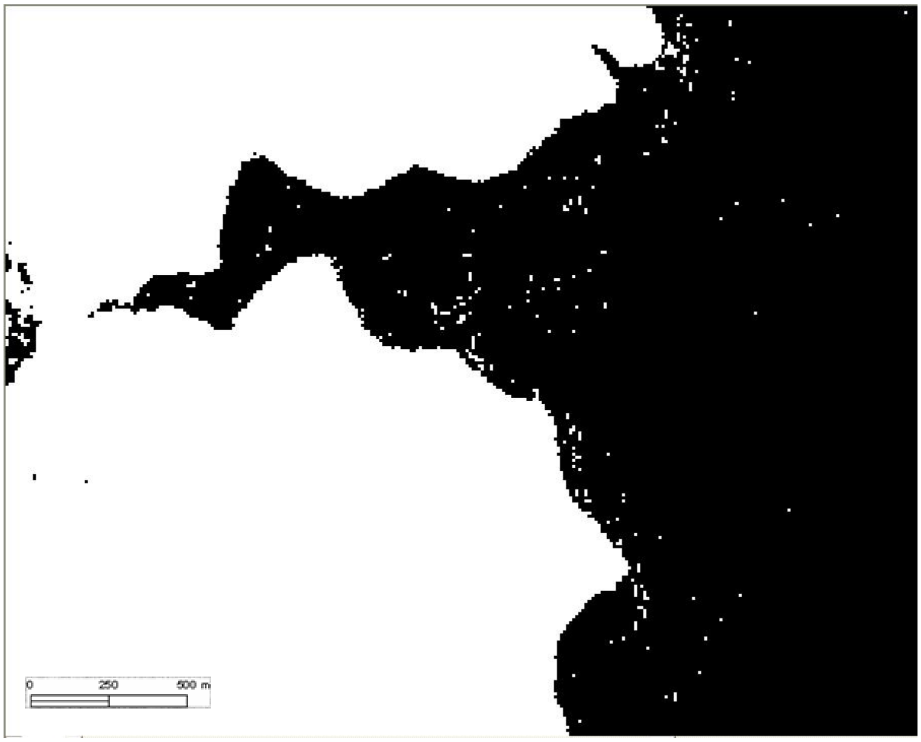

(b)
Figure 3.3 Continued

After removal of isolated image objects, only two large continuous land (white) and ocean (black) objects are left. This effectively eliminates unwanted objects whose boundaries are not part of the coastline.

At the final stage, a robust line tracing algorithm is applied to the binary image to trace and vectorize the boundary pixels between land and water, resulting in a high-resolution coastline which can be loaded into ArcGIS as a line coverage (Figure 3.5).

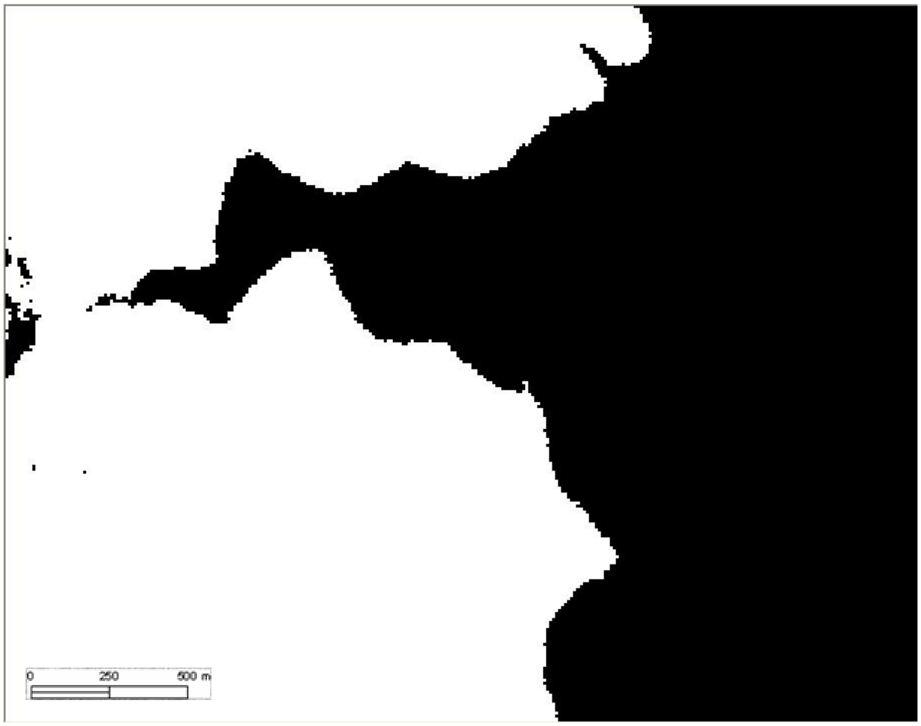

(a)

(b)

Figure 3.4 (a) The first pass of grouping (b) The second pass of grouping

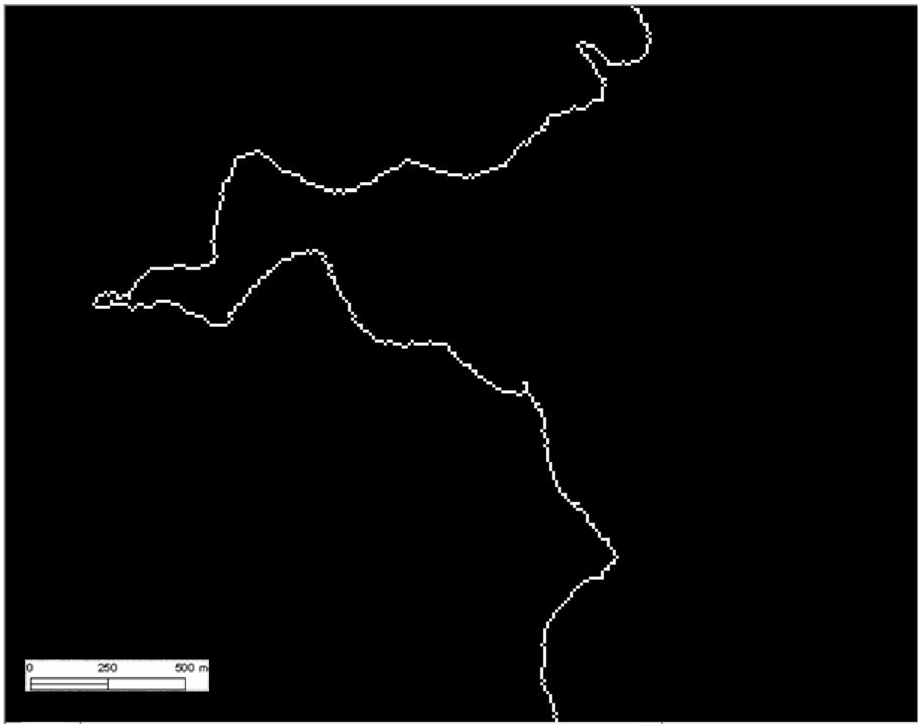

Figure 3.5 The extracted coastline

3.2 Algorithm Improvements

The previous research has demonstrated that the locally adaptive thresholding technique is very effective in automating the coastline extraction from the satellite imagery (Liu & Jezek, 2004a). A complete, high-resolution coastline has been extracted by applying this technique to the 1997 Radarsat SAR images of Antarctica. In this research, further algorithm modifications are made to improve the efficiency for processing the 2000 Radarsat SAR images. The modification aims to take advantage of the previous coastline position to reduce computation cost and improve the reliability of threshold values.

It is assumed that the current coastline is located within a certain range of the previous coastline. Given a maximum possible advance or retreat rate, a buffer zone can be created around the previous coastline. In this way, only portions of image falling within the buffer zone are processed to seek the current coastline, while the large image regions outside the buffer zone can be ignored to save computation time. During three year time period between 1997 and 2000 the maximum possible positional changes ranges from 3 km to 5 km, depending on the location. In the processing of the 2000 SAR images of Antarctica, a 6 to 10 km wide buffer zone was first created along the 1997 coastline by expanding 3-5 km on each side as the search area (Figure 3.6). The black narrow strip in Figure 3.6 indicates the operation zone where the automated algorithm is executed. The modified algorithm reduces the data processing task from the whole image frame to a narrow buffer zone, and hence greatly improves the computation speed and efficiency.

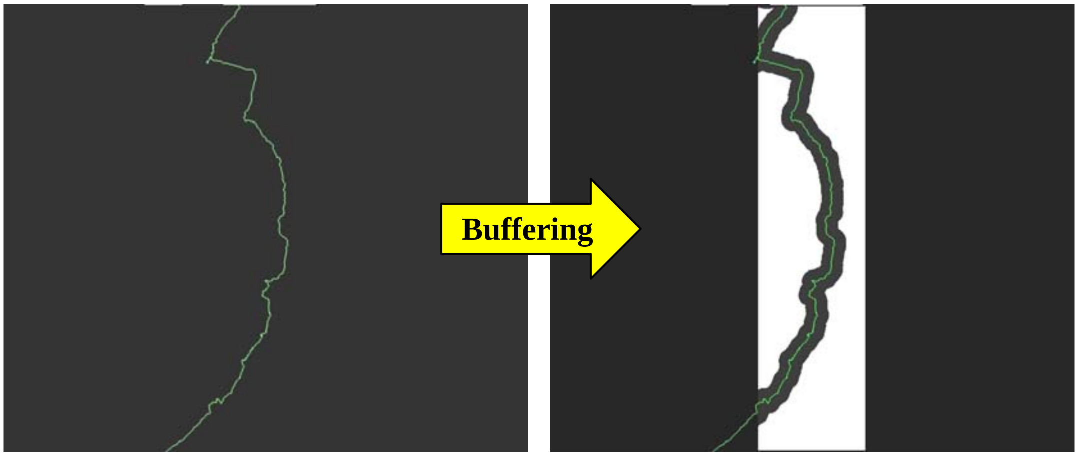

Figure 3.6 The buffer zone (black strip along green line) created according to the 1997 coastline (green line)

The second modification is to vary the density of overlapping image regions. In the original algorithm, the entire image is subdivided into a grid of small overlapping image regions, and the spacing between these small image regions is fixed. The local threshold values are only computed for these regularly distributed small image regions in the original algorithm. In this research, a dense of overlapping small image regions along the previous coastline are added for computing threshold values, besides the regularly spaced small image regions in the original algorithm. For each image pixel located on the previous coastline, a small image region is defined with the coastline pixel as the center and the threshold value is computed for each coastline pixel (Figure 3.7). Since it is more likely for the image regions near the coastline to have the bimodal histograms, the threshold values can be reliably determined.

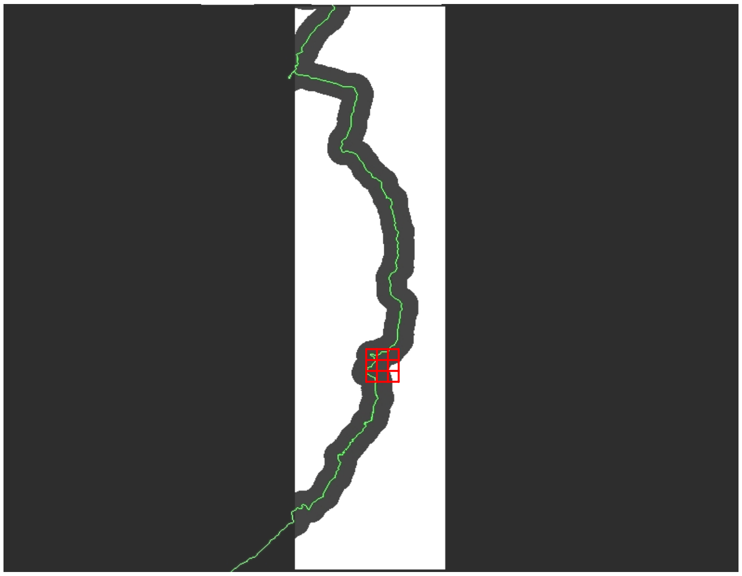

Figure 3.7 The manageable window works within the buffer zone

Since more threshold values are determined near the coastline, the quality of image segmentation is improved. The extracted coastline position is more reliable and accurate.

3.3 Development of Coastline Extraction Extension Module in ArcGIS

The original software tool implemented by Liu and Jezek (2004a) consists of a series of C++ codes, which were compiled as a sequence of commands in a SGI UNIX operation system. The lack of a Graphical User's Interface (GUI) requires users to get familiar with their command syntax and remember the meaning and appropriate value ranges for the relevant parameters. In addition, the original image data had to be converted into generic binary format as the input, and the intermediate processing results and the final coastline needed to be converted into ArcGIS compatible format for visual checking, quality control, and making maps. To construct a user friendly software tool, the original C++ source codes were ported into the C++ .NET environment in the PC Windows operation system. These C++ language codes are modified and compiled into a series of DLLs (Dynamic-Link Library). A DLL file contains one or several functions. DLLs are plug-in components that can be incorporated into other programs. To plug these DLLs into ArcGIS, VB (Visual Basic) .NET programming language and ArcObjects are employed to call and wrap the DLLs to create an ArcGIS extension module. Figures 3.8 through Figure 3.11 show the ArcGIS extension module for automated coastline extraction.

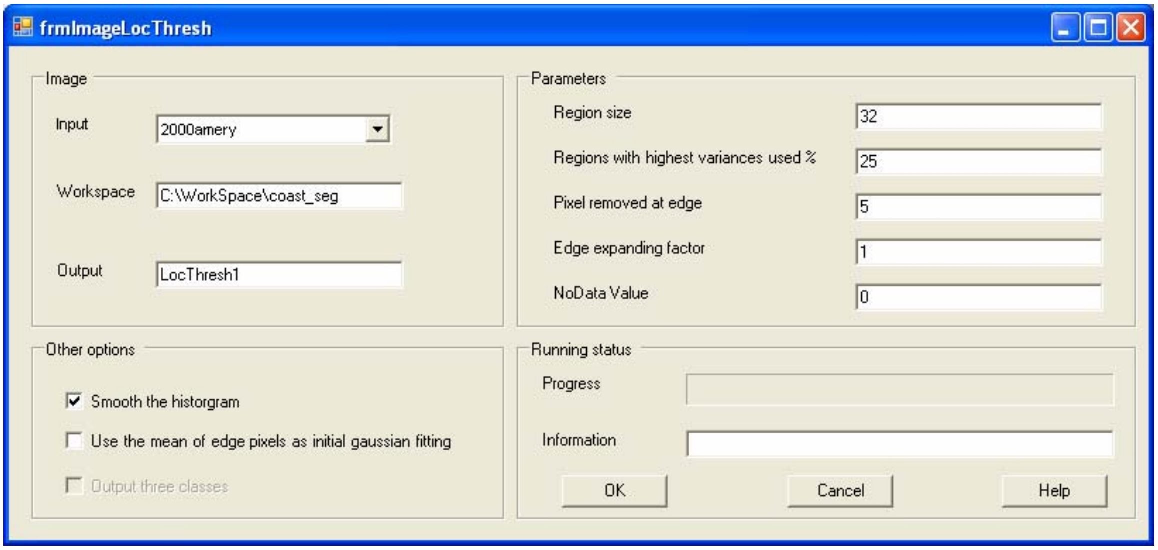

Input: 2000amery
Workspace: C:\WorkSpace\coast_seg
Output: LocThresh1

Region size: 32
Regions with highest variances used %: 25
Pixel removed at edge: 5
Edge expanding factor: 1
NoData Value: 0

☑ Smooth the historgram
☐ Use the mean of edge pixels as initial gaussian fitting
☐ Output three classes

Figure 3.8 The interface of threshold stage

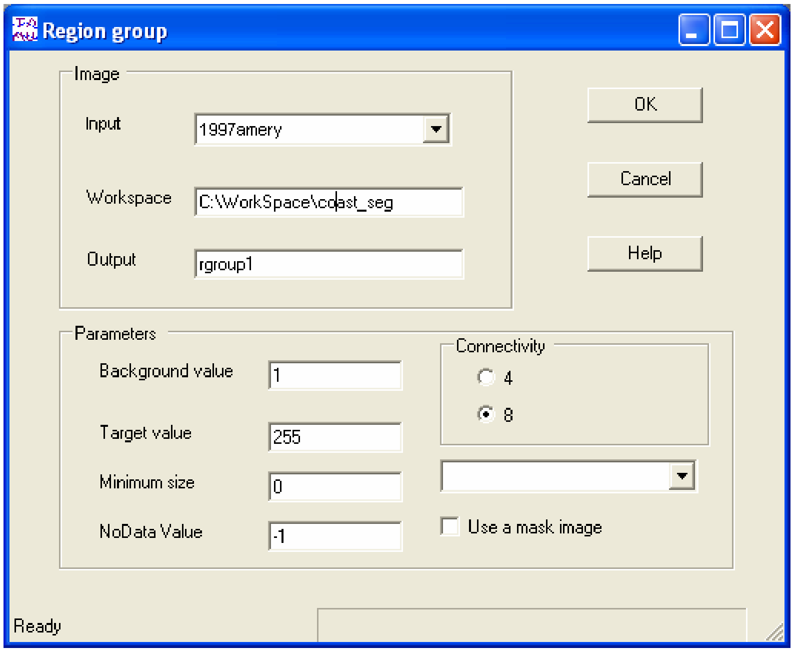

Input: 1997amery
Workspace: C:\WorkSpace\coast_seg
Output: rgroup1

Background value: 1
Target value: 255
Minimum size: 0
NoData Value: -1

Connectivity
○ 4
● 8

☐ Use a mask image

Figure 3.9 The interface of region group stage

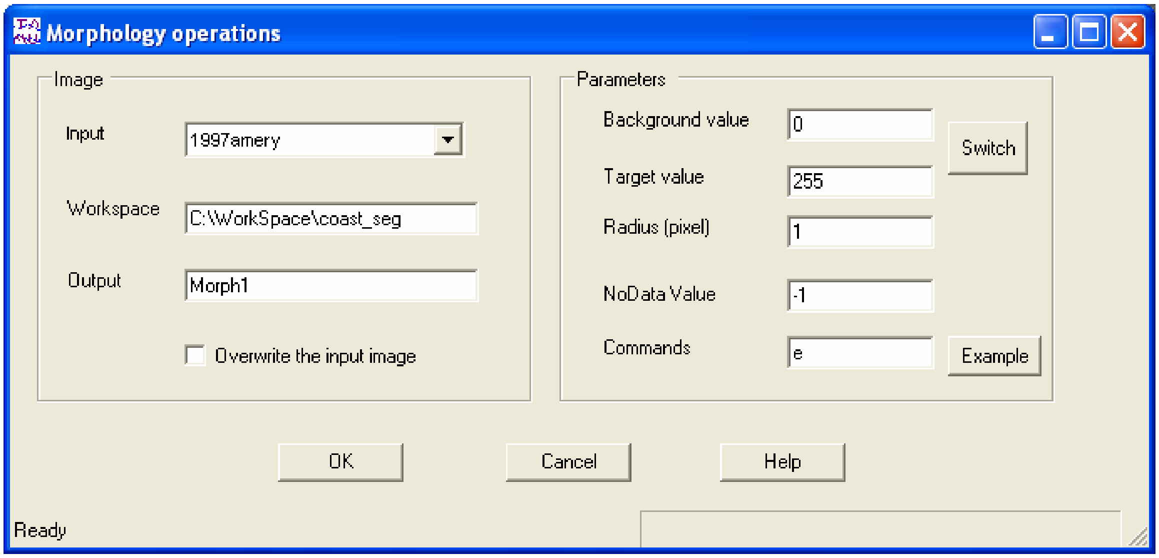

Input: 1997amery
Workspace: C:\WorkSpace\coast_seg
Output: Morph1
☐ Overwrite the input image
Background value: 0
Target value: 255
Radius (pixel): 1
NoData Value: -1
Commands: e

Figure 3.10 The interface of morphology operation

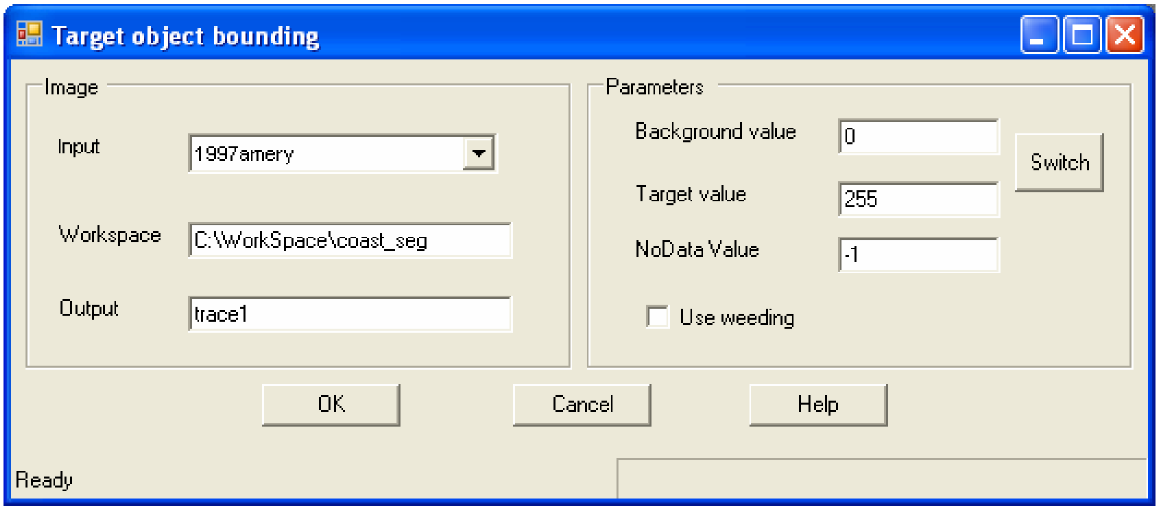

Input: 1997amery
Workspace: C:\WorkSpace\coast_seg
Output: trace1
Background value: 0
Target value: 255
NoData Value: -1
☐ Use weeding

Figure 3.11 The interface of object bounding

The implementation of this ArcGIS extension module greatly facilitates the coastline extraction. The GUIs guide the user to load the input data, to set the relevant parameter values, and to specify the outputs. This eliminates the needs for users to remember the command syntax and relevant parameter values. The data format conversions are no longer necessary. The input data, intermediate and final processing results can be immediately displayed, checked, and analyzed within the ArcGIS environment. The ArcGIS extension module developed in this research can be conveniently used by others in the similar applications for extracting coastline from remote sensing images.

3.4 High-resolution Coastline Extracted from 2000 Radarsat SAR Images

During the first Antarctic Mapping Mission (AMM-1) from September 9, 1997 to October 20, 1997, the Canadian Radarsat-1 Satellite imaged the entire Antarctic continent. The Radar SAR images have been orthorectified at the Byrd Polar Research Center of the Ohio State University, and a high resolution seamless SAR image mosaic has been produced as illustrated in Figure 3.12. By applying the locally adaptive thresholding technique, the complete Antarctic coastline was extracted by Liu and Jezek (2004b) as shown in Figure 3.13. This is the first high resolution (25 m) coastline for Antarctica, and it provides a precise benchmark for the Antarctic margin change detection studies.

During the second Antarctic Mapping Mission (AMM-2) from September 3, 2000 to November 17, 2000, the Antarctic continent was imaged again by the Radarsat-1 SAR sensor. Due to the health concern about the Radarsat-1 Satellite, the orbit maneuver for rotating the normally right-looking SAR to a left-looking mode was not conducted, therefore the interior of the Antarctic continent was not imaged in the AMM-2. The SAR images acquired in the AMM-2 cover the Antarctic continent up to the latitude of 82°S, and there is a circular hole around the South Pole where no SAR images were acquired from the AMM-2 (Figure 3.14). Like, the 2000 Radarsat-1 SAR images from the AMM-2 went through the orthorectification process to correct the terrain distortions and to acquire accurate geographical coordinates at the Byrd Polar Research Center of the Ohio State University. The orthorectified SAR images were further radiometrically corrected and balanced to create the second high resolution SAR image mosaic of Antarctica as shown in Figure 3.14.

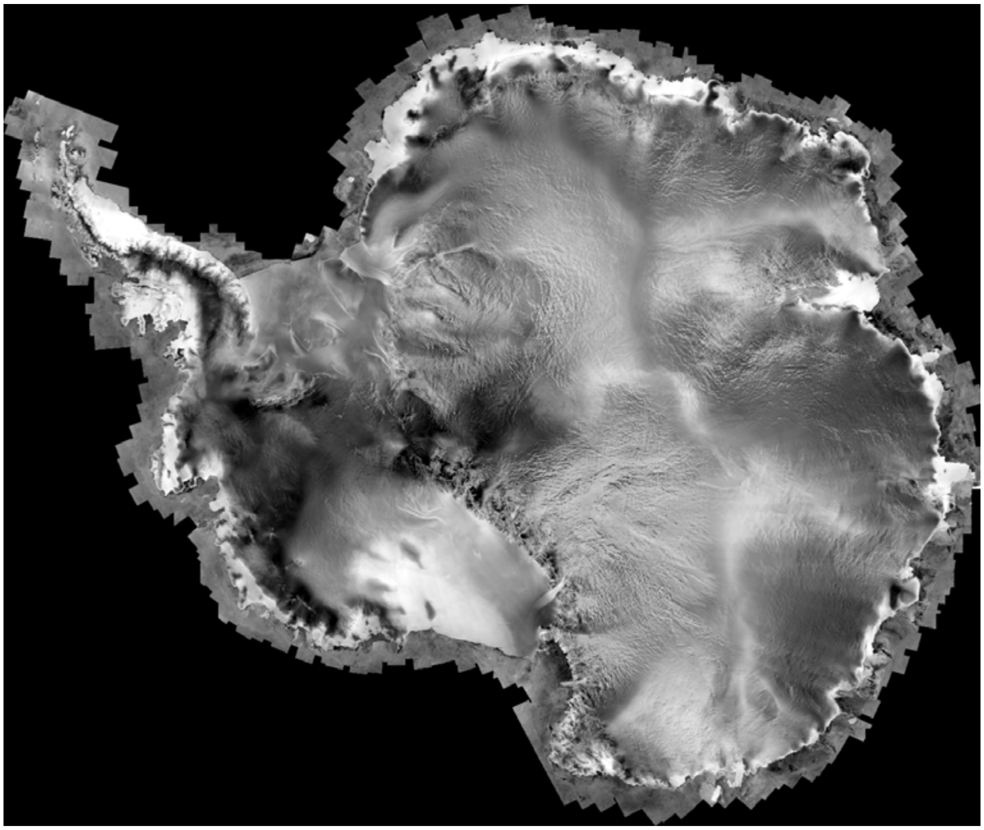

Figure 3.12 This mosaicked image was created from images acquired during the first Antarctic Mapping Mission (AMM-1)

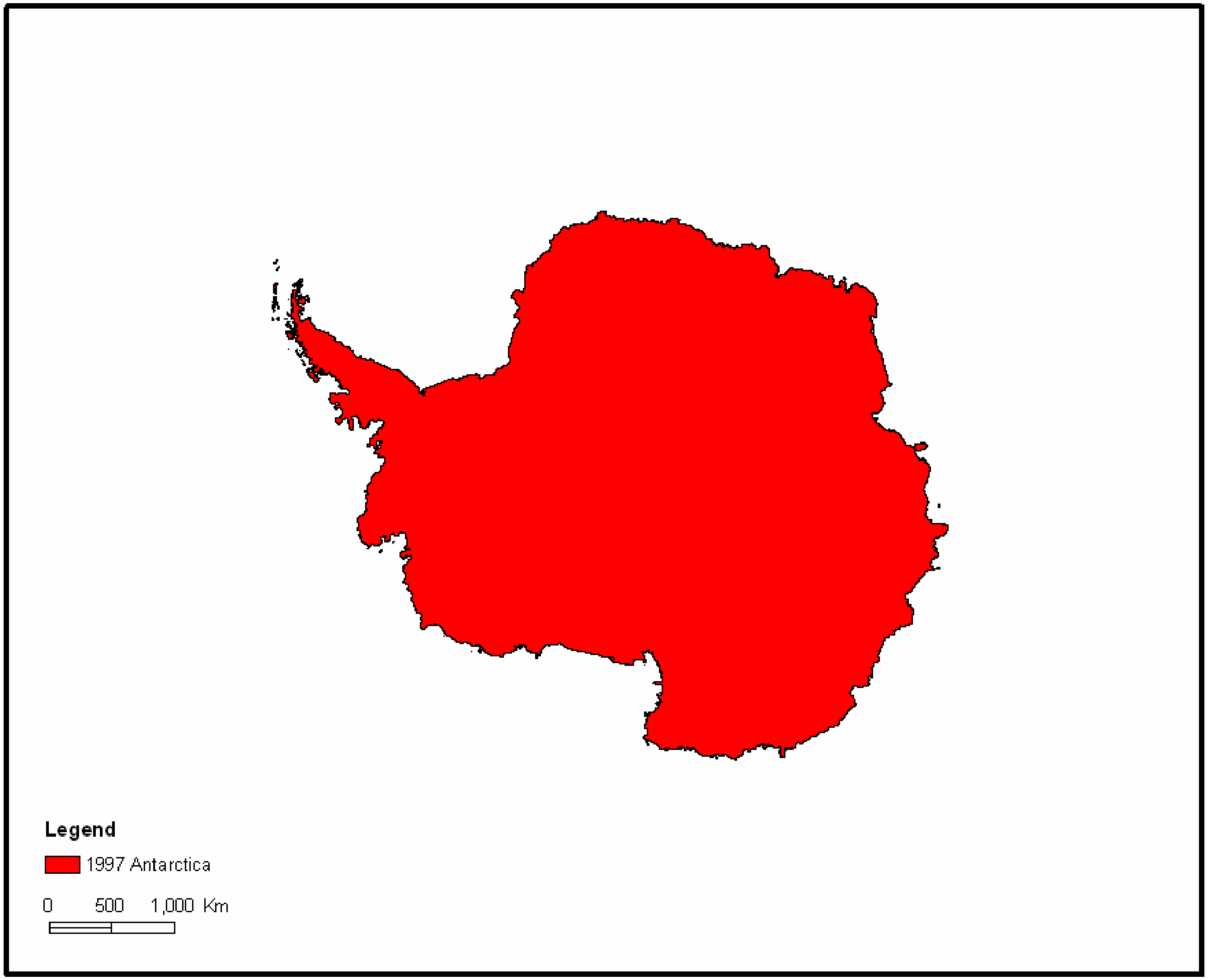

Figure 3.13 The extracted coastlines from sequential Radarsat SAR images in 1997

The orthorectified SAR images acquired from the AMM-2 in 2000 are the image source for the coastline extraction reported in this research. The input SAR images have a full resolution of 25 m. Only image tiles along the Antarctic coast (Figure 3.15) are retrieved from the orthorectified SAR image mosaic for coastline processing. The modified locally adaptive thresholding technique is applied to each image tile, and the coastline is automatically extracted for each image tile. The vector coastlines extracted from adjacent image tiles are edited and merged in ArcGIS environment. After three months of data processing, editing and quality, a complete Antarctic coastline with a 25 m resolution is created. It includes the coastlines for both the conterminous Antarctic continent and surrounding islands (Figure 3.16). The 2000 coastline coverage is in ArcInfo line coverage format and in Polar Stereographic Projection referenced to WGS84 ellipsoid.

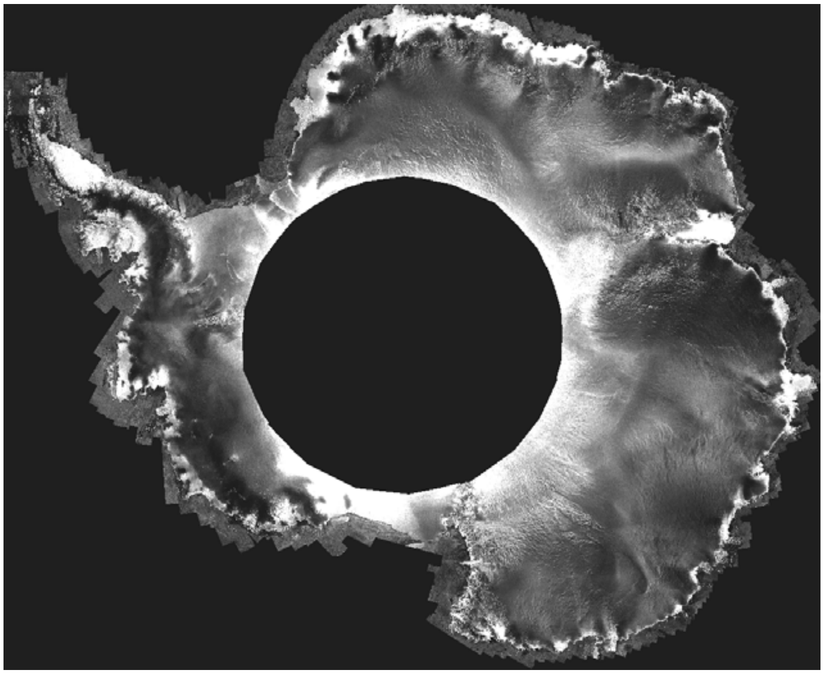

Figure 3.14 This mosaicked image was created from images acquired during the second Antarctic Mapping Mission (AMM-2)

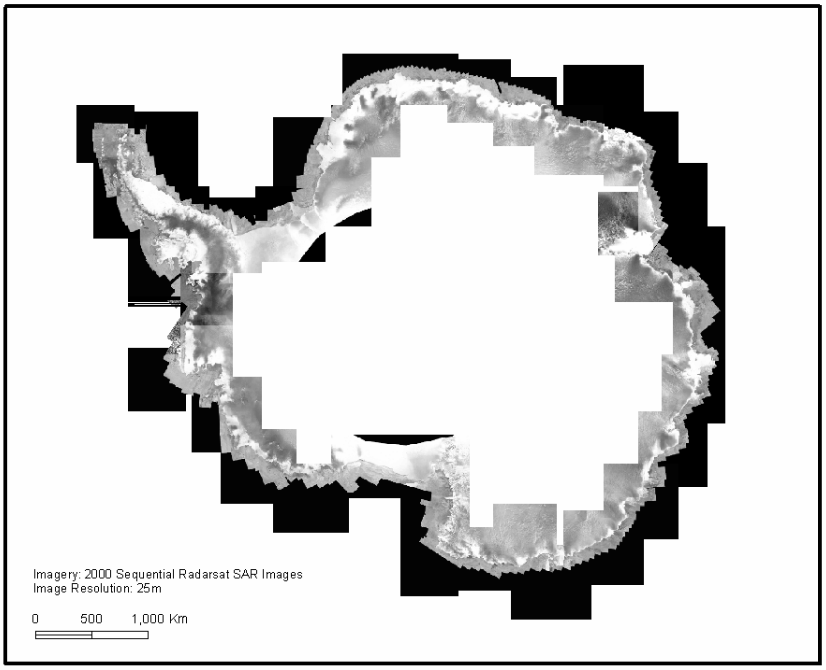

Figure 3.15 Sequential Radarsat SAR images acquired in 2000

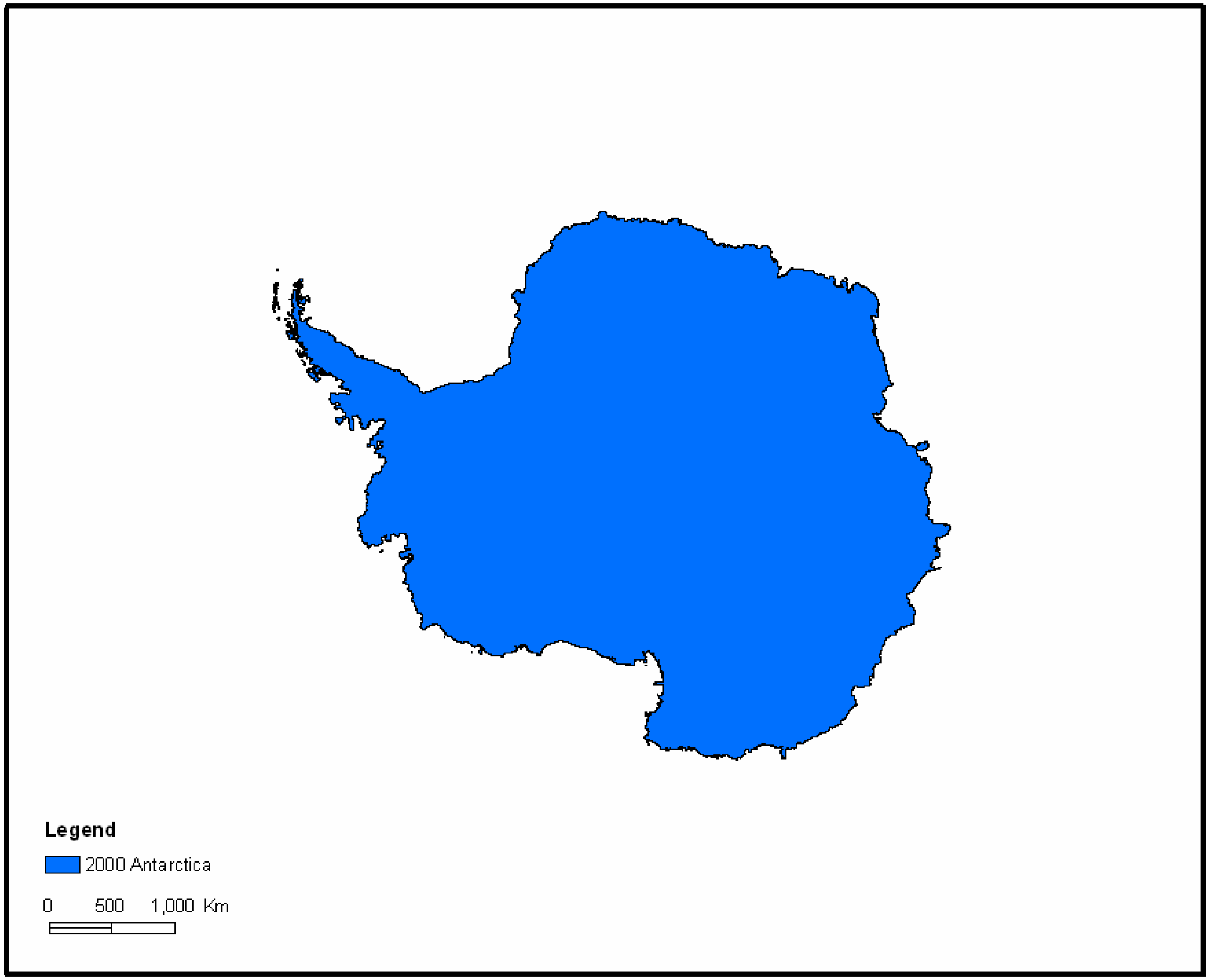

Figure 3.16 The extracted coastlines from sequential Radarsat SAR images in 2000

The absolute positional accuracy of the extracted coastline depends on the source image data. The SAR images from the AMM2 are processed by a rigorous orthorectification process (Liu & Jezek, 2004b). The absolute positional accuracy of pixels in SAR images is approximately 50~100m. The positional accuracy is also influenced by the coastline extraction algorithm. Through visual inspection, the extracted coastlines match human interpretation of coastline features observed on source SAR images at the pixel level. By comparing with coastlines from higher resolution data for the invariant portions of coastline, the overall absolute positional accuracy of the 2000 coastline is about 130 m, similar to that of the 1997 coastline. The coastline change detection depends on the relative positional accuracy of sequential satellite images. By using a number of invariant features (rock outcrops), the relative position accuracy between the 1997 and 2000 coastlines is about 40 m, corresponding to the mis-coregistration error between the 1997 SAR images and 2000 SAR images. This can translate the coastline position change error of 13.36 m/a.

3.5 Advance and Retreat Rates during 1997-2000

Overlaying the newly extracted 2000 coastline with the 1997 coastline enables ice margin change studies for the Antarctic continent. The areas experiencing the advance or retreat between 1997 and 2000 can be identified, and the rate of coastline changes can be computed. Figure 3.17 shows the change detection result, in which the blue color represents advance areas; the red color represents retreat areas. Quite clearly, during 1997-2000 the retreat of the Antarctic coastal margin is the dominant process, compared with the advance. The advance of the coastal margin took place at a smaller scale, and scattered along the Antarctic coast.

In total, some tens of thousands of regions in the Antarctic coast experienced the ice margin advance (Figure 3.18). The total advance area amounts to 12,929 km^2. The major advance regions are listed in Table 3.1 and Figure 3.19. The five regions with the largest advance areas include the Ross Ice Shelf (1,027 km^2, accounting for 8% of the total adavance, Figure 3.22), Thwaites Glacier (728 km^2, 6%, Figure 3.20), Filchner Ice Shelf (550 km^2, 4%, Figure 3.21), Amery Ice Shelf (545 km^2, 4%, Figure 3.23), and Ronne Ice Shelf (328 km^2, 3%, Figure 3.24). The advances of the five major regions during 1997-2000 are highlighted in Figure 3.20 to Figure 3.24.

Table 3.1 The most significant advance areas in the Antarctica

Name of Glacier	**Area(km^2)**
Thwaites Glacier Tongue	728.8019
Filchner Ice Shelf	550.6772
Ross Ice Shelf	1,027.2336
Amery Ice Shelf	545.4222
Ronne Ice Shelf	328.8946
Others	9,748.2126
Sum	**12,929.2421**

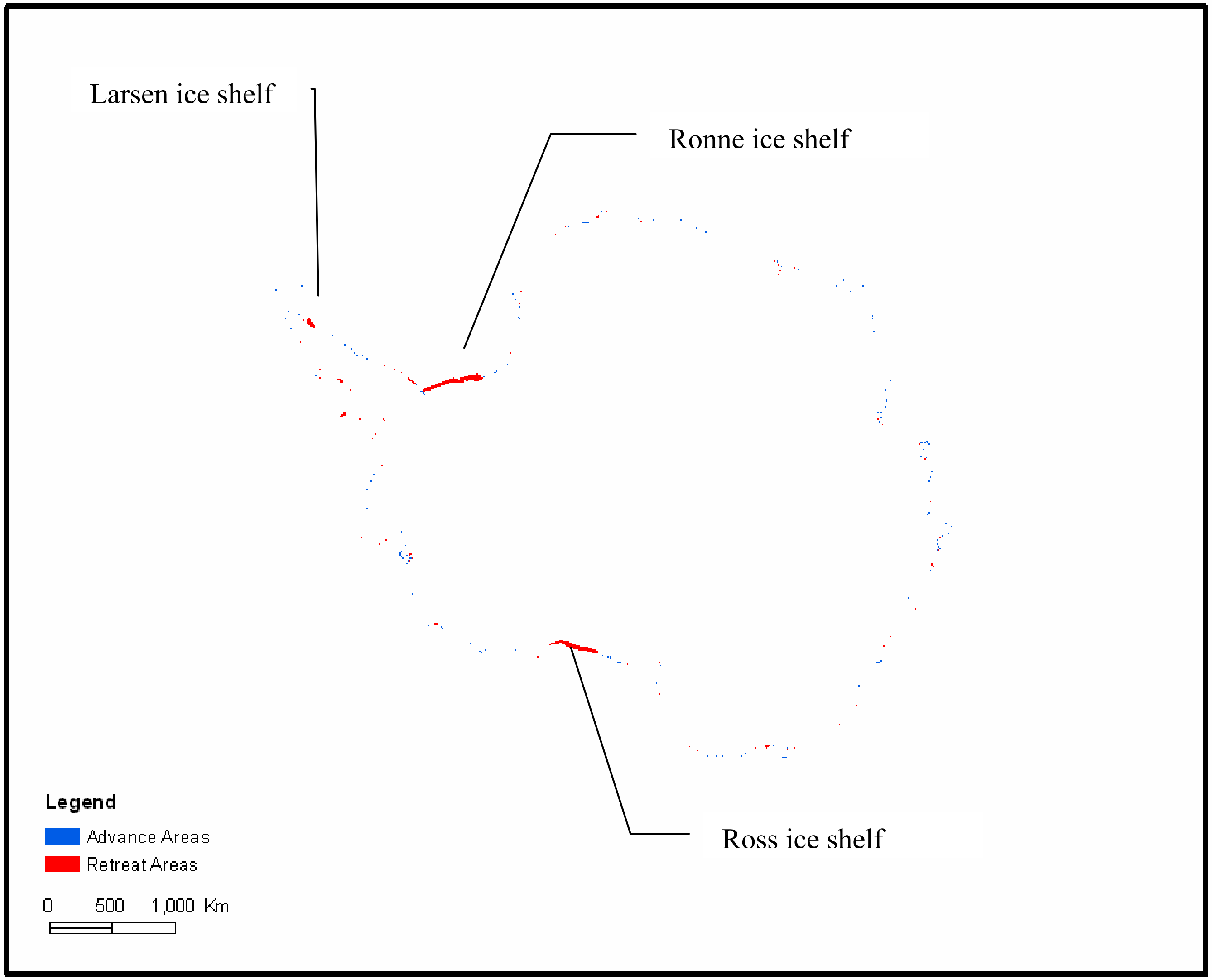

Figure 3.17 The advance and retreat areas of Antarctica comparing 1997 and 2000 coastlines

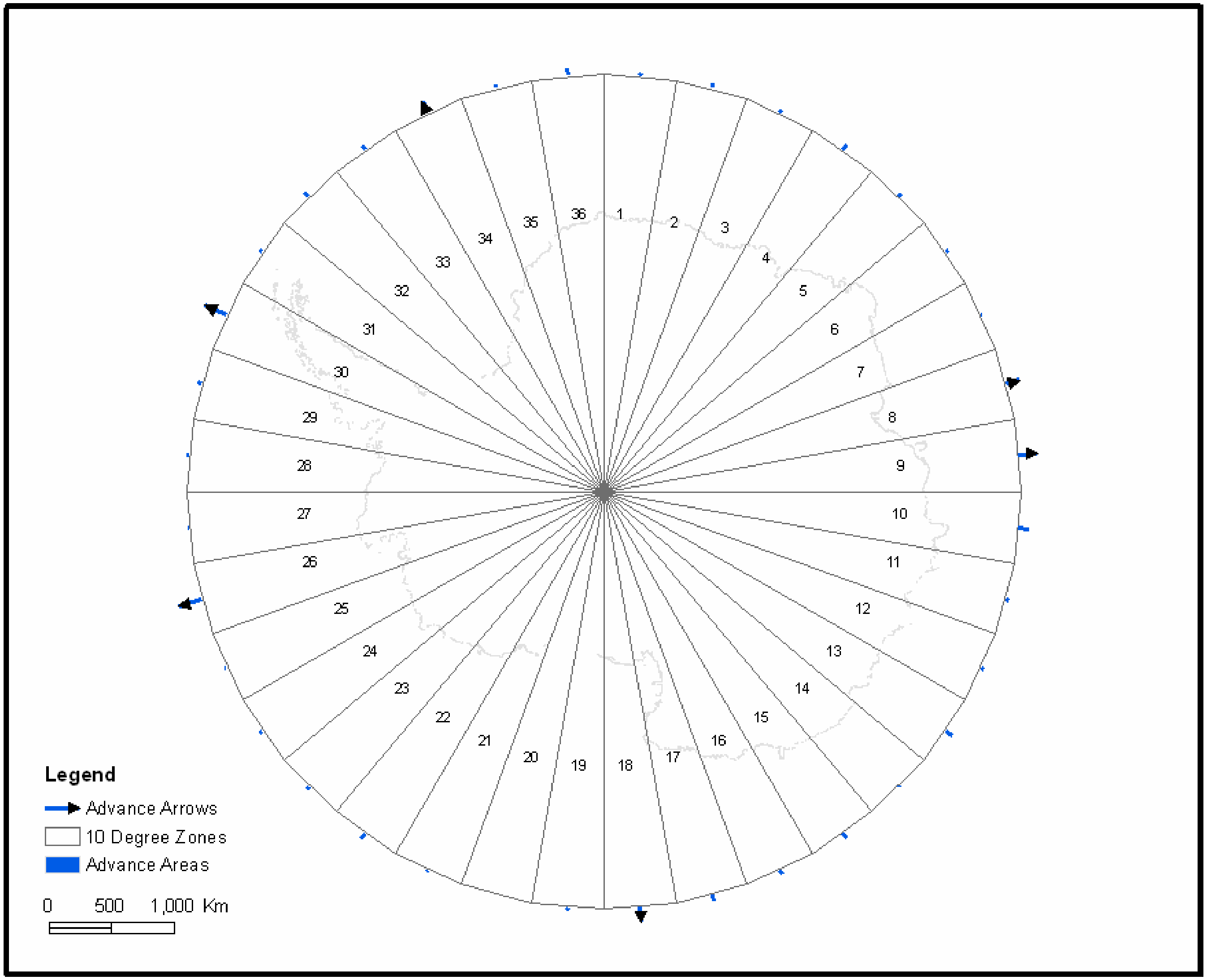

Figure 3.18 Areas of advance are demonstrated using blue arrows

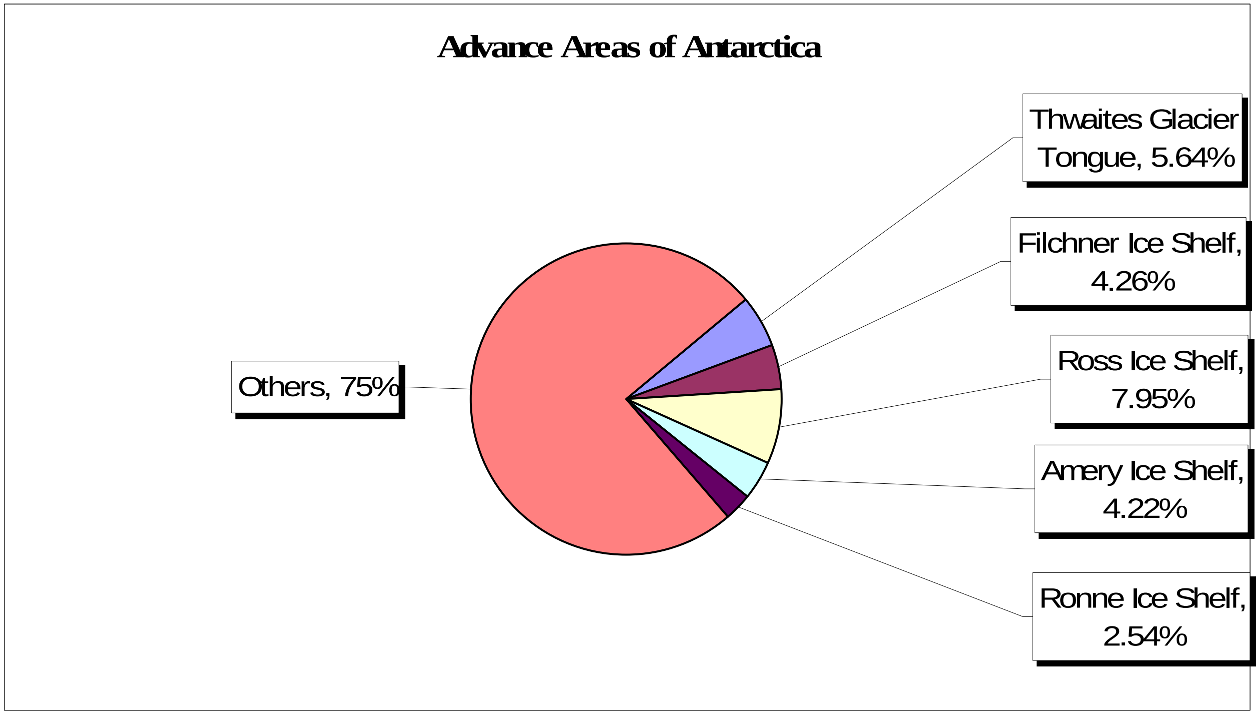

Figure 3.19 The pie chart of advance areas in the Antarctica

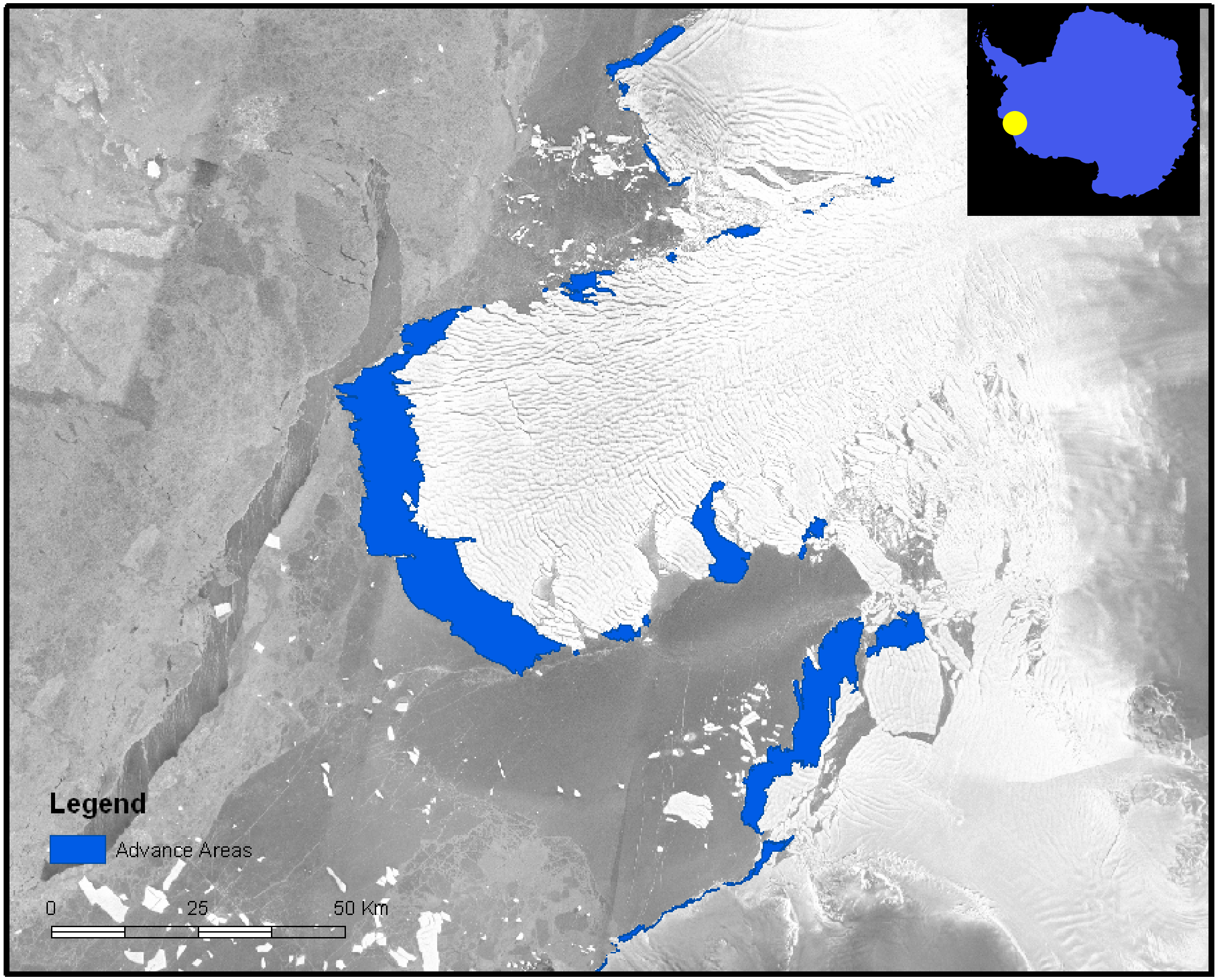

Figure 3.20 Thwaites glacier tongue (Advance)

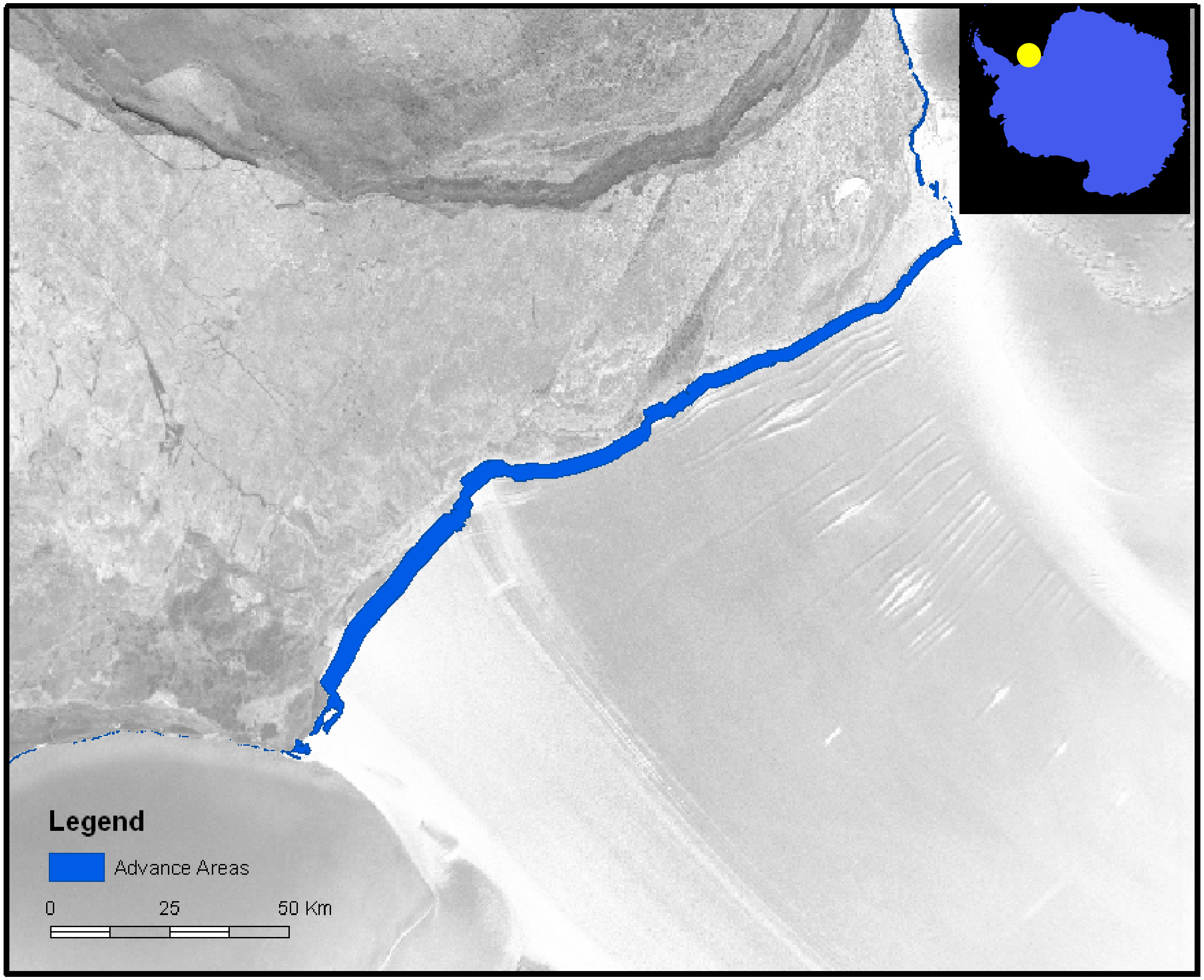

Figure 3.21 Filchner Ice Shelf (Advance)

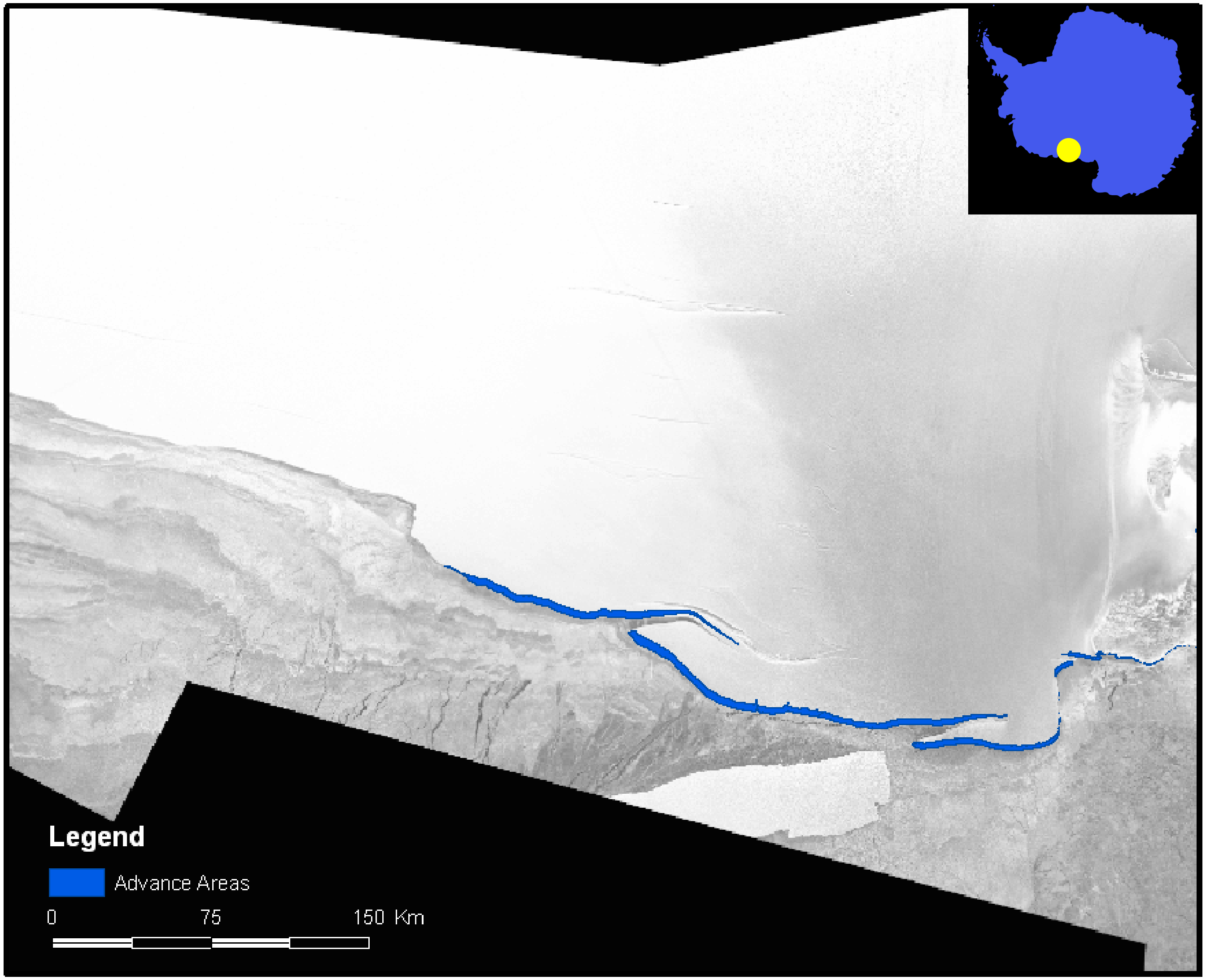

Figure 3.22 Ross Ice Shelf (Advance)

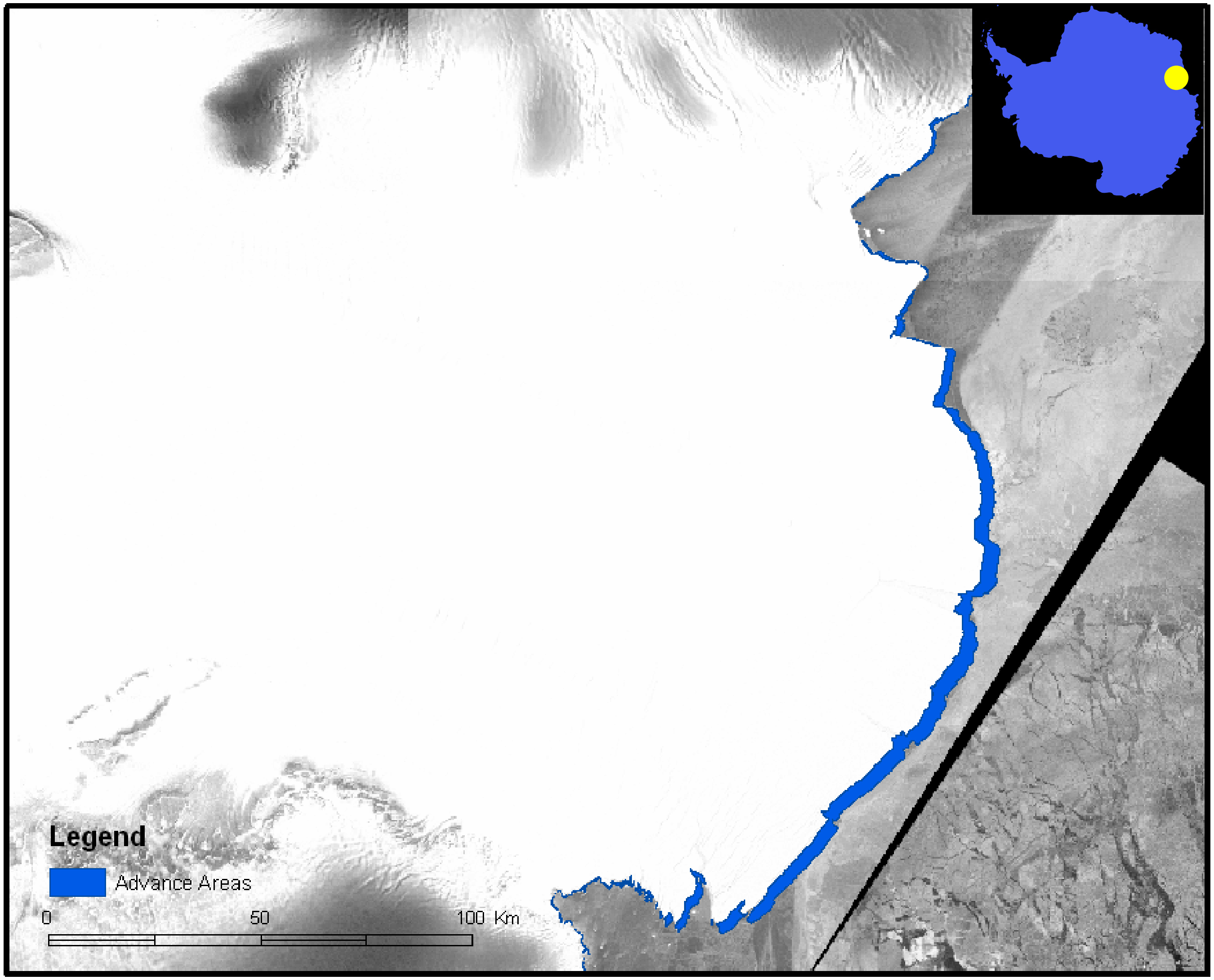

Figure 3.23 Amery Ice Shelf (Advance)

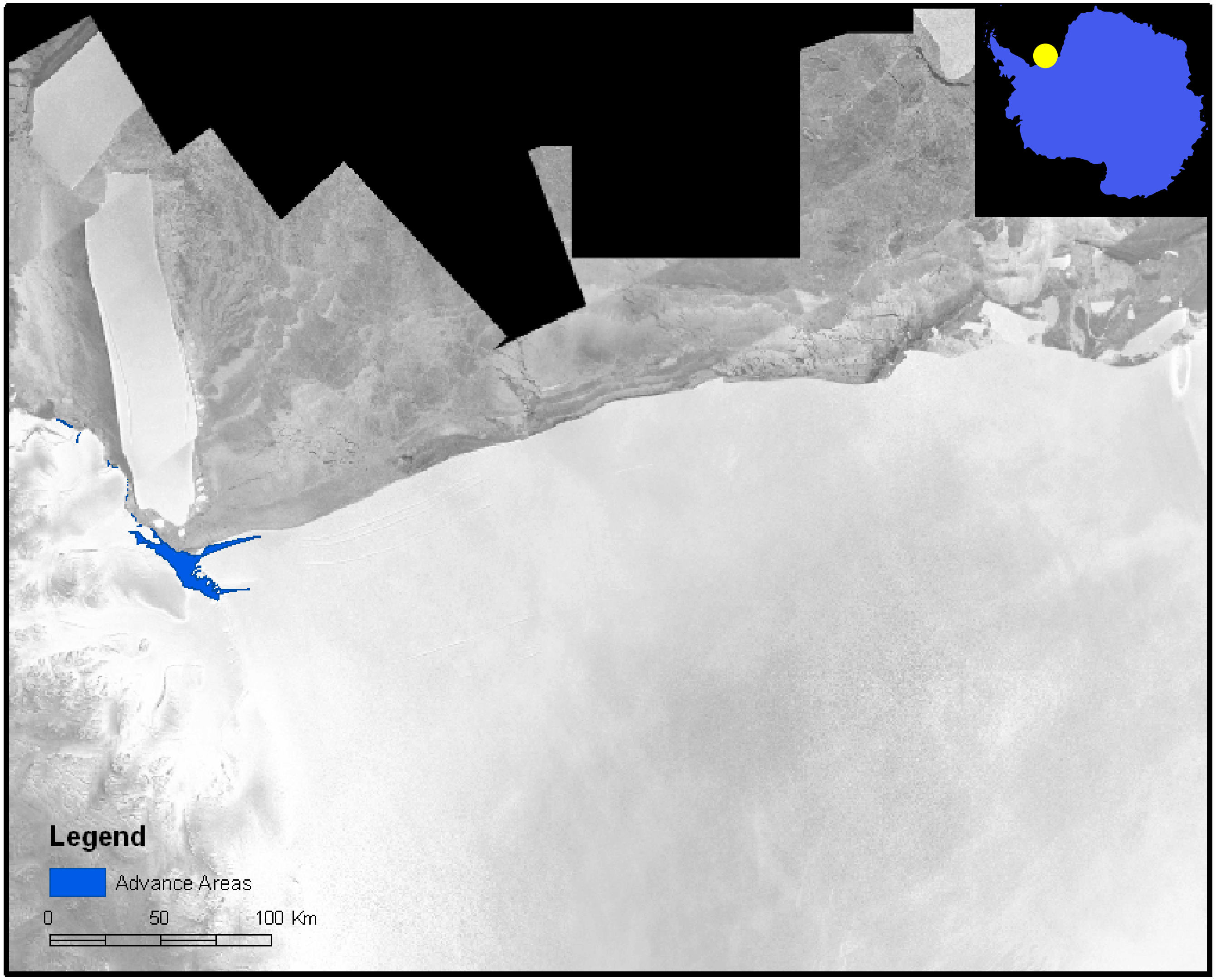

Figure 3.24 Ronne Ice Shelf (Advance)

In contrast, some tens of thousands of regions in the Antarctic coast experiencing the ice margin retreat (Figure 3.25). The total retreat area during 1997-2000 reaches 52,519 km^2. As illustrated in Table 3.2 and Figure 3.26, the major retreat occurred in eight regions, including the Ronne Ice Shelf (17,109 km^2, accounting for 32% of total retreat in Antarctica, Figure 3.27), the Ross Ice Shelf (11,841 km^2, 23%, Figure 3.28), Larsen Ice Shelf (2,699 km^2, 5%, Figure 3.29), Wells Glacier (1,235 km^2, 2%, Figure 3.30), Wilkins Ice Shelf (933 km^2, 2%, Figure 3.31), Wordie Ice Shelf (855.9 km^2, 2%, Figure 3.32), Ninnis Glacier Tongue (840 km^2, 2%, Figure 3.33), and Thwaites Glacier (481 km^2, 1%, Figure 3.34). The retreats of these regions are shown in Figure 3.27 through Figure 3.34.

Table 3.2 The most significant retreat areas in the Antarctica

Name of Glacier	**Areas (km^2)**
Ronne Ice Shelf	17,109.1787
Ross Ice Shelf	11,841.1791
Larsen Ice Shelf	2,699.2733
Wells Glacier	1,235.1939
Wilkins Ice Shelf	933.5777
Wordie Ice Shelf	855.9521
Ninnis Glacier Tongue	840.5043
Thwaites Glacier Tongue	481.1272
Others	16,523.1516
Sum	**52,519.1381**

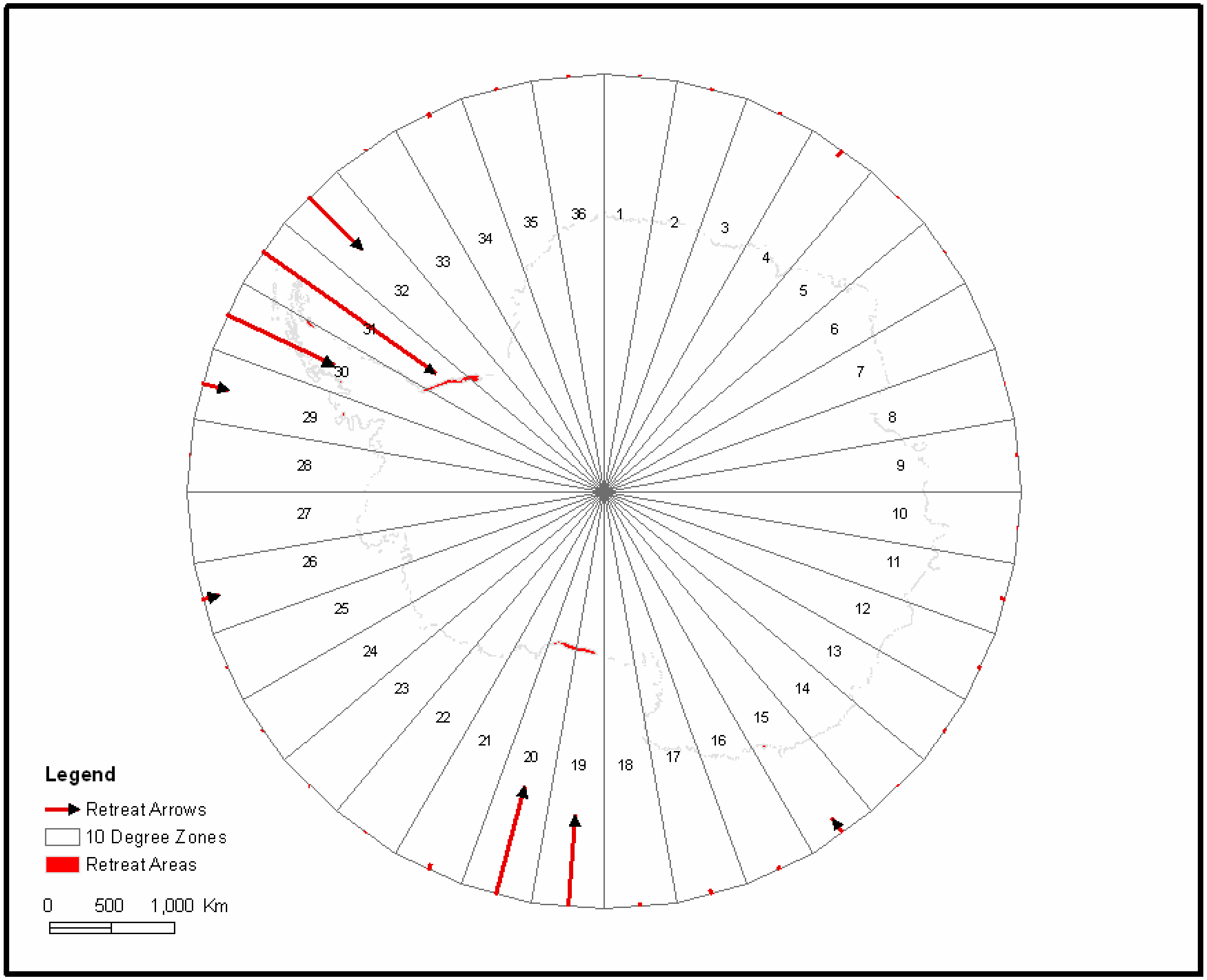

Figure 3.25 Areas of retreat are demonstrated using red arrows

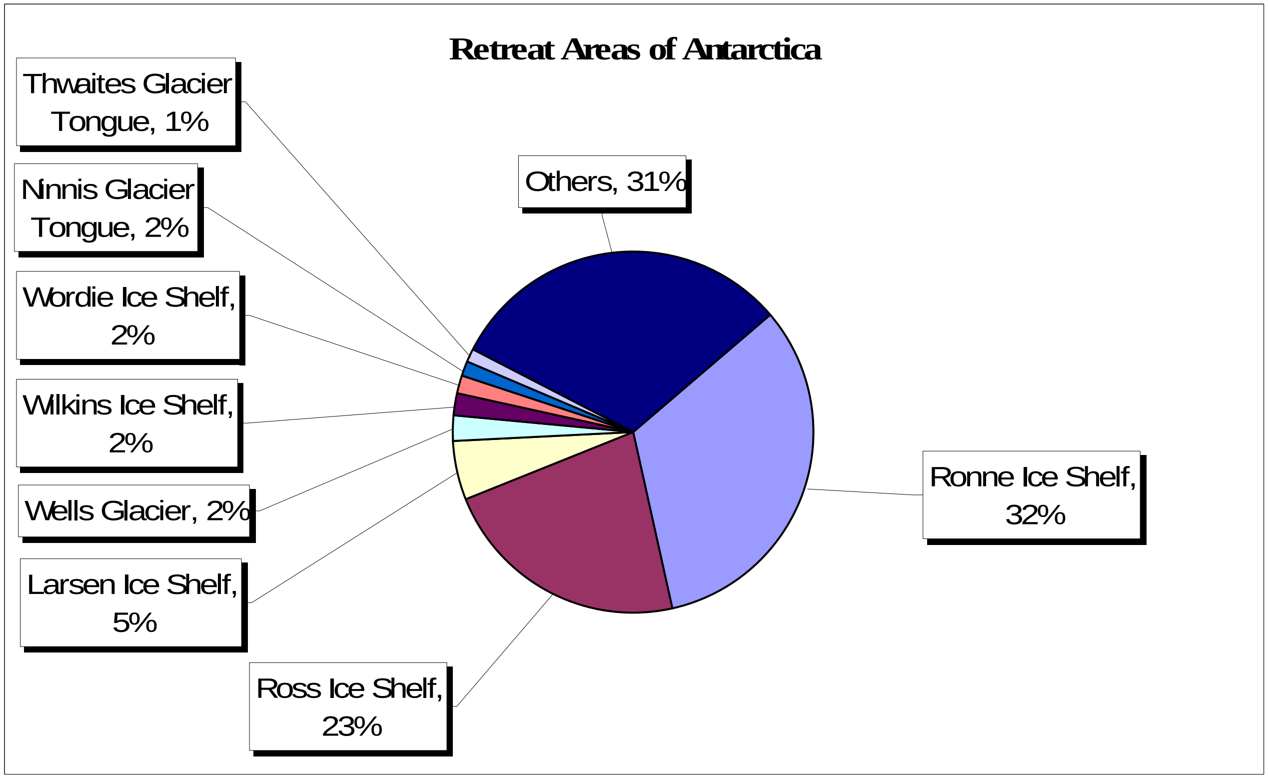

Figure 3.26 The pie chart of retreat areas in the Antarctica

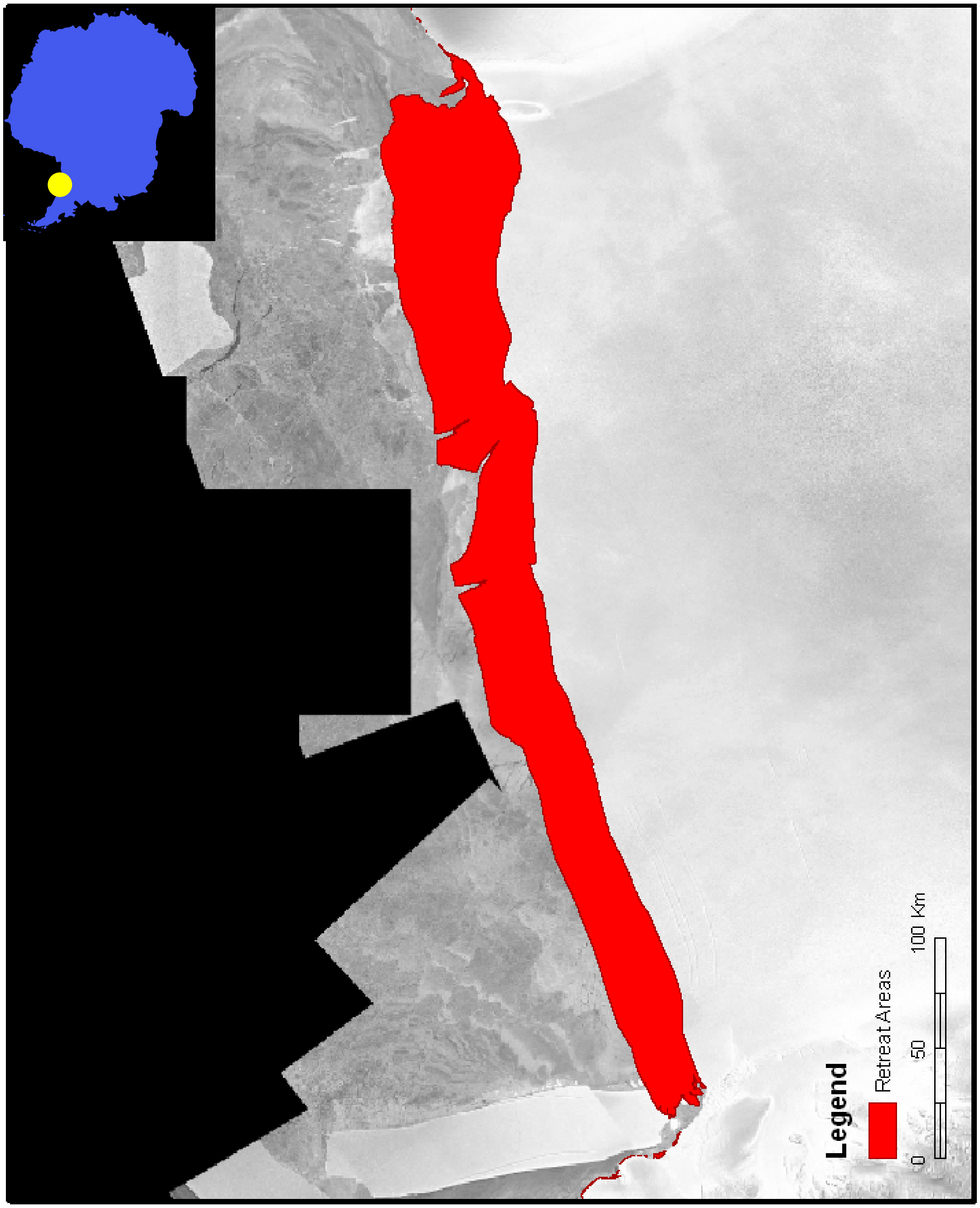

Figure 3.27 Ronne Ice Shelf (Retreat)

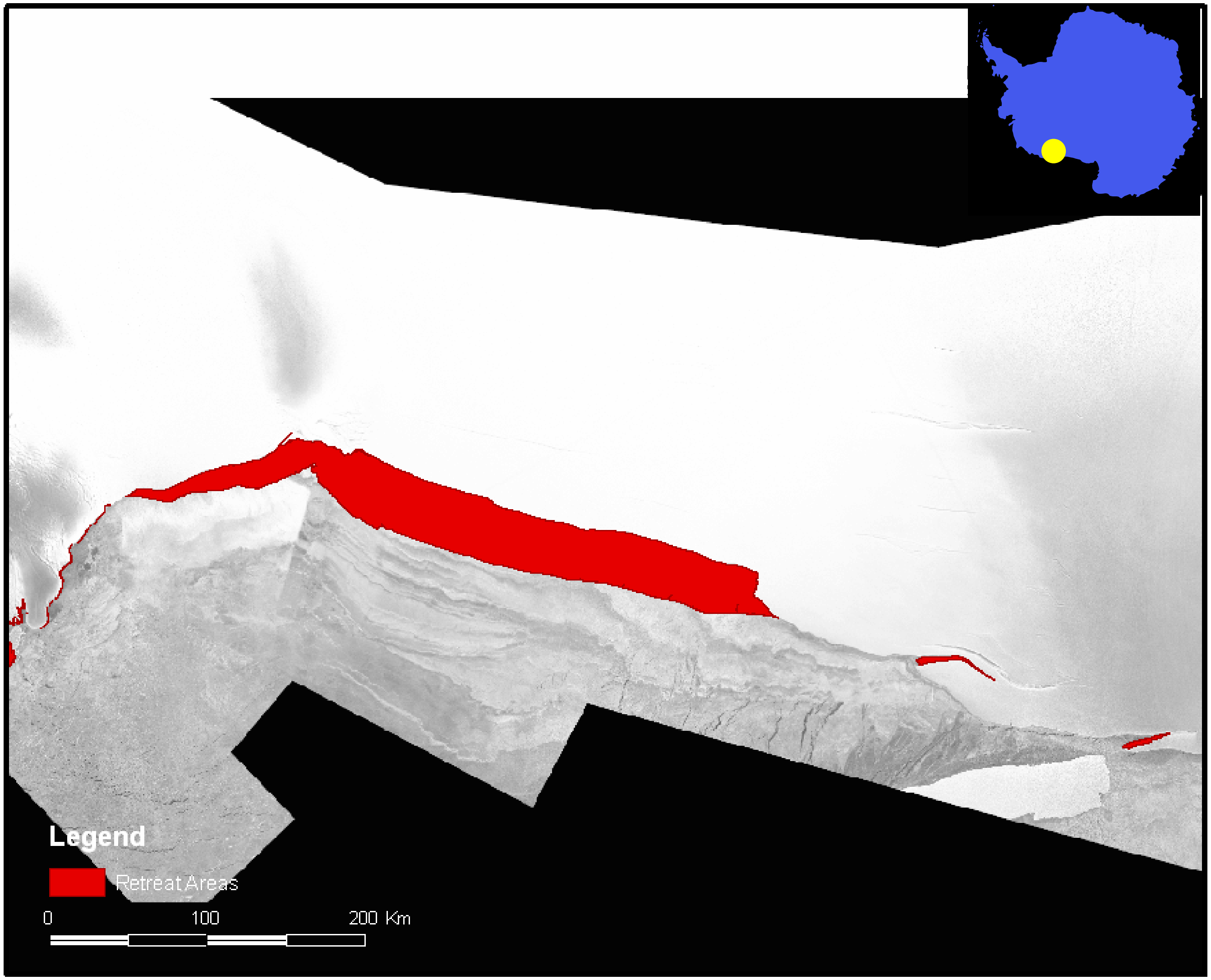

Figure 3.28 Ross Ice Shelf (Retreat)

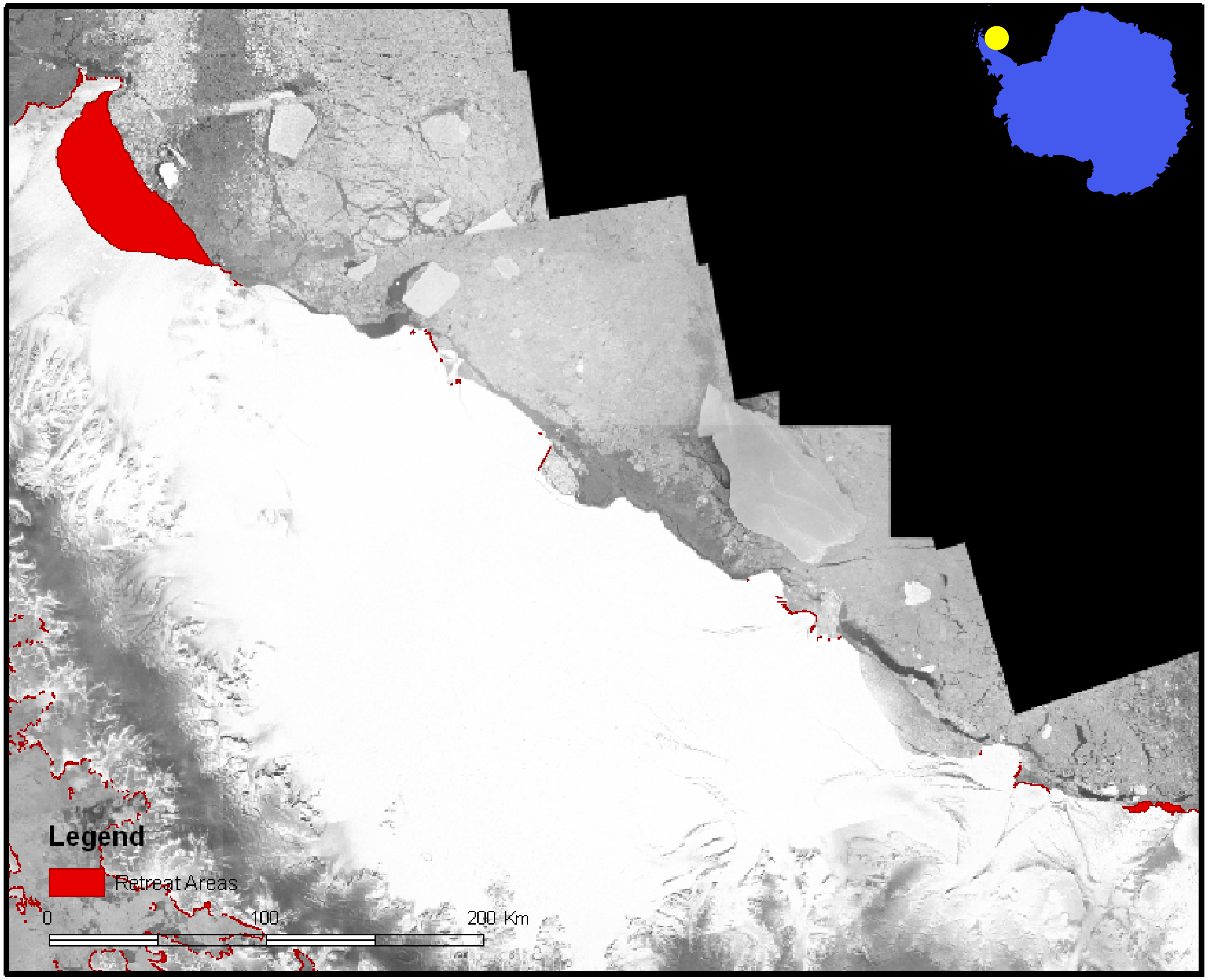

Figure 3.29 Larsen Ice Shelf (Retreat)

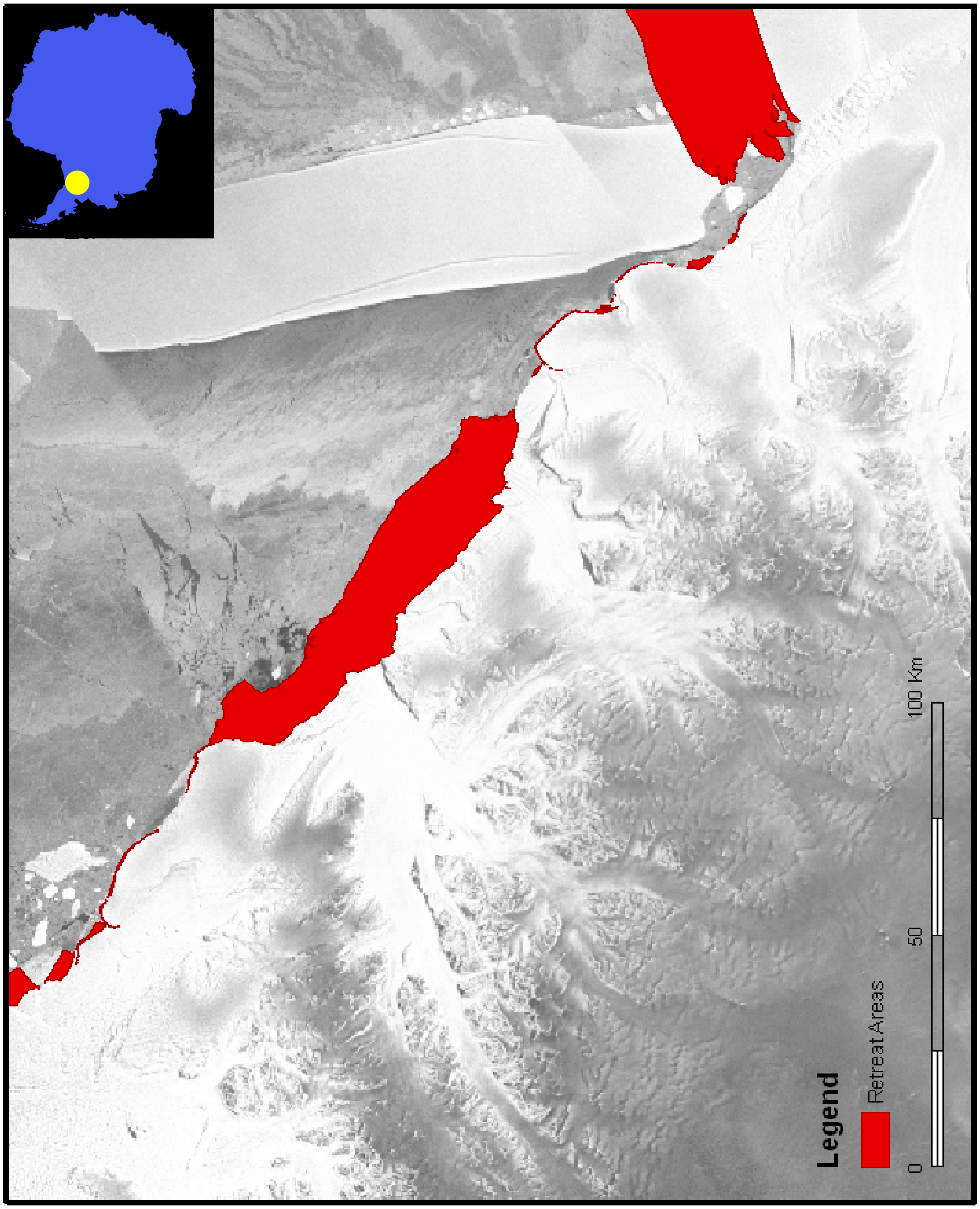

Figure 3.30 Wells glacier (Retreat)

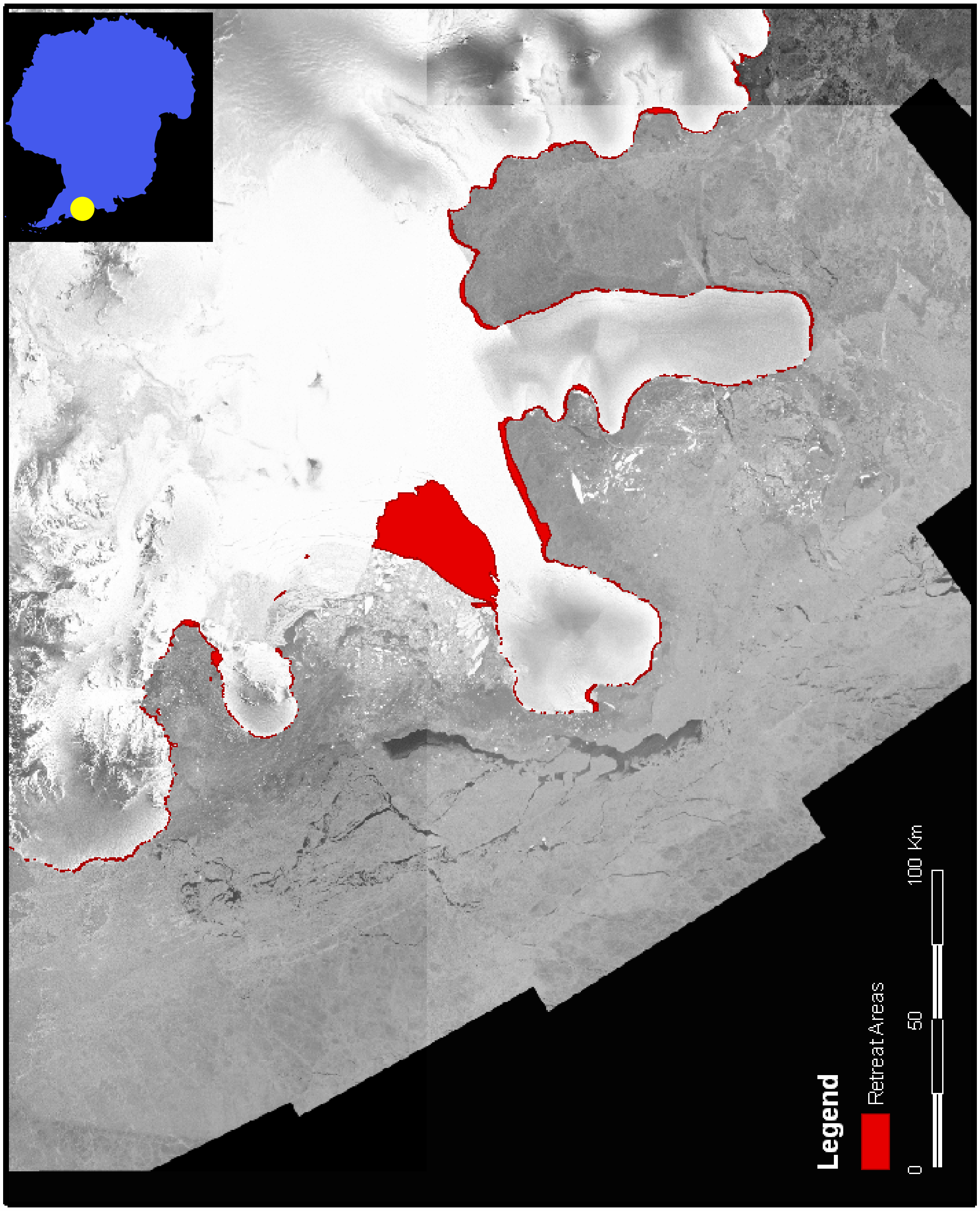

Figure 3.31 Wilkins Ice Shelf (Retreat)

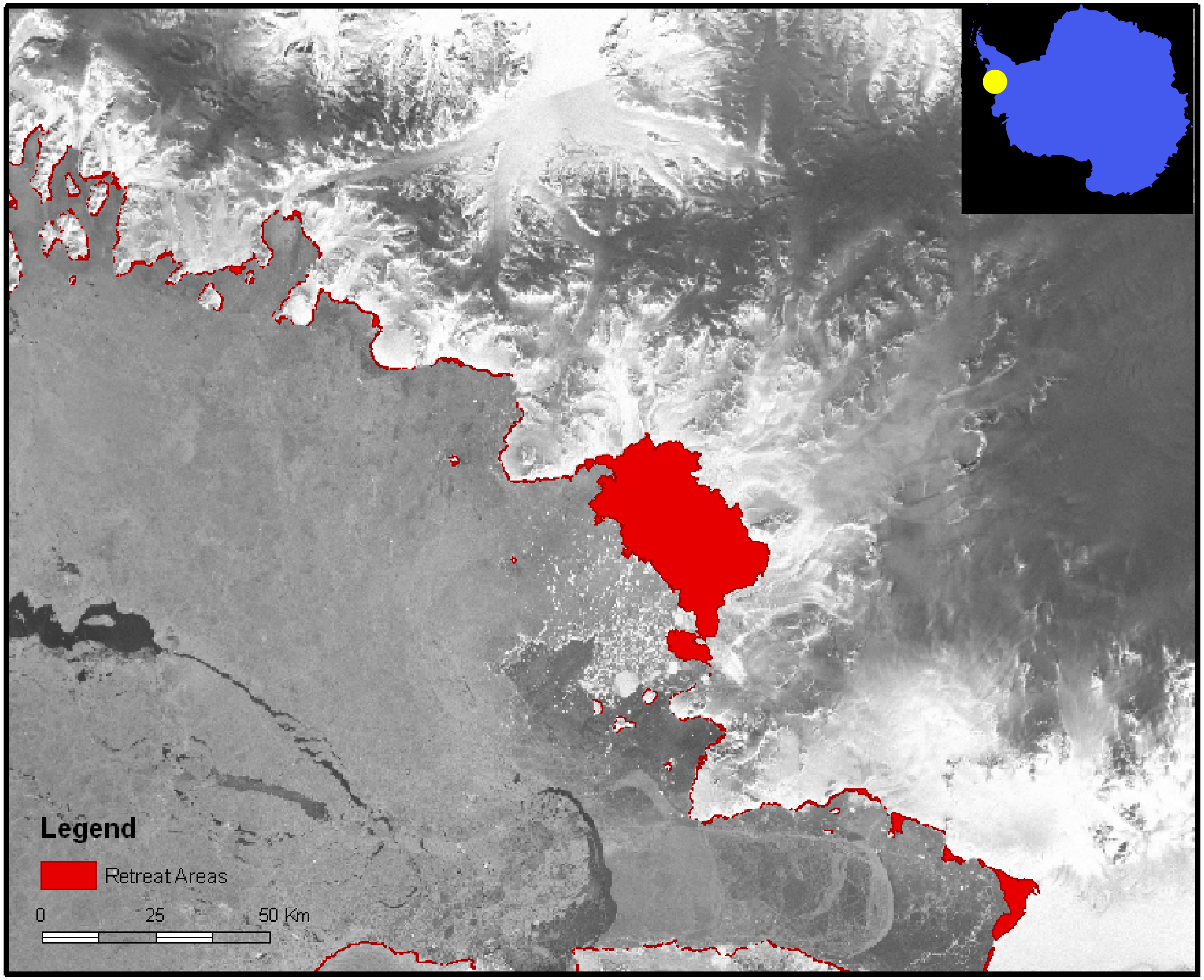

Figure 3.32 Wordie Ice Shelf (Retreat)

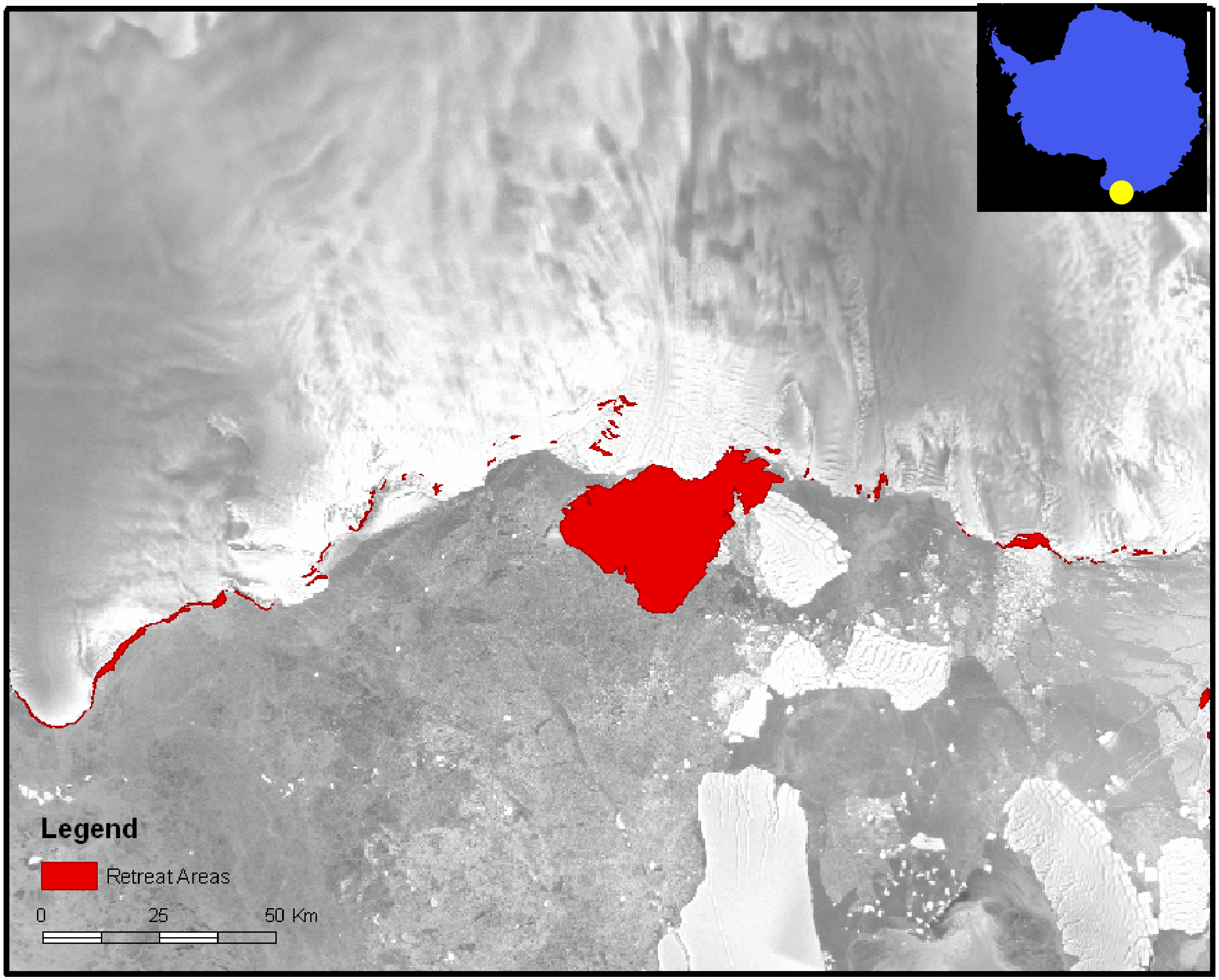

Figure 3.33 Ninnis glacier tongue (Retreat)

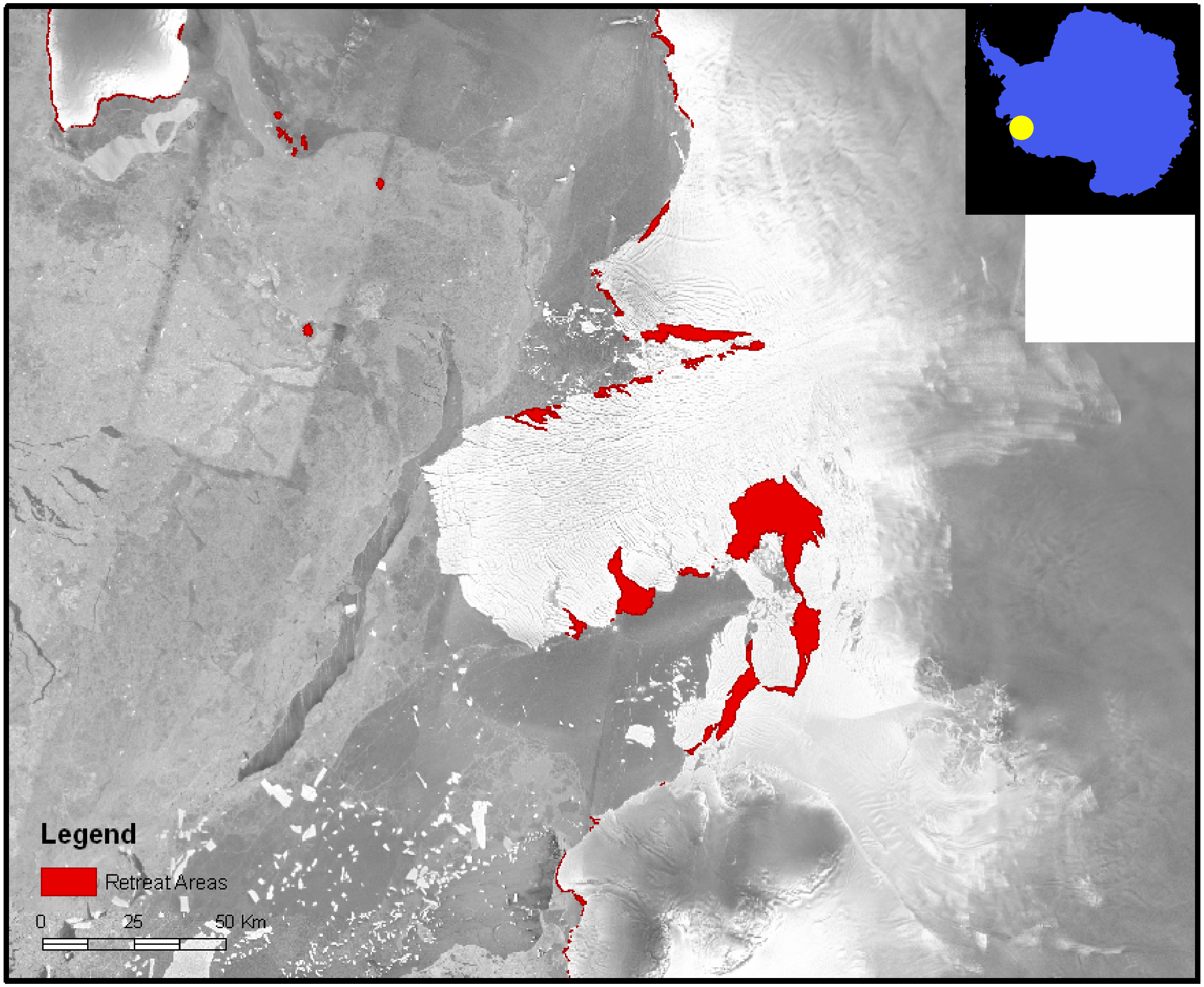

Figure 3.34 Thwaites glacier tongue (Retreat)

As illustrated above, many coastal regions experienced the retreat for some parts of their ice margins and the advance for other parts of their ice margin. It is important to examine the net change by comparing the advance area with the retreat area. In the Antarctic continent, the net areal extent change is about -39,590 km^2 during 1997-2000. Namely, the retreat area is significantly larger than the advance area, and the extent of the Antarctic continent is reduced by 39,590 km^2, which is larger than the area of the State of Maryland. Considering the time interval (1,093 days, 2.994521 year) between AMM1 and AMM2, the annual net retreat rate for the Antarctic Ice sheet is about 13,221 km^2/a.

In order to clearly show the spatial pattern of ice margin advance, retreat, and net changes, two rose diagrams are made as shown in Figure 3.35 and Figure 3.36. In these two diagrams, the Antarctic coast are divided into 36 sectors, the amounts of advance or retreat in each sector are connected to form a rose diagrams. The diagrams reveal the magnitude and direction of ice margin changes and identify the major net advance and retreat coastal regions. Obviously, the Antarctic Peninsula, the Ronne Ice Shelf, and Ross Ice Shelf are the primary regions experienced the largest net retreat. Amery Ice shelf area experienced considerable amount of net advance.

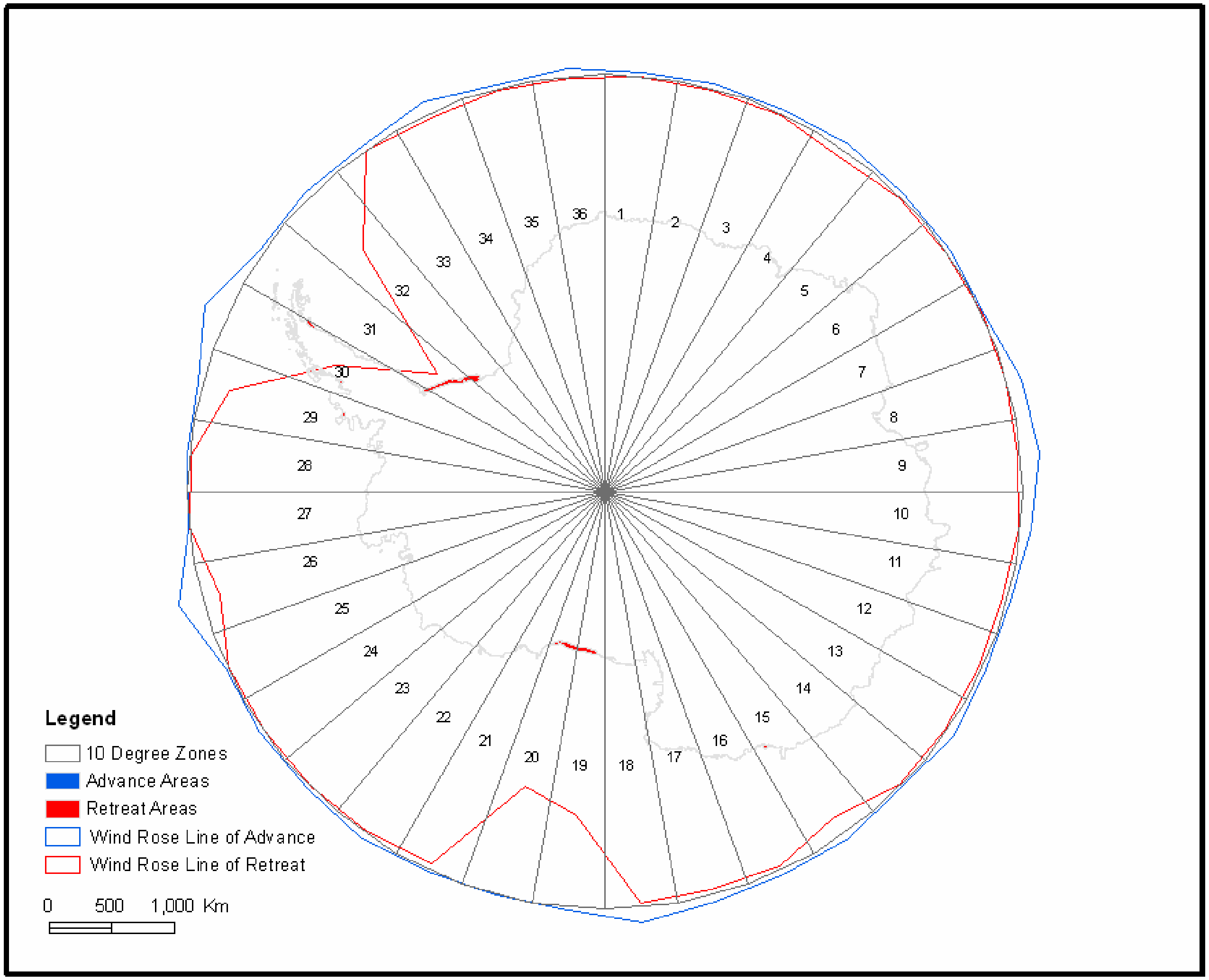

Figure 3.35 The wind rose map of advance and retreat areas

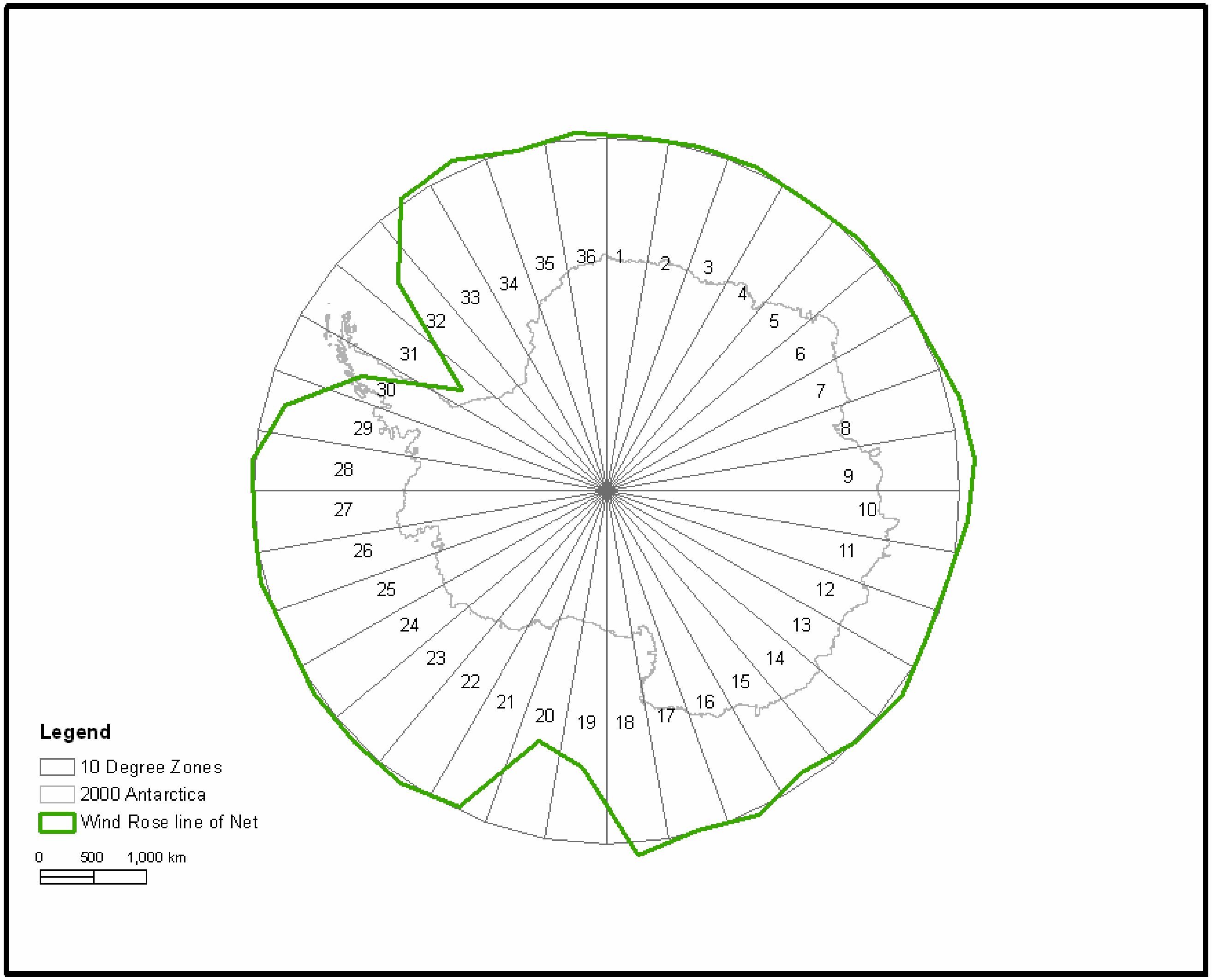

Figure 3.36 The wind rose map of net areas

In terms of specific ice shelves and coastal outlet glaciers, Ronne Ice Shelf, Ross Ice Shelf, Larsen Ice Shelf, Wilkins Ice Shelf, Wordie Ice Shelf, and Ninnis Ice Shelf experienced the largest volume of net areal reductions during 1997-2000 (Table 3.3). Amery Ice Shelf, Filchner Ice Shelf, and Thwaites Glacier are among those experienced the largest amount of net areal expansion (Table 3.3).

Table 3.3 The net results in the Antarctica after the combination of gain and loss

Name of Glacier	**Net Area(Km^2)**
Ronne Ice Shelf	-16,780.28406
Ross Ice Shelf	-10,813.94556
Larsen Ice Shelf	-2,699.27328
Wilkins Ice Shelf	-933.5777434
Wordie Ice Shelf	-855.952139
Ninnis Glacier	-840.504328
Filchner Ice Shelf	550.6771786
Amery Ice Shelf	545.4221937
Thwaites Glacier	247.6746884

To assess the long-term ice margin change trend of the Antarctica, the 1997 coastline extracted from the Radarsat SAR images is also compared with the 1963 Antarctic coastline, which was extracted from Argon DISP (Declassified Intelligence Satellite Photographs) images (Kim et al, 2007). The Argon DISP images have a 140 m spatial resolution, coarser than the Radarsat SAR images. Figure 3.37 illustrates the coastlines from Argon images, and there are some broken line segments because the areas in the images are covered by clouds. Figure 3.38 illustrates the ice margin advance and retreat during 1963-1997. Overall, the extent of the Antarctic Ice Sheet was reduced by 48,327 km^2 over the 34 year of period, and the average annual reduction rate is about 1,421 km^2/a, much smaller the average net retreat rate of 13,221 km^2/a during 1997-2000. This means that the net retreat rate of the Antarctic Ice sheet has been accelerated in recent years.

Although the consistent net retreats, the spatial pattern of ice margin advance and retreat during 1963-1997 is different from that during 1997-2000. Table 3.4 and Figure 3.39 through Figure 3.48 illustrates the advance and retreat details of several ice shelves and outlet glaciers. The regions experienced the largest net ice margin changes during 1992-1997 include Abbot Ice Shelf, Amery Ice Shelf, Fimbul Ice Shelf, Lazarev Ice Shelf, the Antarctic peninsula (Larsen Ice Shelf), Ragnhild Ice Shelf, Ronne-Filchner Ice Shelf, Ross Ice Shelf, and Shackleton Ice Shelf. Overall, the Antarctic Peninsula experienced the continued net retreat throughout 1963-1997 and 1997-2000. Although Ross Ice Shelf and Ronne Ice Shelf experienced the significant net advance during 1963-1997, they underwent considerable net retreat during 1997-2000. On the other hand, the Amery Ice shelf experienced obvious net retreat during 1963-1997, but the net advance expanded its extent during 1997-2000. The Shackleton Ice Shelf experienced a large scale of retreat during 1963-1997, and its change during 1997-2000 is very small.

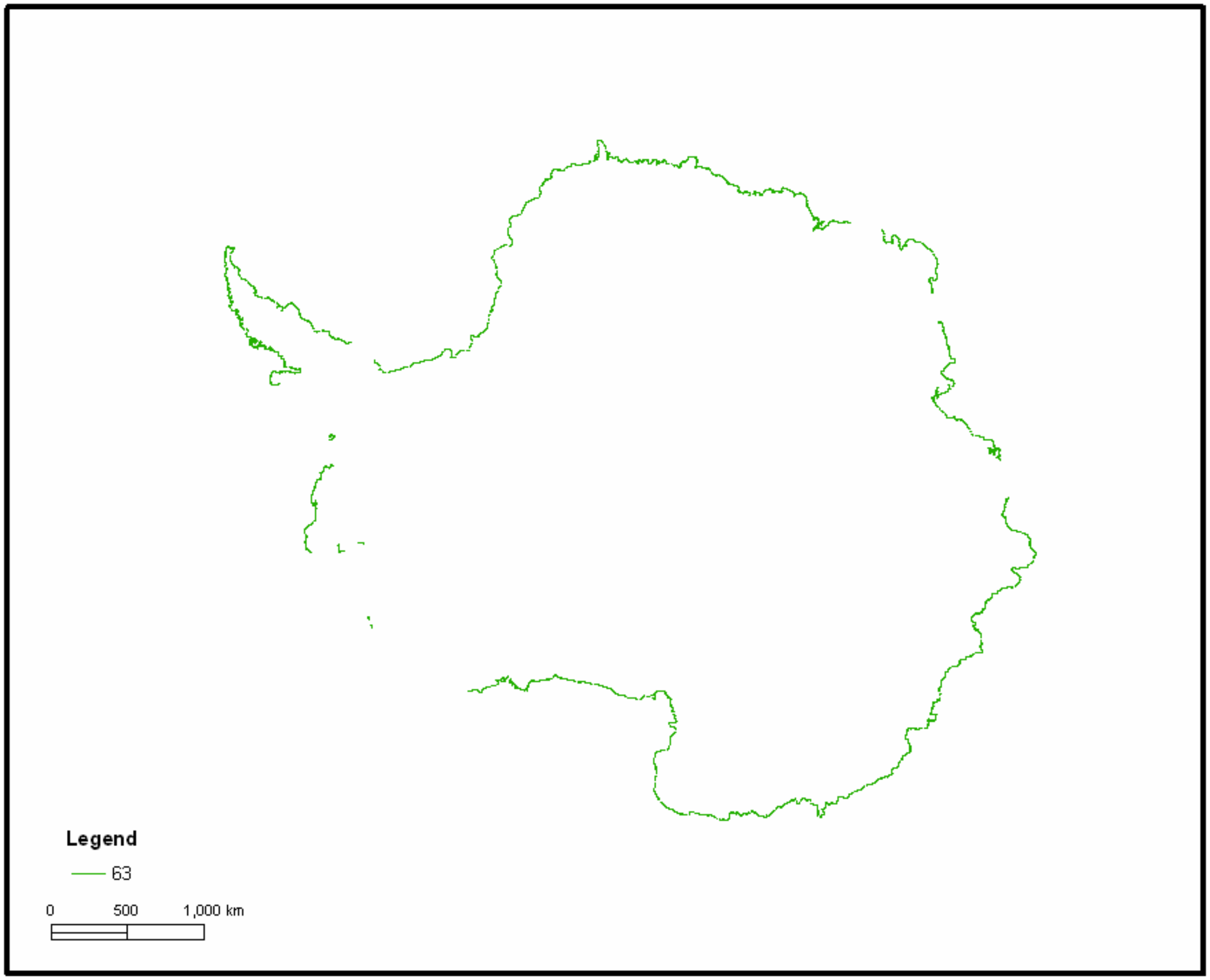

Figure 3.37 The 1963 Antarctic coastlines

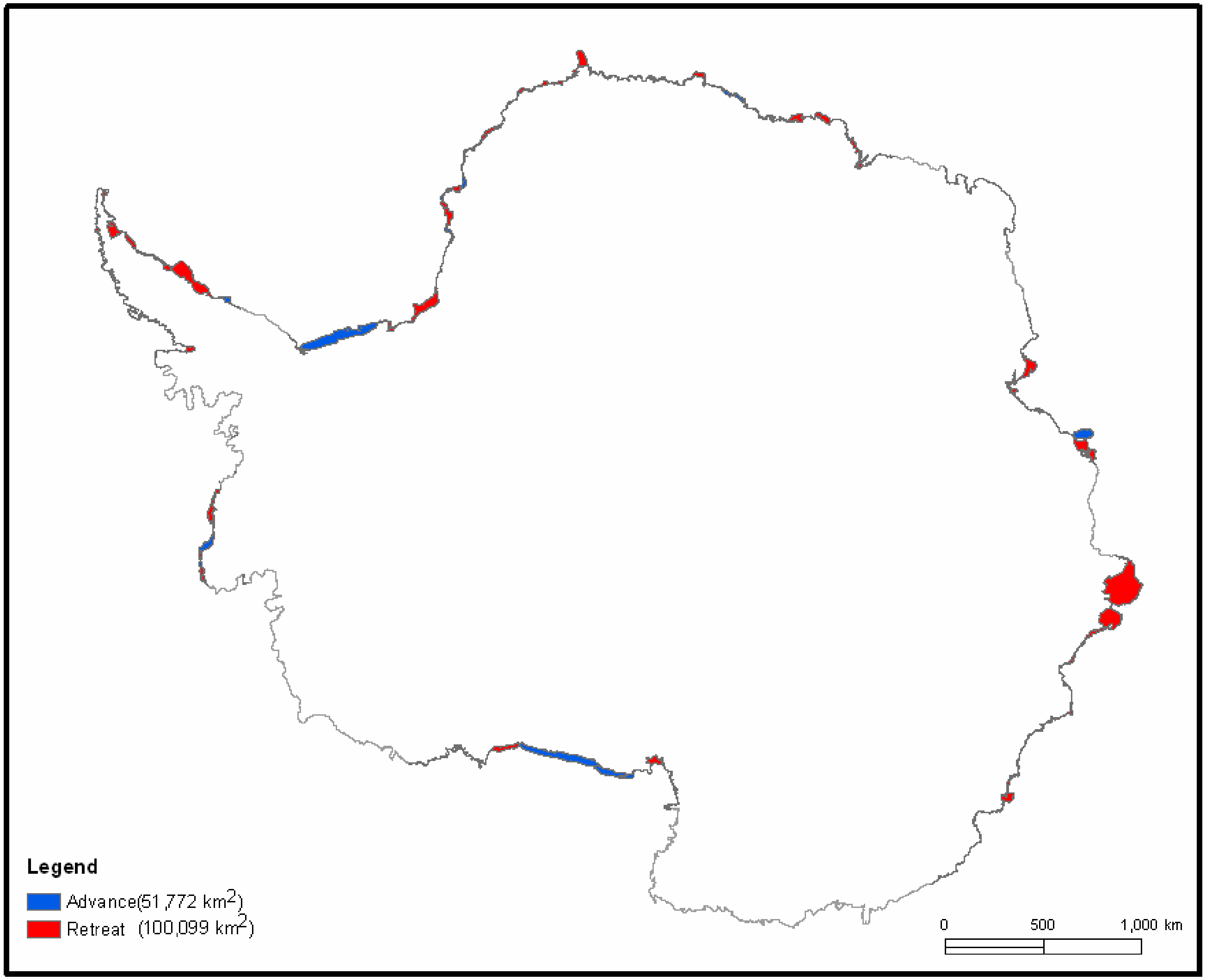

Figure 3.38 A comparison of 1963 and 1997 Antarctic coastlines

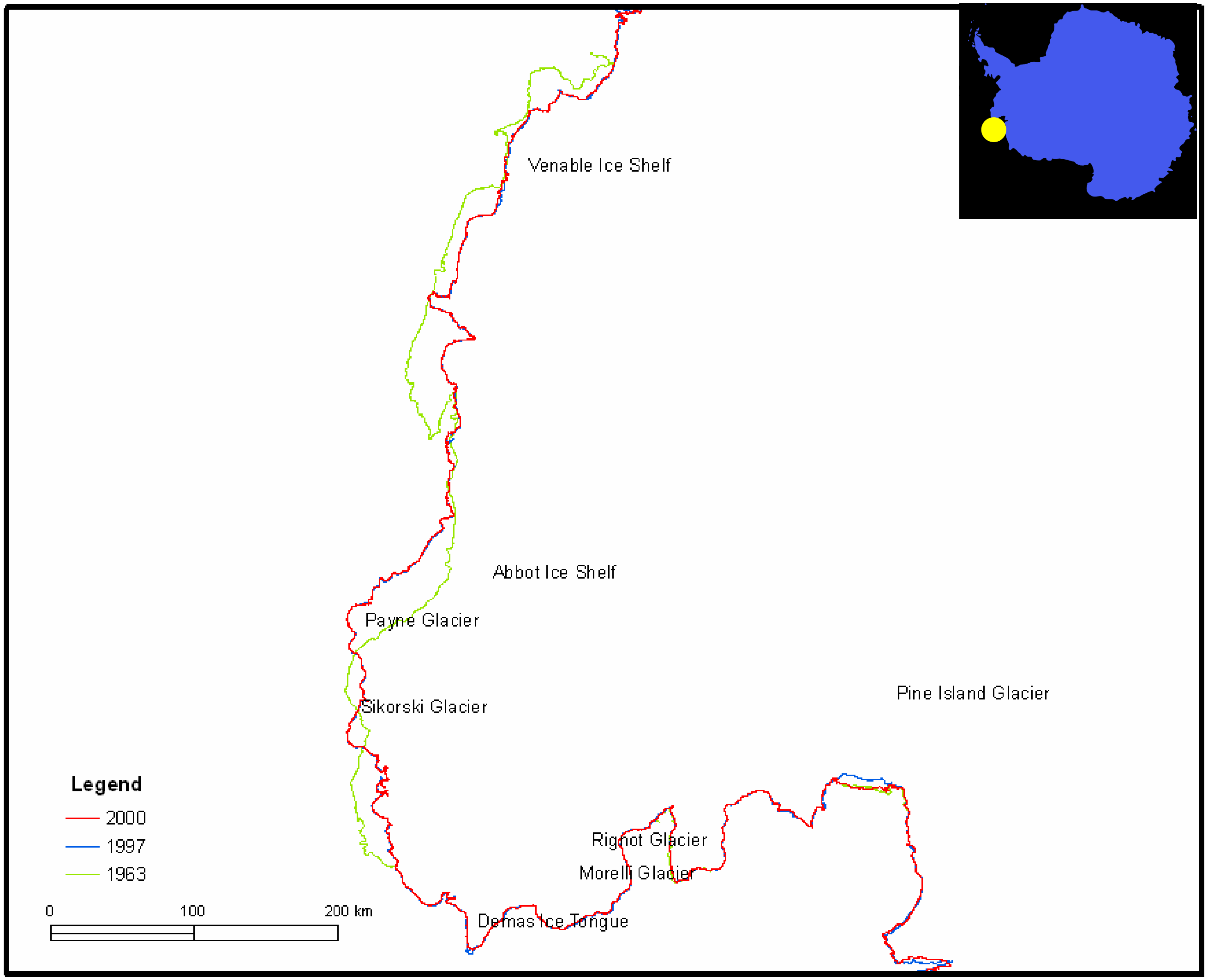

Figure 3.39 Abbot Ice Shelf

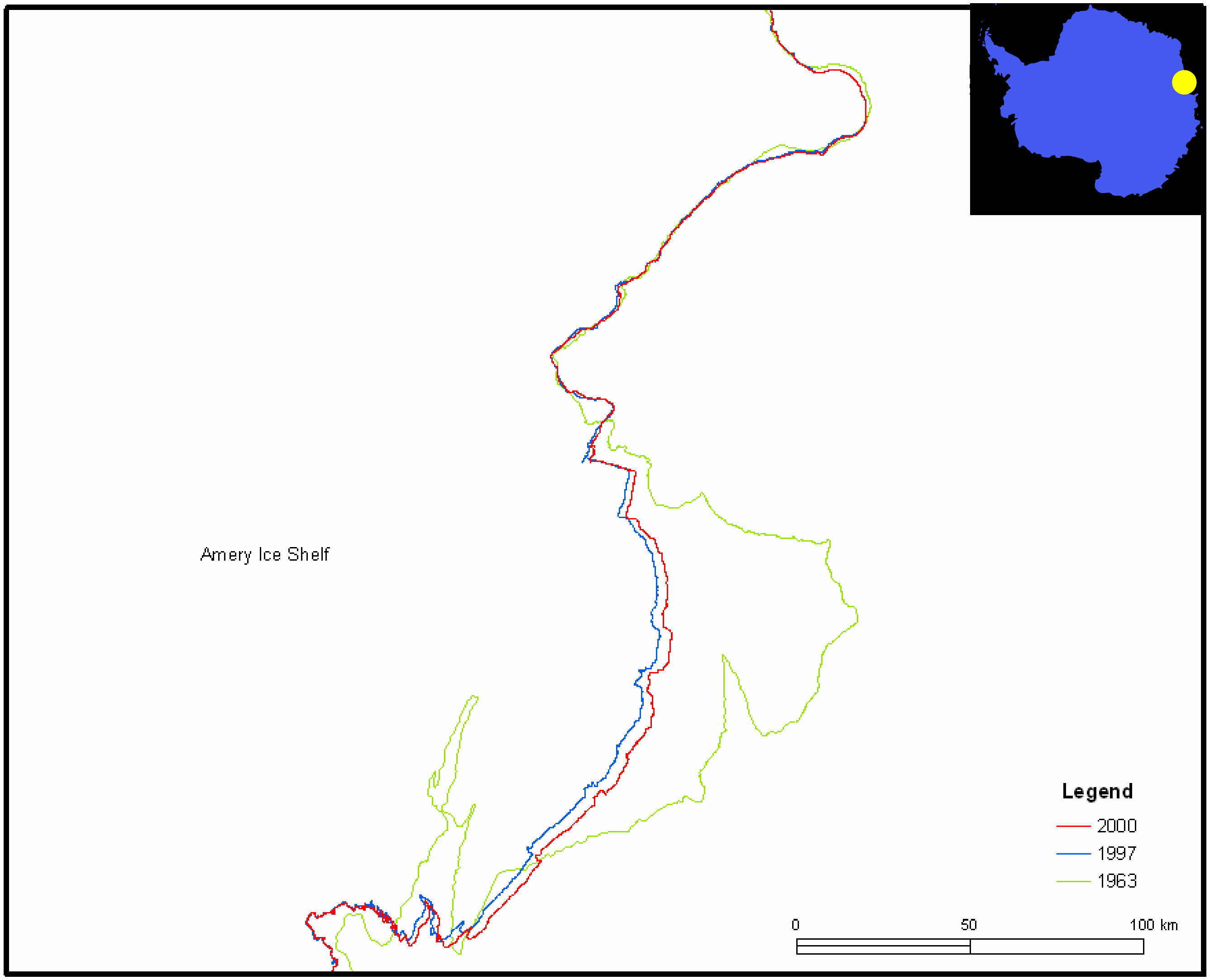

Figure 3.40 Amery Ice Shelf

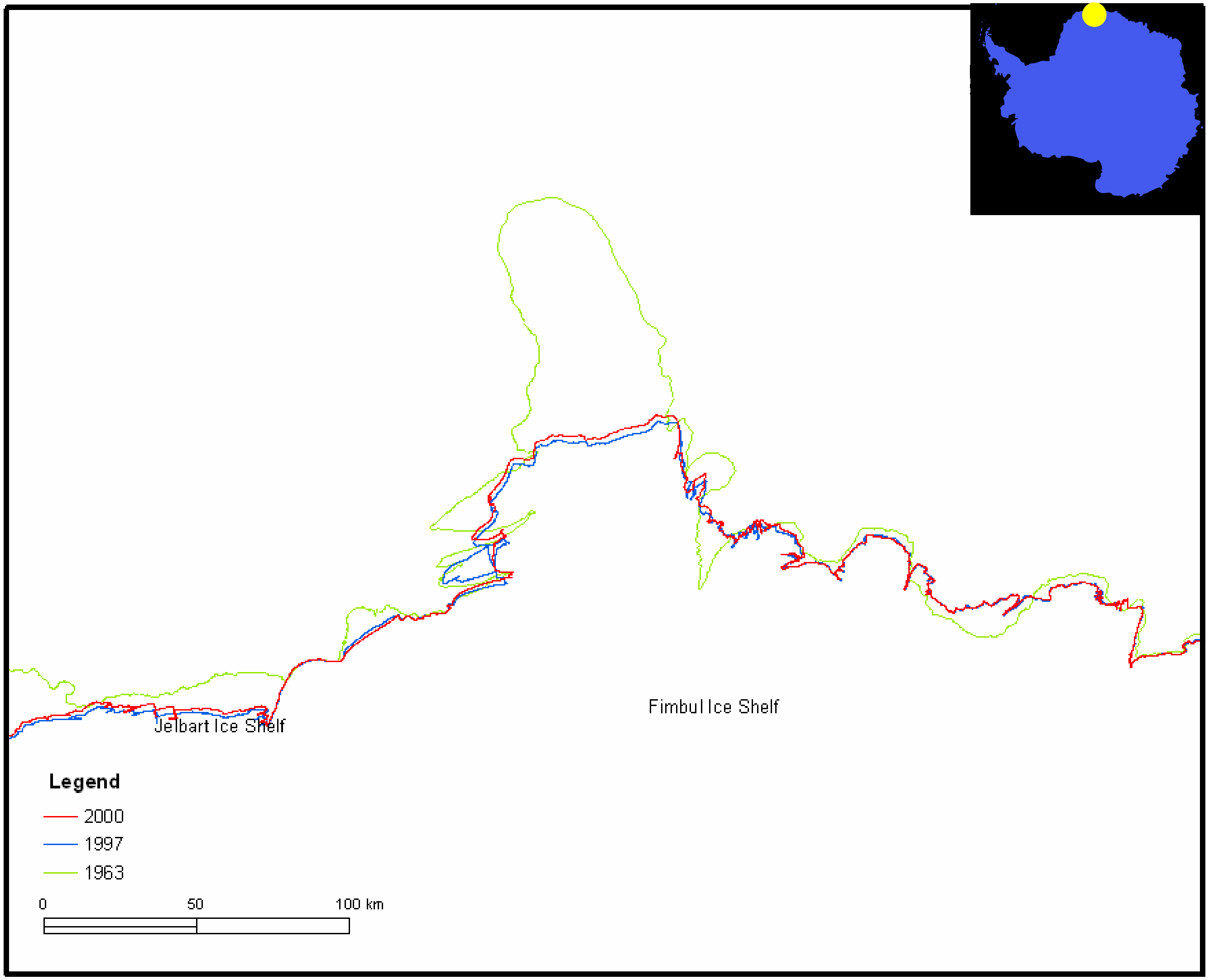

Figure 3.41 Fimbul Ice Shelf

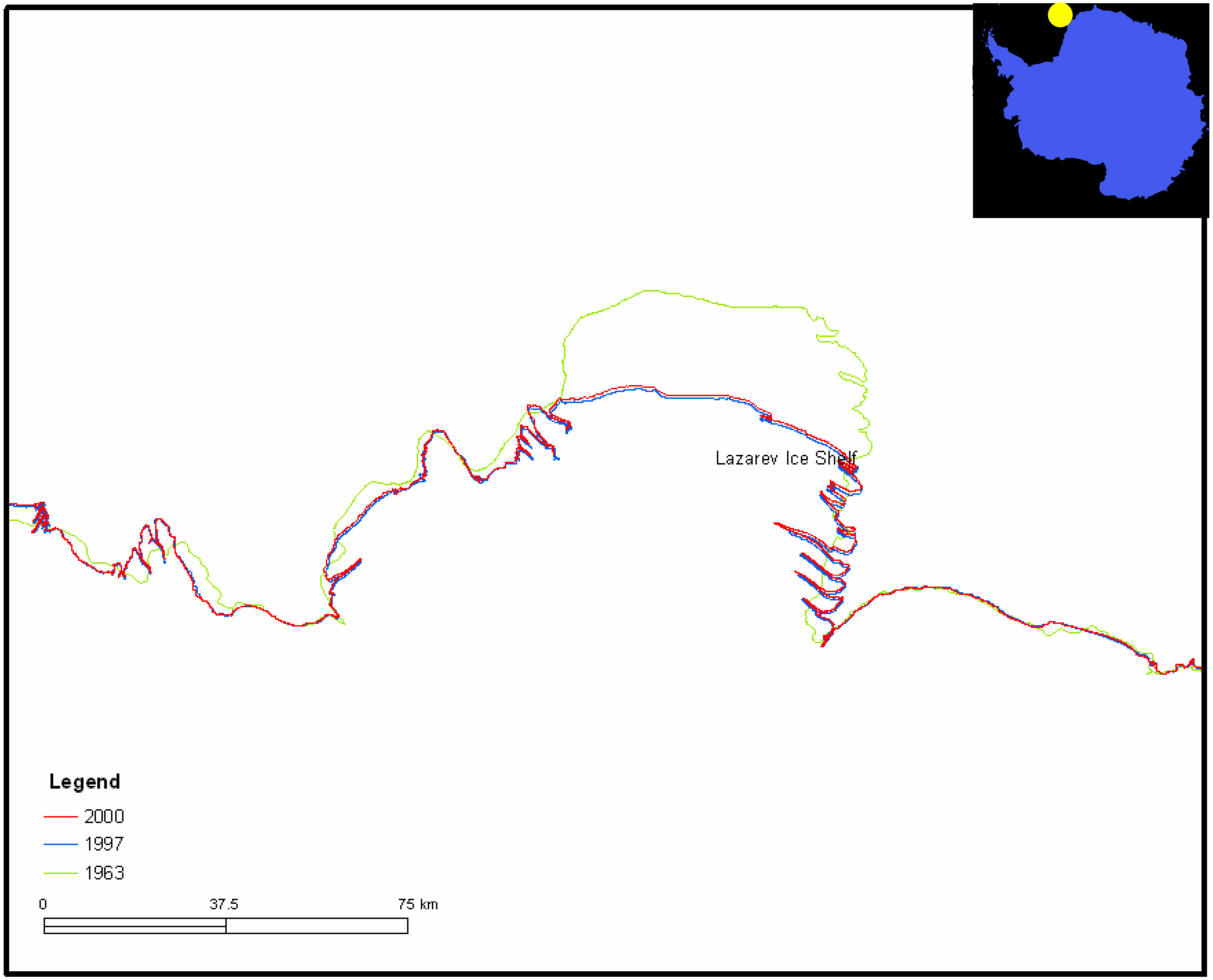

Figure 3.42 Lazarev Ice Shelf

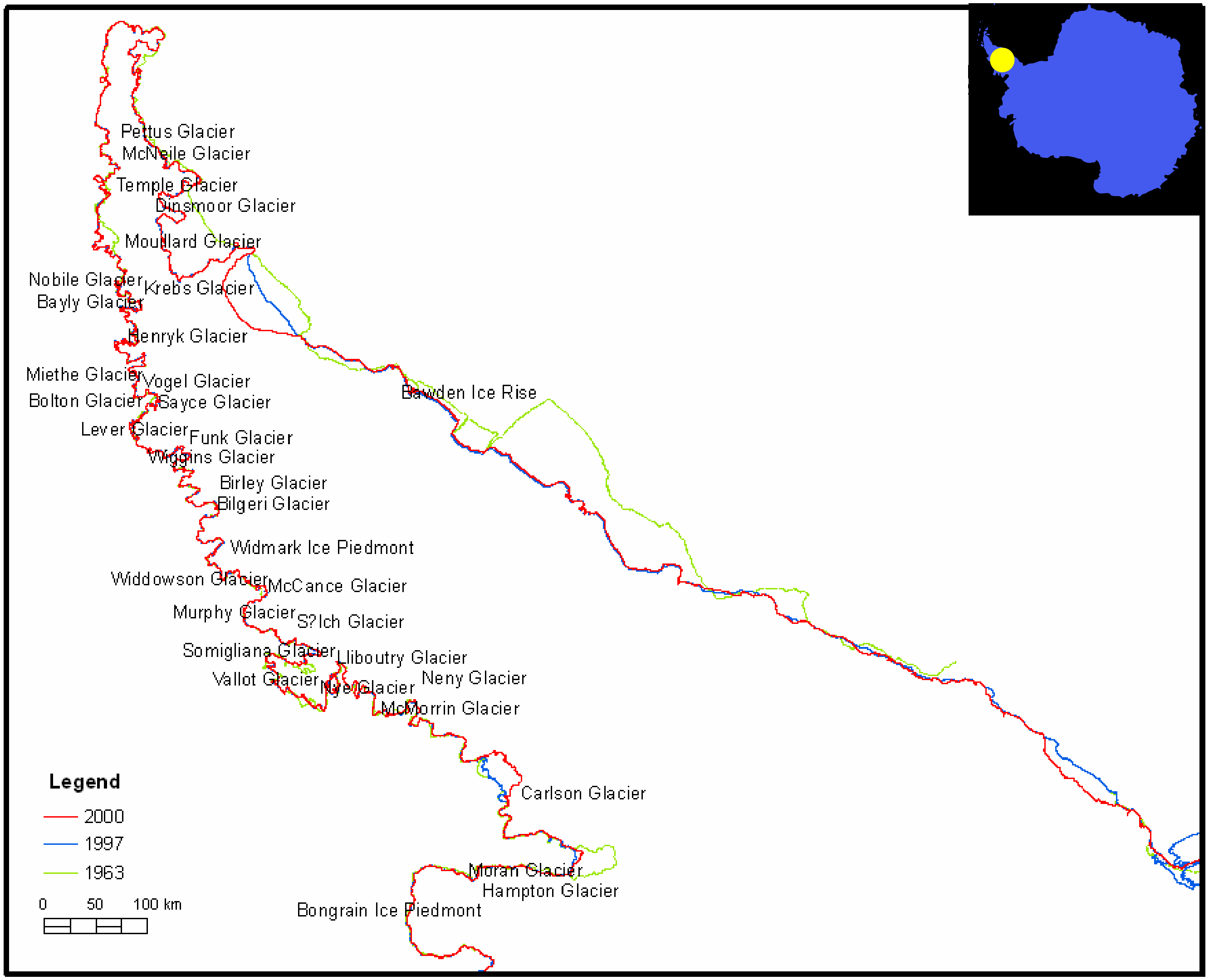

Figure 3.43 The Antarctic Peninsula

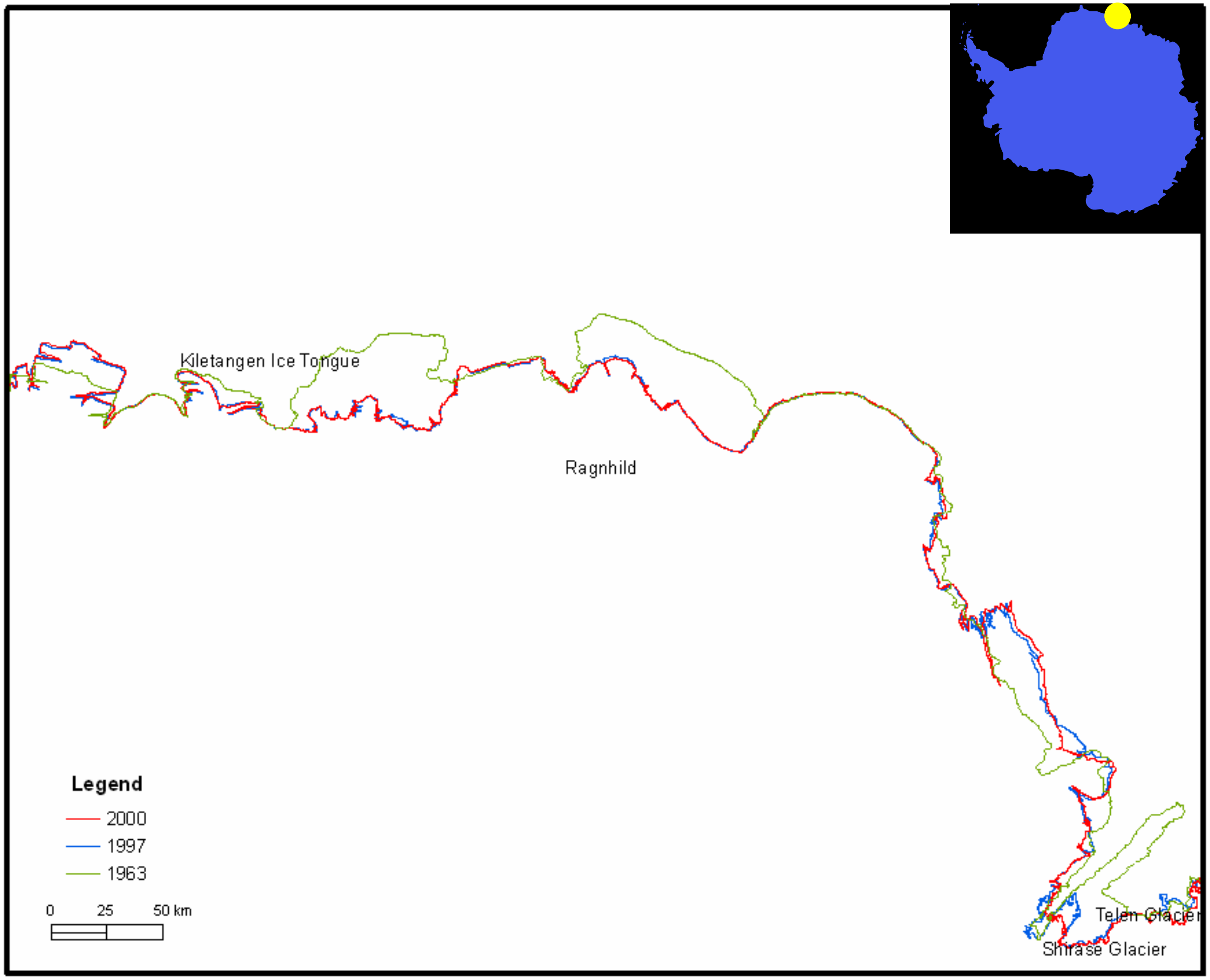

Figure 3.44 Ragnhild Ice Shelf

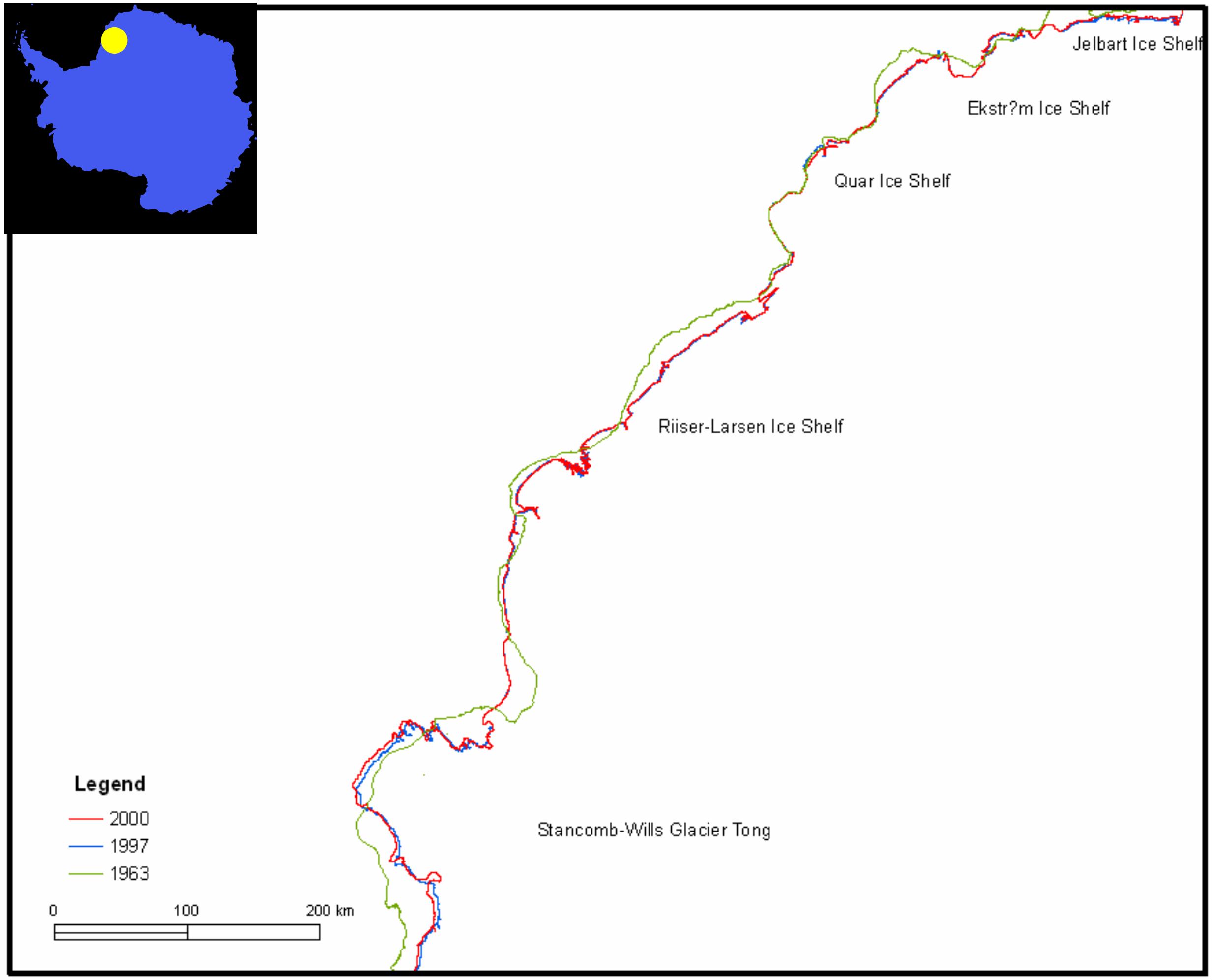

Figure 3.45 Riiser Larsen Ice Shelf

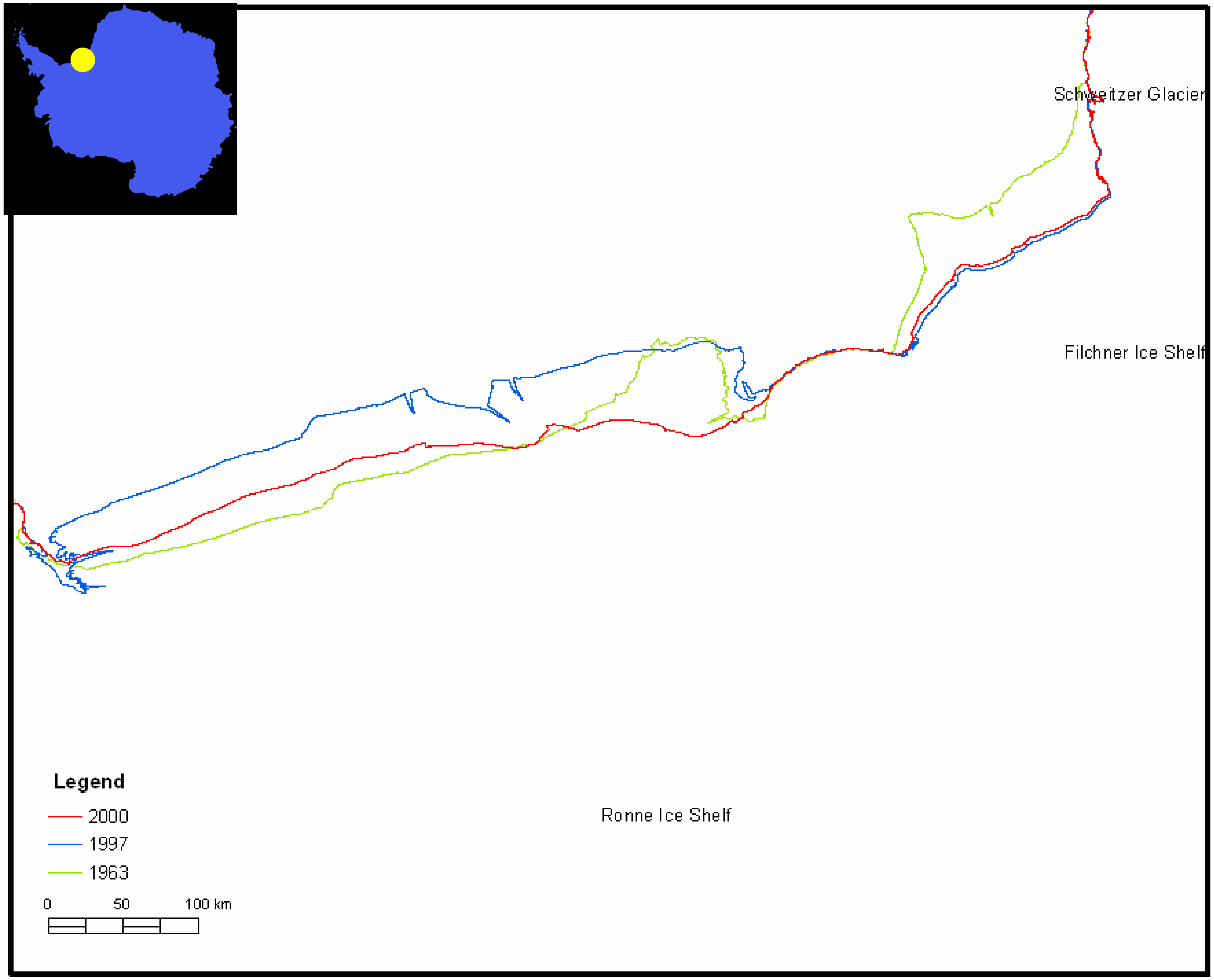

Figure 3.46 Ronne-Filcher Ice Shelf

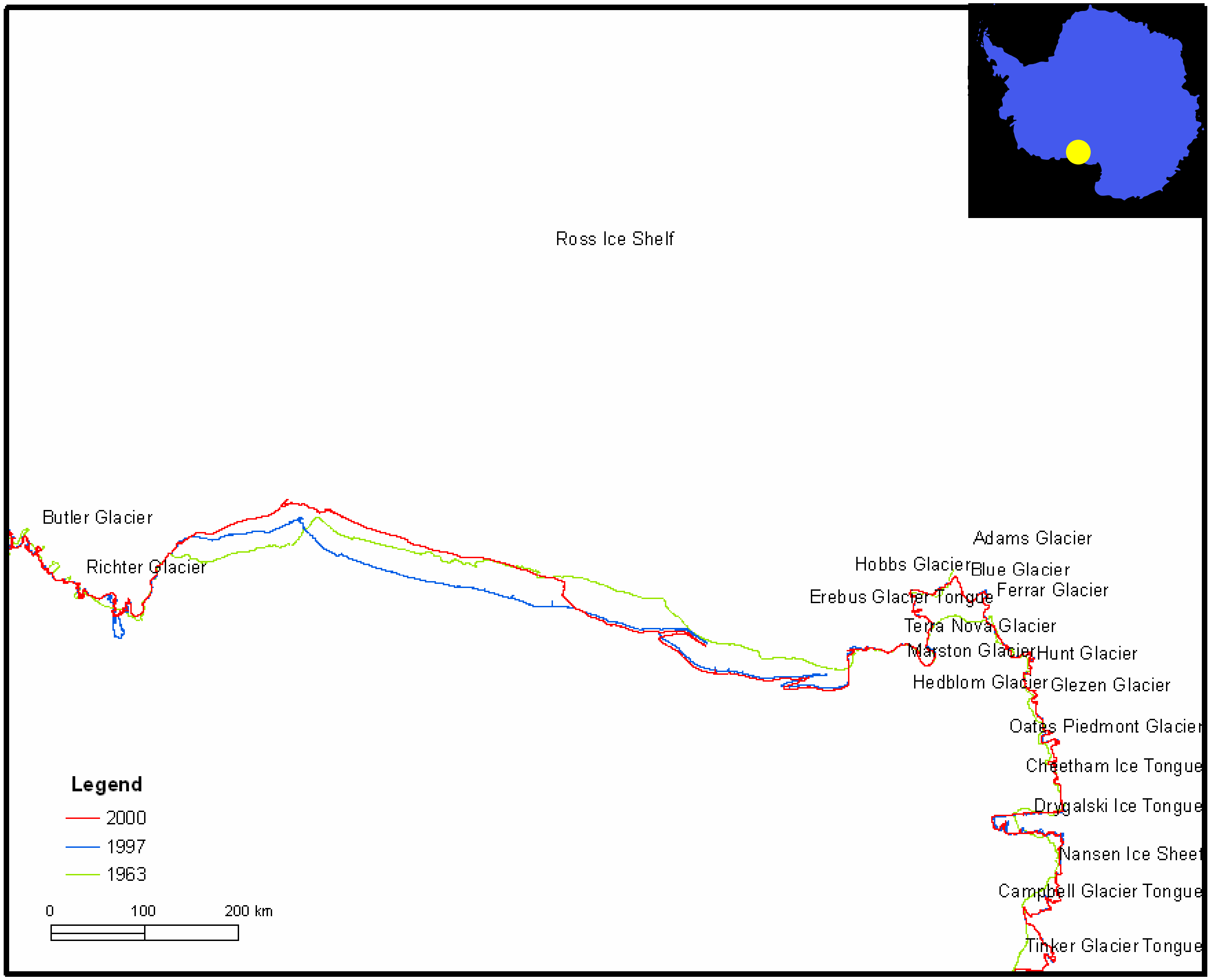

Figure 3.47 Ross Ice Shelf

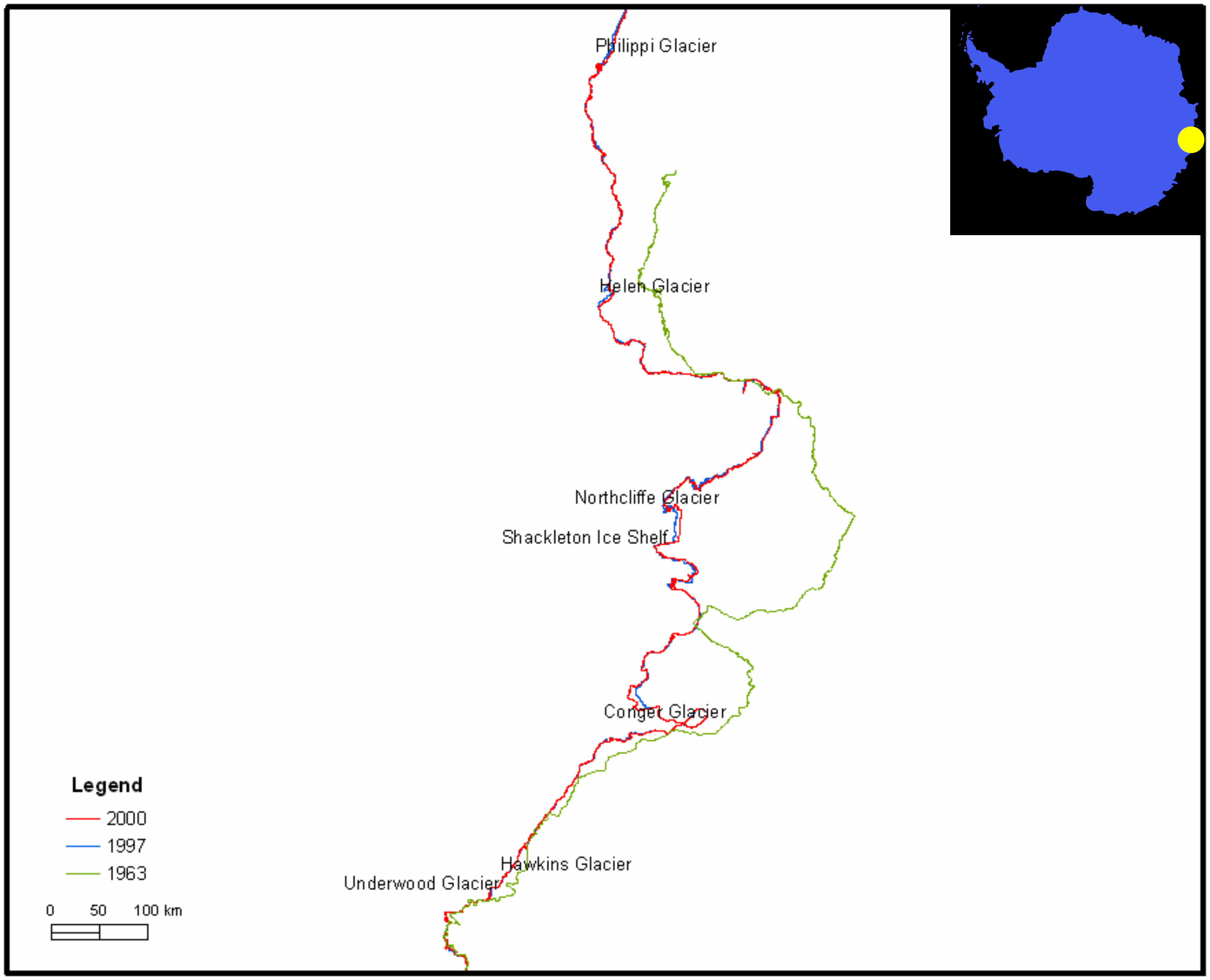

Figure 3.48 Schackleton Ice Shelf

Table 3.4 The advance and retreat areas comparing 1963 and 1997 coastlines

Ice Shelf	**Status**	**Areas(km^2)**
Abbot	R	-1158.50
Amery	R	-3772.90
Fimbul	R	-5737.80
Lazarev	A	41.80
Larsen	R	-15218.40
Ragnhild	R	-3679.50
Riiser-Larsen	R	-4089.30
Ronne-Filchner	A	9541.70
Ross	A	11415.60
Shackleton	R	-36228.30
Others	A	558.20
Sum	R	-48327.4

3.6 Detailed Inventory of Change Rates for Ice Shelves and Coastal Glaciers

Based on the high-resolution coastlines extracted from the 1997 and 2000 Radarsat images, a detailed analysis of the advance, retreat, and net change rates is conducted for 200 ice shelves and coastal glaciers. Not only the area changes but also net advance and retreat distance of the ice front during 1997-2000 are calculated and inventoried for these individual ice shelves and glaciers. Three transect lines are drawn along the advance or retreat direction, and they are respectively located in the left side, central, and right side of the ice shelf front and glacial tongues. The advance distances along three transect lines between the 1997 coastline and the 2000 coastline are measured, and the average advance or retreat speed of the ice front is reported in unit of m/a. Its accuracy is estimated to be about 13.36 m/a. Figure 3.49 shows these 200 ice shelves and glaciers, in the red triangles indicate the retreat glaciers and ice shelves, and the blue ones indicate the advance glaciers or ice shelves. Each ice shelf or glacier is illustrated in Figure 3.50 through Figure 3.61 by the straight bars, which are drawn in proportional to its actual advance or retreat distance. The areal variations and advance or retreat speeds of these ice shelves and glaciers are inventoried in the table in Appendix A. The highest advance speed detected is 3,107 m/a for Thwaites Glacier, and the highest retreat speed is 13,177 m/a for the front of the Ronne Ice Shelf.

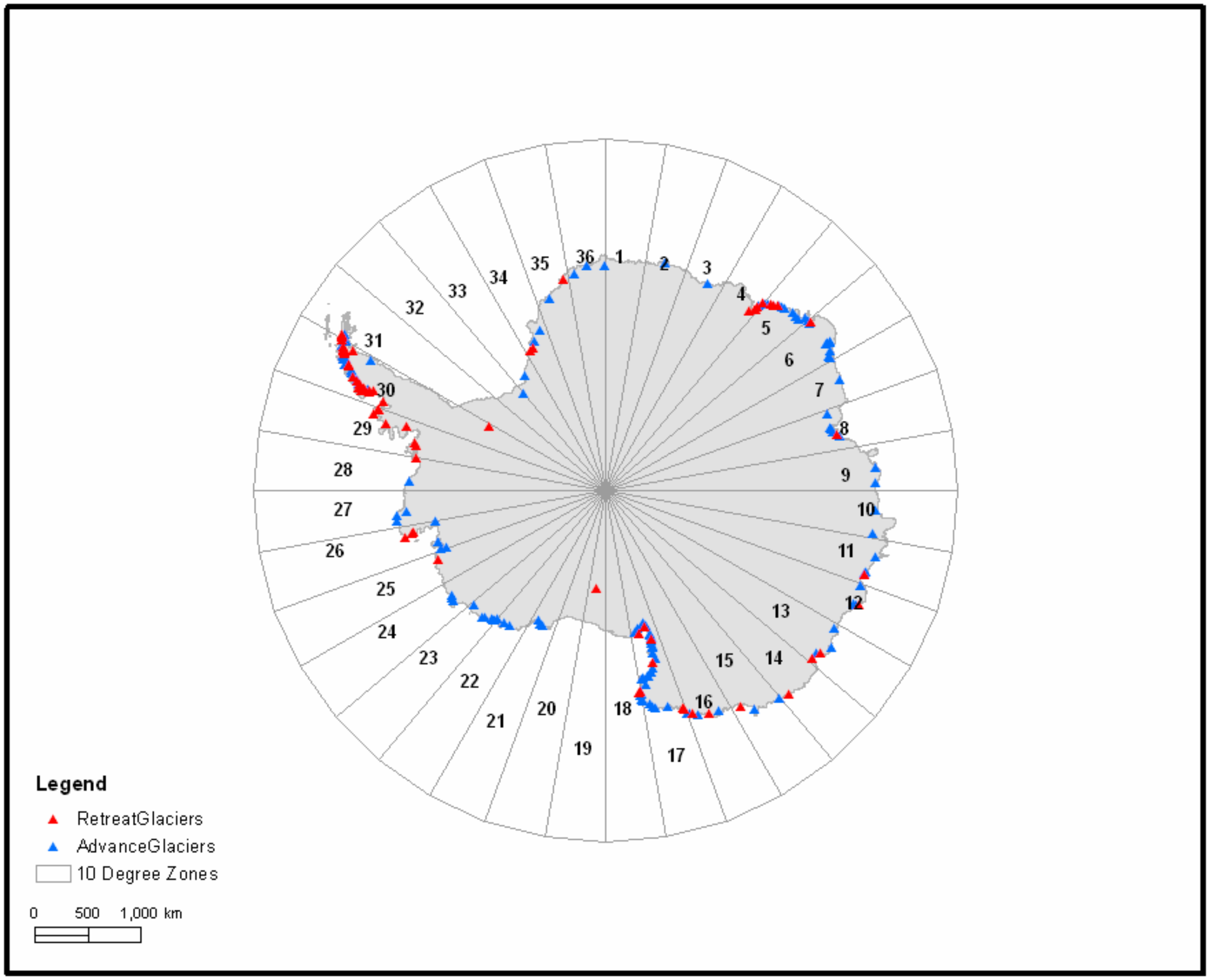

Figure 3.49 The locations of 200 glaciers distributed in 36 zones. The red triangles indicate the retreat glaciers and ice shelves, and the blue ones indicate the advance glaciers or ice shelves.

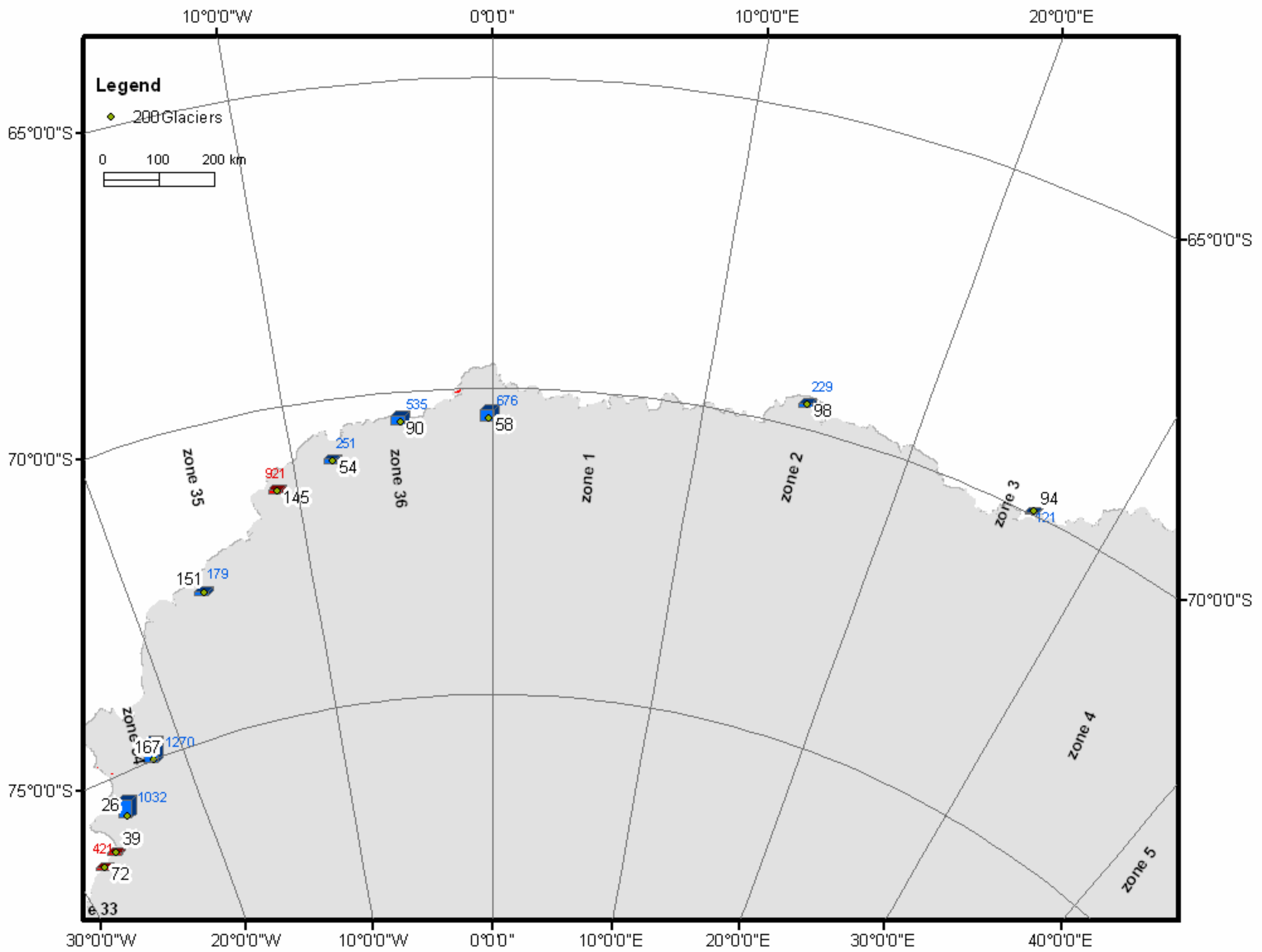

Figure 3.50 The advance and retreat glaciers in zones 1, 2, 3, 35, and 36. The blue numbers indicate their advance length and the red number indicate their retreat length.

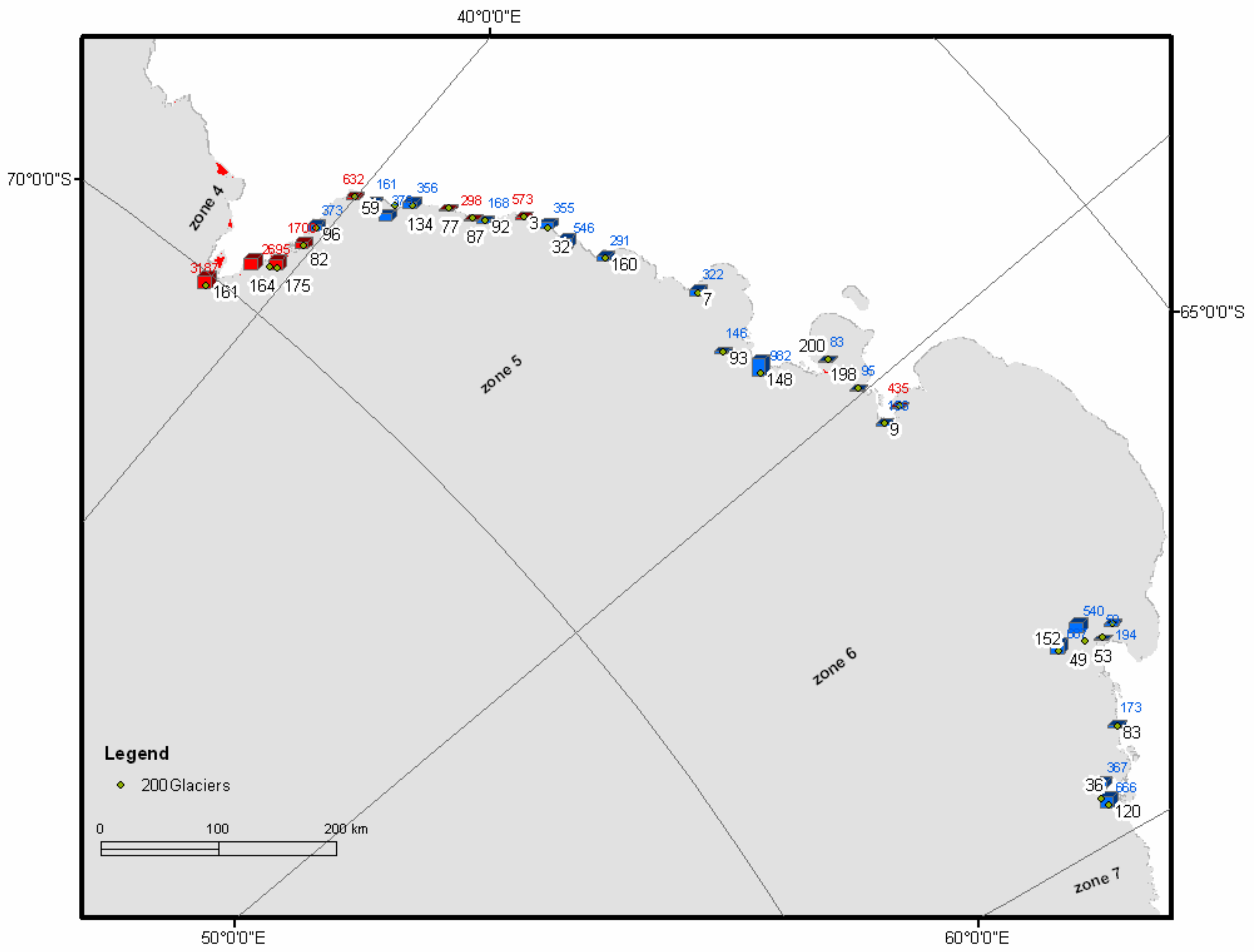

Figure 3.51 The advance and retreat glaciers in zones 4, 5, and 6. The blue numbers indicate their advance length and the red number indicate their retreat length.

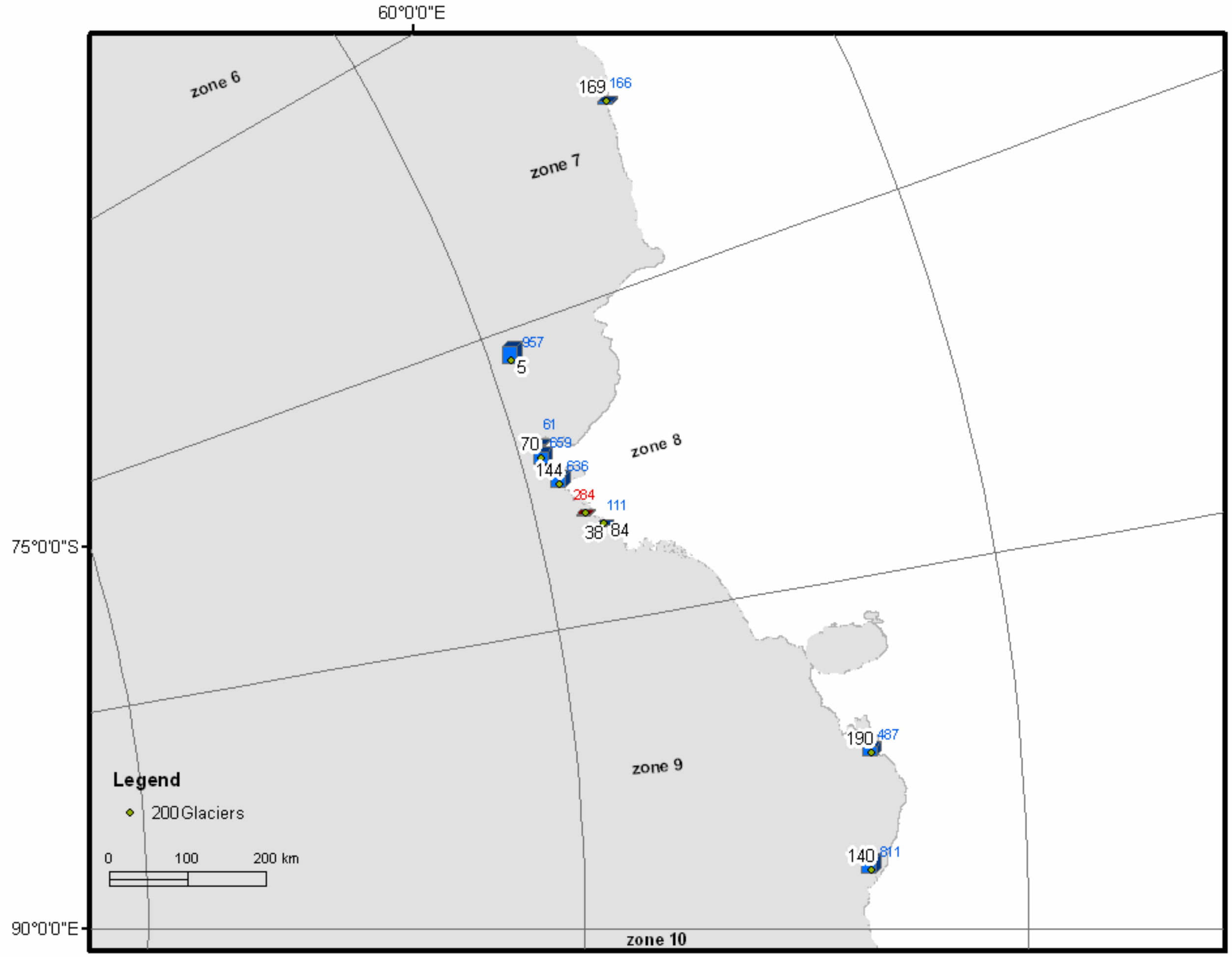

Figure 3.52 The advance and retreat glaciers in zones 7, 8, and 9. The blue numbers indicate their advance length and the red number indicate their retreat length.

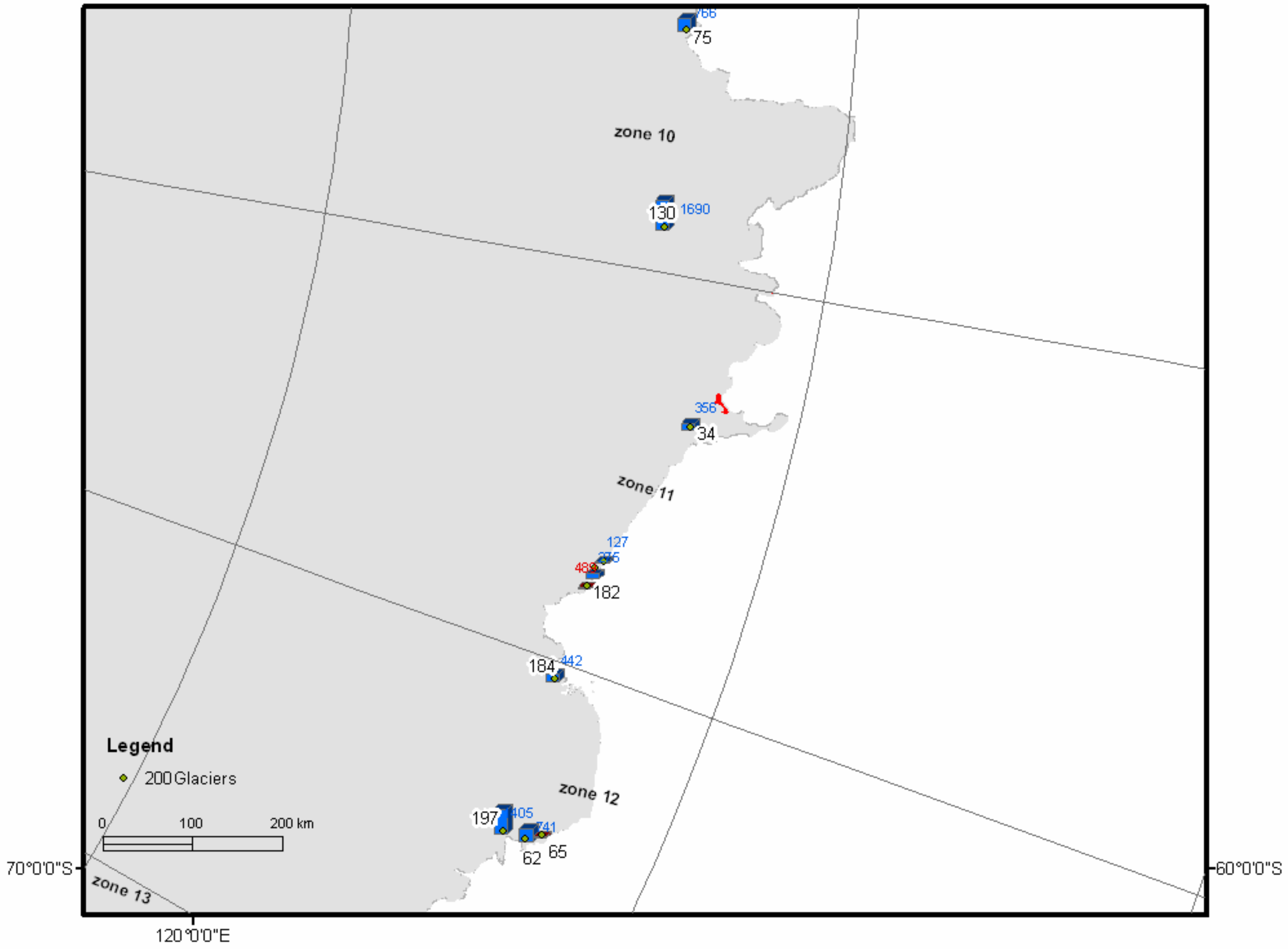

Figure 3.53 The advance and retreat glaciers in zones 10, 11, and 12. The blue numbers indicate their advance length and the red number indicate their retreat length.

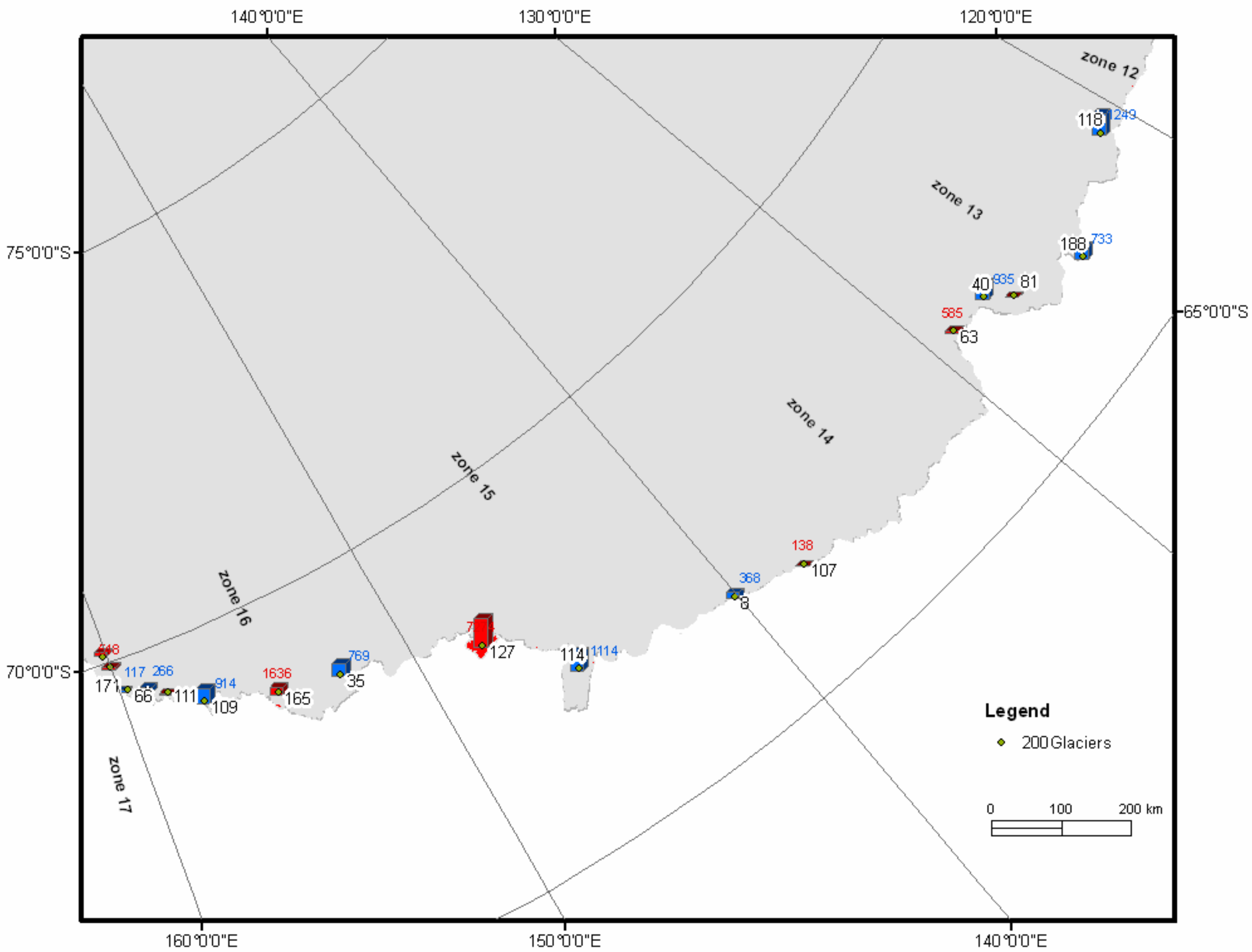

Figure 3.54 The advance and retreat glaciers in zones 13, 14, 15, and 16. The blue numbers indicate their advance length and the red number indicate their retreat length.

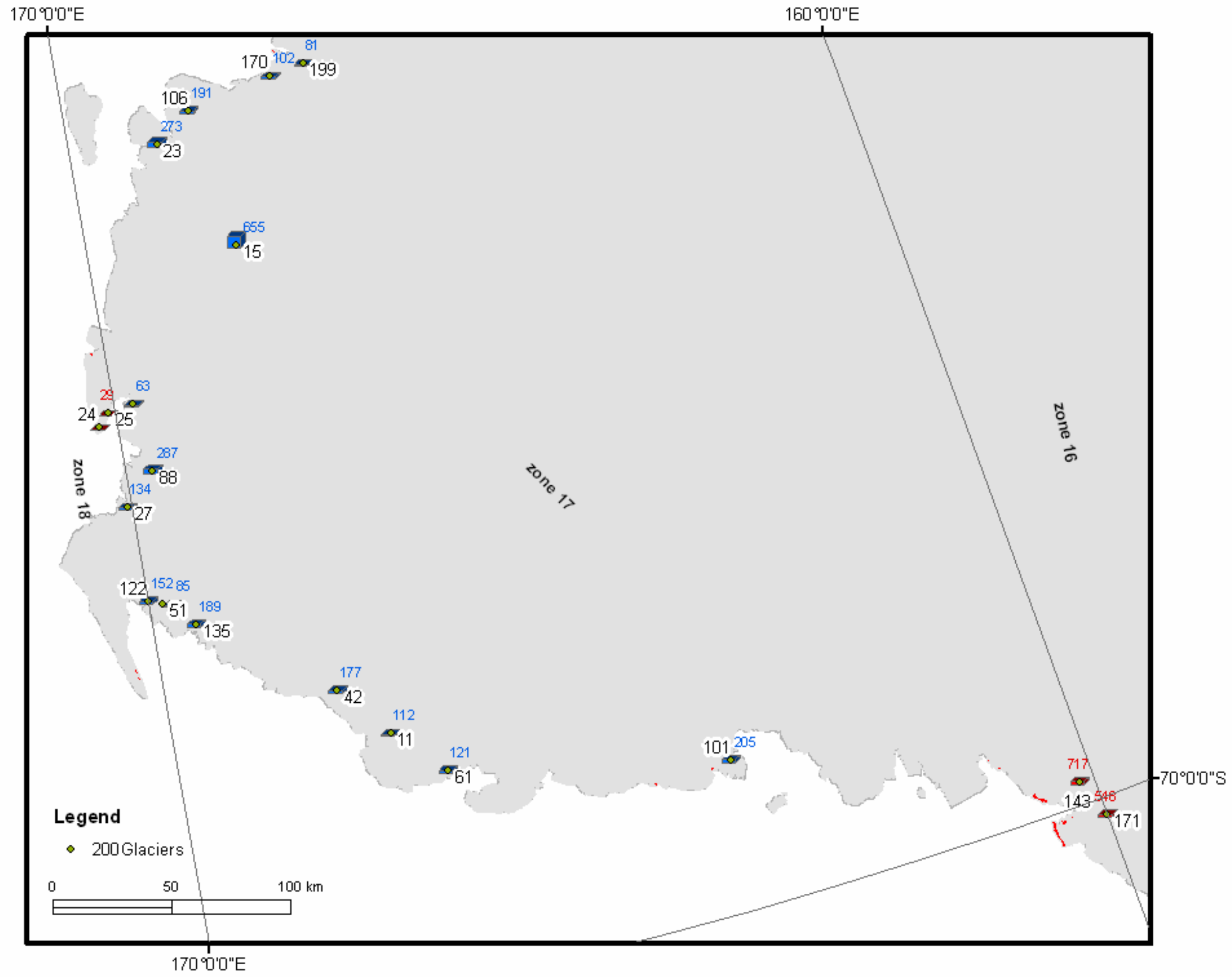

Figure 3.55 The advance and retreat glaciers in zones 17 and 18. The blue numbers indicate their advance length and the red number indicate their retreat length.

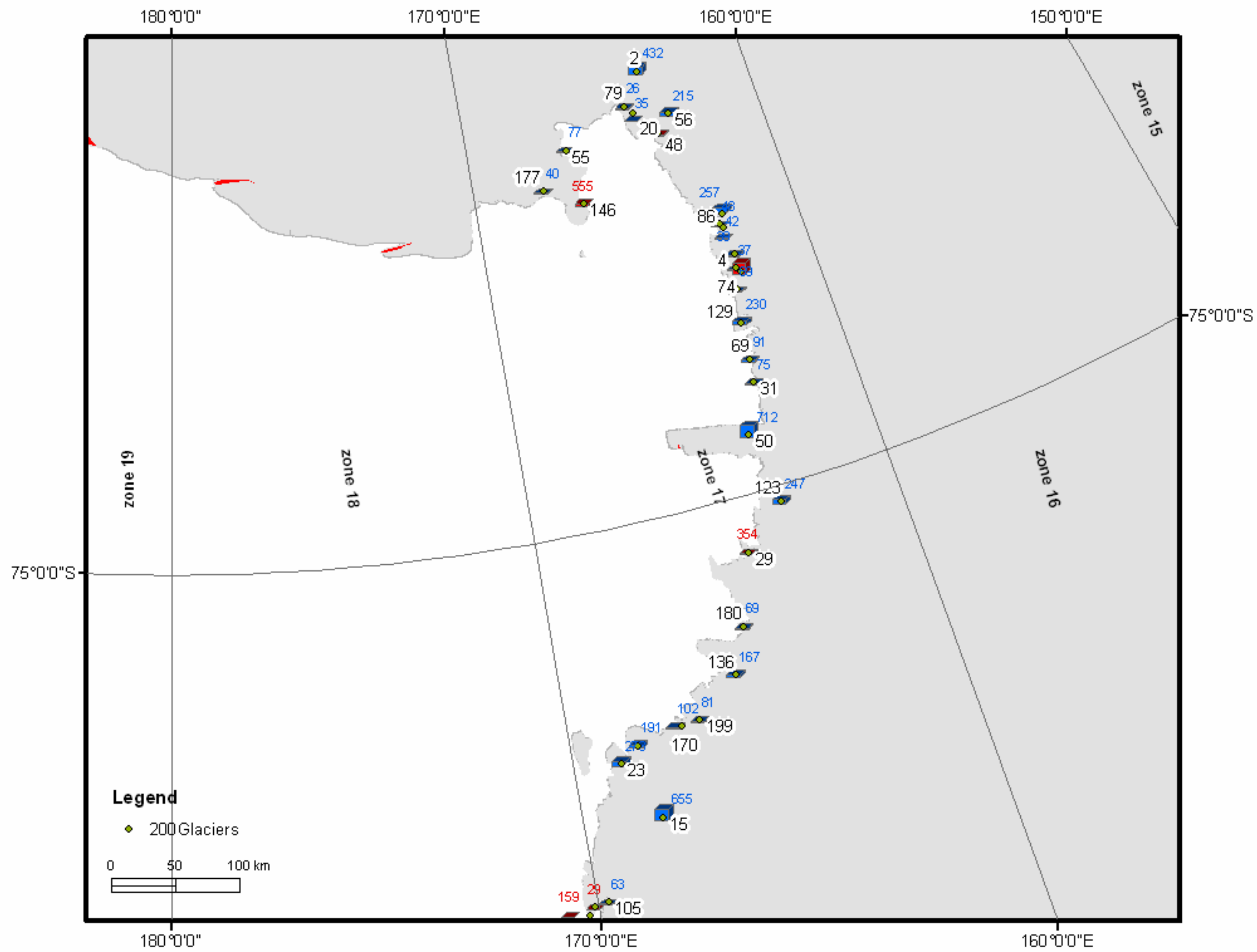

Figure 3.56 The advance and retreat glaciers in zones 17 and 18 (continued). The blue numbers indicate their advance length and the red number indicate their retreat length.

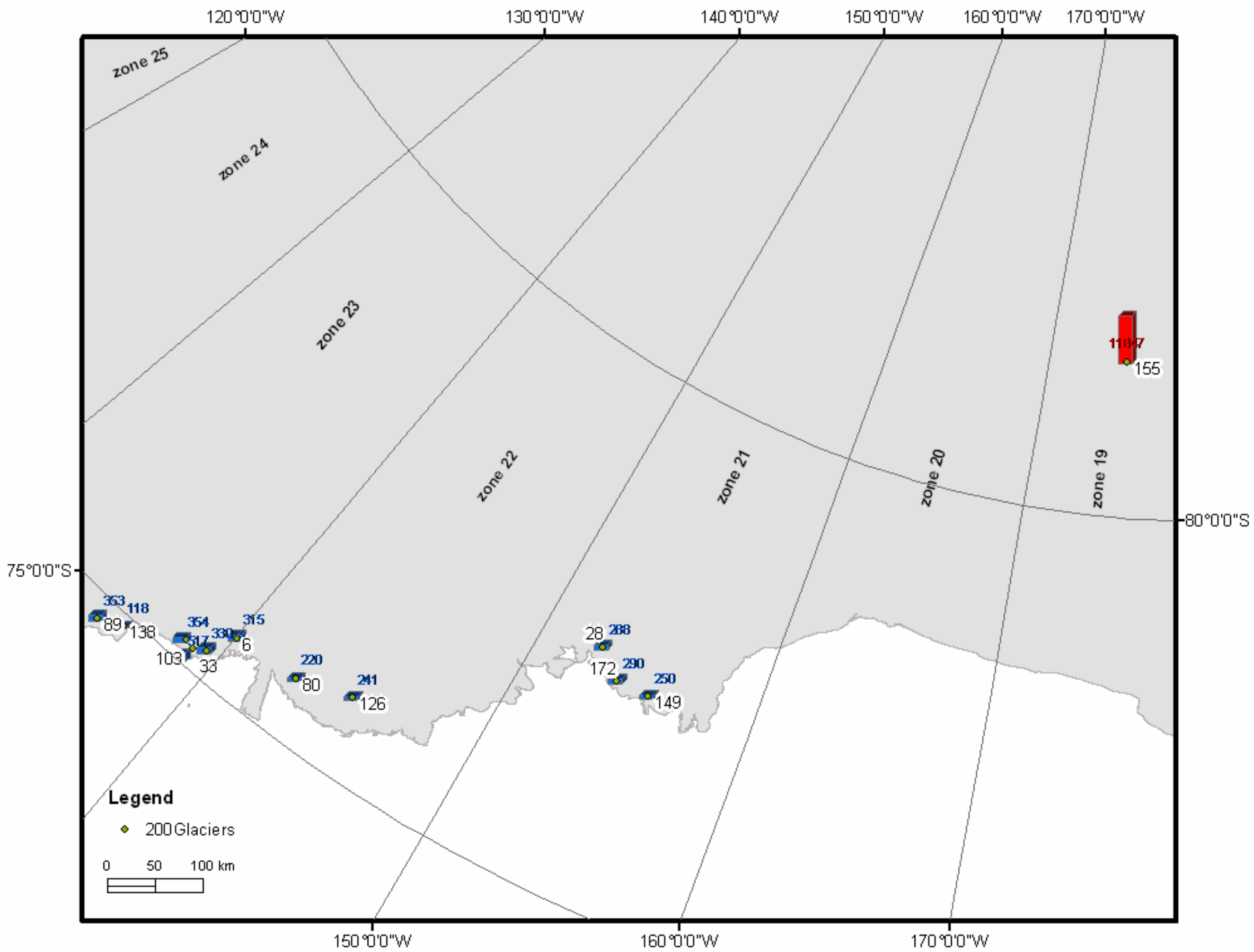

Figure 3.57 The advance and retreat glaciers in zones 19, 20, 21, 22, and 23. The blue numbers indicate their advance length and the red number indicate their retreat length.

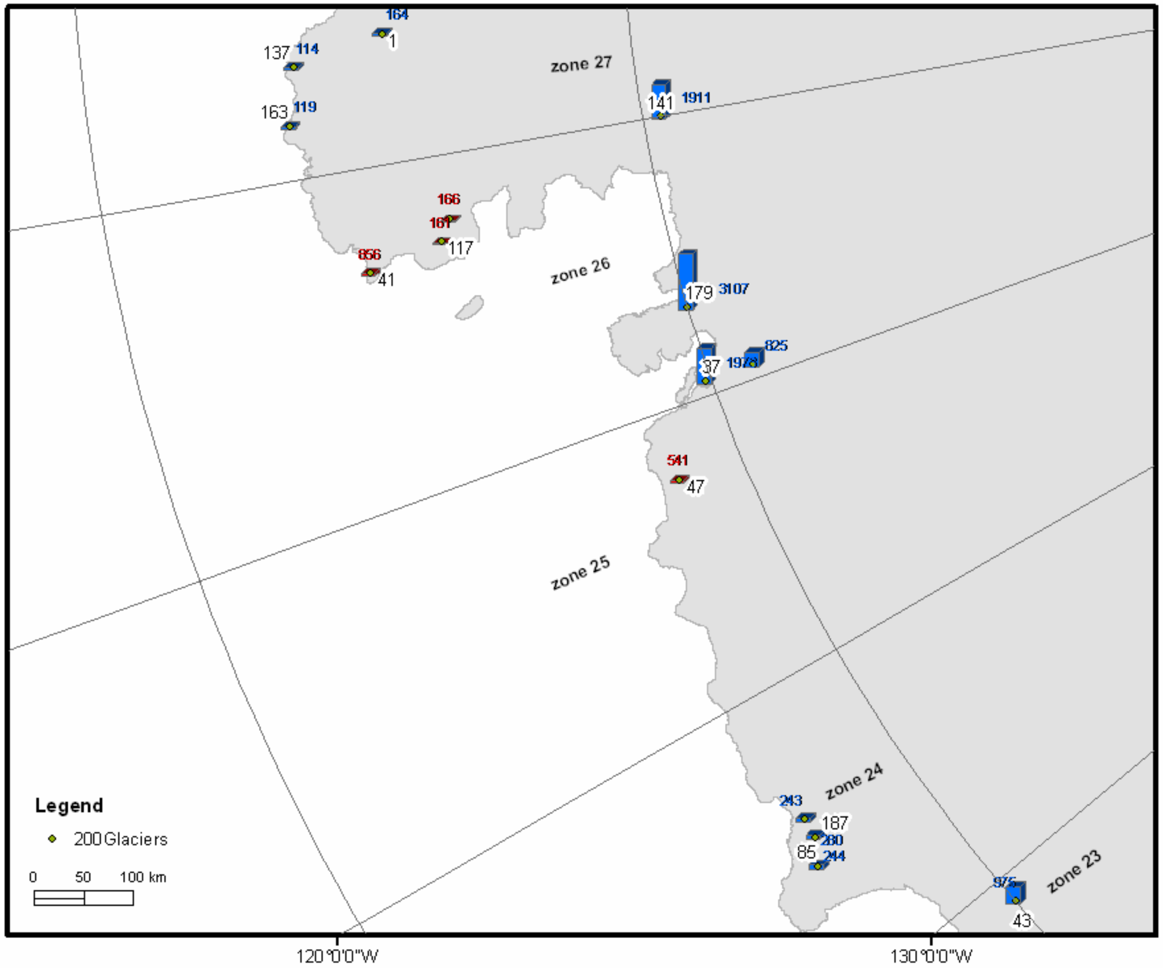

Figure 3.58 The advance and retreat glaciers in zones 24, 25, 26, and 27. The blue numbers indicate their advance length and the red number indicate their retreat length.

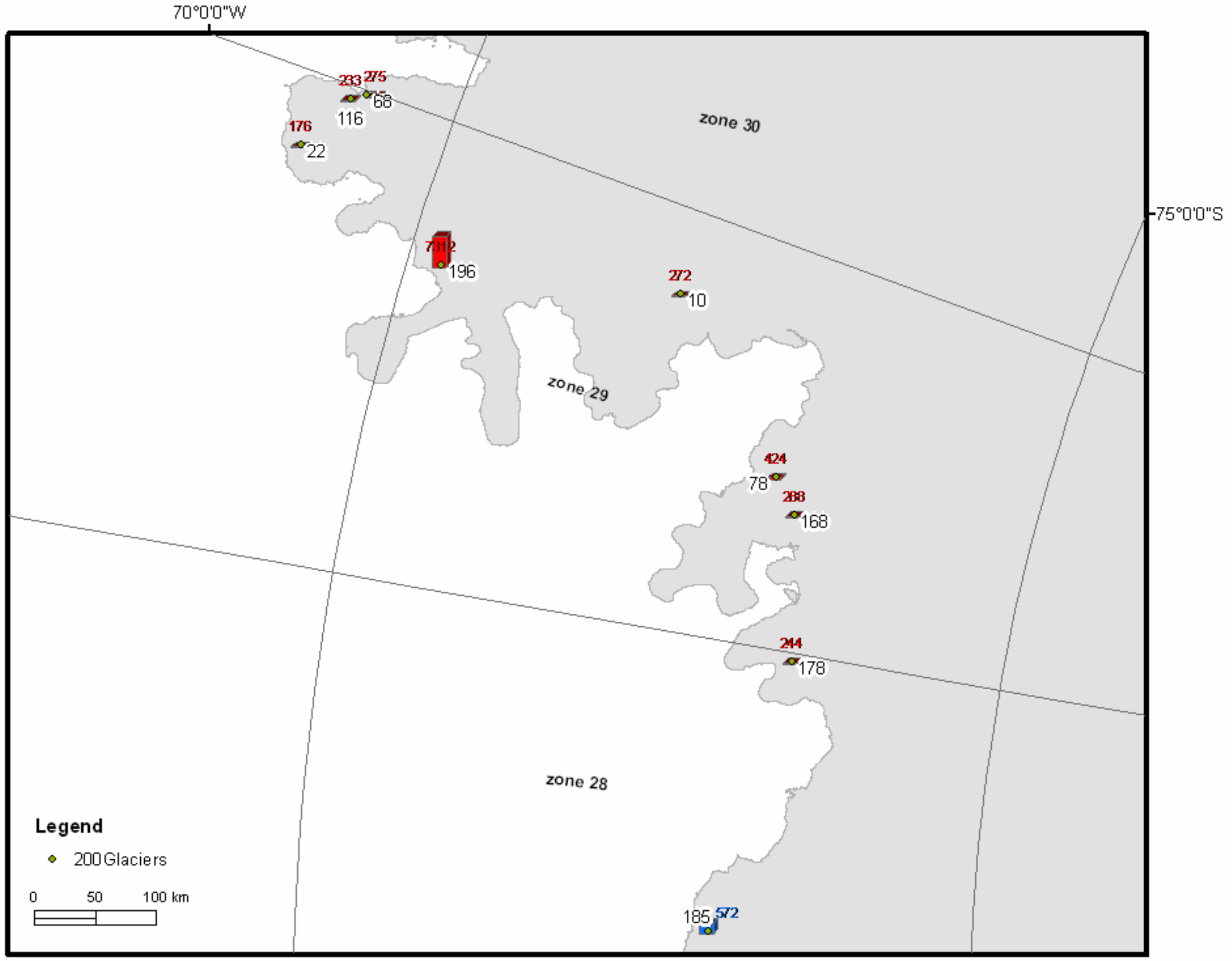

Figure 3.59 The advance and retreat glaciers in zones 28 and 29. The blue numbers indicate their advance length and the red number indicate their retreat length.

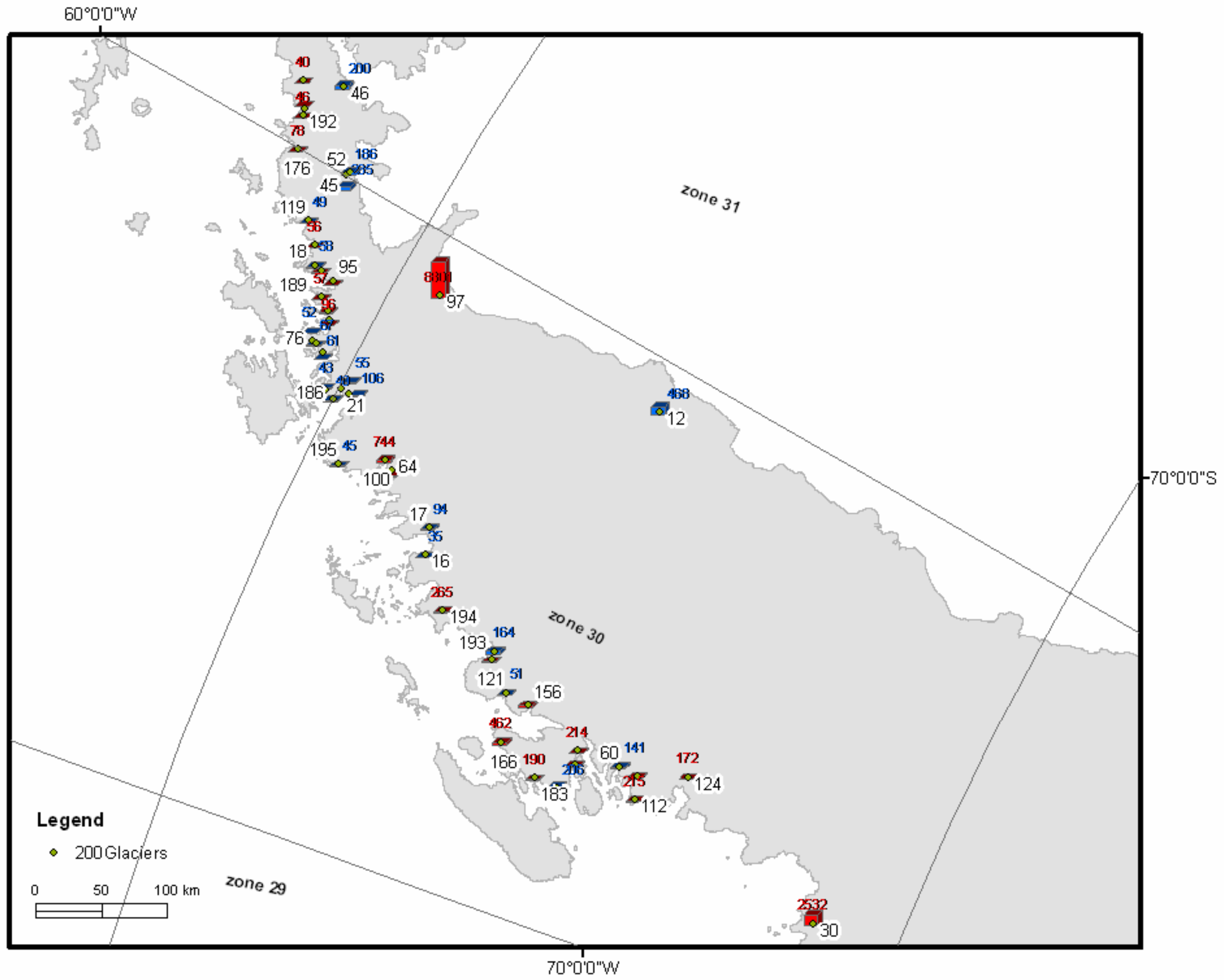

Figure 3.60 The advance and retreat glaciers in zones 30 and 31. The blue numbers indicate their advance length and the red number indicate their retreat length.

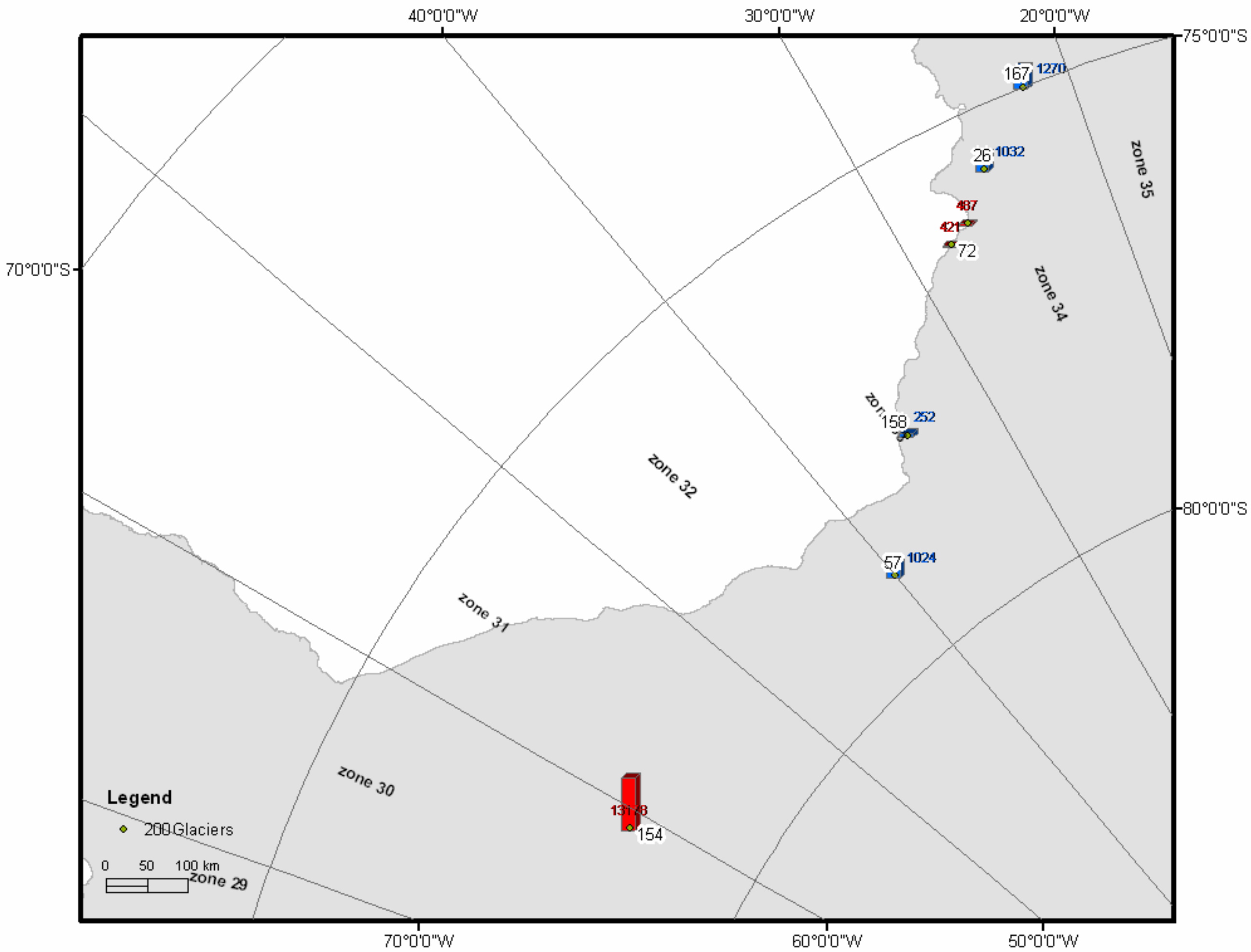

Figure 3.61 The advance and retreat glaciers in zones 31, 32, 33, and 34. The blue numbers indicate their advance length and the red number indicate their retreat length.

4 ICE MOTION MEASUREMENTS AND FLOW PATTERN ANALYSIS

This section begins with a discussion of problems faced by the conventional cross-correlation based image matching method for ice velocity derivation. Then, the multi-scale, hierarchical image matching based feature tracking method is presented. The general procedure of this method is outlined, and algorithm elements are discussed in detail. Then, the implementation of the ArcGIS extension module for the multi-scale, hierarchical image matching method is presented and demonstrated. Next, the accuracy of the velocity measurements from the multi-scale, hierarchical image matching is evaluated. In the final section, the ice dynamic behavior and flow pattern are discussed, and ice calving rates are also examined based on the newly-derived ice velocity fields for several selected regions.

4.1 Problems with Conventional Cross-correlation Method

Feature tracking methods have long been applied to sequential satellite images for measuring ice velocity (Doake & Vaughan, 1991; Lucchitta & Ferguson, 1986). Scambos et al (1992) introduced the image matching algorithm to automate the feature tracking method. Since then, the image matching based feature tracking method has been widely used to process sequential satellite images for ice velocity measurements. The cross-correlation based matching algorithm is most commonly used, in which each image chip (small rectangular image area) selected from the reference image (early image) is searched and correlated with a matching chip in a larger search area within the second image (late subsequent image). The correlation coefficient between the reference chip and the search chip is calculated at every center-pixel location in the search area for which the reference chip will fit entirely within the search area. The match location of conjugate feature can be determined at sub-pixel accuracy. However, conventional cross-correlation algorithms may be computationally intensive to create a dense set of velocity measurements, especially in the high velocity-gradient areas or for sequential images with a relatively large time interval between acquisitions. The velocity variation in the scene can create the variable position shifts of features. Features in the slow moving area may travel only a few pixels, while the features in the fast moving areas can travel tens or even a hundred of pixels. Figure 4.1 through Figure 4.4 illustrate the ice velocities extracted with the conventional method by specifying different search range and systematic offset. As shown in Figure 4.1, a small offset and search range of 20 pixels only successfully derived the surface displacements and velocity values for the areas with the slow moving speed in the left side of the image. With a medium offset and search range (60 pixels) results in the successful matchings and velocity measurements in the middle of the image, but no velocity measurements can be reliably derived in the left slow-moving area and the right fast-moving area (Figure 4.2). The use of a large offset and search range (80 or 100 pixels), as shown in Figure 4.3 and Figure 4.4, can only derive successful matchings and velocity measurements for the right side fast-moving area, and the areas in the red circles cannot be reliably extracted.

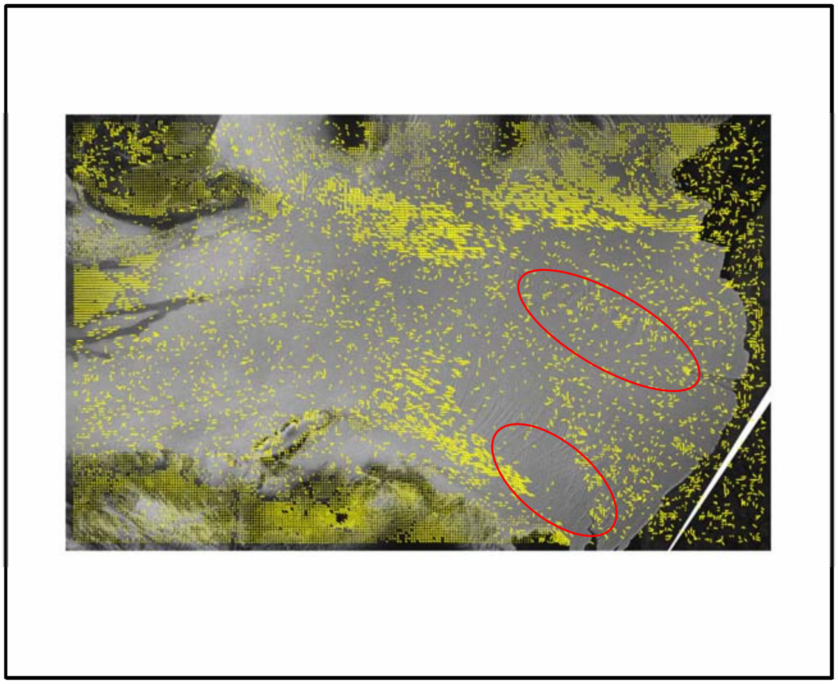

Figure 4.1 Extracted ice velocities using system offset = 20 pixels

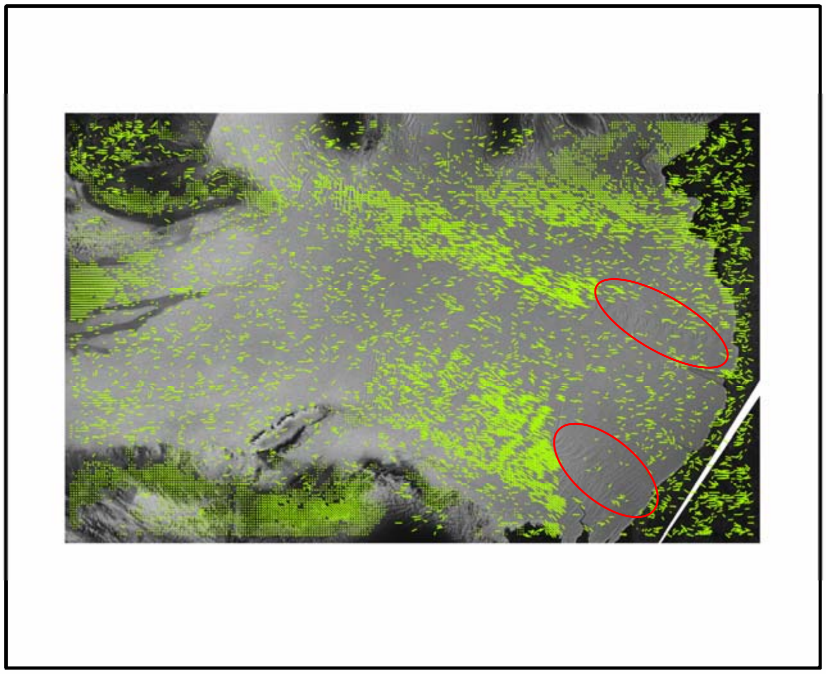

Figure 4.2 Extracted ice velocities using system offset = 60 pixels

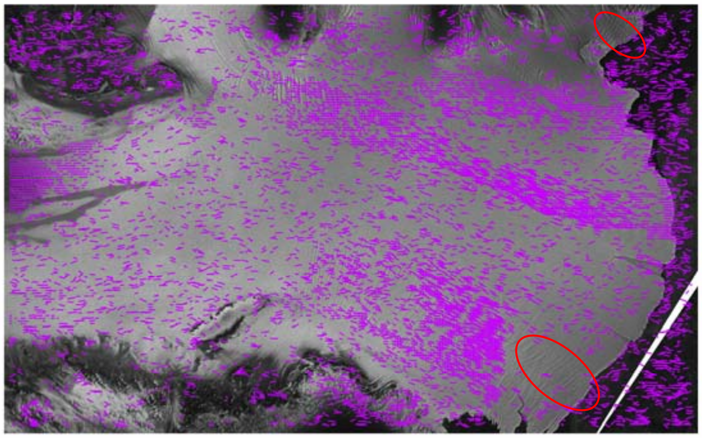

Figure 4.3 Extracted ice velocities using system offset = 80 pixels

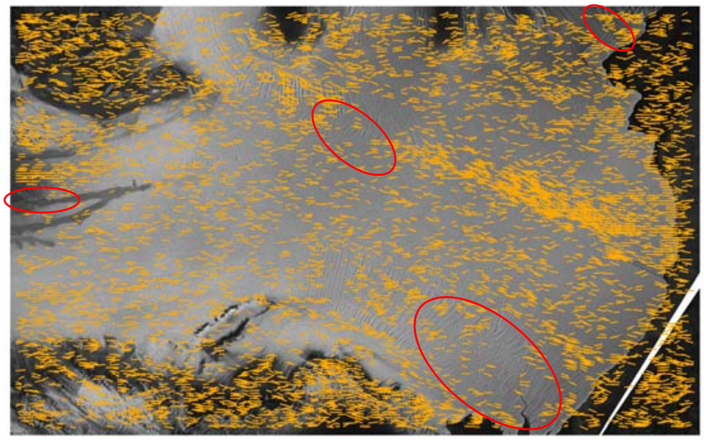

Figure 4.4 Extracted ice velocities using system offset = 100 pixels

Specifying offset and search range is critical for the success of matching operation. To ensure successful matching for all features in the scene, a large search range has to be specified so that the correct match (conjugate) point is located within the specified search area. This will cause a dramatic increase in the computation intensity and processing time, and also generate bad and spurious matches. This is because the greater the search area, the more likely one is to find a spurious match point.

4.2 Development of Multi-scale Hierarchical Image Matching Based Method

To combat the above problems of conventional cross-correlation algorithm, a multi-scale, hierarchical image matching algorithm is developed. The idea of multi-scale, hierarchical image matching is to use the rough and approximate match points obtained at a coarse resolution as a guide for searching for more precise matches at a higher resolution. First, an image pyramid, a sequence of copies of original images with a decreasing resolution and sample density, is first created. The cross-correlation matching is conducted on the coarsest resolution with a largely reduced image. The matching result is then employed as initial seed points to search for more accurate matches in a new iteration of matching operation based on the next level of higher resolution image. This iterative matching process continues until the final matching operation is performed on the full-resolution image. At each matching iteration, the locational accuracy of match points, and hence the accuracy of displacement measurements successively increase. Since most iterations are performed on images of reduced size with a small search range, the multi-scale, hierarchical image matching algorithm significantly speeds up the computation, and also reduces the occurrences of bad and spurious match points from false correlation maxima.

The basic steps of the multi-scale, hierarchical image matching scheme is summarized as follows:

1. Filter noise and speckles from the given input reference and search images.
2. A Lee pyramid $L_{0,}$ L_1, …, L_{n-1} is built, whose basis is $L_{0.}$ The pyramid has n levels, chosen such that L_i will still have significant feature information. The best level number is 3 if the Radarsat SAR image (25m pixel resolution) is utilized for the ice velocity extraction based on the experimental experience.
3. The process of image matching is dealt for the L_{n-1} level, and the extracted results are propagated to $L_{n-2.}$
4. The multi-scale algorithm is implemented until the extracted results in L_0 are obtained.

The processing chain and data flow in multi-scale image matching method is illustrated in Figure 4.5. The following sections will discuss each processing step in detail.

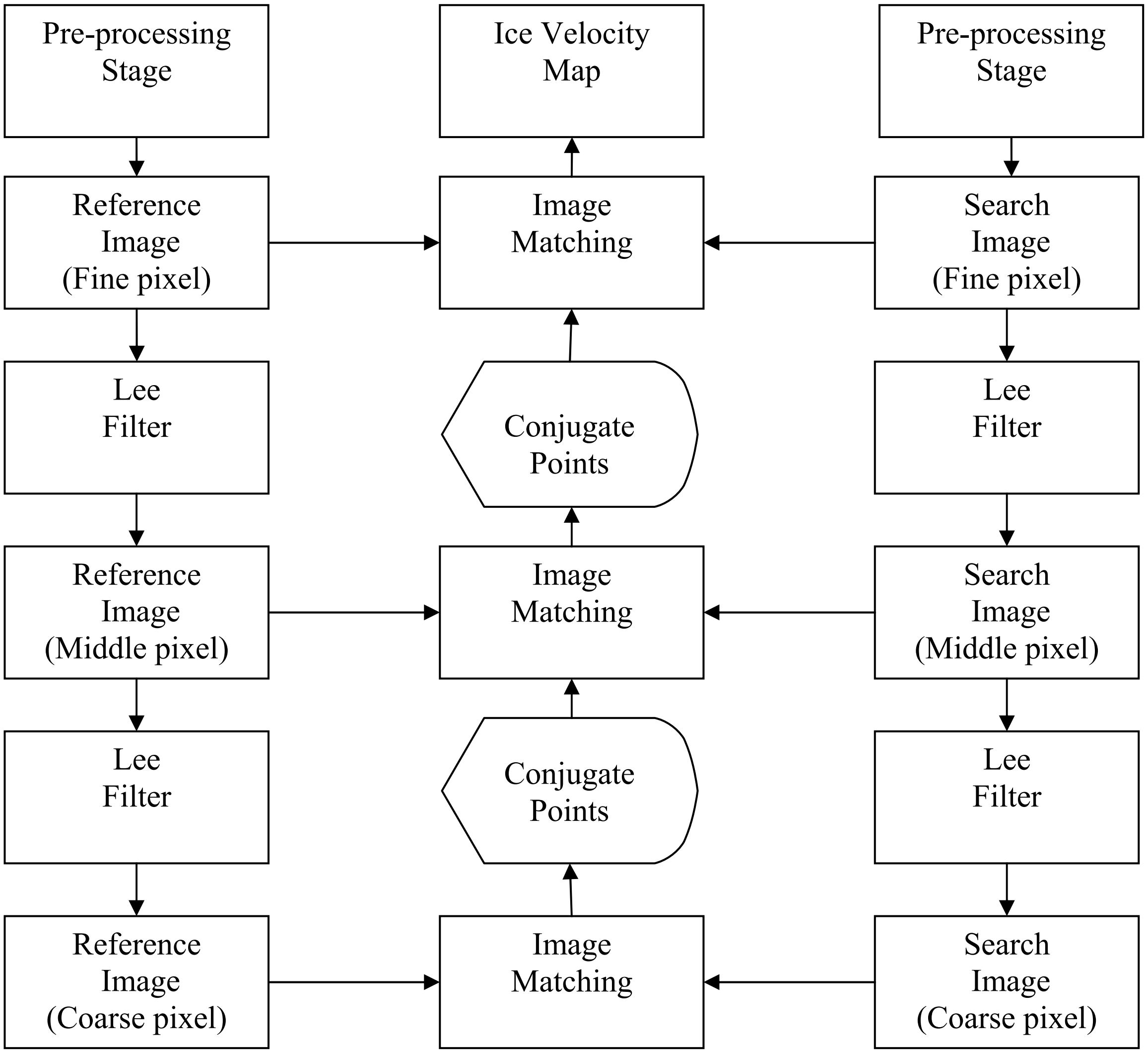

Figure 4.5 Image matching using pyramidal structure approach

4.2.1 Filtering image noise and speckles

Speckling causes a large problem when we try to extract useful information from SAR images. Especially in regards to image matching where the objective is to find conjugate points both in the reference image and the search image. In other words, to catch the same feature points within certain areas using two images with different acquisition times. A point to point relationship will be constructed between two images when conjugate points are found and, therefore, the image information at each point or pixel is critical in the process of extracting ice velocity in glaciers. Speckle is always a major limiting problem and is an undesirable phenomenon that is specific to SAR. The effects of speckle are a characteristic granulation in the image caused by interference coming from many individual scattering signals concentrated on a single pixel.

Conventionally, we can take appropriate procedures to reduce the effects of speckle, such as smoothing or averaging before processing SAR images. The smoothing or averaging filter is a 3 x 3 (or 5 x 5, 7 x 7) window that convolutes with each pixel in SAR imagery. After the operation of convolution, each pixel value is replaced by the arithmetic average of the pixel values from the nine pixels within a 3 x 3 window. However, while suppressing noise, use of these types of filters will result in the loss of some of the textural information in the image.

The Lee filter is applied in this research because it has the advantage of preserving image and feature sharpness while smoothing speckle noise (Lee, 1980). Figure 4.6 and Figure 4.7 illustrate the Radarsat SAR image processed before and after applying the Lee filter, respectively.

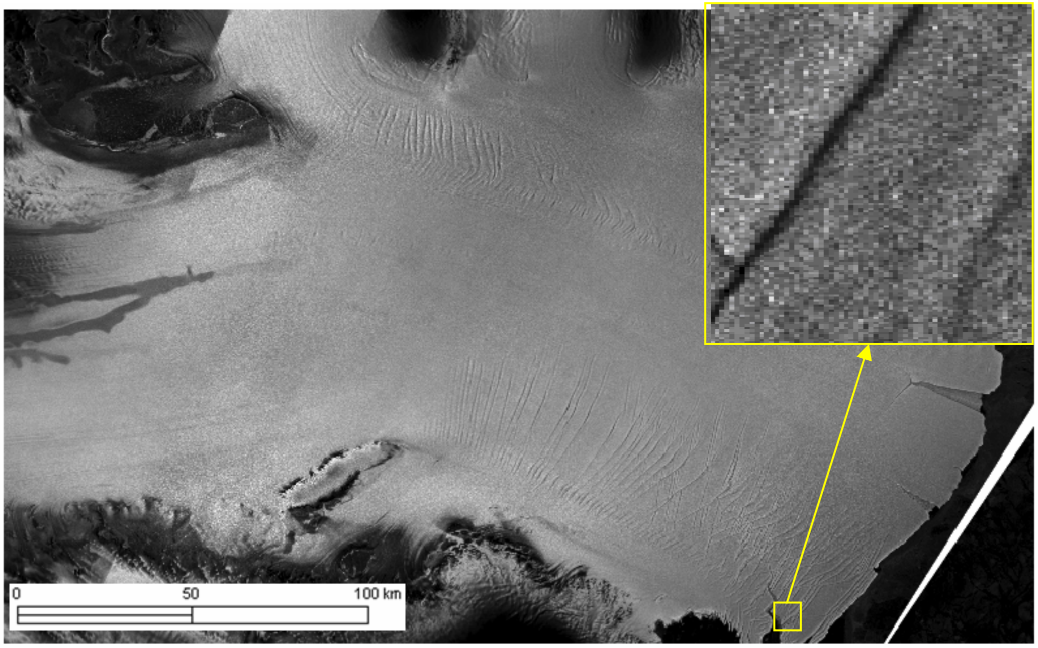

Figure 4.6 Radarsat SAR image before using Lee filter

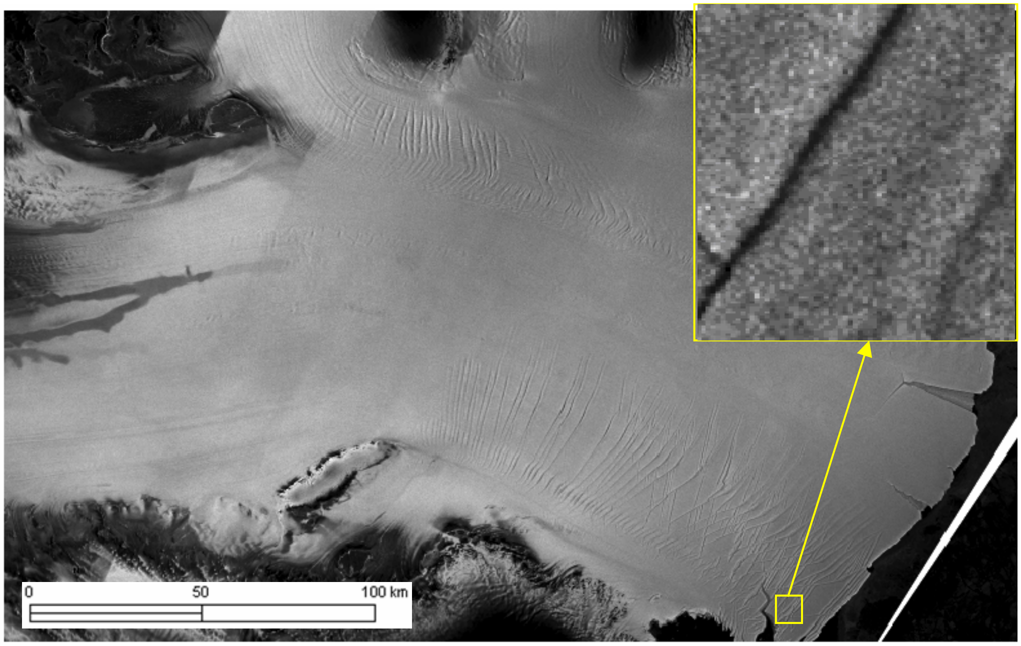

Figure 4.7 Radarsat SAR image after using Lee filter

Table 4.1 illustrates the significant improvement made while using Lee filter to pre-process SAR imagery. There are three parameter sets (setting is the same with Figure 4.1, Figure 4.2, and Figure 4.3) that are used to evaluate the effect of the Lee filter in the study of ice flow. Each parameter set is established with the same parameters in order to equally compare the performance of two sides (before and after Lee filter). Although different parameter leads to different improvement rates, the average improvement rate is increased to 126.42%. This phenomenon also substantiates that the pre-process phase is critical and unavoidable when dealing with SAR images.

Table 4.1 The evaluation of using Lee filter in the case of deriving ice velocity

	Before Lee Filter			**After Lee Filter**			
Setting	**Candidate Points**	**Extracted Points**	**Extraction Rate**	**Candidate Points**	**Extracted Points**	**Extraction Rate**	**Improvement Rate**
Figure 4.1	38500	7376	19.16%	38500	12776	33.18%	73.21%
Figure 4.2	38500	3216	8.35%	38500	8051	20.91%	150.34%
Figure 4.3	38500	3068	7.97%	38500	7845	20.38%	155.70%
						Average	126.42%

4.2.2 Feature enhancement

Features in image matching algorithms are very important. Especially, in the study of ice velocity in glaciers, crevasses and nunataks are very good features to serve as the candidates of conjugate points because both useful and reliable to achieve higher correlation values in crevasse areas. After obtaining the successful conjugate points by pyramidal strategy in image matching, the correlation values of extracted ice velocities are used to explain why features are crucial in this algorithm. Those locations with high correlation values have higher extraction rates at areas filled with features (e.g. crevasses).

Feature enhancement improves the quality and condition of visibility of the image. Features are noticeable objects in images. In other words, the background around features is more homogeneous than the feature themselves, that is, features contain of high spatial frequencies information. There are two methods for conducting features enhancement in image processing. The first is to employ sharpening filters to the images. Sharpening filters enhance pixels with high spatial frequencies in their neighborhood and make edges and points more prominent. As mentioned previously, the basic concept of image matching is to discover conjugate points in both the reference image and search image. Prominent edges or points are valid candidate points in the processing of extracting ice velocity in glaciers. The Laplacian filter is a very general sharpening filter.

The second method enhances features by suppressing low spatial frequencies in the image. A high pass filter is designed for this purpose. Generally, the image quality determines if the methods of features enhancement are required.

4.2.3 Creating hierarchical image pyramid

In the cross-correlation algorithm, the reference and search windows must be large enough to provide sufficient image information to compute and extract conjugate points. However, the time consumed searching for conjugate points in the search image increases as the size of the search window is enlarged, and the possibility of incorrectly identifying conjugate points also increases. On the other hand, if the sizes of reference and search windows are too small, there is no sufficient image information to identify the correct features or conjugate points.

To solve this problem, the pyramidal structure is employed in the process. The pyramidal structure is actually a coarse-to-fine strategy (Figure 4.8).

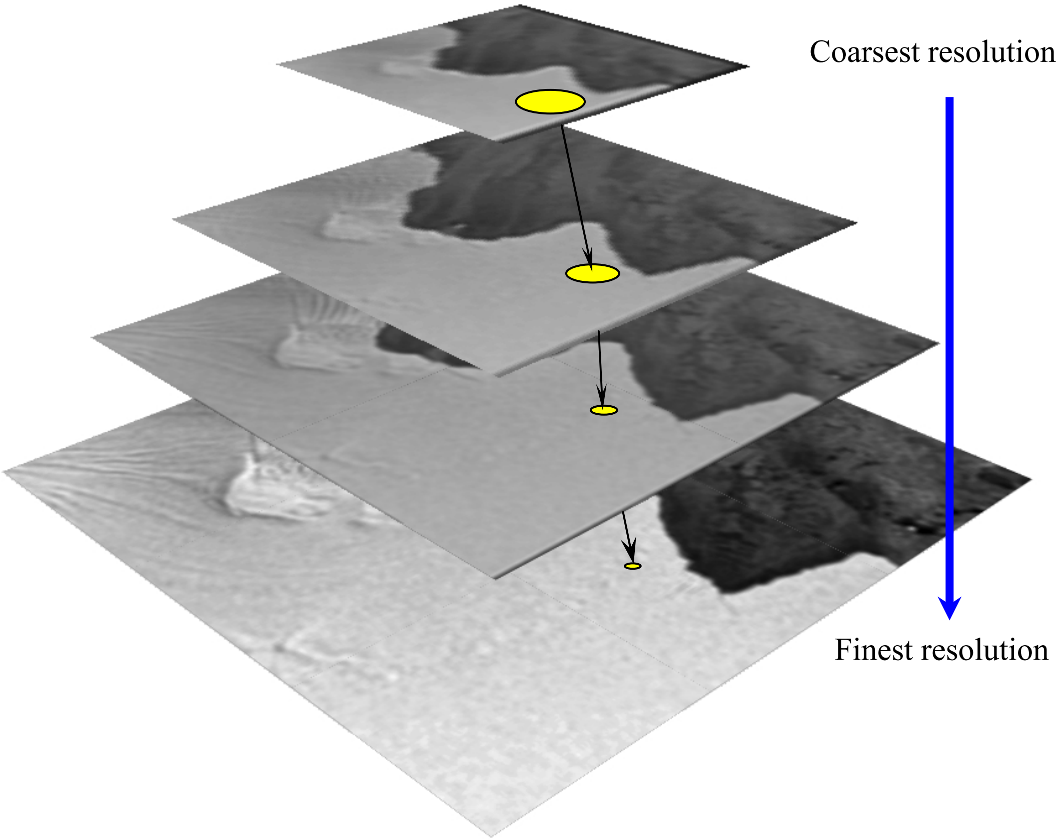

Figure 4.8 The pyramidal structure

In Figure 4.8, the highest layer has the coarsest pixel resolution, and the lowest layer has finest pixel resolution. When these layers are combined, they resemble a pyramid. In this research, the Lee filter, a smoothing filter, serve as a pyramidal generator.

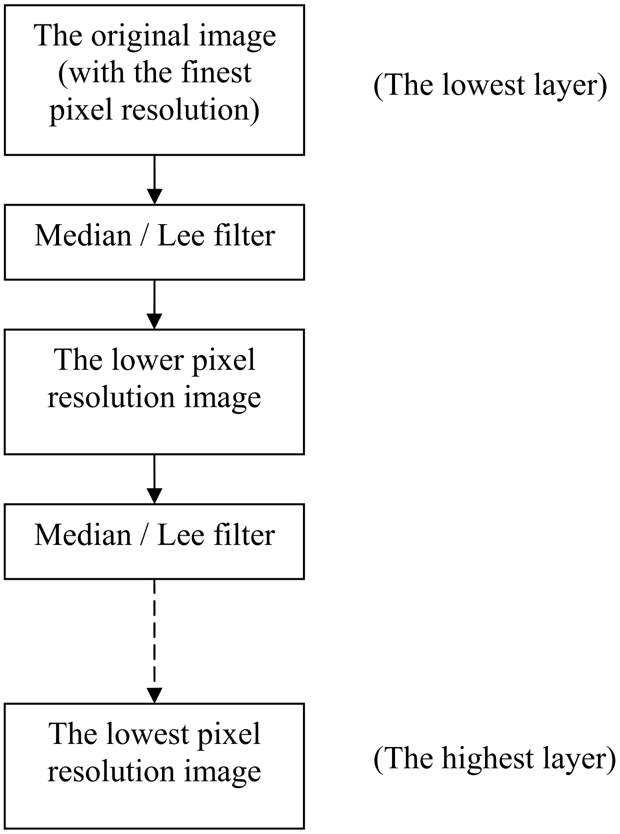

Figure 4.9 The flow chart of generating image pyramid

Figure 4.9 illustrates how the image pyramid is generated. The original image (e.g. 100 cols x 100 rows Radarsat SAR image with 25 m pixel resolution) is smoothed by Gaussian filter, and then the next image or layer is generated (now, a 50 cols x 50 rows Radarsat SAR image with 50 m pixel resolution). The generated image is smoothed by Gaussian filter, and the next image (a 25 cols x 25 rows Radarsat SAR image with

100 m pixel resolution is generated) or layer can be generated. The same procedure can be repeated several times until the coarsest resolution image is obtained.

The process of image matching is implemented on each layer, and the highest layer (the coarsest resolution image) is treated first. The useful information acquired on this layer will be propagated to next layer to help the process of image matching on next layer.

4.2.4 Searching conjugate points

The conceptual framework for searching conjugate points is specified in Figure 4.10. In order to calculate ice motion, the goal is to detect conjugate points P and P′ in 1997 and 2000 images, respectively. The proposed algorithm for image matching is as follows:

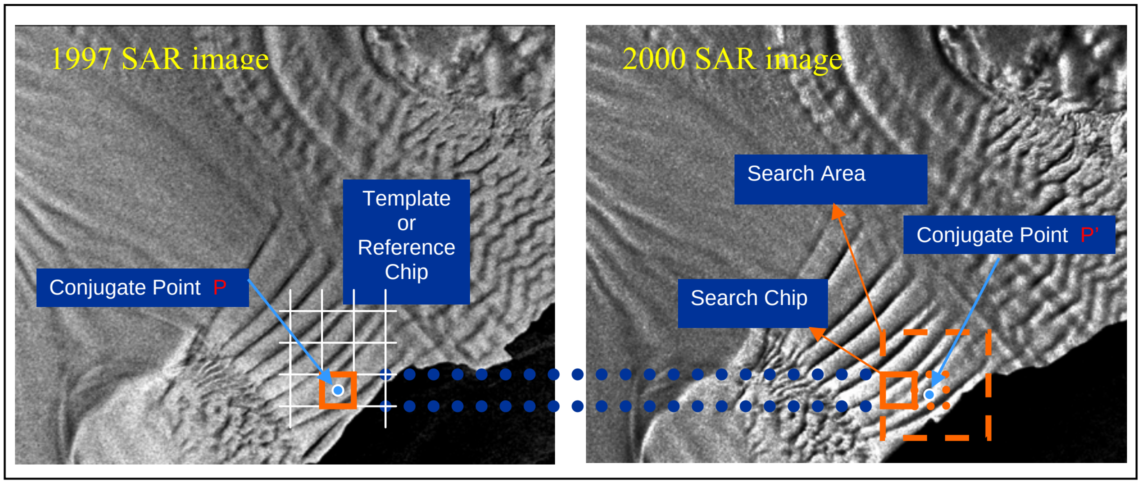

Figure 4.10 The principle of image matching

1. Set suitable sizes for search areas.
2. Set suitable window sizes for reference and search chips.
3. Start searching conjugate points from the first line to the last line (each line starts from left side to right side) on both images.
4. Center the reference chip on each pixel (e.g. P in Figure 4.10), and put search chip on search area according to the coordinate of P or an estimated position given by user.
5. Start searching conjugate point P′ from the first pixel (the upper left corner) to last pixel (the lower right corner), and calculate the correlation value for each pixel by centering matching window on each pixel within the extent of search area.
6. If the qualified correlation value is obtained within the extent of search window, then the conjugate point P′ is identified; otherwise the search for P′ is failed

Besides choosing the widow sizes for reference and search windows, determining the estimated position, in step 4, is critical, and this estimation greatly influences if conjugate point P′ can be found. Over or under estimating will cause search window never approach conjugate point P′, even setting larger search window size to compensate the wrong estimation is in vain. Examining the results of image matching, Figures 4.1 through Figure 4.4, enables understanding why the estimated position is important. Underestimation will cause the higher ice velocities not to be identified; overestimation will cause the lower ice velocities to be ignored.

4.2.5 Compute image correlation coefficient surface

The correlation coefficients are calculated for all pixels in the search area according to the equation given in Section 2.4 of Section 2. The correlation coefficient surface is further modeled to identify the correlation peak point at sub-pixel level.

4.2.6 Conjugate point identification

Analyzing the cross correlation values enable determination of position of corresponding conjugate point in the search image. In other words, the cross correlation values control the accuracy of conjugate points. Figure 4.11 illustrates how the conjugate points are identified. When the center of matching window moves to pixel 1, the matching window and the reference window will be compared by equation (4.1) and the result will be recorded as green star in Section 2.4. The same procedures for calculating correlation values will repeat on pixel 2, 3, 4… until the last pixel is compared. As mentioned in Section 2.4, all green stars are candidate conjugate points, and this research employs a parabola curve (as mentioned in Section 2.4) to approach candidate conjugate points. The maximum cross correlation value will be estimated and its position also will be tracked. This allows the precision of conjugate point increases to subpixel level.

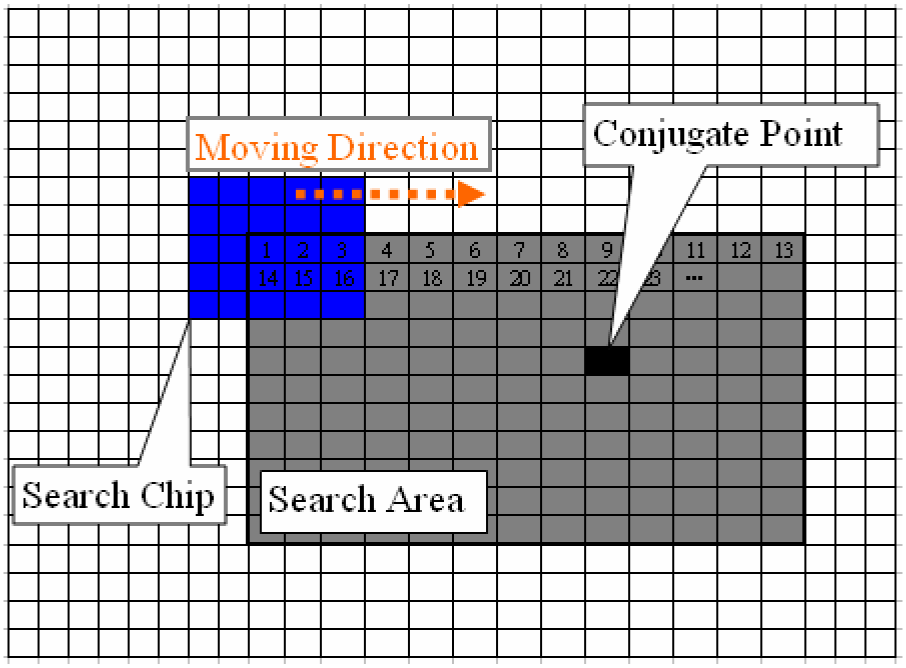

Figure 4.11 The process of generating correlation values

4.2.7 Creating displacement vectors and calculating velocity

Once the conjugate points, P and P′ are identified, the displacement can be calculated by comparing their coordinates. Figure 4.12 illustrates the displacement between conjugate points P and P′. In this research, the extracted ice velocities will be converted into shape file, which can directly display in GIS software, and check their accuracy.

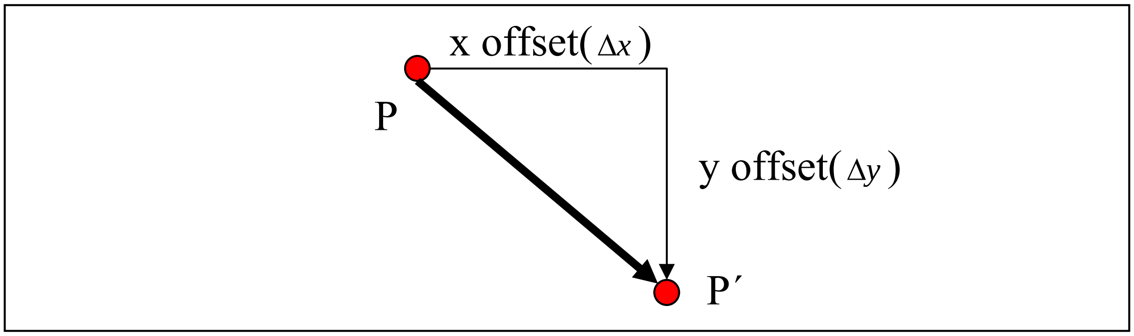

Figure 4.12 The displacement between conjugate points P, and P'

Figure 4.13 The extracted displacement in the highest layer

In this research, there are three layers serve as pyramidal structure, and Figure 4.13 illustrates the ice velocities or displacement on the highest layer in Amery ice shelf. The yellow lines represent displacement after removing wrong results. Each displacement can be divided into two portions, x offset and y offset (Figure 4.13). The x offset and y offset values are the estimated position that we mentioned in the step 4 in Section 4.2.4, and they provide useful information. If this information can be passed to the second layer (next layer) of pyramidal images, the accuracy and search time should be increasingly improved.

First, the points are generated to represent the displacement located on the original displacement. Figure 4.14 illustrates the distribution of points. These points have the same attribution (x offset and y offset values) with the original displacement. Then, the x offset and y offset images are generated based on these points using interpolation method. Figure 4.15 and Figure 4.16 illustrate x offset and y offset images using color ramp. Different colors represent different pixel offset values.

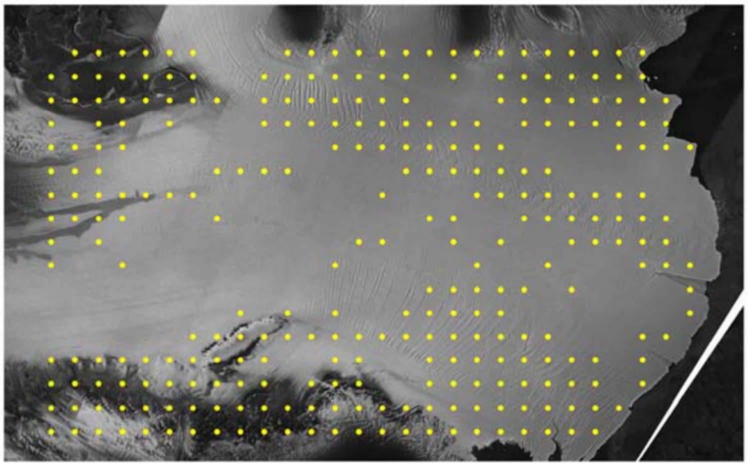

Figure 4.14 The yellow points represent the locations of extracted displacement

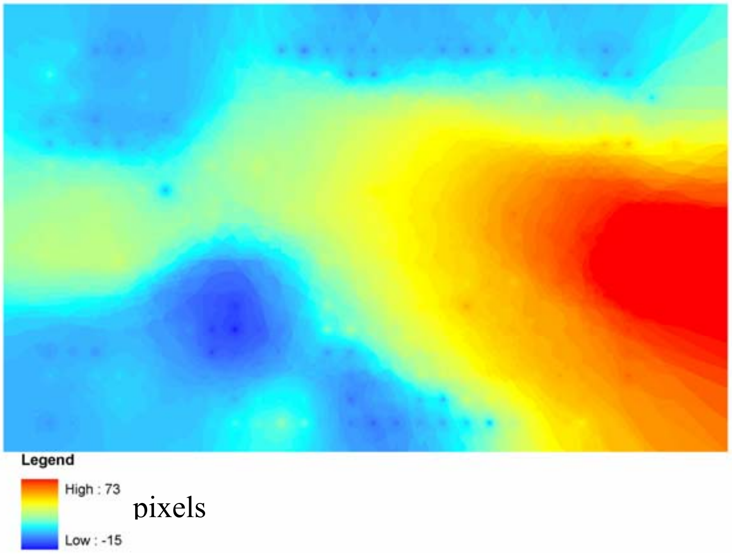

Figure 4.15 The x offset image generated by the extracted ice velocities on the highest layer

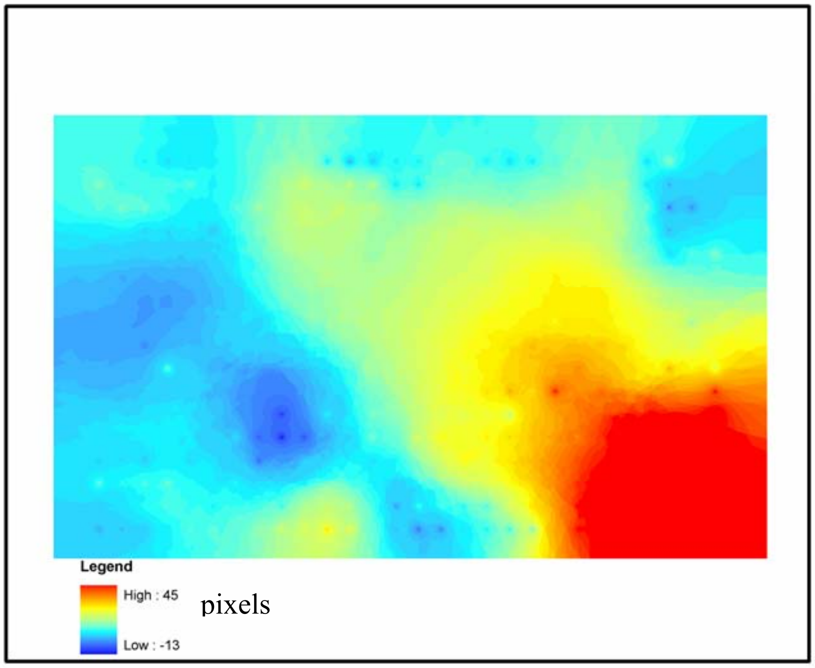

Figure 4.16 The y offset image generated by the extracted ice velocities on the highest layer

On the second layer, the estimated positions will be given according to the x offset and y offset generated by the higher layer. Figure 4.17 illustrates the extracted ice velocities based on the useful information, x offset and y offset, provided by the highest layer.

The same procedure mentioned previously will be implemented on the second layer to generate x offset and y offset images. Figure 4.18 and Figure 4.19 illustrate the x offset and y offset images generated on the second layer.

Figure 4.17 The extracted ice velocities on the second layer

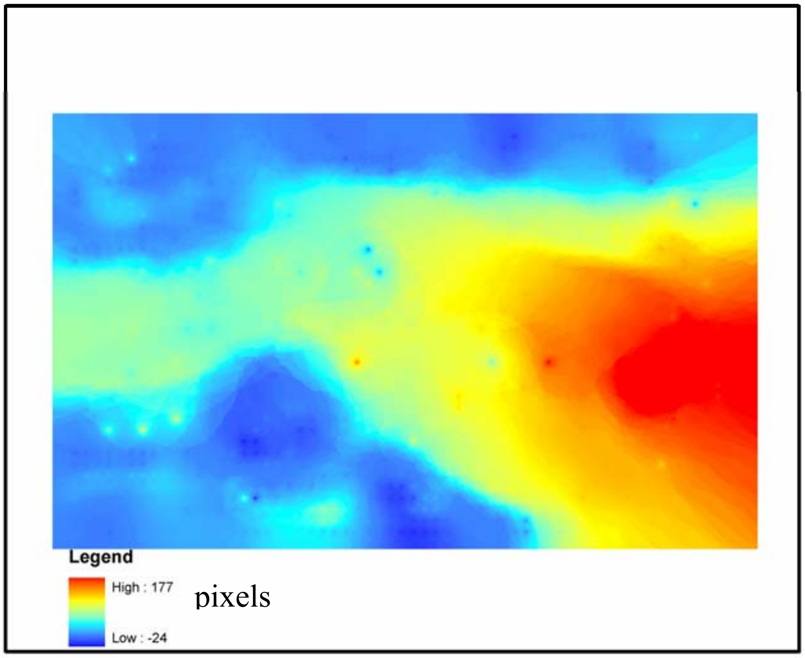

Figure 4.18 The x offset image generated by the extracted ice velocities on the second layer

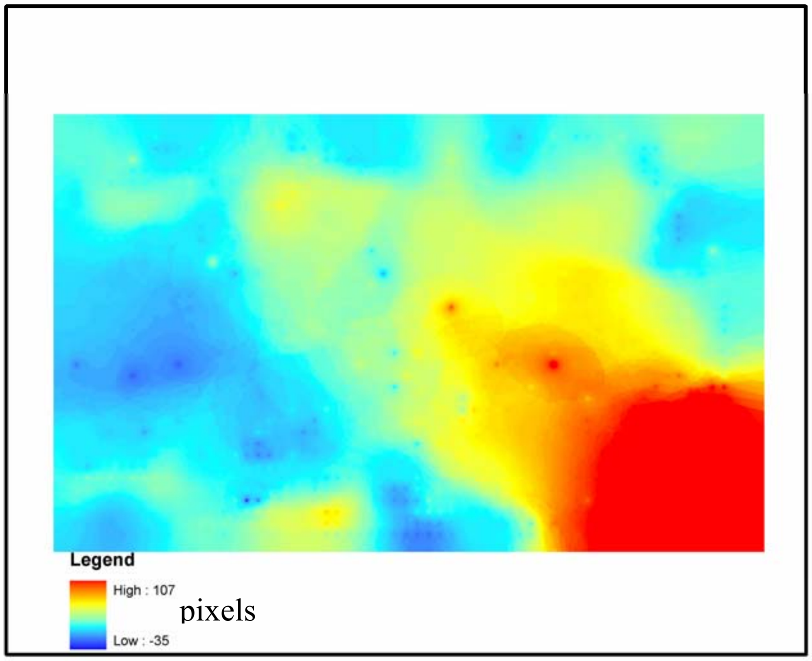

Figure 4.19 The y offset image generated by the extracted ice velocities on the second layer

To obtain the reliable conjugate matching points at the higher layers of the hierarchy of the image pyramid is important. Otherwise, the matching error would be propagated down into the matching operations at the lower layers. In this research, a robust statistical indicator is incorporated in each layer of the hierarchical matching process to filter the match outliers and gross errors and enhance the reliability of the matching results.

In conclusion, the pyramid structure can be explained by the following flow chart in Figure 4.20, and the extracted ice velocities from three layers can be demonstrated in Figure 4.21. As can be seen, the extracted results are denser when the previous offset information is propagated to the next layer.

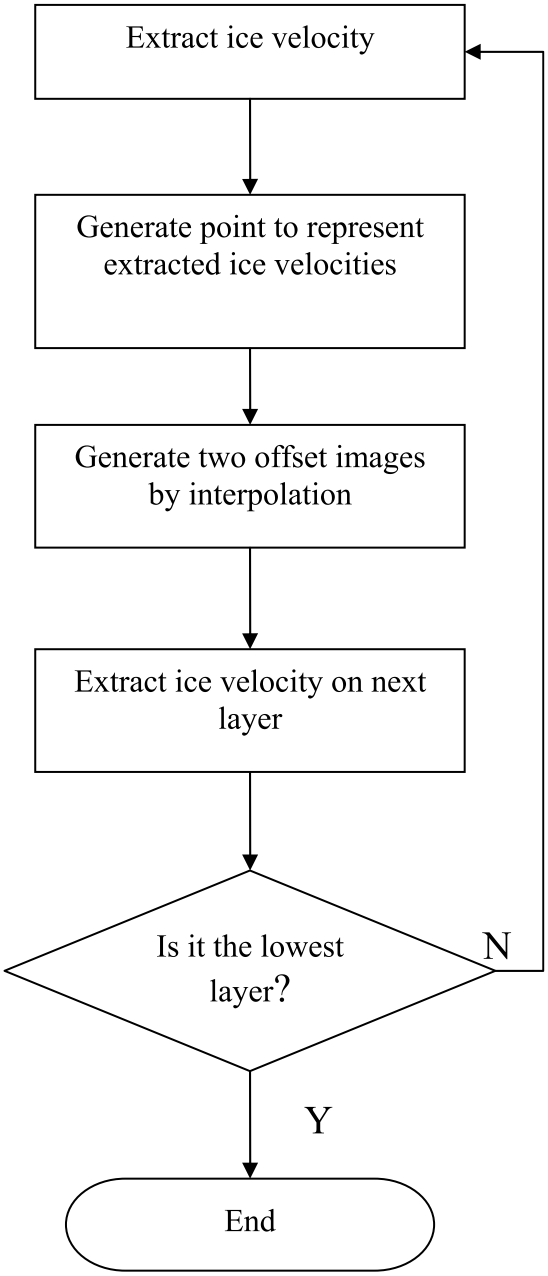

Figure 4.20 The flow chart of implementing pyramidal structure to extract ice velocities

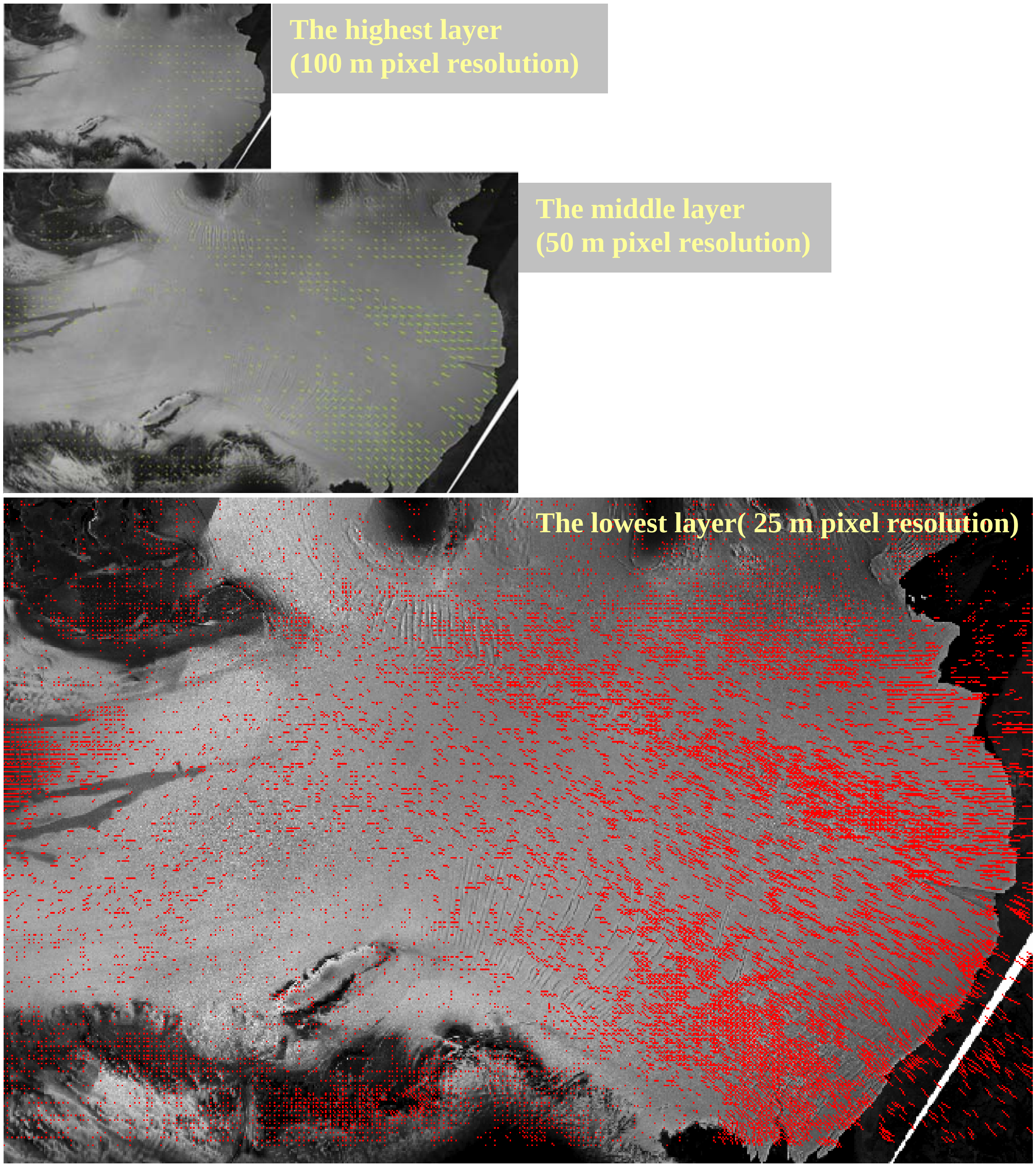

Figure 4.21 The extracted ice velocities on three layers using multi-scale method

4.3 ArcGIS Extension Module for Multi-scale Image Matching Method

As can be seen, in Figure 4.22, the image matching using multi-scale strategy implemented in this research is also converted into a friendly interface that includes some essential parameters. There are four sections including I/O setting, image matching, hierarchic images generation, and interpolation in the interface. The interface also is plugged into the extension module in ArcGIS using the same procedure describes in Section 3.3.

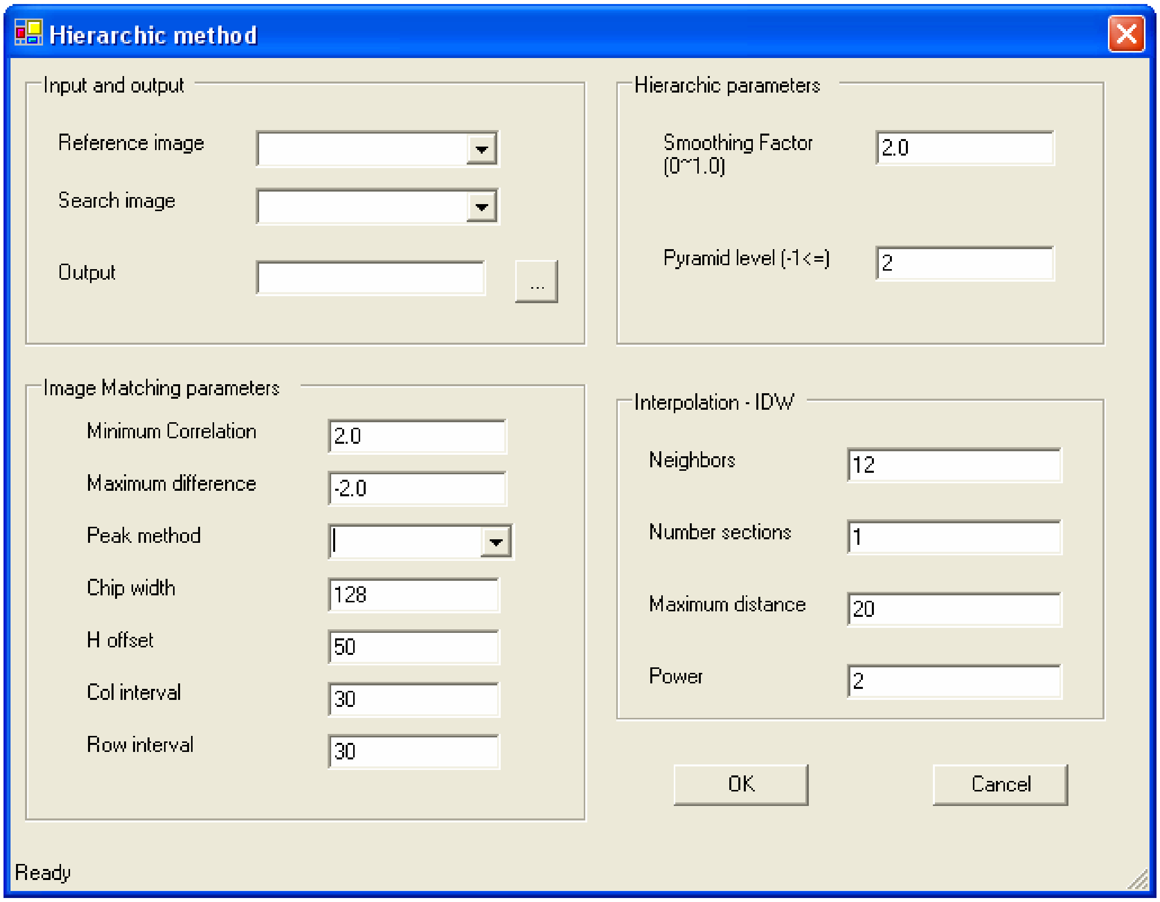

Hierarchic method

Input and output

Reference image

Search image

Output

Hierarchic parameters

Smoothing Factor (0~1.0): 2.0

Pyramid level (-1<=): 2

Image Matching parameters

Minimum Correlation: 2.0

Maximum difference: -2.0

Peak method

Chip width: 128

H offset: 50

Col interval: 30

Row interval: 30

Interpolation - IDW

Neighbors: 12

Number sections: 1

Maximum distance: 20

Power: 2

Ready

Figure 4.22 The interface of image matching based multi-scale method

4.4 Accuracy Evaluation and Validation of Velocity Measurements

In order to evaluate the coregistration between 1997 and 2000 images, ten GCPs (Ground Control Point) were selected and well distributed in both images. The red marks represent ten GCPs in Figure 4.23 and Figure 4.24, and Table 4.2 shows the total RMS (Root Mean Square) value, 1.64 pixels. In addition, the accuracy of parabolic curve is evaluated to reach 0.5 pixels; therefore the ice velocities more than 1.71 pixels (i.e. 42.8 m or about 14 m/a).

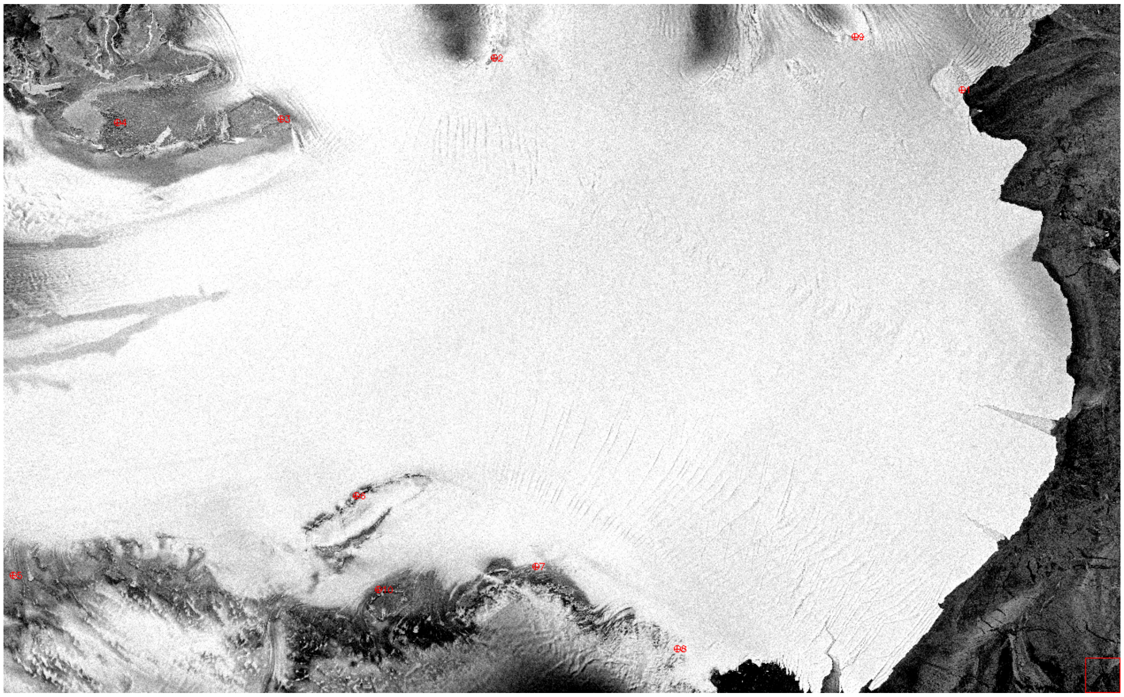

Figure 4.23 The selected GCPs in the 1997 image

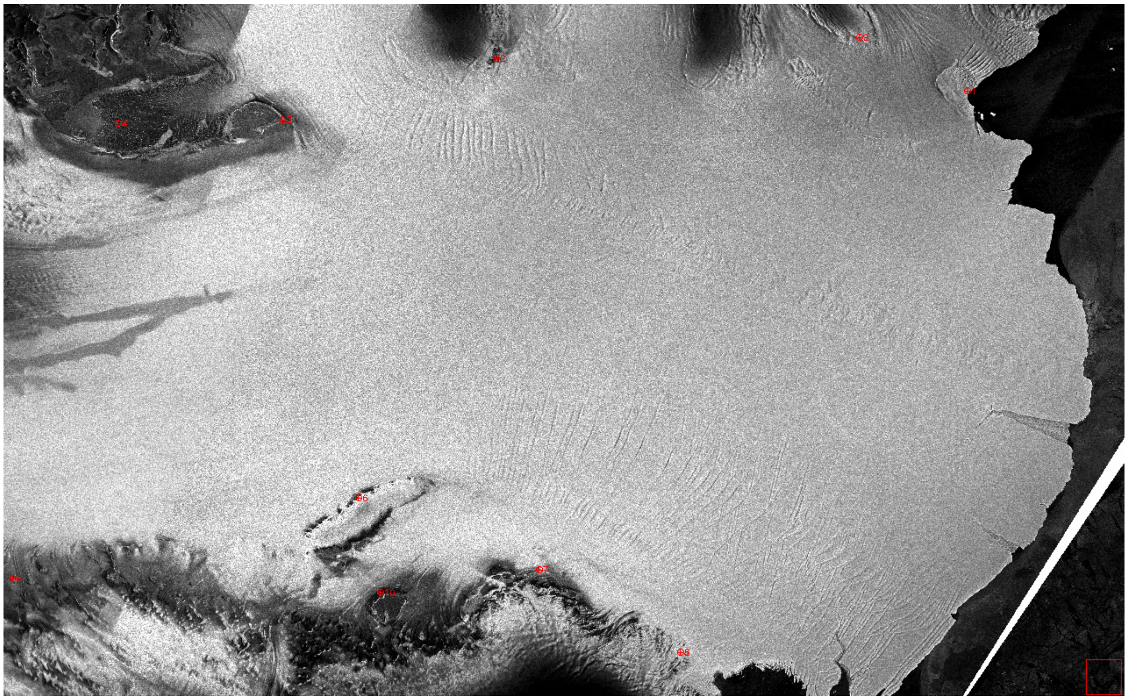

Figure 4.24 The selected GCPs in the 2000 image

Table 4.2 The RMS errors between 1997 and 2000 images

	Base(x)	Base(y)	Warp(x)	Warp(y)	RMS Error
1	10736.00	959.00	10738.20	962.20	3.88
2	5493.86	603.14	5494.14	606.00	2.87
3	3110.00	1288.00	3110.00	1288.00	0.00
4	1274.00	1321.67	1275.67	1322.00	1.70
5	109.00	6397.67	108.00	6396.00	1.95
6	3951.67	5501.67	3951.67	5502.67	1.00
7	5966.00	6299.00	5968.00	6300.00	2.24
8	7548.00	7221.80	7548.20	7221.40	0.45
9	9537.00	367.00	9537.80	368.00	1.28
10	4197.33	6557.67	4196.33	6557.67	1.00
				Average	1.64

To assess the accuracy, a comparison data of ice velocity was obtained, as described in Figure 4.25. Image matching using pyramidal strategy was well discussed in the previous sections. The manually select points, which serve as the comparison data and also include x offset and y offset data to interpolate into x offset and y offset images are implemented to evaluate the effectiveness of the pyramidal strategy. In this way, the multi-scale algorithm can be proved its performance is better than single-scale method (i.e. image matching is only performed in the original image.) The same parameters setting applied in the pyramidal method will be employed in the manually select method. The result of manually select method is shown in Figure 4.25, and the result of pyramidal method is shown in Figure 4.26. The blue circles in Figure 4.25 represent the incomplete extractions by manually selected method. That means if we employ the pyramidal strategy, which implements the image matching on three layers in this research, we can achieve better results than manually select method, which directly implements image matching on the finest layer.

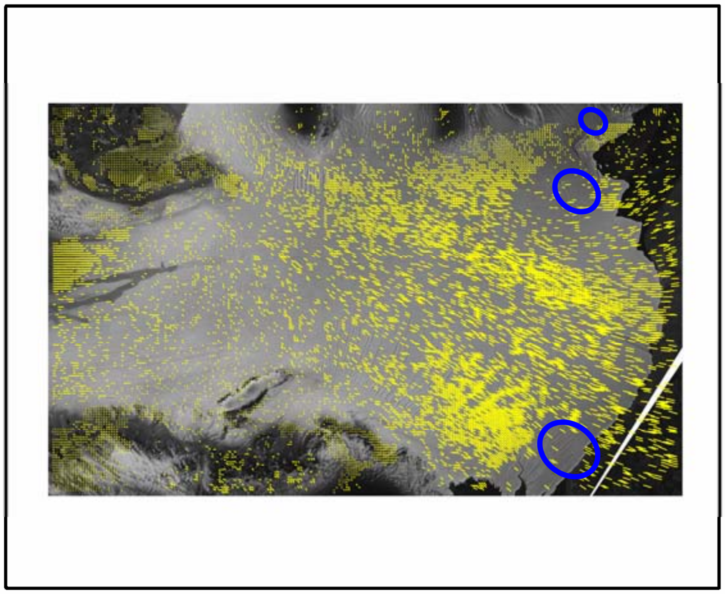

Figure 4.25 Extracted ice velocities by manually select points

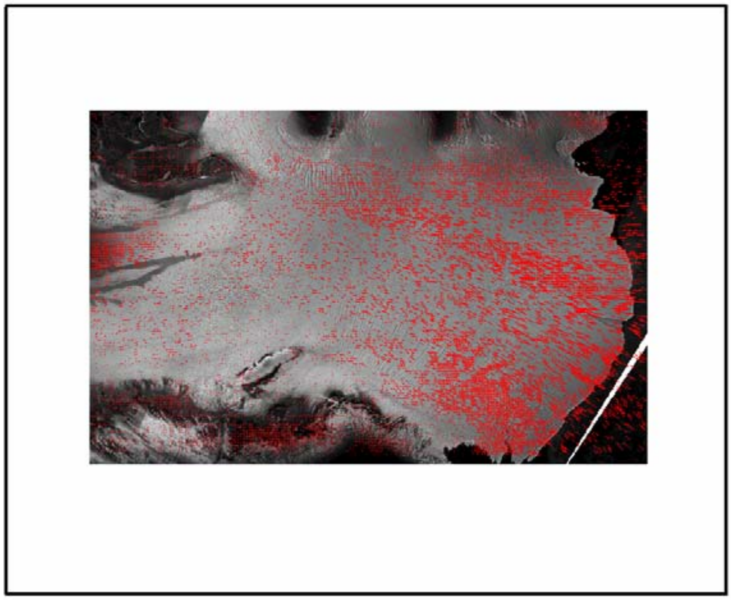

Figure 4.26 Extracted ice velocities by pyramidal method

In addition, for both methods, the extracted ice velocities are visually examined, and shifts of more than 200 meters are considered errors based on the statistic property that out of three standard deviations. The cross correlation values are obtained by comparing the real and predict locations in the process of interpolation. There are 9320 correct results in the total 10482 extracted ice velocities using manual select method; there are 13977 correct results in the total 15281 extracted ice velocities using pyramidal method. The pyramidal strategy has better correct rate 92.02% than the correct rates of manual method. Moreover, the omission rate of manual method reaches to 33.78%.

4.5 Analysis of Ice Dynamic Behavior and Flow Pattern

The velocity fields are extracted for selected ice shelves and outlet glaciers by using the multi-scale, hierarchical image matching algorithm. The derived velocity fields are compared with the historical velocity measurements and recent InSAR measurements, and the dynamic behavior of ice shelves and outlet glaciers are examined. The ice advance and retreat rates derived from comparing sequential coastlines will be integrated with the ice flow velocity derived by multi-scale image matching to ice calving rates and gauge ice mass loss to the ocean.

Figure 4.27 illustrates the extracted ice velocities in Amery ice shelf. The ice velocities range from 7 m to 4632 m per 2.994521 years (or 3 m/a ~1549 m/a). Figure 4.28 illustrates the ice velocities generated by interpolation.

The image matching employs pyramid strategy compares well to the InSAR approach. Figure 4.29 illustrates the extracted ice velocities in Amery ice shelf by InSAR. The time resolution (or acquisition period) is 24 days. The extracted ice velocities over 24 days are converted into annual values. As can be seen, the highest ice velocity is 1607 m/a, and there are some areas, where new snow fell during the 24 days interval causing InSAR to fail. On the other hand, the pyramidal method can complete the blank or no data areas (Figure 4.30); moreover the ice velocities extracted by pyramidal method close to the ice velocities predicted by InSAR. The disadvantage compared to InSAR is image matching methods cannot detect conjugate points during too short period and too long period between two images. Because the extracted ice velocities during too short period cannot guarantee their reliability, and the image matching methods probably fail during too long period due to loss of conjugate points.

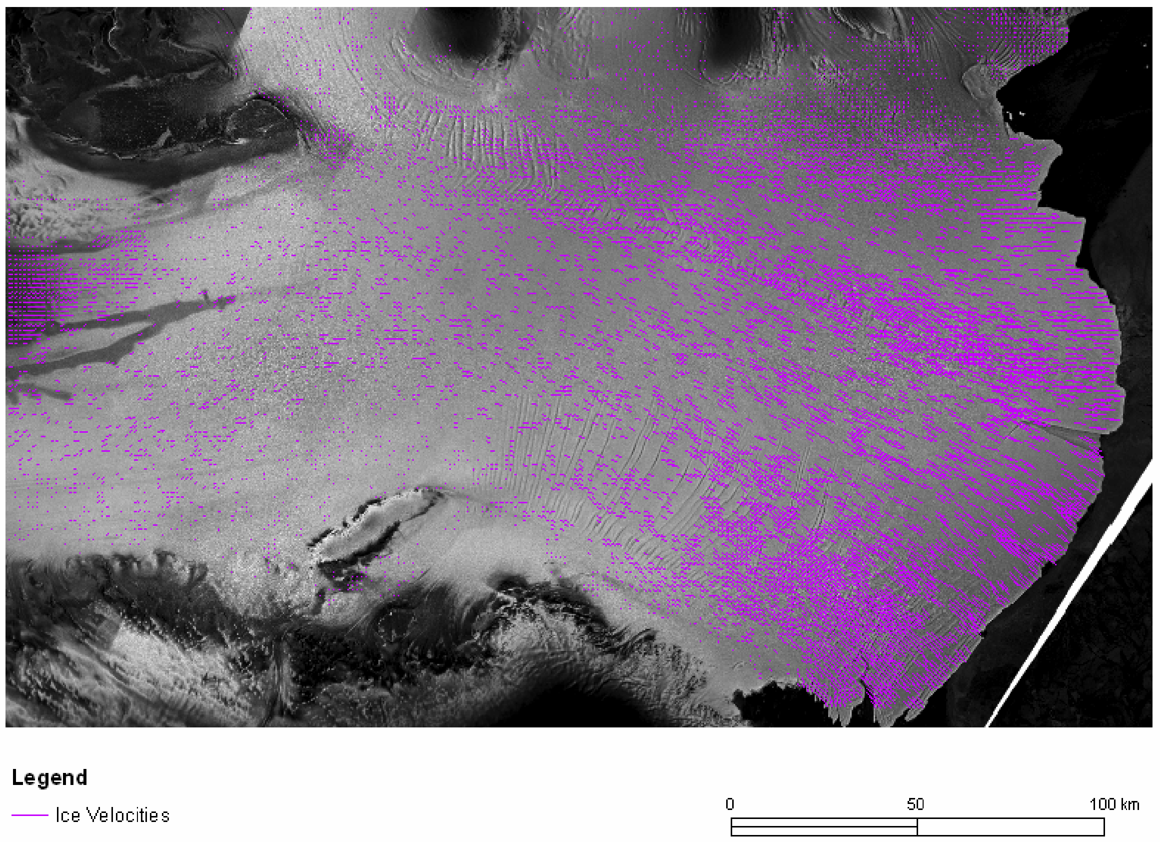

Figure 4.27 Ice velocities in Amery Ice Shelf

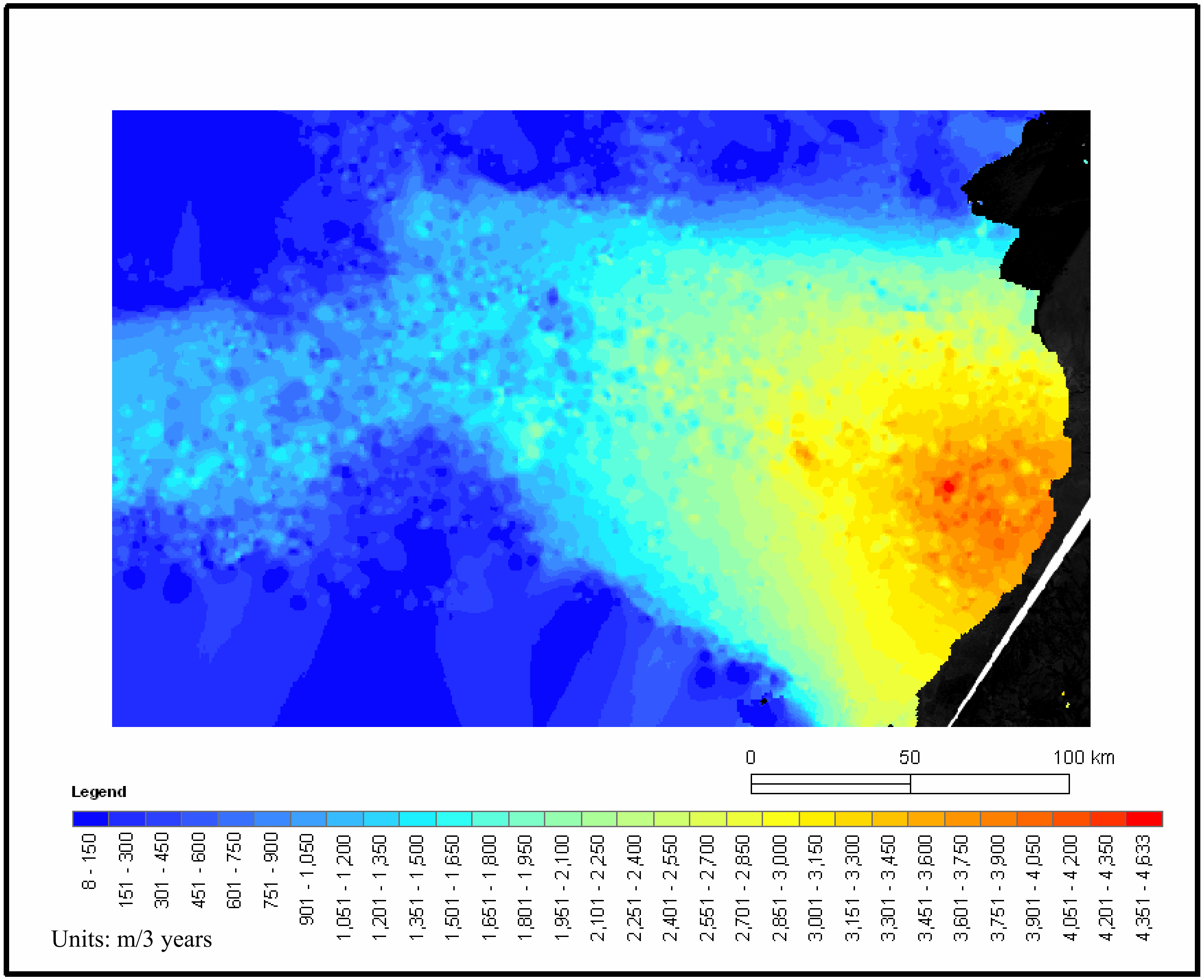

Figure 4.28 Ice velocities in Amery Ice Shelf (color ramp)

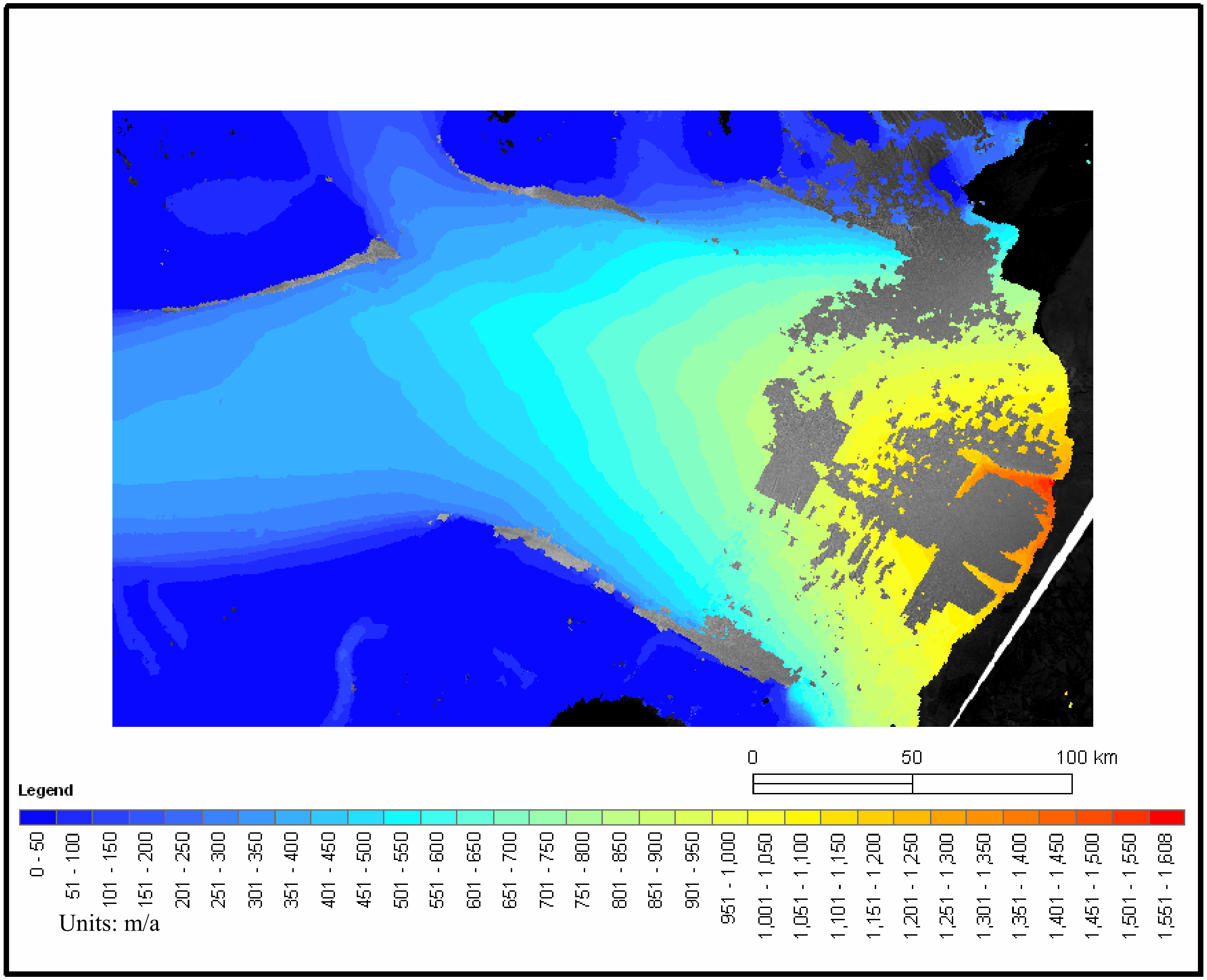

Figure 4.29 Extracted ice velocities per year in Amery Ice Shelf by InSAR

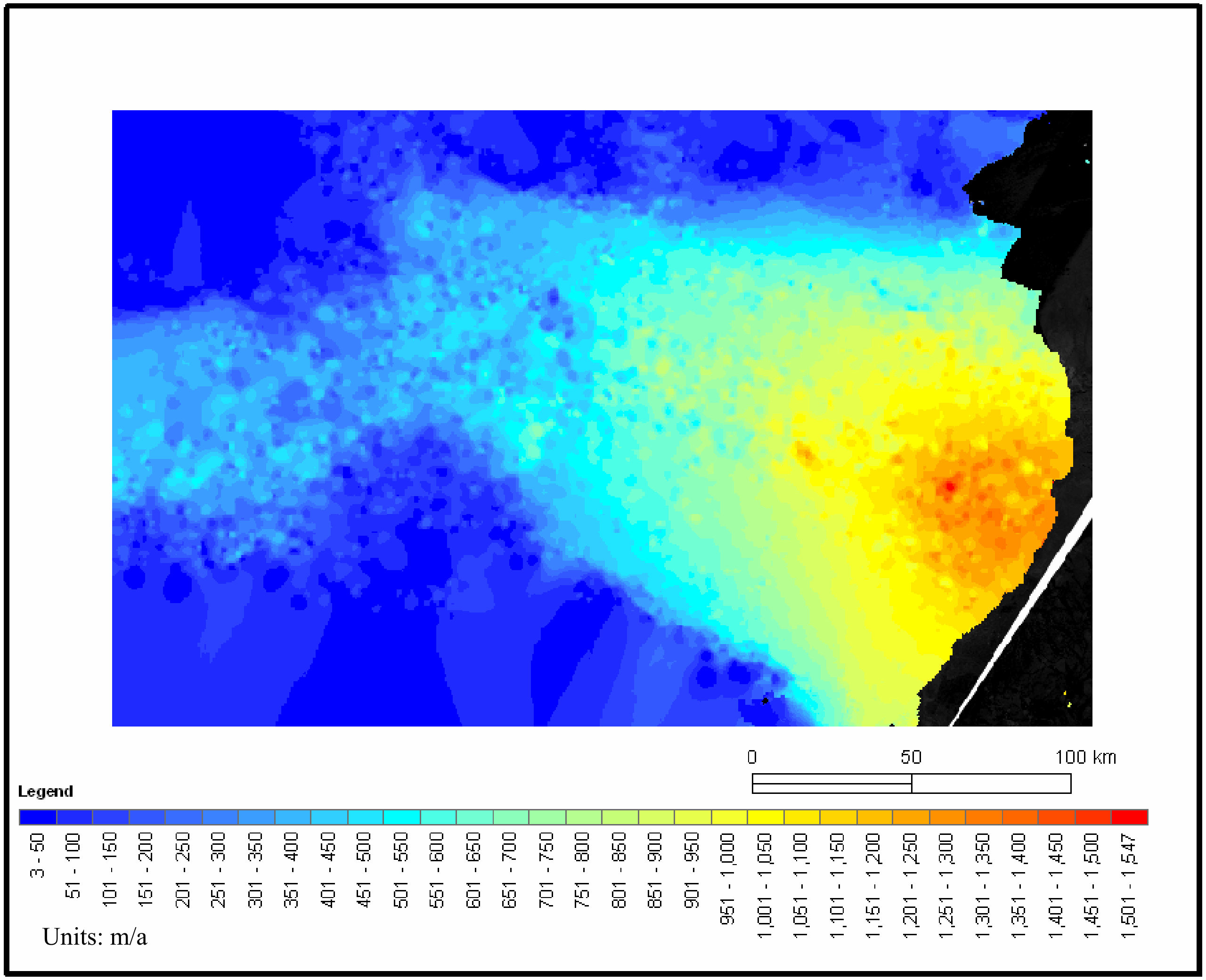

Figure 4.30 Extracted ice velocities per year in Amery Ice Shelf by the pyramid method

The field survey data, measured in 1970, are used to analyze the long-term ice velocity trend. Figure 4.31 and Figure 4.32 illustrate the 85 measuring points between 1970 and 1971. These field survey data will be compared with the ice velocities extracted by InSAR and this research (using "SAR" represents the ice velocities extracted from the multi-scale image matching method). Appendix B illustrates the comparison, and the columns of "InSAR minus Field Survey" and "SAR minus Field Survey" are employed to generate the line-column charts in Figure 4.33 and Figure 4.34. The x-axis represents the measuring location; the y-axis represents the amount of increased or decreased ice velocity. As can be seen, the items, from 70 to 81 (Figure 4.35, red circle), have significant increased. That means there are higher ice velocities in the middle of Amery ice shelf. The InSAR measuring data show that the ice velocities are increased from 5.74% to 522.76% for item 70~81; the SAR measuring data show that the ice velocities are increased from 8.06% to 482.33% for item 70 through 81 If we pay attention on the items 2 through 9 (blue circle), we can find the same increased changes, but the amounts are not quite significant.

Figure 4.31 The comparison of ice velocities obtained from field survey (green bar), InSAR (yellow bar), and SAR (red bar)

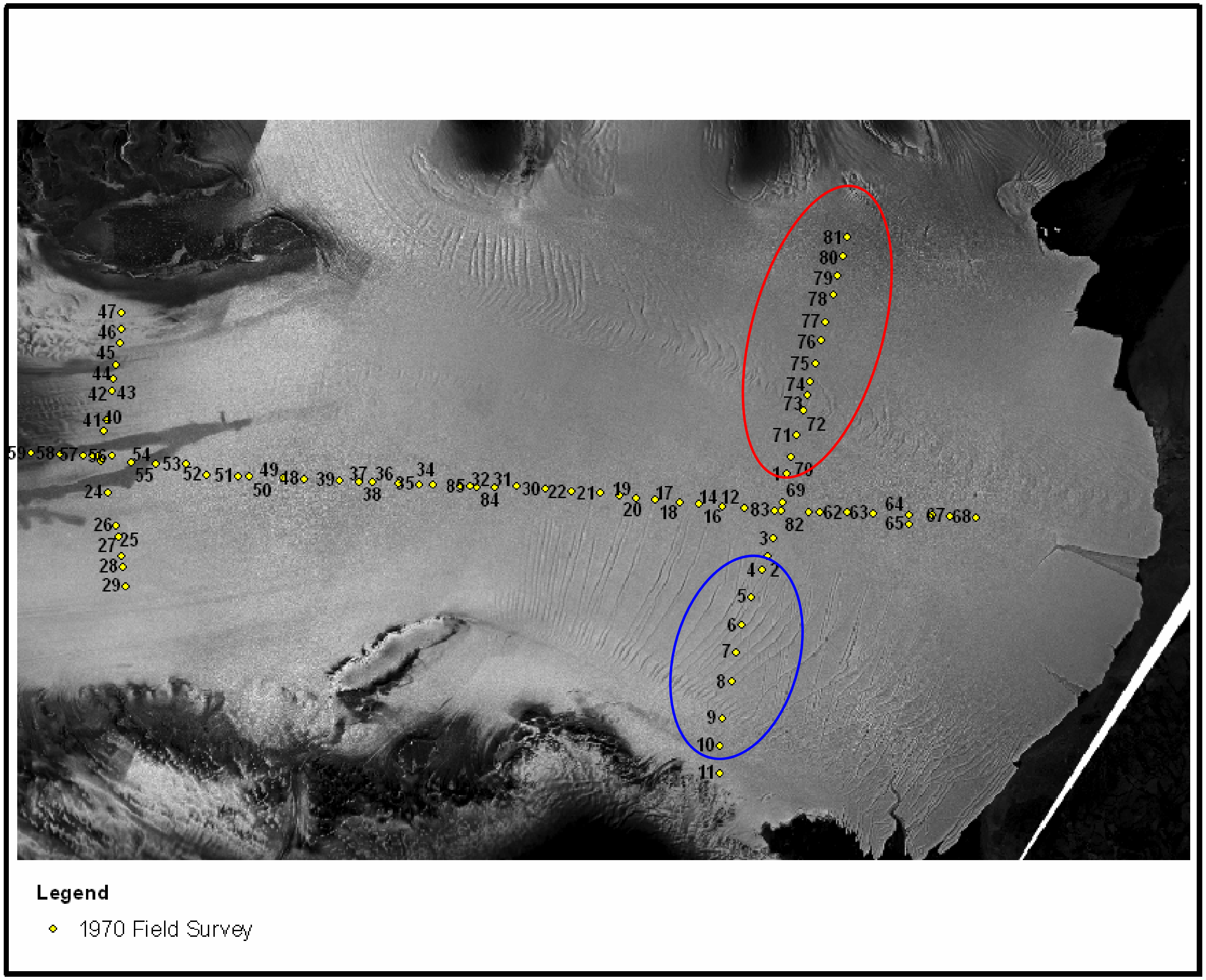

Figure 4.32 The 85 positions of field survey measured in 1970

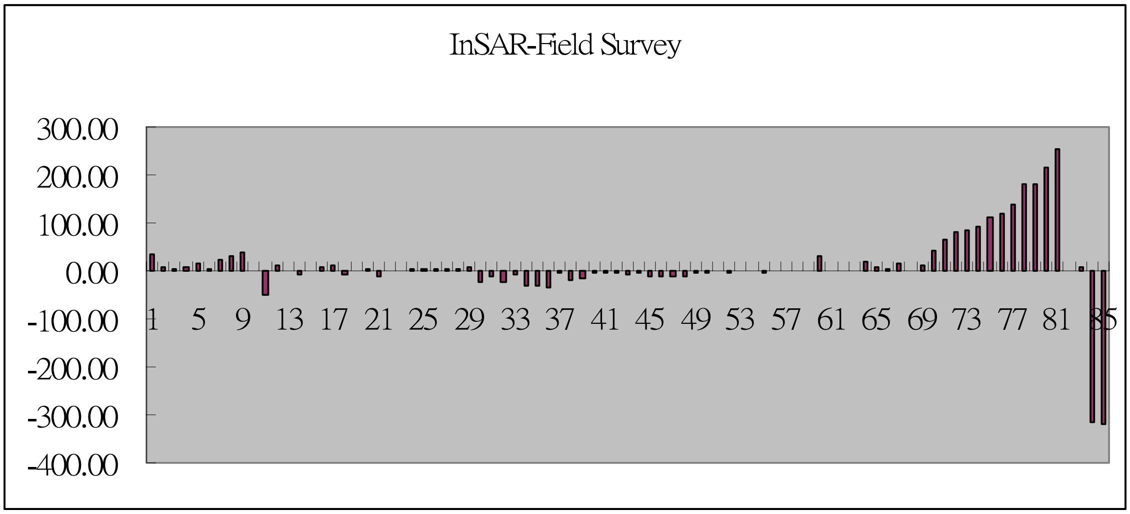

Figure 4.33 The line-column chart of InSAR data minus field survey data.

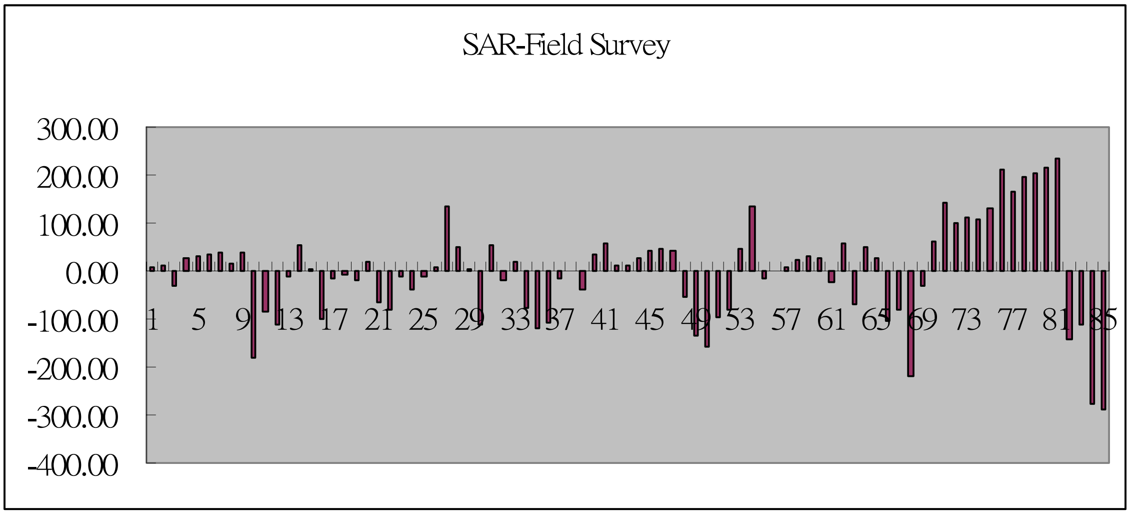

Figure 4.34 The line-column chart of SAR data minus field survey data.

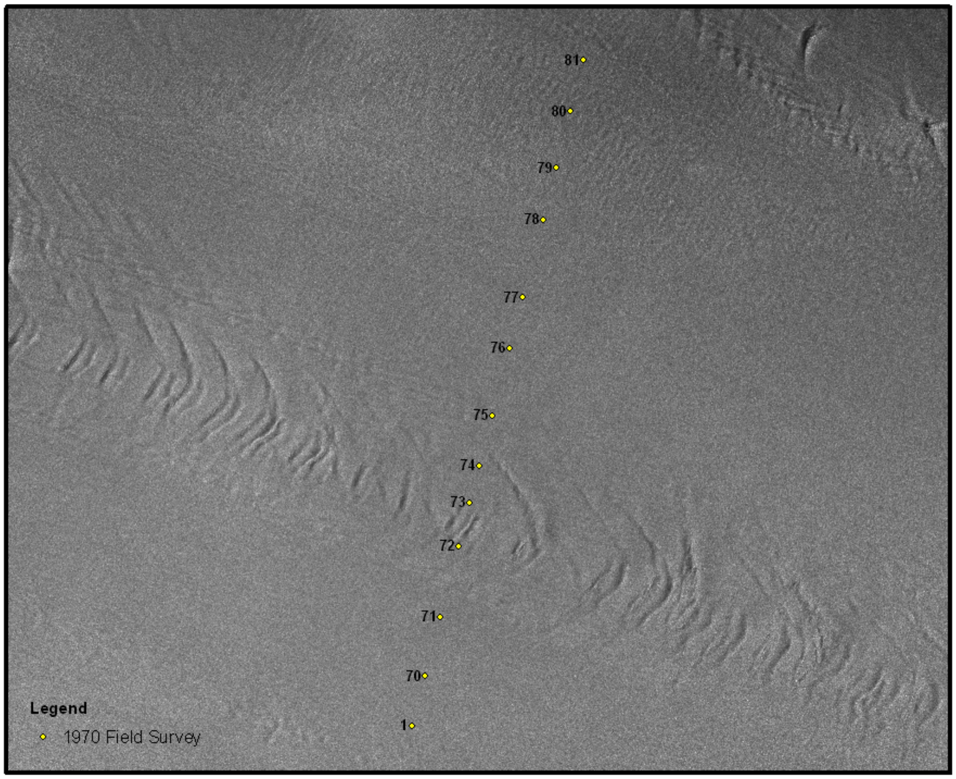

Figure 4.35 The area of increased ice velocities

4.5.1 *Ice calving rates analysis*

In the interior of the Antarctic ice sheets, snow accumulation is low due to the scarce precipitation. In the Antarctic coast, on the contrary, there is an increase in snowfall compared to interior. Therefore, the ice reach the Antarctic coast is not derived from the interior of Antarctica. Once the ice streams reach and push out to the ocean, there is mass loss happening. The mass loss from Antarctic ice sheets is by iceberg calving into the sea, surface melting, run-off and melting underneath the floating ice shelves. The amount of surface melting is trivial when it is compared with the amount of iceberg calving and melting underneath the floating ice shelves, and so far, there is no precise measuring to evaluate the underneath melting. Therefore, to measure the ice calving rate is important.

In order to determine the ice calving rate near the Amery coastlines, the advance areas and ice velocities are required. Figure 4.36 illustrates the relationship between them. The areas A, B, C, and D in Figure 4.36 are used to calculate ice calving rates in Amery ice shelf. The blue hatch areas represent the advance areas obtained by Section 3.5.

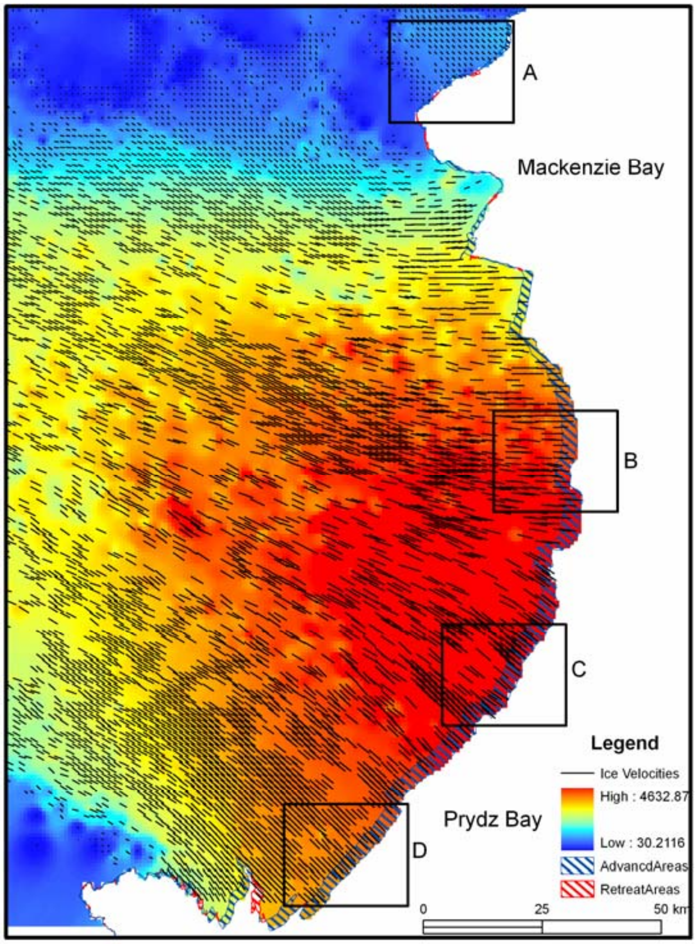

Figure 4.36 The status of ice velocities and advance areas in Amery Ice Shelf

In Figure 4.37, near Mackenzie Bay, arrows illustrate the original ice velocities, and the numbers above the arrows indicate their quantity of velocities. The ice velocities within blue background represent they are in the same classification in color ramp. In order to obtain the representative value of ice velocity for area A, the outliers will not be counted. Therefore the mean of ice velocities are 676.11 meters per 2.994521 years (or 226.12 m/a). The average advance length is 588.33 m per 2.994521 years (or 196.47 m/a) for area A. Therefore the ice calving rate for area A is 87.78 m per 2.994521 years or 29.36 m/a.

For area B, in Figure 4.38, the same analysis is implemented. The mean of ice velocities are 3081.66 meters per 2.994521 years (or 1030.65 m/a). The average advance length is 3145 m per 2.994521 years (or 1051.83 m/a) for area B. Therefore the ice calving rate for area B is -63.34 m per 2.994521 years or -21.18 m/a (“ – “ indicates the advance status).

For area C, in Figure 4.39, the mean of ice velocities are 3750.96 meters per 2.994521 years (or 1254.5 m/a). The average advance length is 3815 m per 2.994521 years (or 1275.92 m/a) for area C. Therefore the ice calving rate for area C is -64.06 m per 2.994521 years or -21.42 m/a.

For area D, in Figure 4.40, the mean of ice velocities are 2797.83 meters per 2.994521 years (or 934.32 m/a). The average advance length is 2943.33 m per 2.994521 years (or 984.39 m/a) for area D. Therefore the ice calving rate for area D is -145.44 m per 2.994521 years or -48.64 m/a.

Besides the Amery ice shelf, three glaciers (area A, B, and C in Figure 4.41) around Waldron Cape (116.41ºE, 66.69ºS) are also analyzed for their ice calving rates. For area A, in Figure 4.42, it is more complicate situation because some ice fronts are advances and some are retreats. The mean of ice velocities are 4933.29 meters per 2.994521 years (or 1649.93 m/a). For the advance analysis, the average advance length is 1833 m per 2.994521 years (or 613.04 m/a). Therefore the ice calving rate is 3100.29 m per 2.994521 years or 1036.89 m/a; for the retreat analysis. The average retreat length is 1377 m per 2.994521 years (or 460.54 m/a). Therefore the ice calving rate is 6310.29 m per 2.994521 years or 2110.47 m/a. For the total ice calving rates in the ice fronts are from 1036.89 ~ 2110.47 m/a.

For area B, in Figure 4.43, the mean of ice velocities are 1091.4 meters per 2.994521 years (or 365.02 m/a). The average retreat length is 1841.33 m per 2.994521 years (or 615.83 m/a) for area B. Therefore the ice calving rate for area B is 2932.73 m per 2.994521 years or 980.85 m/a.

For area C, in Figure 4.44, the mean of ice velocities are 1510.51 meters per 2.994521 years (or 475.33 m/a). The average retreat length is 1881 m per 2.994521 years (or 629.09 m/a) for area C. Therefore the ice calving rate for area C is 3391.51 m per 2.994521 years or 1134.28 m/a.

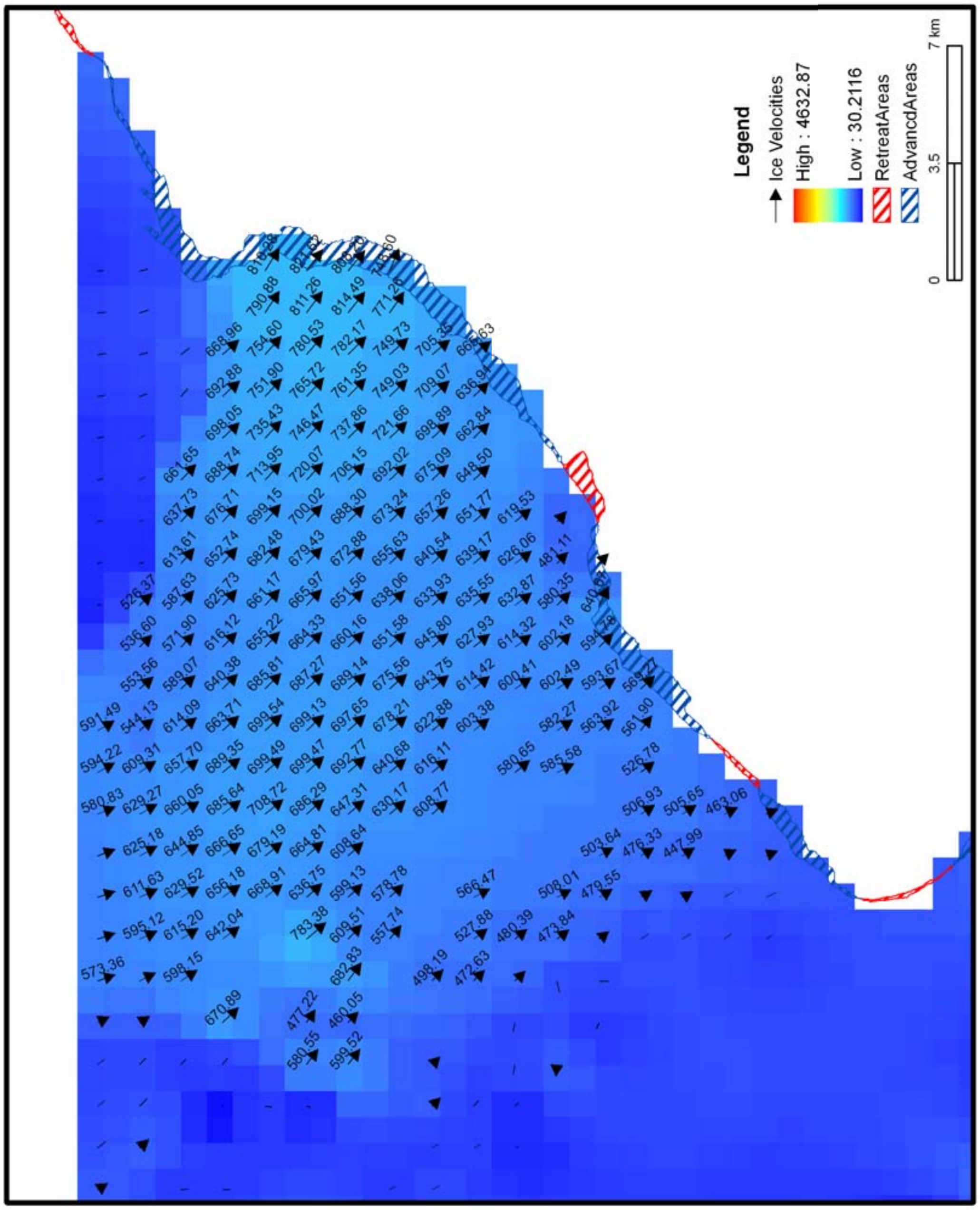

Figure 4.37 The status of ice velocities and advance areas in area A

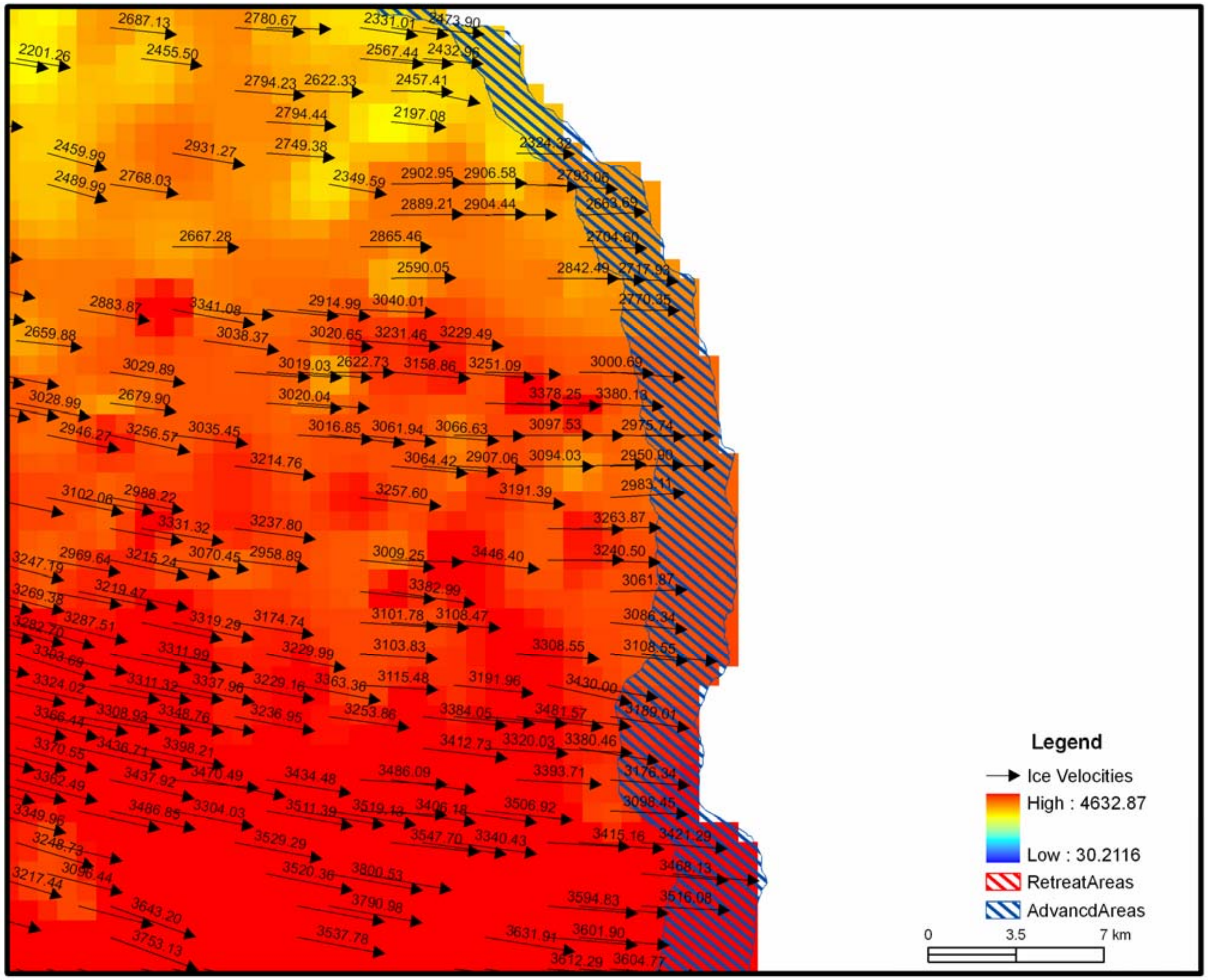

Figure 4.38 The status of ice velocities and advance areas in area B

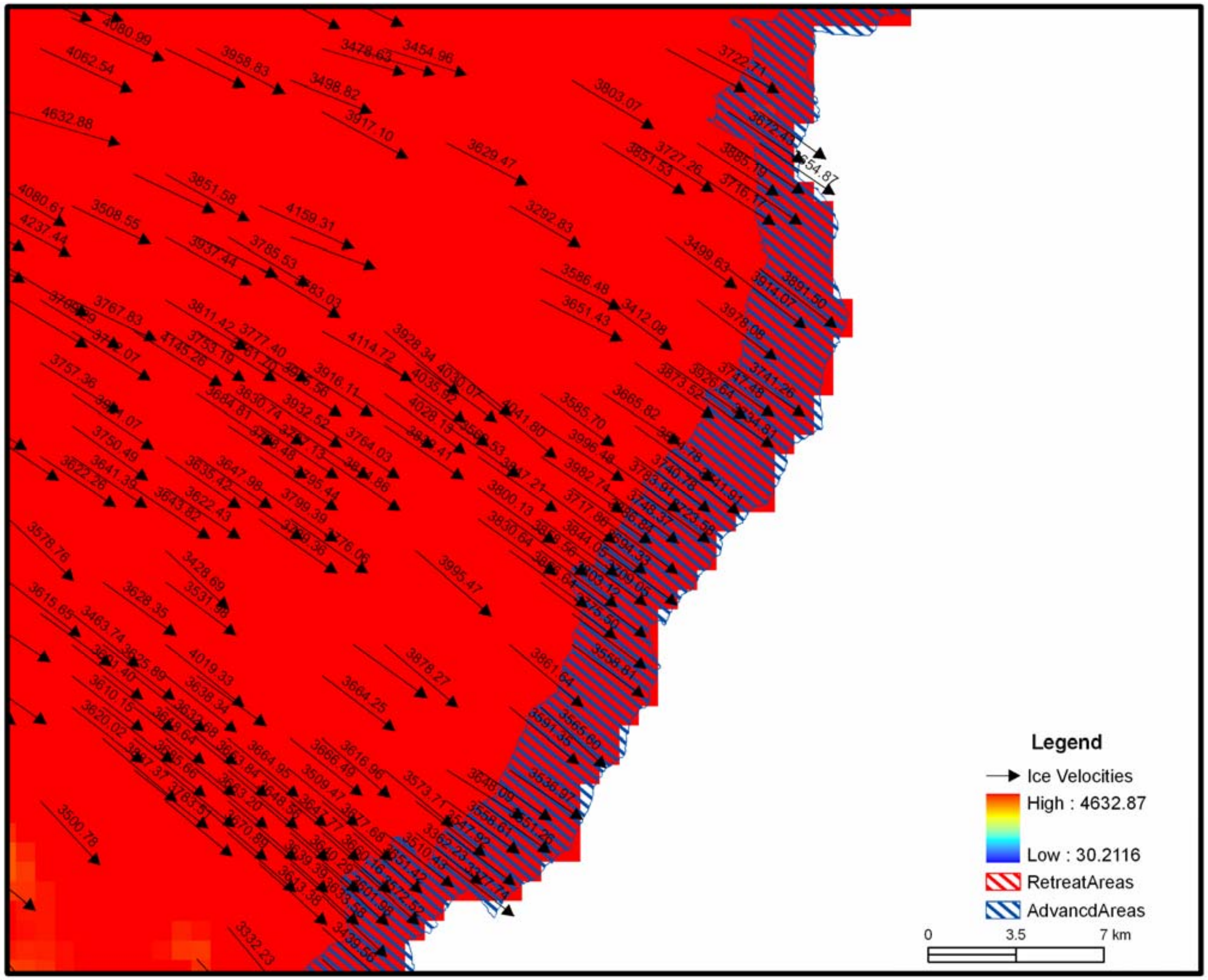

Figure 4.39 The status of ice velocities and advance areas in area C

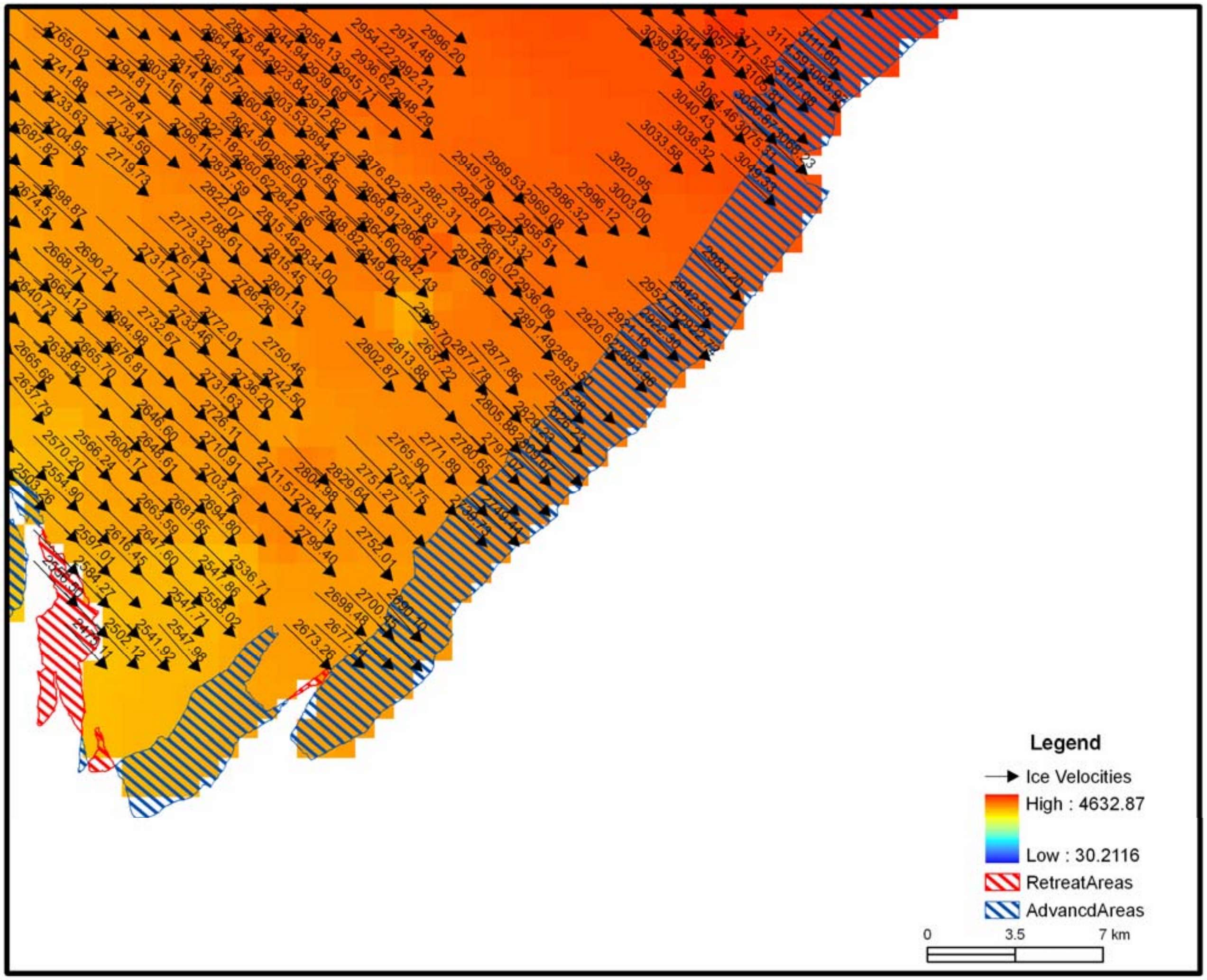

Figure 4.40 The status of ice velocities and advance areas in area D

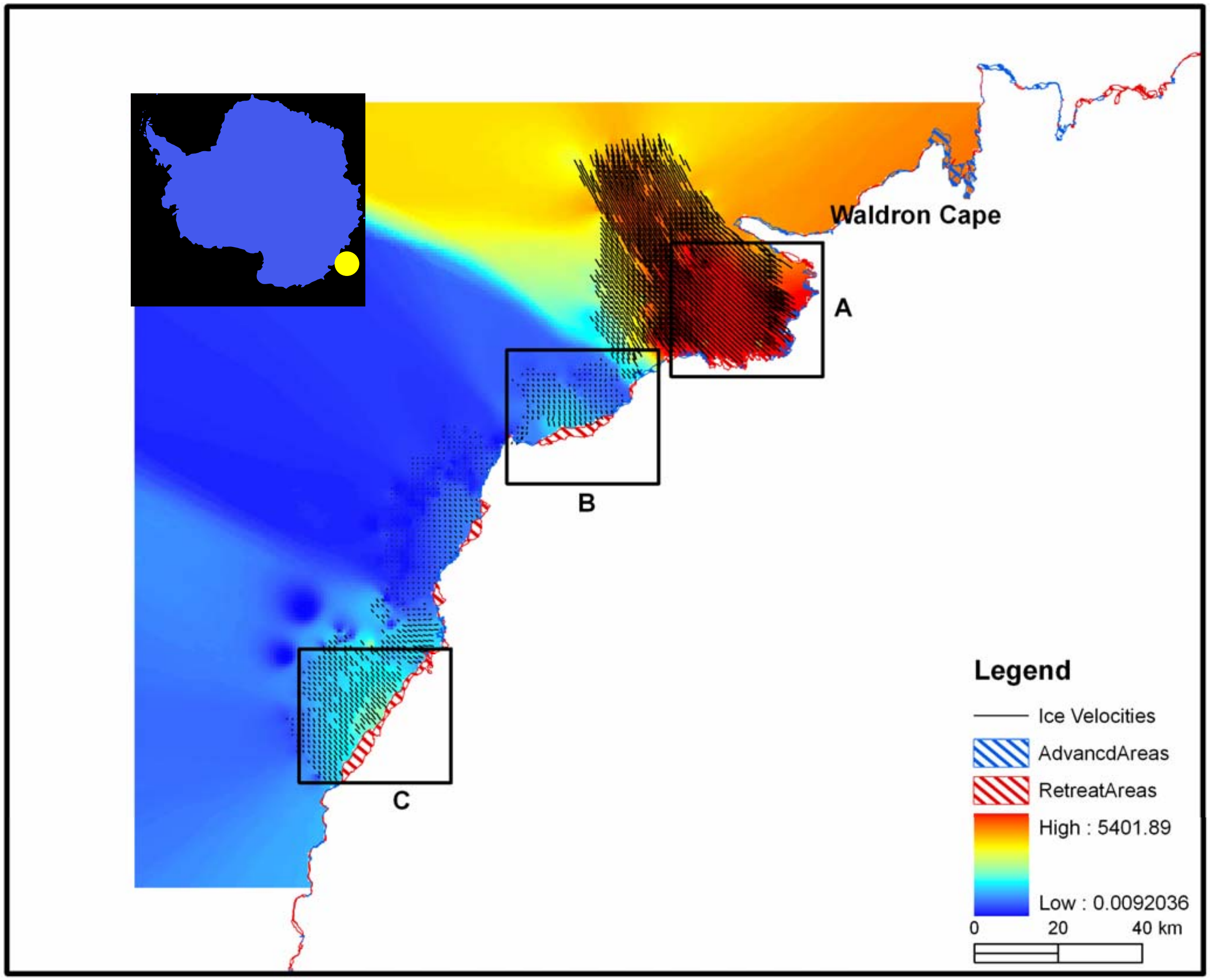

Figure 4.41 The status of ice velocities, retreat and advance areas near Waldron Cape

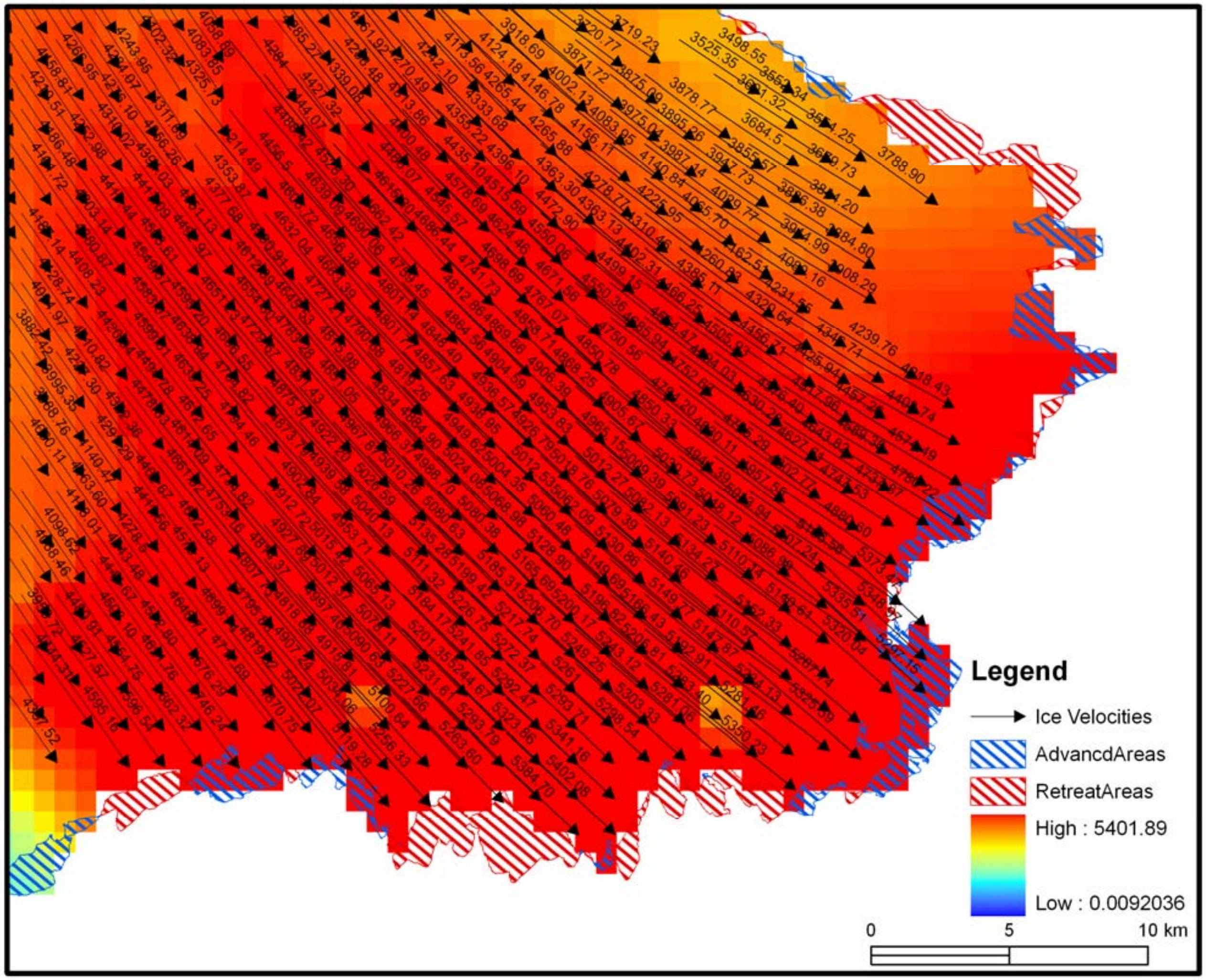

Figure 4.42 The status of ice velocities in area A

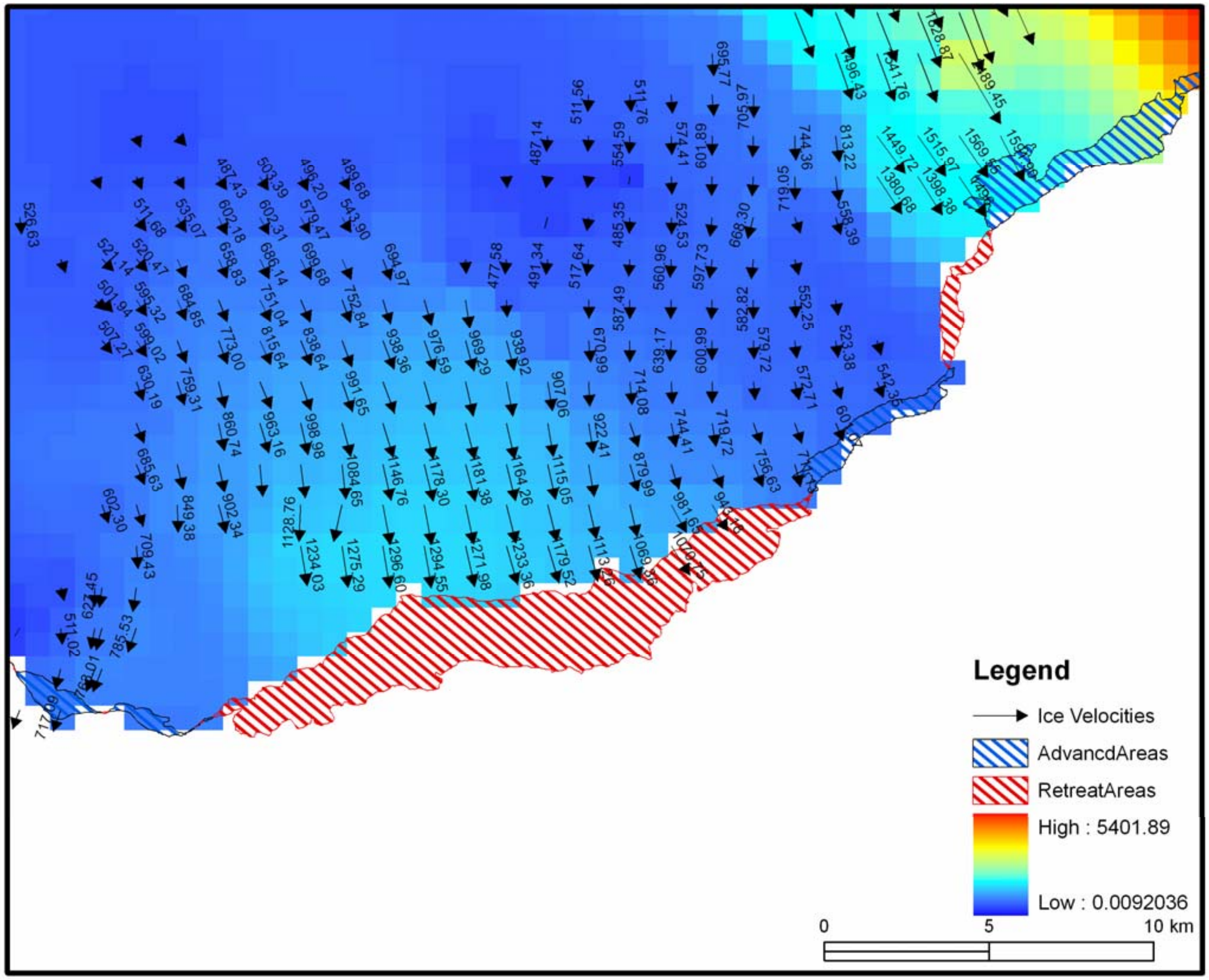

Figure 4.43 The status of ice velocities in area B

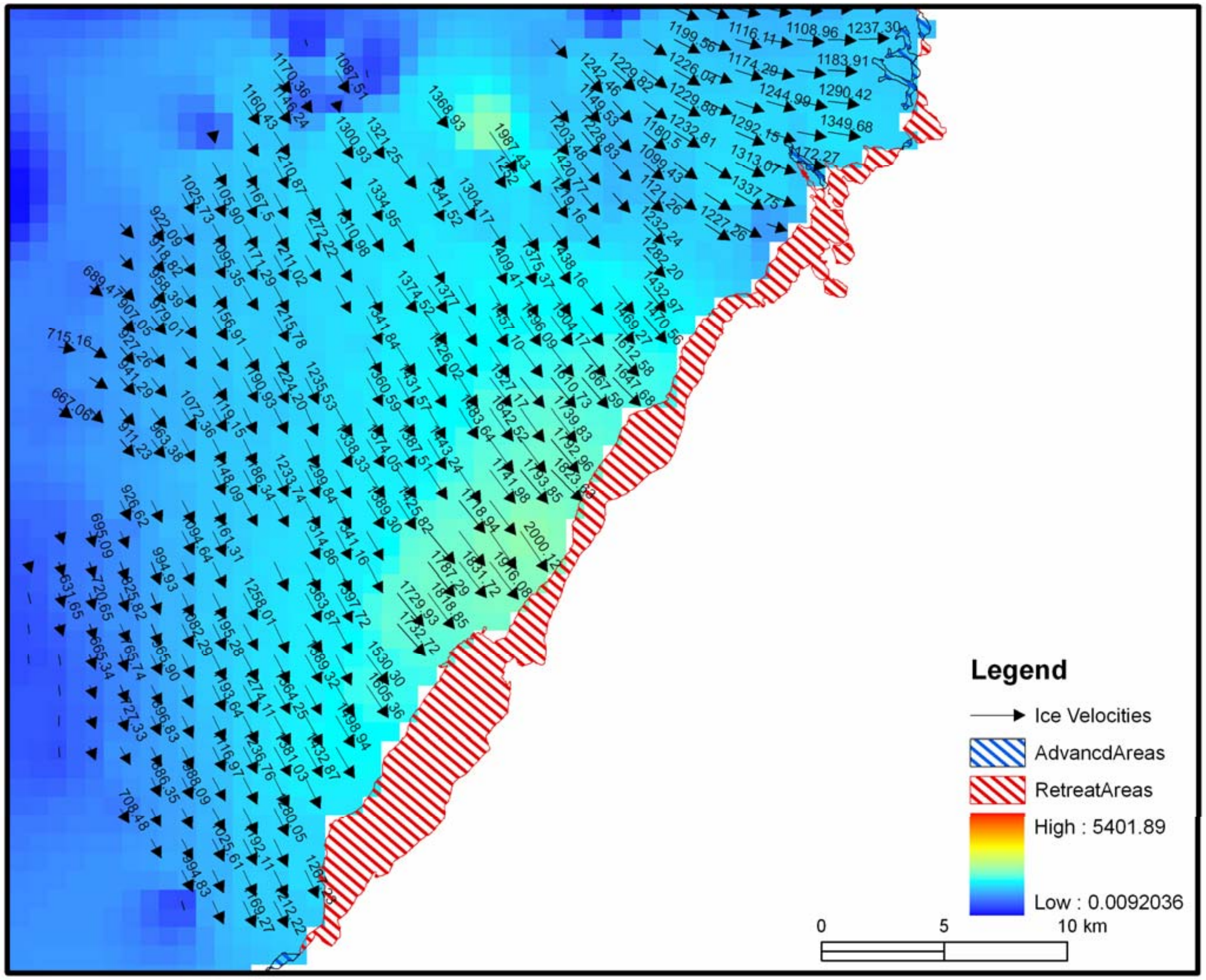

Figure 4.44 The status of ice velocities in area C

4.5.2 *Mass loss analysis*

To calculate the main three mass loss, including Ronne, Ross, and Larsen Ice Shelf, during 1997~2000, the ice density, retreat areas obtained from Section 3.8, are their average thickness are incorporated together to calculate their contribution to the ocean. Table 4.3 illustrates the results of mass loss for three mass loss during 1997~ 2000. The overall estimation ranges from 7762~8575 Gt. The loss in volume is larger than the Irish Sea.

Table 4.3 The three mass loss during 1997~2000

Feature	**Retreat Areas (m^2)**	**Average Thickness (m)**	**Ice Density (kg/m^3)**	Mass loss(Gt)
Ronne Ice Shelf	17109178680.40	300	830~917	4260~1706
Ross Ice Shelf	11841179125.90	304.2	830~917	2989~3303
Larsen Ice Shelf	2699273279.52	228.6	830~917	512~565
			Sum	7762~8575

5 CONCLUSIONS

This research has examined the ice dynamics of the Antarctic coast by using the sequential high resolution Radarsat SAR images acquired respectively in 1997 and 2000. The methodological contributions of this research include the improvement of the existing coastline extraction method, the development of a new image matching method for effectively deriving ice velocities from sequential satellite images, and implementation of two ArcGIS extension modules. The scientific contributions include the extraction of a complete, high resolution coastline for Antarctica from the 2000 SAR images, the derivation of two dimensional velocity fields for selected coastal regions from the 1997 and 2000 SAR images pairs, and the observations and findings about the ice margin variation and ice flow pattern changes of the Antarctic coast. These observation and findings are useful and helpful for improving our knowledge and understanding of the ice dynamics of the Antarctic Ice Sheet and its relationship with the current and future global and regional climate changes.

The locally adaptive thresholding method for automated coastline extraction has been further enhanced in this research. By taking advantage of previous coastline, the enhanced method limits the image processing to a narrow buffer zone for the current coastline detection and increases the number of threshold values to be computed along the coastal zone. In this way, the modified method improves the accuracy of the extracted coastline position. The source codes written in C++ .NET have been embedded into ArcGIS as an extension module by using VB .NET and ArcObjects programming.

This extension module in ArcGIS is useful for other future coastline extraction applications.

Conventional cross-correlation image matching methods have a difficulty in deriving a complete, dense velocity filed for the areas with a large flow speed variation. This problem is even exacerbated when sequential satellite images have a large time interval. To overcome the problem, a multi-scale, hierarchical image matching method is developed in this research and is implemented as an ArcGIS image matching extension module. Extensive experiments demonstrate that the newly developed multi-scale, hierarchical image matching method has greatly improved the computational speed and the quality of the derived velocity measurements. It can effectively handle the area with a strong spatial velocity variation like the Amery Ice Shelf where the ice flow speed ranges from 3 m/a to 1549 m/a. The statistical analysis suggests that the accuracy of velocity measurements resulted from applying the multi-scale, hierarchical image matching method to the 1997 and 2000 Radarsat SAR sequential image pairs is about 14 m/a). Although the accuracy is not as high as those derived from the InSAR technique, it found that the image matching based feature tracking method is complementary to the InSAR technique. The experiment in the Amery Ice Shelf demonstrates that large data gaps caused by the temporal decorrelation in the InSAR analysis can be filled in by the measurements derived from image matching based feature tracking method. The other advantage over the InSAR technique is that the image matching based feature tracking method can be applied optical satellite images (e.g. Landsat and SPOT images) and aerial photographs acquired decades ago to derive ice flow fields in history, when no interferometric SAR data were acquired at that time.

With the enhanced locally adaptive thresholding method, the 2000 coastline has been numerically delineated for the Antarctic Ice Sheet. It has a 25 m spatial resolution, and an absolute positional accuracy of about 130 m. This complete, continent scale coastline is a result of three months of day and night efforts for data processing, editing and quality control activities. By applying the multi-scale, hierarchical image matching technique, accurate and dense velocity fields have been derived for a number of selected regions, including the Amery Ice Shelf and three glaciers around Waldron Cape. These velocity measurements are utilized to analyze the ice flow pattern changes and ice front calving rates by comparing the historic observations of ice velocity and the ice margin change rates detected by coastline comparisons.

The 2000 Antarctic coastline has been compared with the 1997 coastline from the Radarsat SAR images and the 1963 coastline derived from historic Argon DISP satellite photographs. The comparisons clearly show that the Antarctic ice margin has experience dramatic changes during the past four decades. The most dynamic features along the Antarctic coast are ice shelves and outlet glaciers, and they could retreat as much as 13,177 meters per year like the front of the Ronne Ice Shelf and also could advance by 3,107 meters per year like Thwaites Glacier. The advance or retreat magnitude in terms of area extent and annual front position moving rate are calculated and inventoried for 200 ice shelves and outlet glaciers along the Antarctic coast. The grounded ice margins beyond the ice shelves and outlet glaciers are relatively stable, and their positional changes are minimal.

In the past four decades, the Antarctic ice sheet experienced net retreat and its areal extent has been reduced significantly. The net retreat rate of the Antarctic Ice sheet extent is increasing in the recent years. During 1963-1997, the Antarctic Ice Sheet was reduced by 48,327 km^2, with an annual reduction rate of about 1,421 km^2/a. During 1997-2000, the extent of the Antarctic Ice sheet was further reduced by 39,590 km^2, larger than the state of Maryland. This represents a much increased net retreat rate of 13221 km^2/a.

Despite a consistent overall net retreat trend, strong spatial variations and complex pattern in advance and retreat has been highlighted during 1963-2000. The analysis results show that the ice shelves and glaciers on the Antarctic Peninsula have a sustained retreating trend in the past four decades. This observation is consistent with the reports of the regional climate warming trend and a series of ice shelf collapses in this region (Blunier et al., 1998; Fyfe et al., 1999; Huybrechts & Oerlemans, 1990; Rignot et al., 2004; Rott et al., 1996; Rott et al., 2002). During 1997-2000, a portion of the Larsen Ice Shelf on the Antarctic Peninsula as large as 2,699 km^2 was disintegrated. It is detected that during 1997-2000 the Ross Ice Shelf and Ronne Ice Shelf underwent the most significant net retreat, the Amery Ice shelf experienced the considerable net advance, and the Shackleton Ice Shelf remain unchanged. However, the dynamic behaviors of these ice shelves were in totally different or opposite direction during 1963-1997.

The comparison of the ice velocities during 1997-2000 derived from the sequential Radarsat SAR images with the ice velocity observations during 1970-1971 by conventional ground surveys reveals that the ice flow speed in the front part of the Amery Ice Shelf has increased by about 50-200 m/a. The possible reason is that the large scale of ice calving took place during 1963-1997 and the loss of a large area of ice mass in the front reduced the buttress force. The reduction in the buttress force of the ice shelf might have induced the increase in ice flow velocity in the current front part of the ice shelf. The substantial velocity increase (upsurge) would change the strain rate and stability of the ice shelf. Its possible impacts need to be monitored and investigated in the future research.

It is also demonstrated that the iceberg calving rate can be calculated by integrating the ice margin change measurement with the ice flow velocity at the terminus of the outlet glacier (i.e. the underneath melting does not include in the the process of calculation). During 1997-2000, the glaciers around Waldron Cape had an ice calving rates about 980-2110 m/a. By combining the ice thickness information, the ice loss of the Antarctic Ice Sheet to the ocean can be calculated. During 1997-2000, the total ice mass loss of Ross Ice Shelf, Ronne Ice Shelf, and Larsen Ice Shelf is estimated to be 7762~8575 Gt, with an annual loss rate of about 2596~2868 Gt/a.

It should be pointed out that the density and precision of the velocity filed derived from the multi-scale, hierarchical image matching based feature tracking method are still inferior to those derived from the InSAR technique. The success of the image matching based feature tracking method largely depends on the existence of surface features and texture. Despite the improvement in computational speed and measurement reliability, the multi-scale, hierarchical image matching method may fail to generate velocity measurements in the featureless or texture-poor areas. In addition, the current image matching algorithm arbitrarily selects a set of regularly spaced pixels as the candidate pixels where the displacement and velocity measurements are attempted by the image matching process. Because some of these arbitrarily selected candidate pixels may locate in the featureless or texture-poor areas, the rate of successful matching is limited.

In the future research, the interesting point detector like Moravec operator will be evaluated to identify the corner-type pixels as the candidate pixels for matching. Since the neighborhood of such a corner-type pixel has a large intensity variation and high contrast, it is expected that the matching success rate would be enhanced by the introduction of interesting point detector to identify good candidate pixels for matching attempts. Due to the time constraint, the velocity fields are only derived for a small number of selected areas. The 1997 and 2000 sequential Radarsat SAR images are available for all the Antarctic coast. In addition, the velocity measurements derived from sequential Landsat Satellite data acquired during 1980s and 1990s are also available in many locations, such as Byrd Glacier, Ice Streams in West Antarctica, Mertz Glacier, Thwaites Glacier, Pine Island Glacier, Rutford Ice Stream, etc. In future research, the sequential 1997 and 2000 Radarsat SAR images over these regions will be processed using the multi-scale, hierarchical image matching based feature tracking method to derive the velocity fields, which will be compared with the velocity measurements in

1980s and 1990s from the sequential Landsat images for a detailed examination of the ice flow behavior and pattern.

In addition, the ice velocities between 1997 and 2000 along the Antarctic coastline can be extracted by the multi-scale image matching method and the two-year coastlines has already been delineated. The mass loss during 2.99 years can be calculated if the ice calving rate and ice thickness estimation, derived from ICESat altimetric measurement, are incorporated in the process of calculation.

REFERENCES

Allen, J.R., & Long, D.G. (2006). Microwave observations of daily Antarctic sea-ice edge expansion and contraction rates. *IEEE Geoscience and Remote Sensing Letters, 3*, 54 - 58

Arendt, A.A., Echelmeyer, K.A., Harrison, W.D., Lingle, C.S., & Valentine, V.B. (2002). Rapid wastage of Alaska glaciers and their contribution to rising sea level *Science, 297*, 382-386.

Bamber, J.L., & Payne, A.J. (2004). *Mass balance of the cryosphere*. Cambridge: Cambridge University Press. 662 pp.

Bender, M., Sowers, T., Dickson, M.L., Orchardo, J., Grootes, P., Mayewski, P.A., & Meese, D.A. (2002). Climate correlations between Greenland and Antarctica during the past 100,000 years. *Nature, 372*, 663-666.

Bezdek, J.C., Hall, L.O., & Clarke, L.P. (1993). Review of Mr image segmentation techniques using pattern-recognition. *Medical Physics, 20*, 1033-1048.

Bindschadler, R.A., & Scambos, T.A. (1991). Satellite-image-derived velocity field of an Antarctic ice stream. *Science, 252*, 242 - 246.

Bindschadler, R.A., Vornberger, P., Blankenship, D., Scambos, T.A., & Jacobel, R. (1996). Surface velocity and mass balance of ice streams d and e, West Antarctica. *Journal of Glaciology, 42*, 461-475.

Blunier, T., Chappellaz, J., Schwander, J., Dällenbach, A., Stauffer, B., Stocker, T.F., Raynaud, D., Jouzel, J., Clausen, H.B., & Hammer, C.U. (1998). Asynchrony of Antarctic and Greenland climate change during the last glacial period. *Nature, 394*, 739-743.

Canny, J. (1986). A computational approach to edge detection. *IEEE Transactions on Pattern Analysis and Machine Intelligence, 8*, 679-698.

Chow, C.K., & Kaneko, T. (1972). Automatic boundary detection of the left ventricle from cineangiograms *Computers and Biomedical Research 5*, 388-410.

Collings, A., Williams, R.N., Young, N., & Hyland, G. (2006). A semi-automated line tracing technique for monitoring ice margins in Antarctic images. *International Journal of Remote Sensing 27*, 433 - 448.

Cufi, X., Munoz, X., Freixenet, J., & Marti, J. (2002). A review of image segmentation techniques integrating region and boundary information. *Advances in Imaging and Electron Physics, 120*, 1-39.

Dash, M.K., Bhandari, S.M., Vyas, N.K., Khare, N., Mitra, A., & Pandey, P.C. (2001). Oceansat-MSMR imaging of the Antarctic and the southern Polar Ocean. *International Journal of Remote Sensing 22*, 3253 - 3259.

Dellepiane, S., Laurentiis, R.D., & Giordano, F. (2004). Coastline extraction from SAR images and a method for the evaluation of the coastline precision *Pattern Recognition Letters 25*, 1461-1470.

Doake, C.S.M., & Vaughan, D.G. (1991). Rapid disintegration of the Wordie Ice Shelf in response to atmospheric warming. *Nature, 350*, 328-330.

El-Rabbany, A. (2002). Introduction to GPS: The global positioning system. MA: Artech House Publishers. 218 pp.

Evans, A.N. (2000). Glacier surface motion computation from digital image sequences. *IEEE Transactions on Geoscience and Remote Sensing, 38*, 1064-1072.

Fahnestock, M., Bindschadler, R., Kwok, R., & Jezek, K. (1993). Greenland ice sheet surface properties and ice dynamics from ERS-1 SAR imagery. *Science, 262*, 1530-1534.

Fox, A.J., & Cooper, A.P.R. (1994). Measured properties of the Antarctic ice sheet derived from the scar Antarctic digital database. *Polar Record, 30*, 201-206.

Fyfe, J.C., Boer, G.J., & Flato, G.M. (1999). Arctic and Antarctic oscillations and their projected changes under global warming. *Geophysical Research Letters, 26*, 1601-1604.

Gens, R., & Van Genderen, J.L. (1996). SAR interferometry: Issues, techniques, applications. *International Journal of Remote Sensing, 17*, 1803-1836.

Gill, P.E., & Murray, W. (1978). Algorithms for the solution of the nonlinear least-squares problem. *SIAM Journal on Numerical Analysis, 15*, 977-992.

Gruen, A. (1985). Adaptive least squares correlation: A powerful image matching technique. *South African Journal of Photogrammetry, Remote Sensing and Cartography, 14*, 175-187.

Hagen, J.O., Melvold, K., Eiken, T., Isaksson, E., & Lefauconnier, B. (1999). Mass balance methods on Kongsvegen, Svalbard. *Geografiska Annaler: Series A, Physical Geography, 81*, 593-601.

Haverkamp, D., Soh, L.K., & Tsatsoulis, C. (1995). A comprehensive, automated approach to determining sea ice thickness from SAR data. *IEEE Transactions on Geoscience and Remote Sensing 33*, 46-57.

Herzfeld, U.C. (1999). Geostatistical interpolation and classification of remote sensing data from ice surfaces. *International Journal of Remote Sensing 20*, 307 - 327.

Hobrough, U. (1959). Automatic stereoplotting. *Photogrammetric Engineering & Remote Sensing, 25*, 763-769.

Hooke, R.L. (2005). *Principles of glacier mechanics*. Cambridge: Cambridge University Press. 429 pp.

Huybrechts, P., & Oerlemans, J. (1990). Response of the Antarctic ice sheet to future greenhouse warming. *Climate Dynamics, 5*, 93-102.

IPCC (2001). Climate change 2001: The scientific basis. In J. T. Houghton, Y. Ding, D. J. Griggs, M. Noguer, P. J. van der Linden, X. Dai, K. Maskell, & C. A. Johnson (Eds.), *Contribution of working group 1 to the third assessment report of the intergovernmental panel on climate change*. Cambridge: Cambridge University Press. 881 pp.

Jezek, K.C., Farness, K., Carande, R., Wu, X., & Labelle-Hamer, N. (2003). Radarsat 1 synthetic aperture radar observations of Antarctica: Modified Antarctic mapping mission, 2000. *Radio Science, 38*, 8067.

Jezek, K.C., Carsey, F., Crawford, J., Curlander, J., Holt, B., Kaupp, V., Lord, K., Labelle-Hammer, N., Mahmood, A., & Ondrus, P. (1998). Snapshots of Antarctica from radarsat-1. *Geoscience and Remote Sensing Symposium Proceedings, 1998. IGARSS'98. 1998 IEEE International, 3*, 1428-1430.

Joughin, I. (2006). Climate change: Greenland rumbles louder as glaciers accelerate *Science, 311*, 1719-1720.

Kääb, A., Paul, F., & Huggel, C. (2003). Glacier monitoring from aster imagery: Accuracy and applications. *Proceedings of EARSeL-LISSIG-Workshop Observing our Cryosphere from Space, 2*, 43-53.

Lee, J.S. (1980). Digital image enhancement and noise filtering by use of local statistics. *IEEE Transactions on Pattern Analysis and Machine Intelligence, PAMI-2*, 165-168.

Lee, J.S., & Jurkevich, I. (1990). Coastline detection and tracing in SAR images. *IEEE Transactions on Geoscience and Remote Sensing, 28*, 662 - 668

Levenberg, K. (1944). A method for the solution of certain non-linear problems in least squares. *Quarterly of Applied Mathematics, 2*, 164-168.

Liu, H., & Jezek, K.C. (2004a). Automated extraction of coastline from satellite imagery by integrating Canny edge detection and locally adaptive thresholding methods. *International Journal of Remote Sensing, 25*, 937-958.

Liu, H., & Jezek, K.C. (2004b). A complete high-resolution coastline of Antarctica extracted from orthorectified radarsat SAR imagery. *Photogrammetric Engineering & Remote Sensing, 70*, 605-616.

Lucchitta, B.K., & Ferguson, H.M. (1986). Antarctica-measuring glacier velocity from satellite images. *Science, 234*, 1105-1108.

Lucchitta, B.K., Rosanova, C.E., & Mullins, K.F. (1995). Velocities of pine island glacier, West Antarctica, from ERS-1 SAR images. *Annals of Glaciology, 21*, 277-283.

Manson, R., Coleman, R., Morgan, P., & King, M. (2000). Ice velocities of the Lambert glacier from static GPS observations. *Earth Plants and Space, 52*, 1031-1036.

Marquardt, D.W. (1963). An algorithm for least-squares estimation of nonlinear parameters. *Journal of the Society for Industrial and Applied Mathematics, 11*, 431-441.

Mason, D.C., & Davenport, I.J. (1996). Accurate and efficient determination of the shoreline in ERS-1 SAR images. *IEEE Transactions on Geoscience and Remote Sensing 34*, 1243 - 1253.

McConnell, R., Kwok, R., Curlander, J.C., Kober, W., & Pang, S.S. (1991). Ψ-s correlation and dynamic time warping: Two methods for tracking ice floes in SAR images. *IEEE Transactions on Geoscience and Remote Sensing, 29*, 1004-1012.

Moctezuma, M., Maitre, F.H., & Parmiggiani, F. (1995). Sea-ice velocity fields estimation on Ross Sea with NOAA-AVHRR. *IEEE Transactions on Geoscience and Remote Sensing, 33*, 1286-1290.

Oerlemans, J. (2005). Extracting a climate signal from 169 glacier records. *Science, 308*, 675-677.

Pal, N.R., & Pal, S.K. (1993). A review on image segmentation techniques. *Pattern Recognition, 26*, 1277-1294.

Paterson, W.S.B. (1994). *The physics of glaciers* (3rd ed.). Oxford, Unied Kingdom: Elsevier Science Ltd. 481 pp.

Petit, J.R., Jouzel, J., Raynaud, D., Barkov, N.I., Barnola, J.M., Basile, I., Bender, M., Chappellaz, J., Davis, M., & Delaygue, G. (1999). Climate and atmospheric history of the past 420, 000 years from the Vostok Ice Core, Antarctica. *Nature, 399*, 429-436.

Remy, F., & Minster, J.F. (1997). Antarctica ice sheet curvature and its relation with ice flow and boundary conditions. *Geophysical Research Letters, 24*, 1039-1042.

Remy, F., & Legresy, B. (2004). Antarctic ice sheet shape response to changes in outlet flow boundary conditions. *Global and Planetary Change, 42*, 133-142.

Rignot, E., Casassa, G., Gogineni, P., Krabill, W., Rivera, A., & Thomas, R. (2004). Accelerated ice discharge from the Antarctic peninsula following the collapse of Larsen b ice shelf. *Geophysical Research Letters, 31*, L18401.

Rott, H., Skvarca, P., & Nagler, T. (1996). Rapid collapse of northern Larsen ice shelf, Antarctica. *Science, 271*, 788-792.

Rott, H., Rack, W., Skvarca, P., & De Angelis, H. (2002). Northern Larsen ice shelf, Antarctica: Further retreat after collapse. *Annals of Glaciology, 34*, 277-282.

Scambos, T.A., Dutkiewicz, M.J., Wilson, J.C., & Bindschadler, R.A. (1992). Application of image cross-correlation to the measurement of glacier velocity using satellite image data. *Remote Sensing of Environment, 42*, 177-186.

Schenk, T. (1999). Digital photogrammetry. OH: TerraScience. 428 pp.

Schenk, T., Li, J.C., & Toth, C. (1991). Towards an autonomous system for orienting digital stereopairs. *Photogrammetric Engineering & Remote Sensing, 57*, 1057-1064.

Schwerdtfeger, W. (1984). *Weather and climate of the Antarctic*. Amsterdam: Elsevier. 262 pp.

Sohn, H.-G., & Jezek, K.C. (1999). Mapping ice sheet margins from ERS-1 SAR and spot imagery. *International Journal of Remote Sensing 20*, 3201 - 3216.

Tarachandani, A., & Boltz, D. (2006). Review of the basic image processing and segmentation techniques for biological images. *Journal of Imaging Science and Technology, 50*, 233-242.

Touzi, R., Lopes, A., & Bousquet, P. (1988). A statistical and geometrical edge detector for SAR images. *IEEE Transactions on Geoscience and Remote Sensing, 26*, 764 - 773

van der Kooij, M.W.A., Armour, B., Ehrismann, J., Schwichow, H., & Sato, S. (1996). A workstation for spaceborne interferometric SAR data. In, *Geoscience and Remote*

Sensing Symposium, 1996. IGARSS'96.'Remote Sensing for a Sustainable Future.', International (pp. 339-341). Lincoln, NE, USA

Young, N.W., & Hyland, G. (2002). Velocity and strain rates derived from insar analysis over the amery ice shelf, east Antarctica. *Annals of Glaciology, 34*, 228-234.

APPENDIX A

The list of the advance or retreat distance of 200 ice shelves or glaciers

Item	Status	Feature Name	LONGITUDE	LATITUDE	Left (m)	Central (m)	Right (m)	Average Change(m)	Annual Rate(m)
1	advance	Abbot Ice Shelf	-96.0000	-72.7500	382	576	513	490	164
2	advance	Adams Glacier	163.6333	-78.1160	426	1677	1774	1292	432
3	retreat	Akebono Glacier	42.8833	-68.1160	-486	-4387	-279	-1717	-573
4	advance	Albrecht Penck Glacier	162.3333	-76.6660	119	100	131	117	39
5	advance	Amery Ice Shelf	71.0000	-69.7500	1805	3967	2826	2866	957
6	advance	Anandakrishnan Glacier	-140.0833	-75.5330	871	899	1057	942	315
7	advance	Assender Glacier	46.4167	-67.6000	2024	504	362	963	322
8	advance	Astrolabe Glacier Tongue	140.0833	-66.7000	637	1449	1223	1103	368
9	advance	Auster Glacier	50.7500	-67.2000	539	567	299	468	156
10	retreat	Bach Ice Shelf	-72.0000	-72.0000	-521	-1167	-752	-813	-272
11	advance	Barnett Glacier	167.5000	-70.9830	281	403	321	335	112
12	advance	Bawden Ice Rise	-60.8333	-66.9830	772	1632	1797	1400	468
13	retreat	Bayly Glacier	-61.8333	-64.6160	-162	-141	-208	-170	-57
14	retreat	Beaver Glacier	50.6667	-67.0330	-2169	-928	-811	-1303	-435
15	advance	Behr Glacier	168.0833	-72.9160	2342	2476	1066	1961	655
16	advance	Bilgeri Glacier	-64.7833	-66.0160	105	144	67	105	35
17	advance	Birley Glacier	-64.3500	-65.9660	194	300	349	281	94
18	retreat	Bl?riot Glacier	-61.1667	-64.4160	-198	-122	-184	-168	-56
19	retreat	Blanchard Glacier	-62.0833	-64.7330	-94	-606	-164	-288	-96
20	advance	Blue Glacier	164.1667	-77.8330	87	78	151	106	35
21	advance	Bolton Glacier	-62.9667	-65.0160	257	136	102	165	55
22	retreat	Bongrain Ice Piedmont	-71.5000	-69.0000	-375	-367	-841	-528	-176

23	advance	Borchgrevink Glacier Tongue	168.8333	-73.3500	772	738	939	817	273
24	retreat	Bornmann Glacier	170.2167	-72.3330	-195	-484	-749	-476	-159
25	retreat	Bridgman Glacier	170.0833	-72.3830	-90	-76	-90	-85	-29
26	advance	Brunt Ice Shelf	-25.0000	-75.6660	2127	2988	4157	3090	1032
27	advance	Burnette Glacier	170.0500	-72.0160	389	426	392	403	134
28	advance	Butler Glacier	-152.7000	-77.4000	107	1332	1150	863	288
29	retreat	Campbell Glacier Tongue	164.4000	-74.6000	-378	-2283	-515	-1059	-354
30	retreat	Carlson Glacier	-68.0500	-69.4160	-6967	-9652	-6130	-7583	-2532
31	advance	Cheetham Ice Tongue	162.9167	-75.7500	195	235	247	226	75
32	advance	Chijire Glacier	43.3833	-68.0500	1053	1205	932	1063	355
33	advance	Clarke Glacier	-139.1000	-75.1830	1581	1452	1611	1548	517
34	advance	Conger Glacier	103.5500	-66.0330	1178	1104	919	1067	356
35	advance	Cook Ice Shelf	152.5000	-68.6660	2337	2251	2318	2302	769
36	advance	Cosgrove Glacier	59.1667	-67.4830	463	783	2053	1100	367
37	advance	Crosson Ice Shelf	-109.5000	-74.9500	3457	5378	8887	5907	1973
38	retreat	D?lk Glacier	76.4500	-69.4330	-698	-1131	-724	-851	-284
39	retreat	Dawson-Lambton Glacier	-26.7500	-76.1330	-1834	-1412	-1126	-1457	-487
40	advance	De Haven Glacier	127.5333	-67.0500	2558	4468	1375	2801	935
41	retreat	Demas Ice Tongue	-103.1167	-72.2830	-1421	-3562	-2703	-2562	-856
42	advance	Dennistoun Glacier	168.0000	-71.1830	470	604	515	530	177
43	advance	DeVicq Glacier	-131.0000	-75.0000	2156	3364	3239	2920	975
44	advance	Deville Glacier	-62.5833	-64.8000	109	169	266	181	61
45	advance	Dinsmoor Glacier	-59.9833	-64.3660	958	737	420	705	235
46	advance	Diplock Glacier	-58.8333	-64.0500	512	636	647	598	200
47	retreat	Dotson Ice Shelf	-112.3667	-74.4000	-1300	-1943	-1621	-1621	-541
48	retreat	Double Curtain Glacier	163.5167	-77.6500	-930	-825	-945	-900	-301
49	advance	Downer Glacier	56.4167	-66.9660	1584	1999	1270	1618	540
50	advance	Drygalski Ice Tongue	163.5000	-75.4000	2107	2009	2276	2131	712

51	advance	Dugdale Glacier	169.8333	-71.6330	255	300	212	256	85
52	advance	Edgeworth Glacier	-59.9167	-64.3830	234	483	954	557	186
53	advance	Edward VIII Ice Shelf	56.5500	-66.8330	205	190	133	176	59
54	advance	Ekstr?m Ice Shelf	-8.0000	-71.0000	634	792	833	753	251
55	advance	Erebus Glacier Tongue	166.6667	-77.7000	213	262	219	231	77
56	advance	Ferrar Glacier	163.0000	-77.7660	619	245	1072	645	215
57	advance	Filchner Ice Shelf	-40.0000	-79.0000	4147	3138	1916	3067	1024
58	advance	Fimbul Ice Shelf	-0.1667	-70.5000	1858	1826	2391	2025	676
59	retreat	Flattunga	40.0000	-68.8500	-1686	-1727	-2264	-1892	-632
60	advance	Forbes Glacier	-66.7333	-67.8000	217	565	487	423	141
61	advance	Fortenberry Glacier	166.9500	-70.8000	376	353	355	361	121
62	advance	Fox Glacier	114.3333	-66.2500	1654	2790	2216	2220	741
63	retreat	Frost Glacier	129.0000	-67.0830	-1535	-2241	-1480	-1752	-585
64	retreat	Funk Glacier	-63.7667	-65.5660	-710	-1724	-997	-1144	-382
65	retreat	Gilchrist Glacier	114.1000	-66.1160	-203	-1537	-1428	-1056	-353
66	advance	Gillett Ice Shelf	159.7000	-69.5830	167	487	396	350	117
67	retreat	Glezen Glacier	162.3000	-76.5330	-6243	-7567	-9584	-7798	-2604
68	retreat	Hampton Glacier	-70.0833	-69.3330	-1138	-392	-941	-824	-275
69	advance	Harbord Glacier Tongue	162.8333	-75.9160	257	243	321	274	91
70	advance	Hargreaves Glacier	74.3333	-69.7660	99	261	187	182	61
71	advance	Hawkins Glacier	107.5167	-66.5660	730	857	882	823	275
72	retreat	Hayes Glacier	-27.9000	-76.2660	-1197	-899	-1687	-1261	-421
73	advance	Haynes Glacier	-109.5000	-75.4160	1796	2721	2898	2472	825
74	advance	Hedblom Glacier	162.4000	-76.5660	124	110	100	111	37
75	advance	Helen Glacier	93.9167	-66.6660	1147	2851	2887	2295	766
76	advance	Henryk Glacier	-62.5000	-64.7000	101	248	119	156	52
77	retreat	Higashi-naga-iwa Glacier	41.6333	-68.4500	-687	-1623	-1289	-1200	-401
78	retreat	Hill Glacier	-75.6667	-73.0500	-1338	-1222	-1246	-1269	-424
79	advance	Hobbs Glacier	164.4000	-77.9000	84	73	78	79	26

80	advance	Holcomb Glacier	-142.8000	-75.5830	597	742	640	660	220
81	retreat	Holmes Glacier	126.9000	-66.7660	-465	-316	-1151	-644	-215
82	retreat	Honn?r Glacier	39.8333	-69.3830	-4553	-7004	-3717	-5092	-1700
83	advance	Hoseason Glacier	58.1167	-67.1000	131	466	957	518	173
84	advance	Hovde Glacier	76.9167	-69.2500	159	453	382	331	111
85	advance	Hulbe Glacier	-125.9167	-73.7830	382	795	1017	731	244
86	advance	Hunt Glacier	162.4167	-76.8660	161	124	93	126	42
87	retreat	Ichime Glacier	42.1333	-68.3830	-333	-1235	-1107	-892	-298
88	advance	Ironside Glacier	169.6667	-72.1330	1105	862	614	861	287
89	advance	Jackson Glacier	-135.7500	-74.7830	997	1368	808	1058	353
90	advance	Jelbart Ice Shelf	-4.5000	-70.5000	1092	1688	2026	1602	535
91	retreat	Jones Ice Shelf	-67.0167	-67.5160	-538	-1888	-997	-1141	-381
92	advance	Kasumi Glacier	42.3500	-68.3330	525	548	435	502	168
93	advance	Kichenside Glacier	47.6000	-67.7660	567	577	170	438	146
94	advance	Kiletangen Ice Tongue	26.4167	-69.9500	329	479	281	363	121
95	retreat	Krebs Glacier	-61.5167	-64.6330	-485	-710	-445	-547	-183
96	advance	Langhovde Glacier	39.8000	-69.2160	584	590	2175	1116	373
97	retreat	Larsen B Ice Shelf	-65.3100	-60.9100	-25279	-30446	-23335	-26353	-8801
98	advance	Lazarev Ice Shelf	14.7500	-69.6160	734	675	644	684	229
99	retreat	Leonardo Glacier	-61.9667	-64.7000	-185	-806	-1360	-784	-262
100	retreat	Lever Glacier	-63.6667	-65.5000	-2325	-2165	-2195	-2228	-744
101	advance	Lillie Glacier Tongue	163.8000	-70.5660	630	638	577	615	205
102	retreat	Lliboutry Glacier	-66.7667	-67.5000	-464	-764	-694	-641	-214
103	advance	Lord Glacier	-138.6833	-75.2000	1428	1235	517	1060	354
104	advance	Mackay Glacier Tongue	162.3333	-76.9660	754	727	825	769	257
105	advance	Manhaul Glacier	169.7500	-72.4000	135	243	192	190	63
106	advance	Mariner Glacier Tongue	168.3333	-73.4500	674	565	479	573	191
107	retreat	Marret Glacier	137.7333	-66.4330	-255	-448	-533	-412	-138

108	advance	Marston Glacier	162.5000	-76.9000	146	150	136	144	48
109	advance	Matusevich Glacier Tongue	157.2500	-69.0830	2764	2645	2802	2737	914
110	retreat	McCance Glacier	-65.9167	-66.7160	-102	-194	-504	-267	-89
111	retreat	McLeod Glacier	158.3667	-69.3660	-993	-867	-1219	-1026	-343
112	retreat	McMorrin Glacier	-67.1667	-67.9830	-698	-649	-581	-643	-215
113	retreat	McNeile Glacier	-59.4333	-63.9000	-113	-159	-151	-141	-47
114	advance	Mertz Glacier Tongue	145.5000	-67.1660	2435	3680	3893	3336	1114
115	advance	Miethe Glacier	-63.1000	-64.9330	141	109	133	128	43
116	retreat	Moran Glacier	-70.2667	-69.2330	-605	-1041	-446	-697	-233
117	retreat	Morelli Glacier	-102.6333	-72.9830	-478	-387	-582	-482	-161
118	advance	Moscow University Ice Shelf	121.0000	-67.0000	3401	4382	3439	3740	1249
119	advance	Mouillard Glacier	-60.8833	-64.3000	127	146	164	146	49
120	advance	Mulebreen	59.3500	-67.4660	1612	2112	2256	1994	666
121	advance	Murphy Glacier	-66.3333	-66.9000	129	184	145	153	51
122	advance	Murray Glacier	170.0000	-71.6500	759	278	324	454	152
123	advance	Nansen Ice Sheet	163.1667	-74.8830	506	690	1024	740	247
124	retreat	Neny Glacier	-66.4167	-68.2500	-900	-343	-305	-516	-172
125	advance	Nereson Glacier	-124.4000	-73.9330	790	694	702	729	243
126	advance	Nickerson Ice Shelf	-145.0000	-75.7500	613	640	915	723	241
127	retreat	Ninnis Glacier Tongue	147.7500	-68.0830	-12414	-29088	-23842	-21782	-7274
128	retreat	Nobile Glacier	-61.4667	-64.5330	-614	-471	-195	-427	-142
129	advance	Nordenskjld Ice Tongue	162.7500	-76.1830	760	650	656	689	230
130	advance	Northcliffe Glacier	98.8667	-66.6660	4827	5104	5248	5060	1690
131	advance	Nye Glacier	-67.5167	-67.4660	544	726	579	616	206
132	advance	Oates Piedmont Glacier	162.5833	-76.4160	140	264	213	206	69
133	advance	Oku-iwa Glacier	40.7667	-68.7000	1155	1465	776	1132	378
134	advance	Omega Glacier	41.0167	-68.6160	184	1673	1338	1065	356
135	advance	Ommanney Glacier	169.4833	-71.5330	517	472	706	565	189

136	advance	Parker Glacier	165.5500	-73.7830	379	590	531	500	167
137	advance	Payne Glacier	-96.7000	-71.9160	451	383	188	341	114
138	advance	Perkins Glacier	-136.6167	-74.9000	517	66	475	353	118
139	retreat	Pettus Glacier	-59.0667	-63.8000	-157	-98	-107	-120	-40
140	advance	Philippi Glacier	88.3333	-66.7500	2349	2297	2641	2429	811
141	advance	Pine Island Glacier	-100.0000	-75.1660	4334	6421	6412	5722	1911
142	advance	Polar Times Glacier	74.5833	-69.7660	1297	1950	2674	1974	659
143	retreat	Pryor Glacier	160.1667	-70.0830	-2818	-1475	-2150	-2148	-717
144	advance	Publications Ice Shelf	75.3333	-69.6330	2439	2028	1248	1905	636
145	retreat	Quar Ice Shelf	-11.0000	-71.3330	-2847	-2411	-3016	-2758	-921
146	retreat	Quaternary Icefall	166.5000	-77.3000	-1802	-1835	-1344	-1660	-555
147	advance	Rakuda Glacier	43.9000	-68.0500	1997	1581	1330	1636	546
148	advance	Rayner Glacier	48.4167	-67.6660	2166	3296	3358	2940	982
149	advance	Richter Glacier	-155.4167	-77.1660	982	623	637	747	250
150	retreat	Rignot Glacier	-102.0000	-73.1000	-305	-628	-560	-498	-166
151	advance	Riiser-Larsen Ice Shelf	-16.0000	-72.6660	485	690	431	535	179
152	advance	Robert Glacier	56.3000	-67.1660	2603	1869	1696	2056	687
153	advance	Robinson Glacier	107.2667	-66.5000	79	300	763	381	127
154	retreat	Ronne Ice Shelf	-61.0000	-78.5000	-24685	-33463	-60236	-39461	-13178
155	retreat	Ross Ice Shelf	-175.0000	-81.5000	-31250	-35477	-39703	-35477	-11847
156	retreat	S?lch Glacier	-66.3833	-67.0660	-1153	-2386	-1465	-1668	-557
157	advance	Sayce Glacier	-62.9833	-65.0830	361	270	322	318	106
158	advance	Schweitzer Glacier	-34.6667	-77.8330	645	821	798	755	252
159	advance	Seaton Glacier	56.4333	-66.7160	578	594	571	581	194
160	advance	Shinnan Glacier	44.6333	-67.9160	1135	310	1165	870	291
161	retreat	Shirase Glacier	38.7500	-70.0830	-9777	-10136	-8722	-9545	-3187
162	advance	Shuman Glacier	-139.5000	-75.2500	1086	954	929	989	330
163	advance	Sikorski Glacier	-98.4000	-71.8160	293	351	423	356	119

164	retreat	Skallen Glacier	39.5500	-69.6660	-9219	-7087	-8898	-8401	-2805
165	retreat	Slava Ice Shelf	154.7333	-68.8160	-4135	-5203	-5357	-4898	-1636
166	retreat	Somigliana Glacier	-67.1500	-67.0000	-1441	-1370	-1337	-1382	-462
167	advance	Stancomb-Wills Glacier Tong	-22.0000	-75.0000	4290	3900	3218	3803	1270
168	retreat	Stange Ice Shelf	-76.5000	-73.2500	-509	-1202	-874	-862	-288
169	advance	Strahan Glacier	64.6167	-67.6330	164	676	654	498	166
170	advance	Suter Glacier	167.1667	-73.5160	293	348	273	305	102
171	retreat	Suvorov Glacier	160.0000	-69.9330	-1761	-1341	-1825	-1642	-548
172	advance	Swinburne Ice Shelf	-153.9167	-77.1660	1659	470	472	867	290
173	retreat	Swithinbank Glacier	-66.7667	-67.9330	-704	-415	-784	-634	-212
174	advance	Tama Glacier	40.3667	-68.7830	528	564	354	482	161
175	retreat	Telen Glacier	39.7000	-69.6330	-8052	-8380	-7778	-8070	-2695
176	retreat	Temple Glacier	-60.0167	-64.0000	-142	-261	-298	-233	-78
177	advance	Terra Nova Glacier	167.7000	-77.4500	170	114	76	120	40
178	retreat	Thomson Glacier	-80.2167	-73.4500	-344	-1405	-447	-732	-244
179	advance	Thwaites Glacier Tongue	-106.8333	-75.0000	8906	9316	9692	9305	3107
180	advance	Tinker Glacier Tongue	165.0333	-74.1000	228	207	187	207	69
181	advance	Tomilin Glacier	159.0000	-69.5000	1153	205	1035	798	266
182	retreat	Underwood Glacier	108.0000	-66.5830	-1021	-1249	-2126	-1466	-489
183	retreat	Vallot Glacier	-67.5000	-67.3000	-609	-570	-529	-569	-190
184	advance	Vanderford Glacier	110.4333	-66.5830	1238	919	1812	1323	442
185	advance	Venable Ice Shelf	-87.3333	-73.0500	1896	1431	1808	1712	572
186	advance	Vogel Glacier	-63.1667	-65.0000	165	80	118	121	40
187	advance	Vornberger Glacier	-125.0667	-73.9160	834	818	862	838	280
188	advance	Voyeykov Ice Shelf	124.6333	-66.3330	2156	1991	2434	2194	733
189	advance	Wellman Glacier	-61.4333	-64.4830	200	170	149	173	58
190	advance	West Ice Shelf	85.0000	-66.6660	1835	1425	1115	1458	487
191	advance	Wheatstone Glacier	-62.5167	-64.7330	173	238	190	200	67

192	retreat	Whitecloud Glacier	-59.5333	-63.9160	-131	-135	-145	-137	-46
193	advance	Widdowson Glacier	-65.7667	-66.7160	364	502	610	492	164
194	retreat	Widmark Ice Piedmont	-65.5000	-66.2830	-678	-1142	-563	-795	-265
195	advance	Wiggins Glacier	-64.0500	-65.2330	141	116	148	135	45
196	retreat	Wilkins Ice Shelf	-70.2500	-73.0000	-17225	-20435	-28032	-21897	-7312
197	advance	Williamson Glacier Tongue	114.4000	-66.4830	2528	5425	4666	4206	1405
198	advance	Wyers Ice Shelf	49.9000	-67.1830	327	191	334	284	95
199	advance	Wylde Glacier	166.7000	-73.5330	227	199	298	241	81
200	advance	Zubchatyy Ice Shelf	49.0833	-67.2160	171	299	277	249	83

APPENDIX B

The list of ice velocity comparison of field survey, InSAR, and SAR measuring

	Geo_Location		Ice Velocity(m/a)				
Item	X	Y	Field Survey	InSAR	SAR	InSAR-Field Survey	SAR-Field Survey
1	71.4970	-69.4506	774.42	809.14	783.30	34.72	8.88
2	71.9764	-69.5525	748.69	754.90	761.69	6.21	13.00
3	71.8778	-69.5258	766.25	768.94	735.07	2.69	-31.18
4	72.0564	-69.5755	726.66	734.52	755.45	7.86	28.79
5	72.2034	-69.6171	691.51	706.39	722.02	14.88	30.51
6	72.3667	-69.6588	657.75	662.07	690.79	4.32	33.04
7	72.5263	-69.6914	599.06	622.00	638.51	22.94	39.45
8	72.7070	-69.7215	554.87	587.05	569.05	32.18	14.18
9	72.9237	-69.7689	481.75	521.22	521.66	39.47	39.91
10	73.0948	-69.7933	408.98	408.74	227.20	-0.25	-181.78
11	73.2767	-69.8102	126.19	75.90	43.18	-50.29	-83.01
12	71.6210	-69.5696	725.37	737.95	614.05	12.58	-111.32
13	69.7928	-70.9601	348.98	347.23	337.46	-1.75	-11.52
14	71.5629	-69.6156	714.73	705.78	770.30	-8.95	55.57
15	69.7767	-70.9741	347.45	346.93	352.83	-0.52	5.38
16	71.4981	-69.6665	672.95	679.61	571.21	6.65	-101.74
17	71.4437	-69.7091	650.85	661.85	634.27	11.00	-16.58
18	71.3771	-69.7609	640.46	633.29	631.28	-7.18	-9.18
19	71.3230	-69.8029	615.33	613.75	594.80	-1.58	-20.53
20	71.2767	-69.8386	591.89	596.69	612.40	4.80	20.50
21	71.2198	-69.8773	590.57	577.31	524.64	-13.26	-65.93
22	71.1420	-69.9420	547.91	546.16	468.66	-1.75	-79.25
23	69.8359	-70.9605	348.53	348.87	335.58	0.34	-12.95

24	70.0709	-70.9694	354.45	356.49	316.45	2.04	-38.00
25	70.3170	-70.9788	360.83	363.95	351.03	3.12	-9.80
26	70.3920	-70.9819	359.52	363.62	367.26	4.10	7.74
27	70.5306	-70.9895	350.68	355.71	486.83	5.03	136.15
28	70.6149	-70.9951	341.51	347.23	390.58	5.72	49.07
29	70.7478	-71.0043	327.14	333.31	330.40	6.17	3.26
30	71.0713	-69.9957	544.19	522.40	432.56	-21.79	-111.63
31	70.9889	-70.0580	512.33	501.20	567.30	-11.13	54.97
32	70.9408	-70.1090	508.18	484.78	489.96	-23.40	-18.22
33	70.8573	-70.1831	469.70	461.33	488.95	-8.37	19.24
34	70.7881	-70.2417	471.83	441.76	396.82	-30.07	-75.01
35	70.7515	-70.2725	460.59	431.41	343.20	-29.18	-117.39
36	70.6960	-70.3192	445.06	411.53	335.98	-33.53	-109.08
37	70.6290	-70.3752	397.95	395.38	384.23	-2.57	-13.72
38	70.5920	-70.4061	408.75	390.39	407.48	-18.36	-1.27
39	70.5432	-70.4466	398.37	383.95	358.83	-14.42	-39.54
40	69.6473	-70.9291	345.34	342.55	380.99	-2.79	35.65
41	69.5753	-70.9146	343.91	339.76	399.85	-4.15	55.94
42	69.3902	-70.8789	319.42	313.91	331.31	-5.51	11.89
43	69.3174	-70.8657	299.54	291.37	310.90	-8.17	11.36
44	69.2271	-70.8479	252.17	248.69	278.35	-3.48	26.18
45	69.0909	-70.8201	11.95	1.46	55.67	-10.49	43.72
46	69.0028	-70.8045	12.86	0.77	59.90	-12.09	47.04
47	68.8941	-70.7910	13.90	1.16	57.38	-12.74	43.48
48	70.4496	-70.5240	387.05	376.70	331.38	-10.35	-55.67
49	70.3931	-70.5704	375.75	373.03	239.99	-2.72	-135.76
50	70.3033	-70.6436	372.07	369.18	215.74	-2.89	-156.33
51	70.2747	-70.6668	367.73	367.16	272.49	-0.57	-95.24
52	70.1881	-70.7368	364.43	361.36	282.80	-3.07	-81.63

53	70.0694	-70.7745	358.93	357.80	403.61	-1.13	44.68
54	69.9938	-70.8420	354.90	354.35	489.65	-0.55	134.75
55	69.9209	-70.8943	354.39	351.32	340.36	-3.07	-14.03
56	69.8336	-70.9303	349.08	348.57	349.89	-0.51	0.81
57	69.7544	-70.9934	345.76	346.13	353.88	0.37	8.12
58	69.6856	-71.0458	342.99	343.47	365.91	0.48	22.92
59	69.6096	-71.1088	340.07	339.11	369.82	-0.96	29.75
60	71.7794	-69.4290	840.05	871.71	866.61	31.66	26.56
61	71.8042	-69.4047	852.98	No Data	828.28	No Data	-24.70
62	71.8674	-69.3429	900.58	No Data	958.26	No Data	57.68
63	71.9263	-69.2848	970.30	No Data	901.32	No Data	-68.98
64	72.0054	-69.2062	998.05	1016.00	1046.95	17.95	48.90
65	72.0665	-69.2148	1005.33	1014.42	1031.63	9.09	26.30
66	72.0544	-69.1569	1028.57	1032.69	925.30	4.12	-103.27
67	72.0972	-69.1148	1050.94	1065.62	971.96	14.68	-78.98
68	72.1548	-69.0600	1228.21	No Data	1010.35	No Data	-217.86
69	71.6682	-69.4798	793.34	804.45	763.11	11.11	-30.23
70	71.3955	-69.4272	758.20	801.69	819.32	43.49	61.12
71	71.2751	-69.3994	731.68	798.69	872.42	67.01	140.74
72	71.1311	-69.3658	692.42	774.71	791.08	82.29	98.66
73	71.0430	-69.3453	673.58	758.34	785.21	84.75	111.63
74	70.9674	-69.3275	649.81	740.50	759.19	90.69	109.38
75	70.8660	-69.3036	617.60	727.31	748.62	109.71	131.02
76	70.7304	-69.2716	568.47	685.97	780.15	117.50	211.68
77	70.6281	-69.2474	509.10	648.78	672.73	139.68	163.63
78	70.4727	-69.2104	376.02	556.24	571.28	180.22	195.26
79	70.3690	-69.1855	286.85	468.73	492.42	181.88	205.57
80	70.2563	-69.1584	179.02	394.76	394.93	215.74	215.91
81	70.1542	-69.1336	48.84	304.16	284.41	255.32	235.57

82	71.7167	-69.4899	787.75	786.35	646.39	-1.40	-141.36
83	71.6999	-69.5040	775.87	781.99	663.21	6.12	-112.66
84	70.9001	-70.1481	787.75	471.31	509.54	-316.44	-278.21
85	70.8825	-70.1617	787.75	467.89	500.88	-319.86	-286.87

VITA

Name: Sheng-Jung Tang

Address: 7F.-2, No.421, Sihyuan Rd., Sinjhuang City, Taipei County 24250, Taiwan (R.O.C.)

Email Address: tsj@geog.tamu.edu

Education: B. Eng., National Taiwan University of Science and Technology, Taiwan, 1995
M.S., Geography, Texas A&M University, 2007